AERODYNAMICS AND DYNAMICS OF BLUFF BODIES IN PRESENCE OF THE MOVING SURFACE BOUNDARY-LAYER CONTROL

SANDEEP R. MUNSHI

B.E., Maharaja Sayajirao University, India, 1987
M.Sc.(Engg.), Indian Institute of Science, Bangalore, India, 1990

A THESIS SUBMITTED IN PARTIAL FULFILMENT OF
THE REQUIREMENTS FOR THE DEGREE OF

DOCTOR OF PHILOSOPHY

in

The Faculty of Graduate Studies
Department of Mechanical Engineering

We accept this thesis as conforming
to the required standard

THE UNIVERSITY OF BRITISH COLUMBIA

January 1996

In presenting this thesis in partial fulfilment of the requirements for an advanced degree at the University of British Columbia, I agree that the Library shall make it freely available for reference and study. I further agree that permission for extensive copying of this thesis for scholarly purposes may be granted by the head of my department or by his or her representatives. It is understood that copying or publication of this thesis for financial gain shall not be allowed without my written permission.

Department of MECHANICAL ENGINEERING

The University of British Columbia
Vancouver, Canada

Date JANUARY 31ST, 1996.

ABSTRACT

Moving Surface Boundary-layer Control (MSBC) was applied to several two dimensional bluff bodies using a high speed rotating cylinder as a momentum injecting device. Flow past a symmetric airfoil; a D-section; as well as square and rectangular prisms, representing a family of shapes with progressively increasing bluffness were studied in presence of the MSBC. In the case of the airfoil, the leading edge was replaced by a rotating cylinder; while the cylindrical element formed the top and bottom upstream corners of the D-section, square and rectangular prisms.

Extensive wind tunnel investigation gave data about the effect of system parameters like rate of the momentum injection, angle of attack and the surface condition of the cylinder on steady and fluctuating components of the pressure distribution around the body, vortex shedding frequency (Strouhal number), and the lift and drag coefficients. A gain in the Strouhal number with increasing momentum injection suggest a decrease in the effective bluffness of the body. A significant reduction in the drag (up to 80%) was observed for the prisms at a maximum rate of momentum injection, $U_C/U = 4$ (U_C = cylinder surface speed, U = freestream wind speed). In the case of the airfoil, the lift coefficient increased by 160% and the stall angle was delayed from 10° to 48°. A rough criterion in terms of the location of the stagnation point was established to help decide the reversal in the direction of momentum injection as a function of angle of attack to ensure continued benefit.

Effect of momentum injection in suppressing the vortex resonance and galloping type of instabilities were studied by mounting the bluff prism models on a dynamic test rig inside the wind tunnel test section. The measurement of amplitude and frequency of the transverse oscillations over a range of wind speeds showed complete vibration suppression for momentum injection rates $U_C/U \le 2$. Asymmetric momentum injection (e.g. top cylinder rotating, bottom cylinder stationary) was also found to be effective in disrupting the vortex shedding process and thereby inhibiting vibrations. The suppression of galloping instability in presence of the MSBC was also predicted by the quasisteady analysis.

A numerical panel method was developed to simulate bluff body fluid dynam-

ics in presence of the MSBC. The body is descretized into a large number of panels (100 - 150) with each panel comprising of a continuous distribution of linearly varying vorticity and a constant source strength. A set of linear algebraic equations approximates the Fredholm type integral equation derived from ideal fluid flow assumption. The wake is modelled by upper and lower 'free vortex layers' emanating from the separation points on the body. Vorticity is allowed to be shed and dissipated as it is convected downstream along the panels on the 'free vortex layers'. An analytical expression relates the point vortex modelling a rotating cylinder to the rate of momentum injection. The panel method is capable of treating multielement configurations (e.g. a rotating cylinder and the truncated airfoil). An iterative scheme based on the convergence of the wake shape is used to obtain the final solution. The numerically obtained pressure distribution, the lift and drag coefficients agree well with the experimental results.

Flow visualization studies in a water channel were performed to obtain better physical insight into the MSBC process. Plexiglas models with rotating cylinders in conjunction with a fine suspension of polyvinyl chloride particles and slit lighting were used to visualize the streaklines. The still photographs and video movie recorded, rather dramatically, the effectiveness of the MSBC in suppressing separation and vortex shedding, making the flow approach the potential character.

Overall, the present research firmly establishes potential of the MSBC as a versatile tool for lift augmentation, drag reduction and vibration suppression of several bluff bodies encountered in industrial engineering practice.

TABLE OF CONTENTS

LIST OF SYMBOLS

AR aspect ratio of the bluff body, l_1/h_1

$A_{ji}, B_{ji}, ..., F_{ji}$ influence coefficients

C_P mean pressure coefficient, $(p - p_\infty)/(1/2)\rho V^2$

C_{PB} mean base pressure coefficient

C_{Pj} mean pressure coefficient at the mid-point of the jth panel

C_D drag coefficient, $F_D/(1/2)\rho D U^2$

C_L lift coeffcient, $F_L/(1/2)\rho D U^2$

C_Y lateral force coefficient, $F_Y/(1/2)\rho D V_1^2$

C_L/C_D lift to drag ratio

$|C_D|$ absolute value of the drag coefficient

$|C_L|$ absolute value of the lift coefficient

C airfoil chord

D characteristic dimension of the bluff body

F force

F_D drag force

F_L lift force

F_Y lateral force, $(F_L \cos \alpha + F_D \sin \alpha)$

H_{inner} total pressure inside the wake

H_{outer} total pressure outside the wake

K' proportionality constant

M total number of panels descretizing each 'free vortex line'

N	total number of panels descretizing the body for single element airfoil
N_R	cylinder rotational speed in rpm
P_i	coefficients of the polynomial expansion; i=1,3,5,7
R	characteristic radius of the bluff body, $D/2$
Re	Reynolds number, UD/ν
S	circumferential length along the contour of the bluff body
St	Strouhal number, $f_V D/U$
St,p	Strouhal number based on the projected height normal to the flow, $f_V h/U$
Sr	wake Strouhal number, fh'/U_b
S_U, S_L	lengths along the upper and lower 'free vortex layers', respectively
U	freestream fluid speed
U_B	mean velocity at the edge of the boundary-layer at separation
U_C	rotating cylinder surface speed
U_C/U	momentum injection parameter
V	nondimensional wind speed, $U/\omega_n h$
$\vec{V}$	velocity at any point
$\vec{V_\infty}$	freestream fluid velocity
V_1	relative wind velocity
V_C	critical wind speed necessary to initiate galloping
X	x-coordinate direction
X/C	nondimensional length along the chord of the airfoil
Y	nondimensional transverse amplitude, $y/\omega_n h_1$
a	longitudinal spacing between two successive vortices in a row

b	lateral spacing between the two rows of vortices
b/a	vortex spacing ratio
d	diameter of the rotating cylinder
f	frequency
f_v	frequency of vortex shedding
f_n	structure natural frequency
h	projected height of the bluff body normal to the flow
h'	distnace between two shear layers enclosing the wake
h_1	height of the bluff body
k	stiffness
k_1	base pressure parameter, $\sqrt{1 - C_{PB}}$
l_1	length of the bluff body
m	structure mass per unit length
n	mass parameter, $\rho h^2 l_1 / 2m$
$\vec{n}$	vector denoting normal direction
p	pressure at any point in the flow
p_∞	freestream pressure
q_j	fluid speed at the jth panel
q_{inner}	fluid speed inside the wake
q_{outer}	fluid speed outside the wake
r	radius of the rotating cylinder, $d/2$
t	time
u_t	translational speed of the vortex street

u_i', u_j'	fluctuating velocity in the ith and j^{th} directions respectively; i,j = 1,2,3
u_c, w_c	x, y components of the velocity due to a line vortex
$< u_i' u_j' >$	Reynolds stress
$\vec{u}$	surface velocity of the rotating cylinder
u_j, w_j	perturbation velocity components at the jth panel
ω	circular natural frequency, $2\pi f$
ω_n	structure circular natural frequency, $2\pi f_n = \sqrt{k/m}$
ω_v	circular frequency of vortex shedding, $2\pi f_v$
x	x-coordinate direction
y	y-coordinate direction
y_1	initial vibration amplitude
y_μ	vibration amplitude after μ cycles
Γ	circulation strength of the point vortex
Γ_C	circulation strength of the point vortex
ΔH	decrease in the total pressure in the wake with respect to that at infinity
$\%\Delta C_D$	% change in the drag coeffcient
$\%\Delta C_L$	% change in the lift coeffcient
Ω	angular velocity of the rotating cylinder
α	angle of attack
β	nondimensional damping coeffcient, $r_1/2m\omega_n$
γ	vortex strength
γ_i	vortex strength at the ith panel
δ	fraction of the orginal circulation surviving the vortex formation

δ_1 logarithmic decrement for the decaying vibrations, $1/[(n'-1)ln(y_1/y_n)]$

ζ system damping ratio

ζ_f viscous damping ratio

ζ_t total effective damping ratio

η effciency of momentum injection

λ vortex dissipation factor

ν fluid viscosity

ρ fluid density

σ source strength

τ nondimensionalized time, $\omega_n t$

ϕ potential function for the ideal, incompressible fluid

ϕ_i generalized potential function

LIST OF FIGURES

LIST OF TABLES

ACKNOWLEDGEMENT

Here I wish to express sincere appreciation to those who directly or indirectly helped me, while I was involved with the present research.

First and foremost, I would like to thank my supervisor, Prof. Vinod J. Modi, for all that he has done for me in last five years. His invaluable insight and technical advise has been the guiding spirit behind this research. I have also imbibed from him the art of better organization and presentation. Those friendly discussions on world affairs provided useful balance to the academic pursuit as a graduate student.

I wish to thank Dr. Gautam Bandyopadhyay (IIT Kharagpur, India) for helpful discussions during development of the numerical code when he spent one year as a research associate in our group in 1991-92. I am also grateful to Prof. Toshio Yokomizo for making available the excellent flow visualization facility at the Kanto Gakuin University, Japan. Special thanks go to Mrs. Kyoko Yokomizo for arranging several sightseeing trips which made my stay in Japan an unforgettable experience. Comments of the committee members, Prof. Ian Gartshore, Prof. Sander Calisal and Prof. Michael Quick, are gratefully acknowledged.

I wish to extend my appreciation to Mr. Tony Basic, Mr. Ed Abel and Mr. John Richards at the department workshop for fabricating the bluff body models as well as the experimental set-up.

Of course, I cannot overlook my past and present colleagues and friends, Satyabrata Pradhan, Mae Seto, Anant Grewal, Spiros Kalantzis, Mathieu Caron, Gary Lim, Mark Chu, Shinji Hokamoto, Itzhak Marom, Yuan Chen, Khan Muneer, Zhiyong Ma, Harry Mah, Afzal Suleman, Alfred Ng, Oliver Ying, Simon St.Hill, Andrew Dobric, Faqurrudin Karray, Nagaraja Rudrapatna, and Dipak Ghosh who made my stay at the UBC a memorable one.

Dedicated to my parents,
whose affection and guidance have always motivated me

1. INTRODUCTION

1.1 Preliminary Remarks

Fluid dynamics of bluff bodies, of varying shapes, has been a subject of considerable study ever since the pioneering contributions by Strouhal [1], Prandtl [2], Karman [3], and others. The concept of the boundary-layer was first introduced by Prandtl in 1904. Ever since, engineers and scientists have tried to minimize its adverse effects and control it to advantage. Delay of the wing stall to high angles of attack, as well as increase in lift and reduction in drag of aircraft have been of considerable importance to the aeronautical industry. Rise in the fuel cost and growing environmental awareness have led to design of energy efficient road vehicles such as cars, buses, trucks, etc. Furthermore, wind effects on bluff structures may lead to vortex resonance and galloping type of instabilities.

Flow-induced vibrations of tall buildings, bridges, smoke-stacks, air traffic control towers, transmission lines, etc. have been reported frequently by the engineering industry. Collapse of the Tacoma Narrows Bridge in U.S.A. in 1940, due to torsional instability, is a well known example. Tall buildings have been known to oscillate at low frequency (< 1 Hz) and large amplitude. Recent advances in material science and computer aided design have led to structures with reduced stiffness making them prone to wind, earthquake, as well as ocean waves and current excited oscillations. The twenty first century would witness super tall buildings (> 1000m) and extra long span bridges (> 2000m), as pointed out by Kubo et al. [4,5]. A vast body of literature accumulated over the years has been reviewed by several authors including Wille [6], Marris [7], Morkovin [8], Parkinson [9], Cermak [10], Welt [11,12], and Modi et al. [13].

Streamlined objects such as a thin airfoil aligned with the flow suffer little flow

separation, have negligible wake and the drag is primarily due to viscous skin friction. In contrast, a bluff body immersed in a fluid stream exhibits flow separation resulting in a wide wake downstream. A large contribution to the drag can be ascribed to the presence of a significant difference in pressure between the freestream and the wake. The wake in general carries vorticity, is turbulent and persists for many diameters downstream of the body. At low Reynolds numbers and depending on the shape as well as orientation of the body, the shear layers separating from the top and bottom surface roll-up to form alternately shedding vortices resulting in the well-known Karman vortex street. In the case of a bluff body with sharp corners (e.g. a rectangular prism) location of the boundary-layer separation is fixed, but for a body with curved surface, as in the case of a circular cylinder, the point of separation is sensitive to changes in the Reynolds number. Figure 1-1 illustrates some typical examples of bluff body-flows.

Flow past a circular cylinder [14,15] is a good example illustrating the fluid dynamical phenomena associated with bluff bodies. At a very low Reynolds number (Re < 1), the flow is purely viscous and the wake is absent. For $5 \leq$ Re ≤ 15, an attached symmetric pair of Foppl vortices appear in the immediate vicinity of the cylinder. As the Reynolds number is further increased to around 40, there is a laminar separation of the shear layers and periodic vortex shedding initiates. The shed vortices remain laminar up to Re ≈ 150. A transition to turbulence in vortices occurs for 150 $\leq$ Re ≤ 300. The vortex street becomes fully turbulent as the Reynolds number increases further ($300 \leq$ Re $\leq 3 \times 10^5$). Around 3×10^5 the boundary-layer undergoes laminar to turbulent transition and becomes fully turbulent at Re $\approx 3.5 \times 10^6$. Now the wake narrows significantly, is disorganized, and there is a sudden drop in the total drag force. For Re $> 3.5 \times 10^6$ the turbulent vortex shedding is re-established and the wake widens with a gradual increase in drag, which reaches a stationary value at some higher Reynolds number.

(a)

(b)

1, 2 - POINTS OF SEPARATION

3 - LINES OF SEPARATION

4 - STREAMLINES

SEPARATION BUBBLE

WAKE

SHEAR LAYER

L / H > 3

L   H

(c)
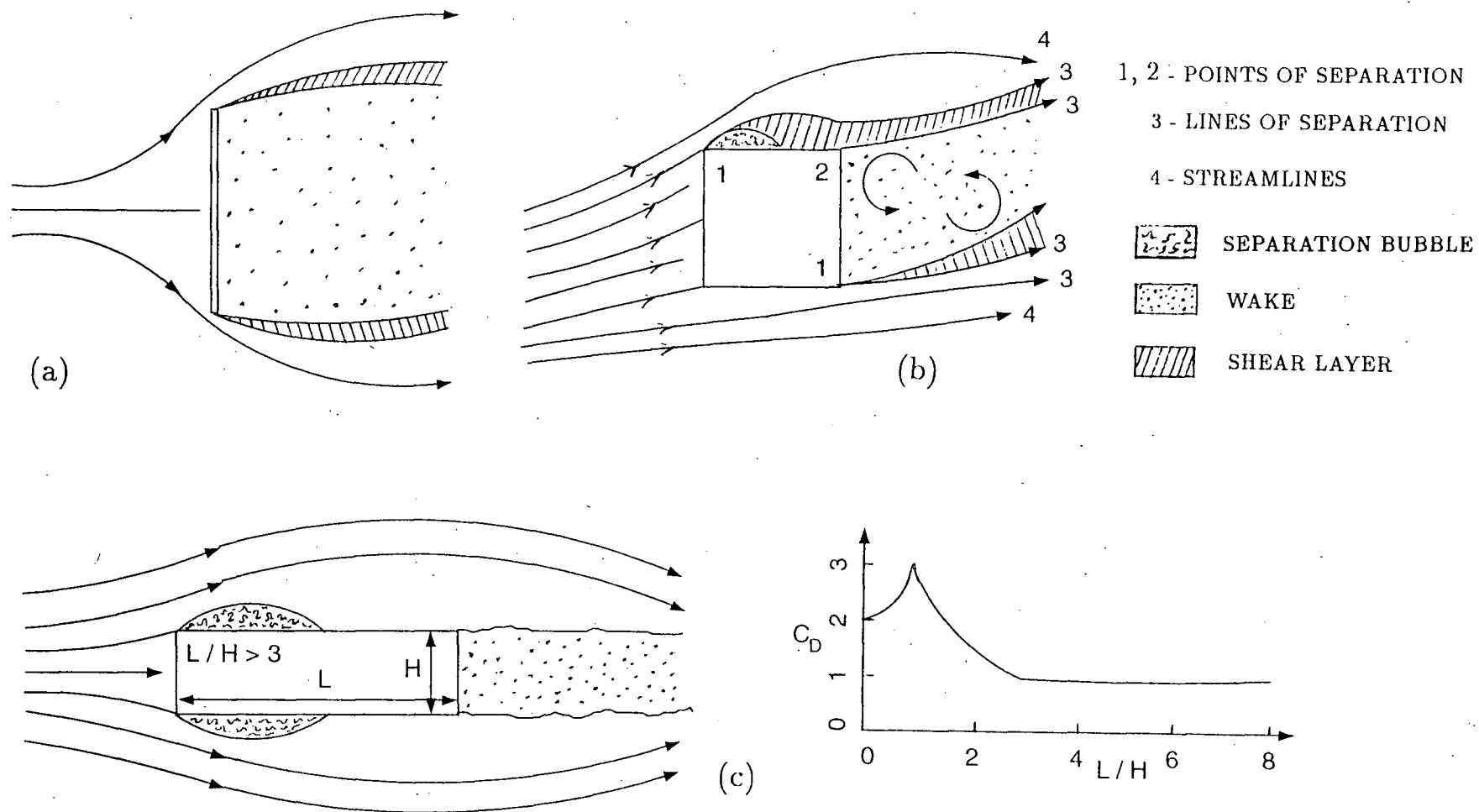
Figure 1-1   Several examples of bluff body flows: (a) normal flat plate with a wide wake; (b) square section showing separating shear layers, reattachment bubble, wake and vortex shedding; (c) shear-layer reattachment on a long rectangular section and effect of aspect ratio on the drag.

The portion of the bluff body lying inside the wake is referred to as the afterbody. In the normal range of the Reynolds number of engineering interest ($10^3 \leq Re \leq 10^8$), a bluff body experiences significant vortex shedding. This creates time-dependent pressure distribution on the top and bottom faces of the body resulting in a fluctuating transverse force. If the frequency of the vortex shedding coincides with the natural frequency of the structure it experiences resonance, a forced vibration phenomenon (Figure 1-2a).

The vortex shedding from a bluff body is mainly a two-dimensional phenomena but the shed vortices are not two-dimensional [16]. Hence spanwise effects play an important role in real-life slender structures which may be considered essentially two-dimensional. As noted by Bearman [16], oscillation of a bluff body dramatically alters the vortex shedding process. The oscillations provide a means for coupling the flow along the span of the body, which is reflected in a higher spanwise correlation of various physical quantities (e.g. pressure fluctuations). The body motion is also responsible for the capture of the vortex shedding frequency by the body frequency over a certain range of fluid velocity, known as frequency 'lock-in'. In fact, in case of an oscillating square prism, the vortex formation process is comprised of the Karman vortex street as well as a second wake vortex system created by the transverse motion of the body [17]. Thus, the term 'lock-in' is usually applied to the the region where there is a strong magnification of the body-frequency signal at the expense of the Strouhal signal.

In-line oscillations have also been observed for structures immersed in a dense fluid (e.g. water). Here the frequency of vibration is twice that of the transverse case. For a circular cylinder, the vortices are first shed in symmetric pairs and the familiar Karman vortex street develops further downstream [16]. Ocean engineering structures (e.g. off-shore oil exploration rigs) are more susceptible to in-line oscillations.

As against the vortex resonance, galloping is a different form of instability

4

(a)

VORTEX SHEDDING
FREQUENCY, f_V

VORTEX RESONANCE, $f_V \approx f_n$

V

R

STRUCTURE NATURAL
FREQUENCY, f_n

(b)

B

V

Y

X

A

F

$\dot{Y}$

$-\alpha$

V_r

V

$\dot{Y}$

α

V

V_r

F

F

α
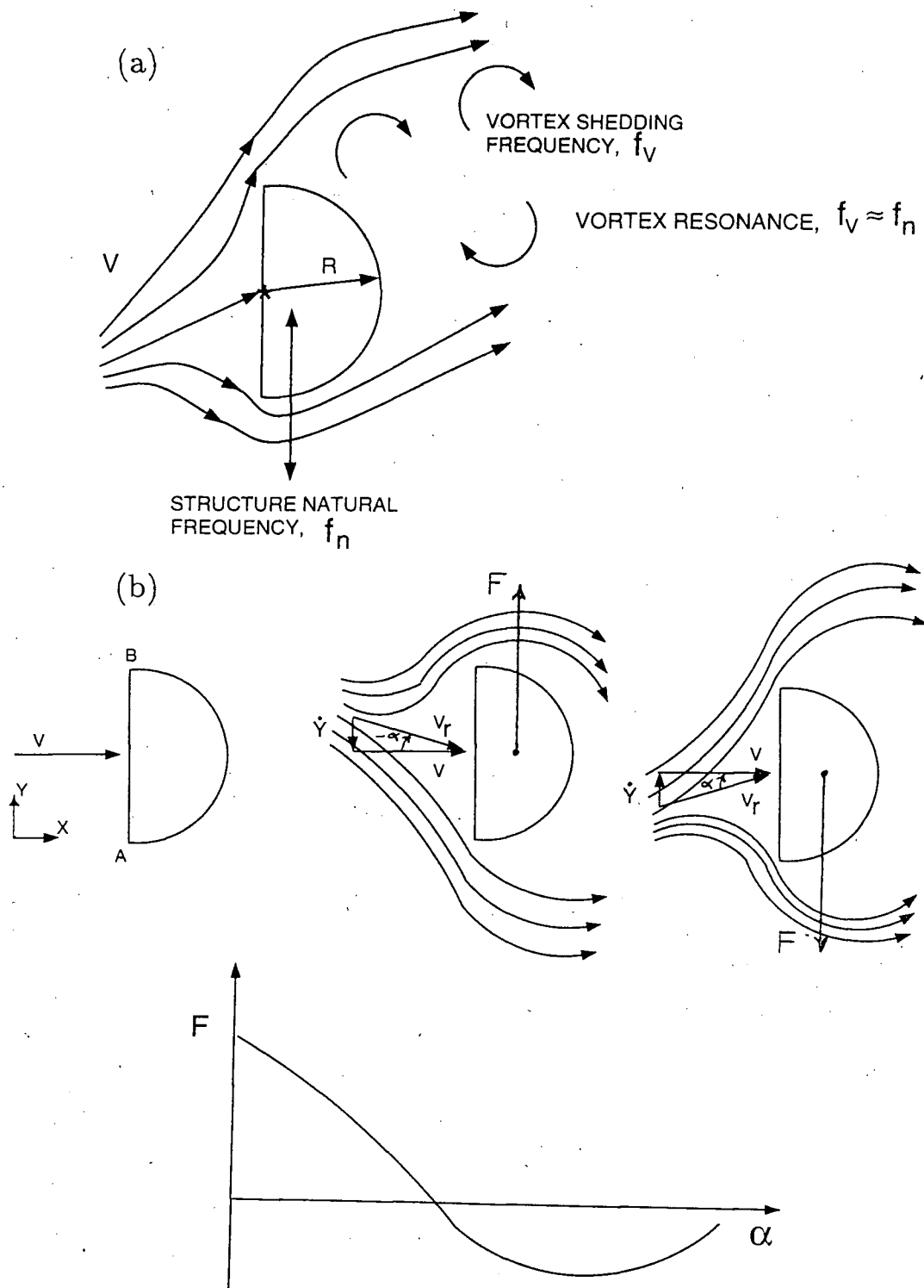
Figure 1-2   Schematic diagrams showing principles of: (a) vortex resonance; and (b) galloping instabilities. Here: St, Strouhal number; V, freestream velocity; V_r, resultant velocity; fv, frequency of vortex shedding; fn, natural frequency of the system; F(α), force on the prism due to motion; y, transverse displacement during vibration.

referred to as the self-excited oscillations. It is exhibited by only a certain family of bluff body geometries (e.g. a square prism). Here the excitation force depends on the motion itself. The amplitude of oscillation grows until the rate at which the energy is extracted from the fluid stream balances the rate at which it is dissipated by the system (Figure 1-2b). In the quasi-steady theory proposed to study the galloping motion [18], the excitation force is approximated through a nonlinear negative damping term in the equation of motion. The theory assumes that the bluff body, at any instant during the galloping cycle, experiences the same lateral force as that when held stationary at the same angle of attack. In galloping, the plunging amplitude could be very large under certain circumstances. A classical example is the galloping of ice-covered transmission cables in an extremely cold weather. A bluff body could also undergo galloping in the torsional mode. In general, experimental results have compared well with prediction of the quasi-steady approach. Another interesting form of self-excited oscillation is flutter, a multidegrees of freedom phenomenon which requires phase difference between the system's generalized coordinates for energy dissipation.

One of the important shape parameters of a bluff geometry is the afterbody length. A section with a relatively short afterbody (e.g. a D-section) is generally stable in galloping. Those with somewhat larger afterbodies (e.g. a square and rectangular prisms) would gallop; but the amplitude decreases as the afterbody becomes longer. Stability is restored for bluff bodies with an aspect ratio (length/height ratio, l_1/h_1) of 3 or more [19]. Irrespective of the afterbody shape, all bluff bodies experience vortex-excited oscillations. Furthermore, the aeroelastic behaviour of bluff bodies is significantly affected by the geometry of the corners. In a study by Bokaian and Geeola [20], it was found that the galloping vibrations of a square section were sensitive to the ratio of corner radius to body dimension. An increase in the rounding radius made the square section less susceptible to galloping instability; and beyond a

critical value (0.318) no vibrations could be detected.

From the structural dynamics point of view, response of a slender elastic body is determined by the various vibration modes involved in the motion. Furthermore, besides Reynolds number and body shape, the bluff body flows are also influenced by factors such as surface roughness, presence of turbulence in the approaching fluid stream and interference effects due to neighbouring structures. A bluff body which behaves as a soft oscillator in a smooth flow becomes less susceptible to galloping instability as the intensity of turbulence is increased [21]. In the same vein, a hard oscillator tends to become relatively soft.

Widespread occurrence of wind induced instabilities of structures with the associated problems of comfort and structural damage have forced engineers to predict and suppress these vibrations in advance. A common approach to control wind induced instabilities is to modify the flow field. This has led to the design of helical strakes, perforated shrouds, slats and similar devices as shown in Figure 1-3. They contribute to aerodynamic damping. Strakes have been frequently installed on smokestacks and ocean based structures, although the associated increase in the drag is a limitation. The effectiveness of helical strakes have been known to deteriorate with an increase in intensity of turbulence [22]. Structural response to wind excitation is also quite sensitive to the damping. This has led to the design of a variety of energy dissipation devices such as tuned mass dampers, hydraulic dashpots, impact dampers, etc. (Figure 1-3). Approximately 3-4% of the structure weight is necessary for such devices to be effective. Of course, there is a limitation as to how large the weight could be as the structure grows taller. For example [23], the 60 storey tall John Hancock Tower Building in Boston, U.S.A., requires two 300 tonnes concrete blocks (one each for two orthogonal directions) for effective vibration control at a cost of US$ 3 million (in 1975). Similar dampers have also been installed on the 110 storey World Trade Center Towers, in New York, U.S.A. In the same category

of passive devices belongs a relatively simple concept involving sloshing of a liquid within a closed container. The dissipation of energy takes place through the action of viscous and turbulent stresses associated with wave breaking. The presence of a free surface permits significant wave motion of the sloshing liquid. An axisymmetric torus shaped container filled with liquid, known as nutation damper, has been studied by Welt and Modi [24,25]. As the frequency encountered in wind induced oscillations of a large structure is usually less than 1 Hz, the nutation damper is ideally suited to this class of problems. Generally a large array of nutation dampers (where each damper is a fraction of a meter in dimension), stacked in a modular fashion, are used in real-life structures. Nutation dampers have been successfully installed in Japan [26].

Apart from the passive control, there is yet another class of active devices requiring a supply of energy for their operation. Boundary-layer suction or blowing fall in this category. These concepts are more suitable where an appreciable boundary-layer growth occurs. In case of bluff bodies, like a rectangular prism, there is no significant growth of the boundary-layer and the flow separates at the top and bottom edges of the front face. In this situation, application of the Moving Surface Boundary-layer Control (MSBC) appears quite promising [5]. As the name implies, a portion of the body-surface exposed to the flow is moving and thus imparts tangential velocity to the approaching fluid. This injection of momentum helps in keeping the flow attached to the surface in the region of adverse pressure gradient. It could result in a substantial increase in lift, reduction in drag and assist in suppression of the flow-induced vibrations. Extensive studies of the concepts like boundary-layer suction, blowing, vortex generators, turbulence promoters, etc. have been carried out over the years. An indepth review of the subject has been presented by Goldstein [27], Lachmann [28], Rosenhead [29], Schlichting [30], Chang [31] and others. Despite the specific recommendations by the Associate Committee on Aerodynamics appointed

Helical Strakes

Shrouds

Slats

optimal pitch = $5d_s$
protusion = $0.10 - 0.12d_s$
location : top 33% of height
drag penalty : $C_d \approx 1.3$
for $8 \times 10^4 \leq Re \leq 2 \times 10^5$
(i.e. 3 times higher in
supercritical range)
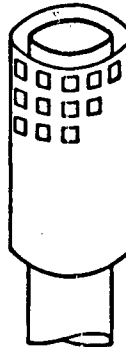
gap : shroud-chimney = $0.12d_s$
open area ratio = 20 - 36%
location = top 25% of height
drag penalty : $C_d \approx 0.9$
for $8 \times 10^4 \leq Re \leq 2 \times 10^6$
(i.e. 2 times higher in
supercritical range)

slat width = $d_s/11.5$
gap : slat-chimney = $d_s/7$
open area ratio = ·40%
drag penalty : $C_d \approx 1.05$ to 1.1
for $1.5 \times 10^4 \leq Re \leq 1.5 \times 10^5$
(i.e. expected 2.5 times higher
in supercritical range)
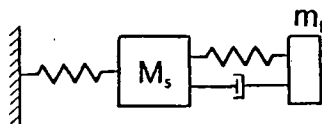
Tuned Mass Damper
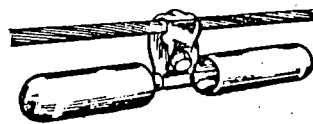
Stockbridge Damper

Internal damping ;
out of phase vibrations
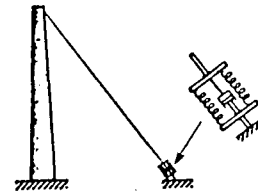
Hydraulic Dashpot
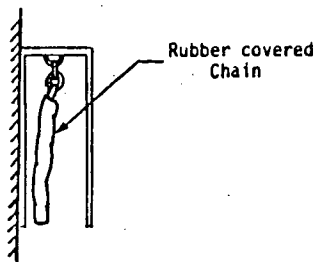
Hanging-Chain Impact Damper

Increase in damping : factor of 3
Increase in weight : 5
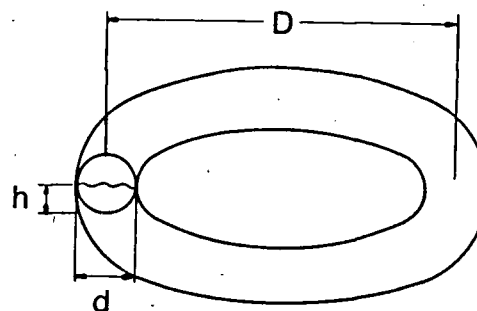
Nutation Damper

Figure 1-3   Some examples of the devices used for the suppression of wind-induced oscillations.

by the National Research Council [32], the subject of moving surface boundary-layer control has received relatively little attention.

The astute mind of Newton [33] was probably the first to notice the effect of spin on the trajectory of a ball without any inkling to its cause. At least two centuries elapsed before Magnus [34] applied the concept of a rotating cylinder to generate lift, replacing the sails of a ship. Further details on the 'Magnus Lift' concept are available in the reviews by Swanson [35] and Iverson [36]. Prandtl [37] demonstrated his "ship of zero resistance" in 1910, which had two counter-rotating cylinders. Flettner [38] in 1924 applied the principle to the ship 'Bachau' for propulsion. Goldstein [27] demonstrated the use of a rotating cylinder at the leading-edge of a flat plate as a boundary-layer control device. Favre [39] applied the concept to an airfoil by replacing the upper surface with a belt moving over two rollers. The airfoil achieved the maximum lift coefficient of 3.5 with the stall delayed to 55°!

No significant research on the concept of the MSBC was reported between 1938-'60. A renewed interest in the subject is indicated through contributions by Alvarez-Calderon [40,41] who reports a successful application of leading-edge rotating cylinder flap to generate high lift for STOL-type aircraft. Flight tests were performed on a single engine high wing research aircraft designed by the Aeronautics Division of the Universidad Nacional de Ingenieria in Lima, Peru. He also suggested possible application of the rotating cylinder for an aircraft wing (Figure 1-4).

During the same period Brooks [42] presented his tests on a hydrofoil with a leading or trailing edge rotating cylinders. Between the two configurations, the latter was found to provide a substantial gain in the lift. The primary motivation behind this research was the improvement in fin performance for torpedo control. Steele and Harding [43] applied a rotating cylinder to a ship rudder to increase its manueverability. Force measurements and flow visualization studies were carried out using a water tunnel and a large circulating water channel. Three different configurations of

rudder were used. The rotating cylinder :

> (i) in isolation;

> (ii) at the leading edge of a rudder;

> (iii) combined with a flap-rudder, the cylinder being at the leading edge of the flap.

From the overall consideration of hydrodynamic performance, mechanical complexity and power consumption, the configuration in (ii) was preferred. An application to a massive tanker (250,000 tonnes) showed the power requirement for 1 m diameter cylinder rotating at 350 rpm to be around 400 kW.

Flight tests were also performed on the North American Rockwell's OV-10A by NASA's Ames Research Center. The leading-edge of the flap was replaced by a high speed rotating cylinder developed by Alvarez-Calderon [40,41]. The flight test program was designed to assess handling qualities of the propeller-driven STOL-type aircraft at higher lift coefficients. The aircraft was flown at a landing speed of 29-31 m/s, with an approach angle of -8°, corresponding to a lift coefficient of 4.3. The pilot's report suggested that any further decrease in the approach speed were limited due to the lateral-directional stability and control characteristics. Excellent photographs (Figure 1-5) of airplane on ground and in flight have been published in the Aviation Week and Space Technology [44,45].

As evident from the discussion above, the use of a rotating cylinder was so far targeted at specific applications and few attempts were made to study the underlying fluid mechanics involved. An effort was made by Tennant in 1971 to assess the effectiveness of a rotating cylinder as a boundary-layer control device when applied to a diffuser with a step change in area [46,47]. The diffuser incorporated rotating cylinders to form a part of its wall at the station of the area change. Preliminary experiments were conducted for the area ratio up to 1:2.5, which showed no separation

WEAK BOUNDARY LAYER

WING

ROTATING CYLINDER

FLAP

REENERGIZED
BOUNDARY LAYER

(a)

HIGH SPEED POSITION

HIGH SPEED POSITION

AIR FLOW

(b)

HIGH LIFT POSITION

HIGH LIFT
POSITION

(c)
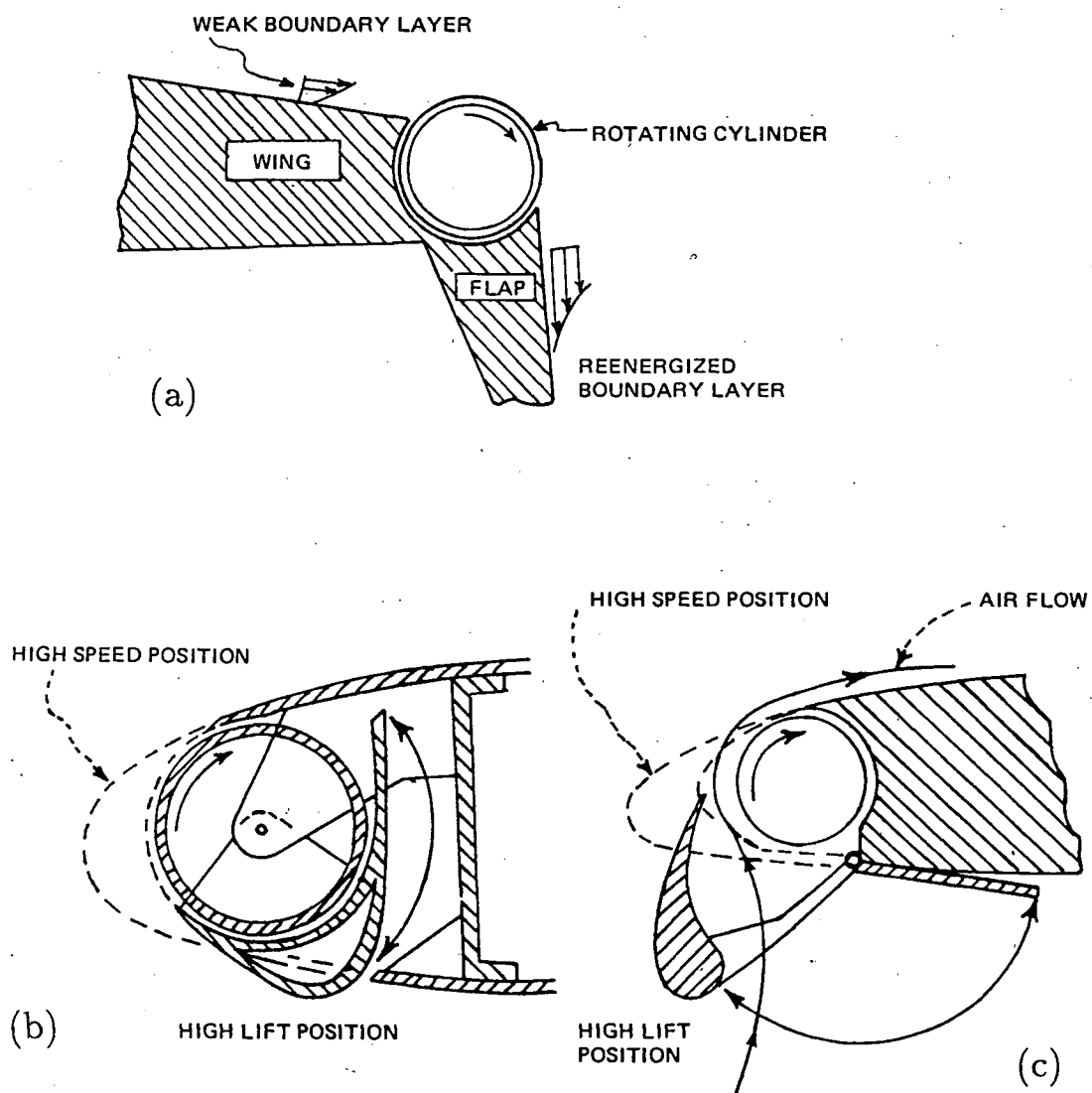
Figure 1-4   Several applications of a rotating cylinder to an aircraft wing: (a) boundary-layer control function of a rotating cylinder flap; (b) high-lift leading-edge rotating cylinder in combination with a droop nose; (c) high-lift rotating cylinder in combination with a slat.

12

Figure 1-5 The North American Rockwell OV-10A aircraft in flight demonstrating a successful application of the rotating cylinder as a high-lift device.

for appropriate moving surface to diffuser inlet velocity ratio. Tennant et al. [48] have also conducted tests with a wedge shaped flap having a rotating cylinder as the leading edge. Flap deflection was limited to 15° and the critical cylinder velocity necessary to suppress separation was determined. Effects of increase in the gap-size (between the cylinder and the flap surface) were also assessed. No effort was made to observe the influence of an increase in the cylinder surface velocity beyond $U_C/U = 1.2$ (U_C = cylinder surface velocity, U = free stream velocity). Subsequently, Tennant et al. [49,50] have reported circulation control for a symmetrical airfoil with a rotating cylinder forming its trailing edge. For zero angle of attack, the lift coefficient (C_L) of 1.2 was attained with $U_C/U = 3$. Of interest is their study concerning boundary-layer growth on moving surfaces accounting for gap effects [51]. Ericsson [52] has also reported use of a rotating cylinder for boundary-layer control on an aircraft wing.

Modi et al. [53-60] were the first to generalize the concept of a rotating cylinder as a versatile boundary-layer control device for diverse applications such as high-lift airfoils, drag reduction of static as well as moving bluff bodies, control of wind induced instabilities of civil engineering structures, reduction in snow deposition over a roof, suppression of wave and current induced oscillations of offshore platforms and marine risers, etc. Mokhtarian and Modi [55] have studied, in a comprehensive manner, application of the Moving Surface Boundary-layer Control (MSBC) with reference to two-dimensional Joukowsky airfoils having one or two cylinders acting as momentum injecting elements. A Joukowski airfoil fitted with a rotating cylinder on its upper surface near the leading edge resulted in an increase in the lift coefficient by 200 % with the stall angle delayed to 48° . As a further application of the MSBC concept at a more fundamental level, a flat plate and several rectangular prisms with momentum injection through rotating cylinders were also studied. A drag reduction of about 75 % was achieved for a normal flat plate with twin cylinders, one at each edge ($U_C/U = 3$). Wind tunnel tests on a tractor-trailer truck model with a rotating cylinder at the top

14

leading edge of the trailer resulted in a significant drag reduction of about 26 %. Flow visualization pictures for the flat plate with the MSBC revealed considerable narrowing of the wake at a cylinder speed of about $U_C/U = 3$. Even for a Joukowski airfoil at a high angle of attack (25°), the momentum injection corresponding to $U_C/U = 4$ was successful in making the flow essentially potential (no separation). A preliminary analysis of the power requirement for a rotating cylinder suggested that the benefits of drag reduction would easily outweigh the energy demand. This fact is also confirmed in the report by Brown [61] on the application of a leading-edge rotating cylinder flap on an aircraft. The flight tests revealed that the total power required to rotate the cylinder was less than 2% of the propeller power.

Increasing air traffic is responsible for the growth in size and speed of airplanes. This, in turn, can only be accomplished by generating higher lift force. Powerful engines producing considerable noise would be required for such applications. Reduction in jet engine noise is difficult to accomplish without paying a price in terms of performance. For communities surrounding an airport, noise-level can be kept to a minimum by employing high-lift take-off and landing at reduced speeds on shorter runways. Moving surface boundary- layer control represents an attractive solution in such a situation, not to mention highly maneuverable military airplanes demanding exacting and superior performance. Every year large amount of goods are transported by the trucking industry using the network of highways. Even a small reduction in the drag of a tractor-trailer truck could result in a significant saving of the fuel cost. Application of rotating elements for boundary-layer control presents one possibility to that end. In the ever competitive construction industry, the engineers are looking for effective, economical and implementable solutions to fluid-structure interaction problems. Here again, application of MSBC represents a potential candidate.

The discussion above touched upon usefulness of a rotating cylinder as an effective boundary-layer control device in the field of applied aerodynamics. Further

advances in this technology can only emerge from an understanding of the basic fluid dynamics involved. The present research aims at exploring MSBC at a fundamental level with particular emphasis on lift augmentation, drag reduction and vibration control of bluff bodies through a comprehensive program involving wind tunnel tests, numerical investigation, and flow visualization.

1.2 Physics of Moving Surface Boundary-layer Control

Since this thesis deals with boundary-layer control using a rotating cylinder, it would be appropriate to outline the basic flow physics involved. An elegant explanation on the generation of circulation is given by Lighthill [62] as follows (Figure 1-6). Consider, a cylinder, rotating in a clockwise sense, immersed in a fluid flowing from left to right with velocity U. The tangential surface velocity of the rotating cylinder is U_C. It is known that the strength of a vortex sheet is equal to the jump in the tangential velocity across the sheet. On the upper surface of the cylinder the vortex sheet strength is $U - U_C$, whereas on the bottom surface it is $U + U_C$. Thus a more of positive vorticity is shed from the lower surface as compared to the top. The wake receives a net positive amount of vorticity. The Kelvin's theorem on the conservation of the total circulation dictates that the body (i.e the rotating cylinder) in turn receive a net negative vorticity. This imparts a lift to the rotating cylinder in accordance with the Magnus effect. Another effect of rotation is to move the point of separation on the upper surface downstream. The external flow velocity at separation is thus further reduced and so contributes additionally to the reduction in the rate of shedding of vorticity from the upper surface.

It is also important to note the presence of a thin boundary-layer on the surface of a rotating cylinder. Vorticity is generated in the boundary-layer around the rotating cylinder. As shown in Figure 1-7, if the wall is moving in the downstream direction, then separation occurs at some height above the wall, and there would be boundary-

16

layer flow beneath the separated region. The velocity profiles are also shown in the inset. If the wall is moving upstream, separation occurs at the wall and there is a small sublayer of recirculating flow ahead of the separation.

The wake behind a rotating cylinder is significantly smaller, the streamlines curve more sharply around the cylinder and the flow approaches an ideal (potential) one. If the rotating cylinder is integral to a bluff body (Figure 1-8), the streamlines bunch together near the rotating element generating a suction pressure field. The separation is delayed and the wake becomes smaller. The pressure in the wake increases. Overall, there is a significant reduction in the drag of a bluff body. The strength of the shed vorticity is reduced considerably and could disappear altogether if the momentum injection is sufficiently strong. The changes produced in the flowfield are proportional to the size and total surface area of the exposed cylinder. The total circulation generated around a rotating cylinder in a real fluid is always less than that computed using the ideal flow considerations. An experimental plot of circulation against rate of cylinder rotation is given by Rauscher [63]. Associated lift and drag coefficients are given by Goldstein [64]. A rotating cylinder can provide extremely high lift but the drag penalty could become severe as the rate of rotation increases. An airfoil with a leading-edge rotating cylinder could provide a good compromise with a higher lift and lower drag.

1.3 A Brief Review of the Relevant Literature

1.3.1 Dynamics and fluid dynamics of bluff bodies

A large number of objects encountered in the industrial aerodynamics practice are not streamlined, e.g. buildings, smokestacks, road vehicles, etc. Even a nominally streamlined airfoil at a high angle of attack presents a bluff geometry. Strouhal [1] was the first to correlate the frequency of vortex shedding to the free stream velocity of fluid and the diameter of a circular cylinder. The ratio, known as the 'Strouhal

17
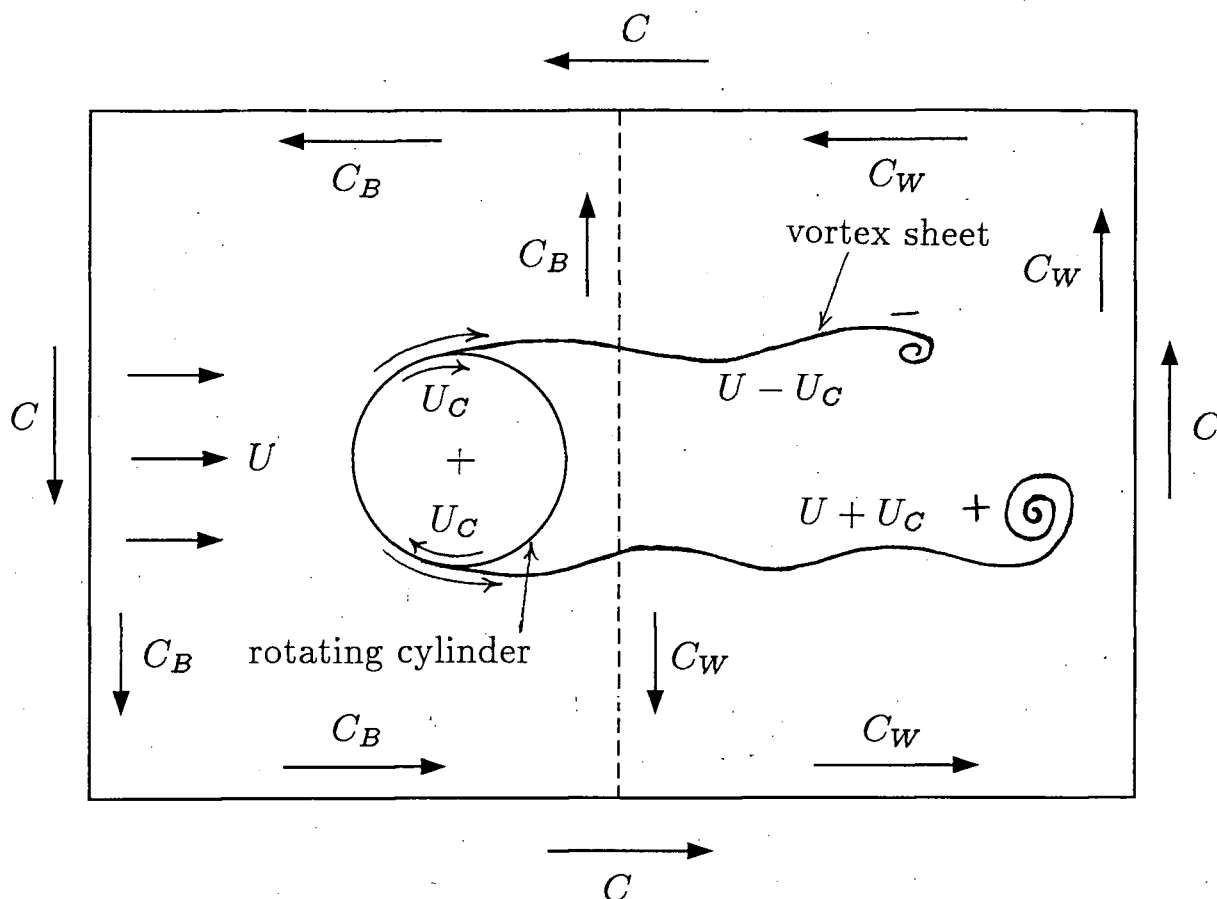
According to Kelvin's Theorem, $D(\int_C \vec{u} \cdot d\vec{x})/Dt = 0$

$$\therefore \int_{C_W} \vec{u} \cdot d\vec{x} = -\int_{C_B} \vec{u} \cdot d\vec{x}, \qquad C = C_B + C_W$$

Figure 1-6 Schematic flow illustrating development of circulation around a rotating cylinder and the associated vortex shedding into the wake. The circulation around the circuit C_W embracing the wake but not the body must have a positive value Γ_C. Therefore, the circulation around a circuit C_B embracing the body but not the wake has a negative value $-\Gamma_C$, as required by the fact that circulation around the closed curve C must be zero.
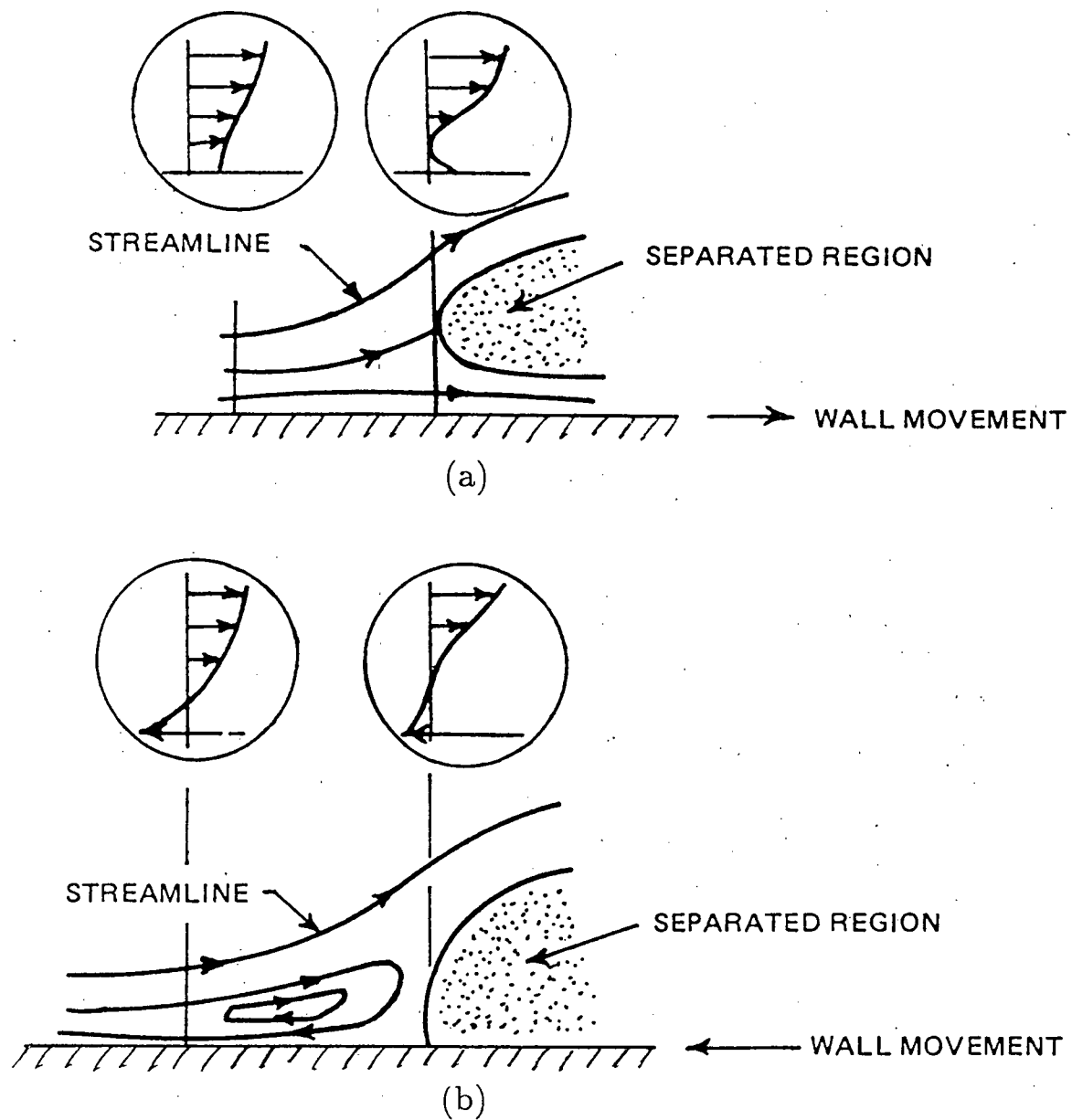
Figure 1-7   Velocity profiles in the neighbourhood of separation: (a) wall moving downstream; (b) wall moving upstream [65].

SEPARATION BUBBLE

(a)

(b)

20
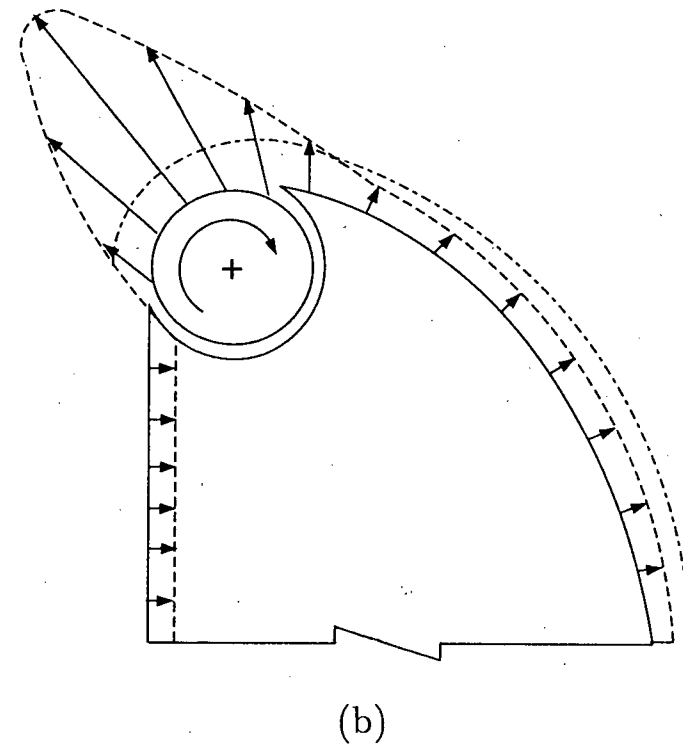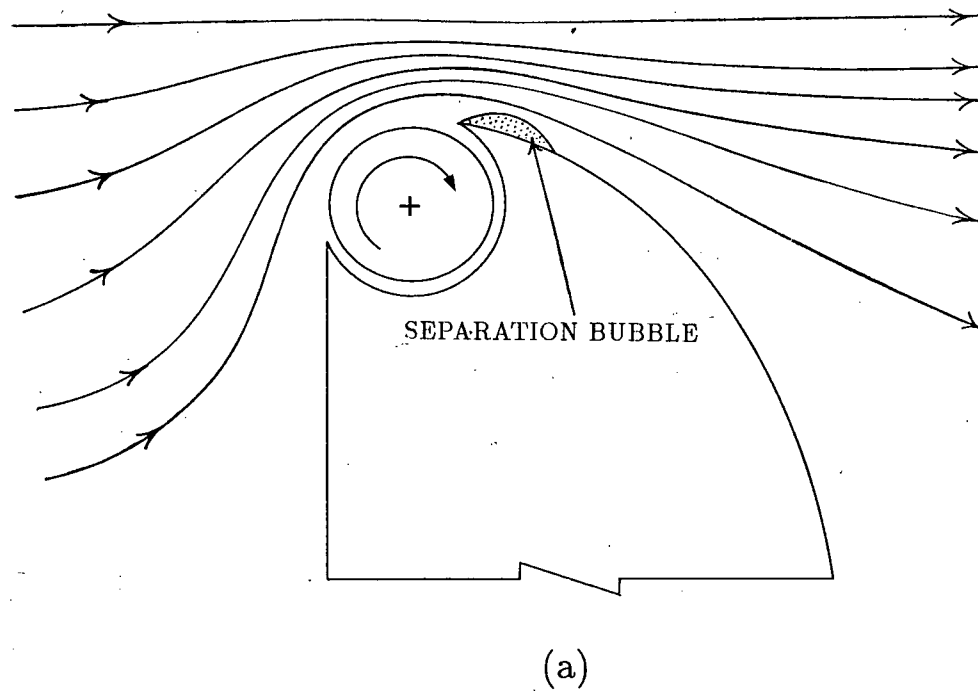
Figure 1-8 A bluff body with a rotating cylinder: (a) streamline patterns, (b) pressure distribution; i) — · — · —┐ no rotation, ii)— — — — —, with rotation.

number', is independent of the Reynolds number in a certain range. The Strouhal number varies with shape and orientations of the object. There have been attempts to define a universal Strouhal number which is independent of the angle of attack for a given bluff body. Modi and Wiland [66,67] have used the projected diameter in case of a two dimensional ellipse and the results indicate that the variation of the Strouhal number with angle of attack is significantly reduced. Pioneering contribution in understanding of the bluff body flows was due to Karman [3]. He presented simple but accurate analysis of the stable vortex wake. It showed that, for stability, the alternately shedding vortices should arrange themselves in a ratio of transverse to longitudinal spacing, b/a, equal to 0.281. Kirchoff [68] was the first to use the concept of free streamlines in a hodograph model of the potential flow past a normal flat plate. But he assumed incorrectly that the base pressure in the wake is equal to the freestream static pressure and obtained a drag coefficient of 0.88 (the correct value is 1.98). Roshko [69] proposed a better hodograph model for a normal flat plate and obtained a value of 2.0 for the drag coefficient. The hodograph models are quite useful but difficult to construct for complicated bluff bodies. A much simpler and more versatile wake source potential flow model was presented by Parkinson [70]. It uses the concept of wake vortices located on a mapping circle to force separation of the incoming flow. The method is applicable to an airfoil, ellipse, circle, normal flat plate, etc. The wake base pressure downstream of the body is required as an input in the analysis.

A number of reviews relating to the bluff body aerodynamics have appeared in past. The book by Blevins [71] on flow-induced vibrations provides useful information to the practicing engineers. Other books related to bluff body aerodynamics, flow-induced vibrations and other topics of interest to wind engineers include those by Simiu and Scanlan [72], Houghton and Carruthers [73], Sachs [74], and Walshe [75]. Some of the recent reviews on the subject are by Bearman [16], and Parkinson [19].

21

Bearman covers mostly experimentally observed vortex shedding phenomenon and its effect on vibrations of a circular cylinder. A paper by Bearman and Davies [76] reports that, for a D-section and a triangular geometry with vertex pointing downstream, there is a decrease in base pressure at lock-in of vortex shedding frequency with the system natural frequency. The review by Parkinson [19] covers flow-induced vibrations of circular, D-section and rectangular cylinders together with a discussion on the quasisteady theory modelling galloping instability.

The department of mechanical engineering at the University of British Columbia has been quite active in studying the flow-induced vibrations of bluff bodies. Several studies have been carried out by Parkinson and Modi et al. over the years. The first series of experiments were carried out by Brooks [77] on the galloping characteristics of rectangular prisms with the aspect ratio (AR) ranging from 0.38 to 2.5. The wake survey and Strouhal number measurements were also conducted. Smith undertook additional experiments up to an aspect ratio of 6 and also studied the effect of varying damping on the vibrations [78]. These results indicate that bluff sections with short afterbodies ($AR < 0.5$), like a D-section, do not gallop from rest but are susceptible to vortex resonance type vibrations. D-section has been found to behave as a hard oscillator requiring a threshold amplitude to initiate galloping over a certain range of wind speeds. Slightly larger afterbodies (AR between 0.75 to 1.5) like a square section gallop from rest as the wind speed is increased from zero (soft oscillator). Long rectangular prisms ($AR > 3$) are stable in the plunging mode at all wind speeds. This is probably due to the reattachment of the separated shear layers on the top and bottom sides of the rectangle. Heine [79] carried out measurements of fluctuating pressure on both stationary and oscillating models of rectangular sections with AR of 0.5 and 2. His results indicate that the self-excited oscillations of a bluff body do not affect the frequency of vortex shedding and pressure fluctuations. Measurements on a circular cylinder by Ferguson [80] suggest presence of amplitude modulations in

the fluctuating pressure signal which are in phase with the vortex-excited response. The results also indicate that the modulations are critically dependent on the wind speed. Santosham [81] conducted force measurements on rectangular and D-section cylinders and compared the dynamical results with predictions of the quasi-steady theory as proposed by Parkinson [19]. It was assumed that the bluff body at any instant during the galloping cycle experiences the same lateral force as that when held stationary at the same angle of attack. The experimental results compared well with the theory.

Feng [82] carried out measurements of span-wise correlation of wake velocity for stationary and oscillating circular as well as D-section cylinders. The results indicate that the vortex wake is highly three dimensional. The response measurements showed hysterisis type behaviour, i.e. higher amplitudes were obtained when the wind velocity was increased over a certain range than when it was decreased back over the same range. The presence of hysterisis is not fully explained yet, but it is believed to be due to nonlinear interaction between the wake and the afterbody, and is not associated with the elastic behaviour of the system.

Wind-induced vibrations of a structural angle section were studied in detail by Slater and Modi [83]. The frequent use of structural angle section in construction of towers, antenna masts and bridges, etc. warrants that their galloping and vortex resonance type response to wind forces be controlled. The wind tunnel tests showed that the angle section is susceptible to galloping in either plunging or torsional degree of freedom. The results correlated well with the predictions of the quasi-steady theory [19]. The quasi-steady theory was applied by Novak [84] to obtain a universal response curve which can be calculated from static force measurements on a rigid section or derived from response of an arbitrary model having the same type of cross-section.

From these studies several important points, as listed by Parkinson [19], emerge:

a)   Conditions in the wake are primarily responsible for all forms of bluff body

vibrations and needs further investigation.

b)   The Karman vortices are the dominant source of excitation. During galloping, their effect is to cause an asymmetric mean pressure on the bluff body to produce transverse vibrations at small angles of attack.

c)   The most important shape parameter for a bluff body is the afterbody length.

d)   The large amplitude oscillations of a bluff body are essentially nonlinear in nature.

1.3.2   Vibration and flow control devices

The suppression of wind induced vibrations has received considerable attention over the years. An excellent review of various techniques developed to this end has been presented by Zdravkovich [85,86]. He has classified and compared a wide variety of aerodynamic and hydrodynamic means for suppression of vortex shedding and associated vibrations of bluff bodies. The three general categories described are: (i) surface protrusions (helical strakes, wires, fins); (ii) shrouds (perforated shrouds, gauze shrouds, axial slats); (iii) Near wake stabilizers (splitter plates, guiding vanes, base-bleed). In general these vibration control devices are passive in character. The surface protrusions like helical strakes, which are probably the most effective, affect the separation lines and the shear layers. The shrouds influence the entrainment condition in the wake. In contrast, the nearwake stabilizers prevent interactions between the entrainment layers. Generally, surface protrusions and shrouds are omni-directional while the near-wake stabilizers are uni-directional. It is of interest to note that most of these devices need to be applied only to the top one-third portion of the structure (e.g. a chimney). Although some of the devices mentioned above are quite successful in suppressing the vortex shedding and the associated vibrations, their application may result in a significant increase in the drag. It has been observed that the effectiveness of strakes decreases with an increase in the intensity of turbulence as well as free stream velocity.

Another novel approach to control oscillations of structures has been studied by Modi et al. [13]. It uses the concept of energy dissipation due to sloshing of liquid in torus shaped nutation dampers. Since the civil engineering structures like buildings, bridges, smokestacks, airport control towers etc. have a natural frequency of about 1 Hz or less, the nutation dampers are especially suitable. Originally they were designed to control the very low frequency librational oscillations of orbiting satellites. A systematic parametric study involving overall mass of the damper as a percentage of the structure mass, damper geometry, liquid height and excitation amplitude, forced and natural frequencies, etc. was carried out by Welt [11–13]. Several designs of nutation dampers have proved to be quite successful in controlling the vibrations of structures and have been implemented in practice.

As mentioned earlier, the concept of moving surface boundary layer control (MSBC) has been studied in detail by Modi et al. [53-60]. Several applications of the MSBC are shown in Figure 1-9. A rotating cylinder is used to inject momentum into the boundary-layer in order to keep it attached to the surface in the region of adverse pressure gradients. A systematic wind tunnel study of the MSBC as applied to a flat plate, an airfoil, rectangular prisms and tractor-trailer truck models has been carried out by Modi et al. [56,58-60]. A rotating cylinder located at the leading edge of a Joukowski airfoil increased the lift by about 200 percent and delayed the stall angle to 48°. Further lift enhancement could be achieved by locating one extra cylinder on the top surface of the airfoil [53-55,57]. Two counter-rotating cylinders located at the top and bottom leading edges of a normal flat plate could reduce the drag coefficient by 75% at $U_C/U = 3$, where U_C/U is the ratio of the cylinder surface speed to the free stream speed. Similar results were achieved for rectangular prisms of varying aspect ratios. The flow visualization pictures taken during the experiments dramatically revealed effectiveness of the MSBC in promoting the attached flow and narrowing the wake. In some case (e.g. a Joukowski airfoil at a high angle of attack of 25°), the

flow field became essentially potential, i.e.the boundary-layer separation was virtually eliminated. A 1:12 model of a tractor-trailer truck fitted with a rotating cylinder at the top leading edge of the trailer resulted in a spectacular drag reduction of 26 % [56,58-60]. The flow-visualization pictures clearly showed that the turbulent vortex wake adjacent to the bluff body is almost eliminated at a sufficiently high speed of rotation of the cylinders. These encouraging results, though preliminary in character, suggest a need for more serious closer look at the concept from both aerodynamic and dynamic considerations. Figure 1-10 shows possible future applications of the MSBC to a bridge-tower and a supertall building.

1.3.3 Numerical simulation of bluff body flows

The past four decades have seen revolutionary progress in the field of computer technology. Today, the subject of computational methods in fluid mechanics and wind engineering has evolved into a major field of research. Historically, Computational Fluid Dynamics (CFD) received serious attention since introduction of the panel method simulating the potential flow around a physical object. At present, supercomputing capability has made it possible to simulate the complete Navier-Stokes equations in three dimensions, accounting for the turbulent flow field. Today, significant amount of design and development activities in the aerospace industry are based on computer simulations. Over the years, several journals and conferences dedicated to CFD have been established to meet the growing demands of the research community. Unprecedented growth in computer technology and sophisticated numerical methods promise a future where considerable amount of research and technological developments in fluid mechanics would be routinely performed using numerical simulation tools. This is especially true for the bluff body flows. Hence in any serious discussion on bluff body fluid dynamics, it is appropriate to provide at least some appreciation as to the state of the art in this important area. Of course, to review the vast body of literature on the CFD, accumulated over the years, is an impossible

(i) The Basic Configuration

Leading-Edge Cylinder

(ii) 0.05 C

Trailing-Edge Cylinder

(iii) 0.067 C 0.72 C

Rear Upper-Surface Cylinder

(iv) 0.58 C

Forward Upper-Surface Cylinder

(v) 0.38 C

Upper Leading-Edge Cylinder

(vi) 0.05 C
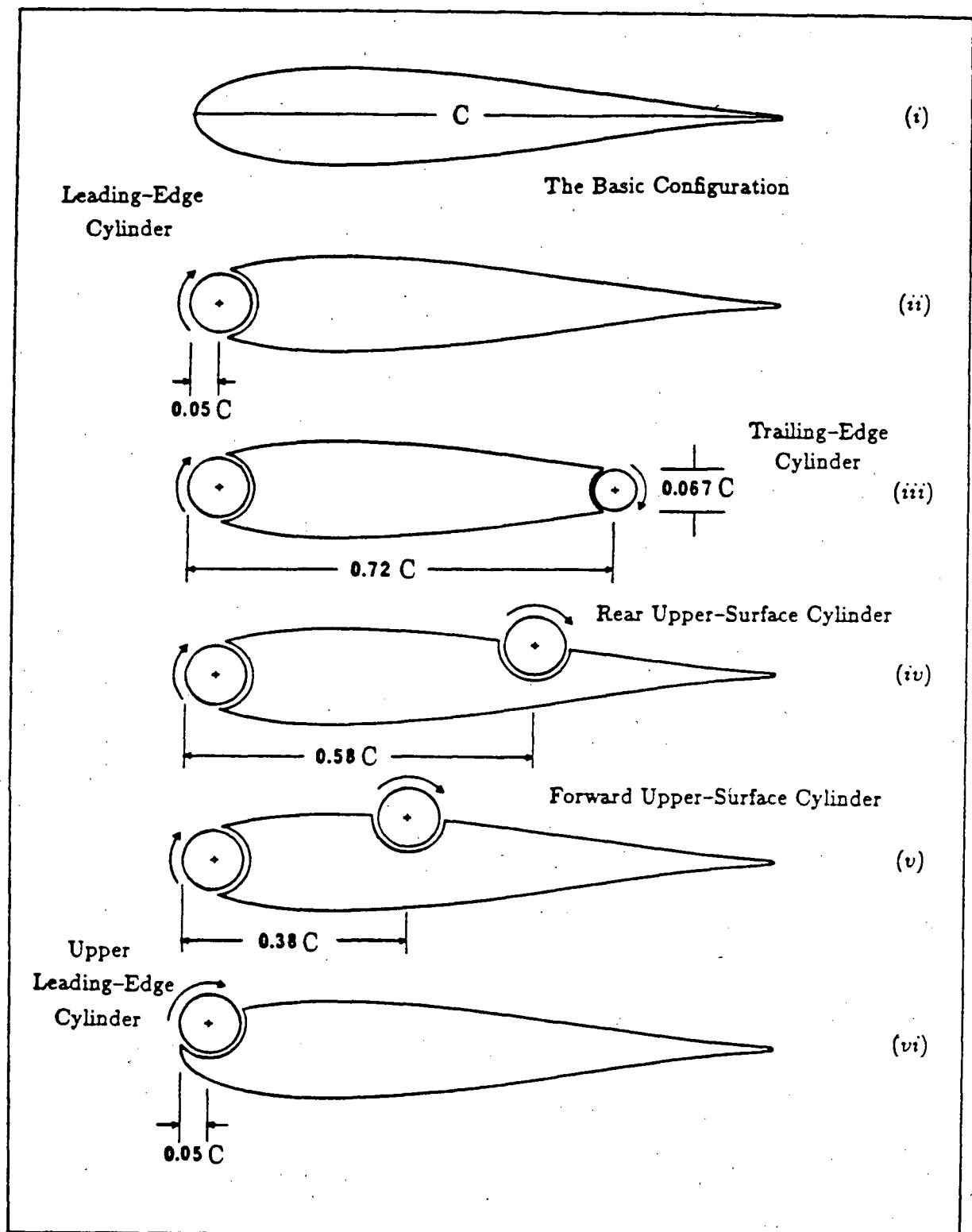
Figure 1-9   Applications of the Moving Surface Boundary-Layer Control (MSBC) procedure: (a) airfoil type geometries.

Two dimensional flat plate
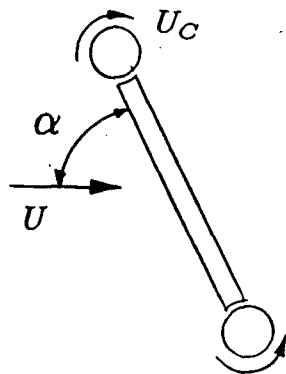
Two dimensional rectangular prisms

U_C

α

U

α

U

H

U_C

L

$L/H = 0.3, 1, 2, 4$

U_C

Tractor-trailer truck configuration

hf

U

bf

3-D prism with fences
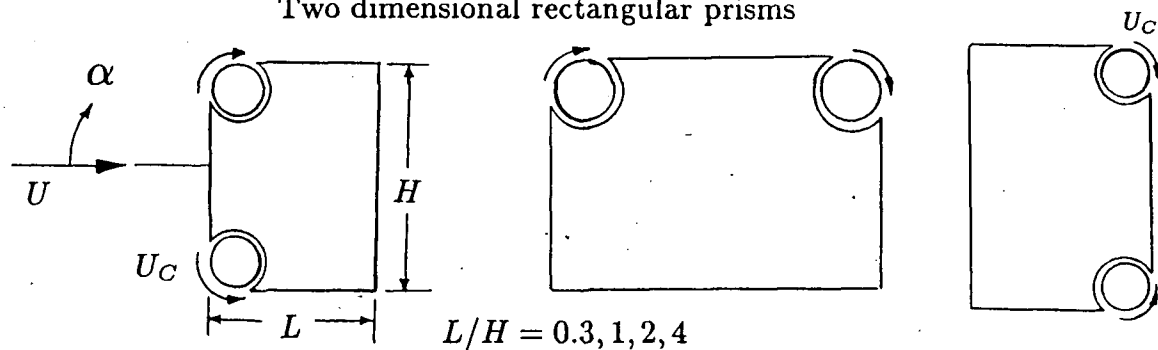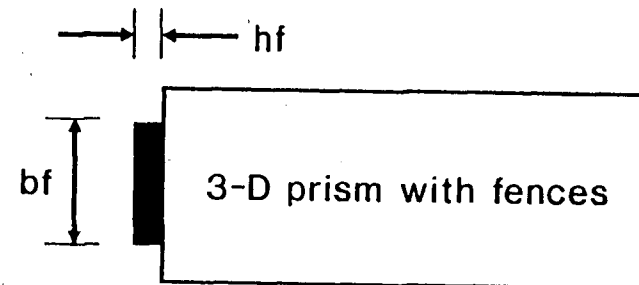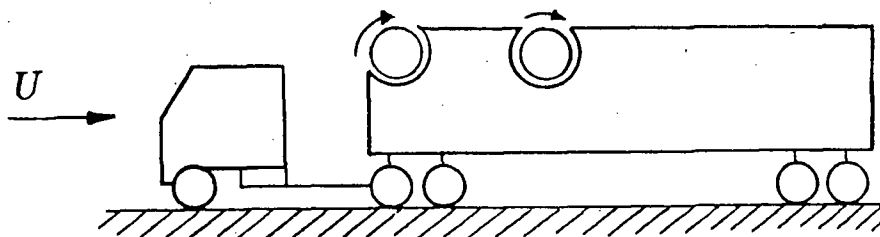
Figure 1-9(cont.) Applications of the Moving Surface Boundary-Layer Control (MSBC) procedure: (b) bluff bodies such as a flat plate at a large angle of attack; rectangular prisms; and tractor-trailer truck configurations. Boundary-layer control and the associated drag reduction through fence type tripping device is also indicated.
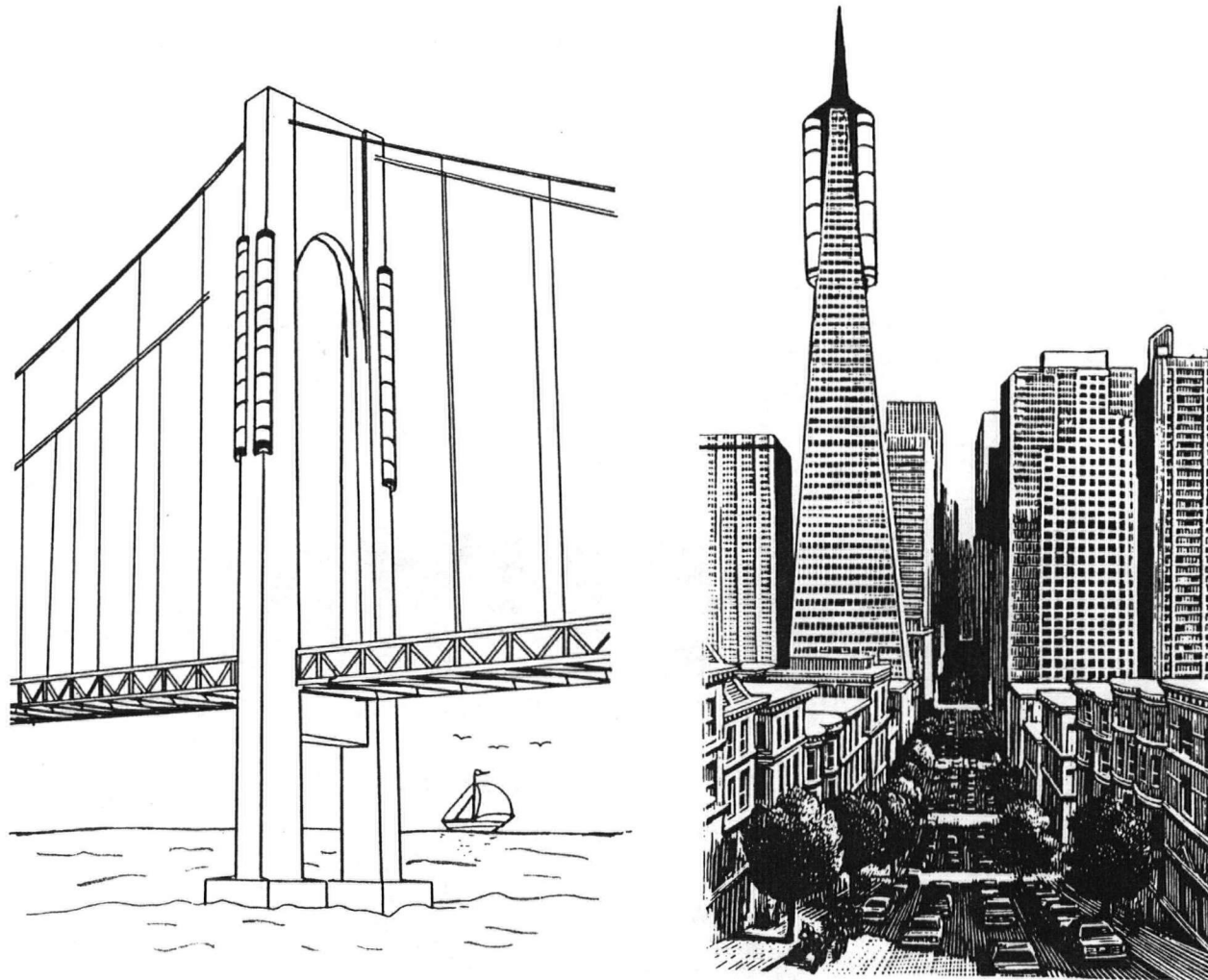
Figure 1-10   The MSBC concept presents an exciting possibility of applications to next generation of civil engineering structures such as bridge-towers and supertall buildings.

task. Here an attempt is made to touch upon only those aspects of the CFD directly relevant to the problem of bluff body fluid dynamics and boundary-layer control. The first ever symposium dedicated to Computational Wind Engineering (CWE) was held in 1992, in Tokyo, Japan. The proceedings of the symposium represent a window to appreciate advances in the field [87].

The Navier-Stokes equations provide a complete mathematical description of the physics involved in a fluid dynamic phenomenon. A set of initial and boundary conditions complement the equations which are unique for every fluid dynamic process and thus impart distinct character to the problem under consideration. A solution would predict fluid flow behaviour such as boundary-layer formation and separation, vortex shedding, momentum transfer in the wake, etc. The phenomenon of turbulence, suspected to be a chaotic behaviour of a deterministic dynamical system, is also governed by the Navier-Stokes equations in conjunction with an appropriate turbulence model.

Low speed bluff body flows are governed by a mixed set of elliptic-parabolic form of the Navier-Stokes equations. A number of books and review articles [87-90] provide a general introduction to the subject of numerical simulation of the Navier-Stokes equations.

There are several popular approaches among the researchers to numerically model the Navier-Stokes equations. One of the earliest and still the most widely used approach is the Finite Difference Method (FDM). The governing nonlinear partial differential equations are descretized using finite difference approximations. An iterative scheme is generally necessary to solve the resulting nonlinear set of algebraic equations. In the last two decades many algorithms have been proposed to incorporate some kind of finite difference scheme. Also for bodies with complicated shapes various mesh generating schemes have been developed. A good introduction to the subject has been given by Roache [88], Patankar [89], Anderson et al [90], and others.

An alternative approach is to use some kind of finite element formulation procedure [91-94] popularly known as the Finite Element Method (FEM). The FEM technique originated in 1950s to analyze complex structural problems of the aircraft industry. Due to nonlinear and dissipative (viscous effects) nature of the Navier-Stokes equations, use of the FEM in fluid mechanics was not preferred for a long time. But the situation is changing rapidly and most of the commercially available CFD softwares have been developed based on the finite element method. The FEM has turned out to be more versatile, since one can readily solve complex problems involving dynamic interactions between the fluid and a structure. This suggests its potential in simulation of bluff body fluid mechanics and fluid-structure interaction problems encountered in wind engineering. As compared to the FDM, the FEM does not require mesh generation programs to descretize a complicated flow domain involving arbitrarily shaped geometries.

In addition to the FDM and the FEM, a totally different class of numerical approaches have been developed which are commonly referred to as the vortex methods. The vorticity transport equation is simulated by a collection of distinct vortices. These methods range from simple to highly sophisticated, requiring the use of a supercomputer. One of the methods (or its variation) known as the Discrete Vortex Method (DVM) has been routinely employed to study vortex shedding past a flat plate, rectangular and circular cylinders, and other bluff bodies.

A numerical study of the stability of rows of vortices individually free to move at induced velocities was made by Abernathy and Kronauer [95]. The results clearly show the pattern of vortices observed in the wake of bluff bodies. Similar methods have been used, notably by Gerrard [96] and Sarpkaya [97], to model the unsteady flow around a circular cylinder. An analogous model was developed by Laird [98] in which the attached boundary-layers were also reproduced and new vortices were added at the separation points. Similar to Laird, Chaplin [99] modelled the flow around a

cylinder free to execute transverse oscillations. The frequency of oscillations obtained numerically agreed with the experiments quite well, but the amplitude of the lift and drag forces exceeded that of the experiments, due to the absence of turbulent entrainment in the shear layers.

Sarpkaya [100] has also modelled vortex shedding from an inclined flat plate using the discrete vortex method. The vortex shedding and Strouhal number results agree favourably with the experimental data, but the calculated normal force coefficient is 20-25% larger than that measured by Fage and Johansen [101]. A similar study of vortex shedding past an inclined plate by Kiya and Arie [102] shows good agreement with the flow visualization results. Their results suggest that the vortex street behind the plate inclines as a whole towards the direction of the time-averaged lift force exerted on the plate. It is also indicated that the vortex shedding from one edge of the plate will not occur at the mid-interval of the successive vortex shedding at the other edge. In another paper, Kiya and Arie [103] have performed discrete-vortex calculation of the near wake velocity profiles, turbulence intensities and Reynolds stresses. They have also introduced a simple constant to achieve the vorticity transfer from large scales to small scales of turbulence.

Several other bluff geometries have been studied using the DVM, such as the flow past a square section [104], a rectangular prism [105], a normal flat plate [106], two parallel plates [107], and two circular cylinders arranged side by side [108]. Chein and Chung [109] have performed discrete vortex calculations on an inclined and vertical plates using a different approach to determine the strength and location of the vortices just shed from the edges of the plate. In their model, the vortices are shed in such a way that their presence in the flow field offsets the singularities that exist at the plate edges as predicted by the potential flow solution. A review of various vortex methods is presented by Leonard [110] and Maull [111]. In a recent study by Leonard and Koumoutsakos [112], new advances in vortex methods for the simulation of un-

steady incompressible flow past a bluff body, the fast-vortex algorithm for convection, and the method of particle-exchange for viscous diffusion are discussed. Results of a transient flow past a circular cylinder for Re = 40–9500 have been reported [112] using a vector supercomputer. This method promises to become a powerful tool for accurate numerical simulation of bluff body flows in three dimensions by utilizing massively parallel computer architecture.

Pan, Chew and Lee [113] have proposed a new vortex calculation method using "generalized conservation of circulation model". By introducing a "generalized velocity field", the generalized circulation for a viscous flow is obtained. This simple algorithm is aimed at reducing the computational effort. In an interesting paper, Bienkiewicz and Kutz [114] discuss the simulation of unsteady separated flow past a bridge-deck section employing the discrete vortex method. Their numerical results show only a fair agreement with experimental data due to difficulties encountered in modelling flow reattachment and identification of the dominant separation nodes. A paper by Fernando and Modi [115] describes in detail a mathematical model based on the DVM for predicting the performance of a Savonius wind turbine. Results show good agreement with flow visualization and wind tunnel data for both stationary and rotating Savonius configurations.

In general, fluid flows in nature exhibit turbulent behaviour to some extent. Turbulence is strongly affected by "extra strains" including stratification, buoyancy, rotation, chemical reaction and compression [116]. The structure of the turbulence varies considerably depending on the flow regime. A unified model of turbulence versatile enough to describe the multitude of phenomena associated with turbulence is still not available. Bluff body flows encountered in wind engineering could be quite complex due to one or more structures immersed in a highly turbulent flow, without any preferred direction of the wind, and may require a full three dimensional treatment.

Although the steady force on an object such as a building can be computed reasonably well by a Reynolds-averaged Navier-Stokes (RANS) turbulence model, e.g. the k-ϵ model (k=turbulent kinetic energy, ϵ=dissipation rate), the intensity and frequency of the unsteady forces are difficult to predict by such a method. Since the geometry demands nothing less than a three dimensional treatment, the computational effort becomes too expensive [116]. Generally, simulation of turbulent flows through the solution of the unsteady Navier-Stokes equations in three dimensions can be accomplished in two different ways.

In the Direct Numerical Simulation (DNS) of a turbulent flow, the Navier-Stokes equations are solved for the largest scale of motion to the smallest scales in the dissipation range (Kolmogorov range). If the boundary and initial conditions are applied accurately and the numerical errors are kept to a minimum, the DNS is capable of reproducing a physical experiment in all of its details. The limitation of the DNS arises from its inability to deal with complex geometries and high Reynolds number flows due to the skyrocketing computational effort. In terms of accurate modelling of turbulence, potential of the DNS is unsurpassed, but it is unlikely to become a practical engineering tool [116].

In general, at low Reynolds numbers, the flow is a laminar, two dimensional periodic motion which can be studied fairly well with the present-day numerical methods. At higher Reynolds numbers, which usually occur in practice, stochastic three dimensional turbulent fluctuations may be superimposed on the two dimensional periodic vortex shedding motions [117]. Although, in principle, this can be accomplished by resorting to the DNS, presently it is feasible only at relatively low Reynolds numbers. The dissipative part of the turbulent motion has such small scales compared to the bluff body dimensions that it cannot be resolved in a numerical calculation. The number of grid points required to resolve this motion increases approximately as Re^3 [117].

A method that can be applied to situations at high Reynolds numbers is the Large-Eddy Simulation (LES) which consider only the larger-scale motions. However, the effect of the smaller-scale motions, which cannot be resolved on a given grid, needs to be accounted for. This effect is mainly dissipative. It can be achieved in two ways : (i) through a sub-grid scale model for determining turbulent stresses introduced by the smaller-scale fluctuations; (ii) the energy dissipation through damping introduced by the numerical scheme [117]. LES is a very powerful tool but it requires enormous amount of computing power and hence very expensive to implement. Attempts have been made to simulate turbulence in vortex shedding flows with statistical models which do not resolve any of the stochastic turbulent motion but average it out altogether [117].

Several statistical turbulence models are available to compute the Reynolds stresses $< u_i' u_j' >$ appearing in the ensemble averaged Navier-Stokes equations simulating the vortex shedding flow past a bluff body. One approach is known as the eddy-viscosity model [117]. Alternatively, the Reynolds-Stress-Equation (RSE) solves the transport equations for the individual Reynolds stresses $< u_i' u_j' >$ [118]. With the various turbulence models, different approaches were tested for handling the near-wall region. Several strategies are discussed by Deng [119], Nagano and Tagawa [120], Franke and Rodi [118], Jansson [121], Norris and Reynolds [122], and others.

A good introduction to the LES method can be found in the review paper by Ferziger [123]. Until now, the numerical methods most frequently used for descretization of spatial derivatives in the DNS and the LES have been spectral in character. For geometrically simpler domains with simple boundary conditions, they offer maximum accuracy at a given cost. This has been reviewed at length in the book by Canuto [124].

It is expected that in the near future the vector supercomputer would reach its ultimate performance limit at the level of 100 GFLOPS (Giga Floating Point Opera-

tions per second) [125]. Any further increases in computational speed is likely to come from parallel processing technology. The CFD applications represent probably the most computational intensive tasks ever presented to a computer to perform. Hence, it is natural that research efforts are being directed towards accelerated implementation of the CFD to other disciplines (e.g structural analysis) on massively parallel computer systems. As noted by Murakami [126], in future, large scale computation of turbulent flows past bluff structures will of necessity rely on the parallel computation methodology. It would be appropriate to have at least some appreciation of the present and future developments in parallel processing, which is soon expected to become a norm.

In USA, the Numerical Aerodynamic Simulation (NAS) Systems Division at NASA Ames Research Center has embarked upon an ambitious program of development and implementation of parallel processing (both hardware and software) technology [127]. The 'High Performance Computing and Communication Program (HPCCP)' at NASA focusses on the use of parallel processing for extremely computation intensive, multidisciplinary applications involving aerodynamic, propulsion, controls, structural and acoustical analysis necessary in aerospace missions of the future. These grand challenge problems may involve: 5,000,000 grid points; 50,000 iterations; 5,000 operations per point per second; and 10^{15} operations per problem! For an automated design process requiring 0.1-0.01 hour turn-around time, it would involve 3-30 TFLOPS (Tera Floating Point Operations per second) capability with 4-40 gigawords of memory storage per problem [127].

An example of the current state of the art in parallel processing as applied to the CFD can be found in the paper by Kato et al. [125]. Computations were carried out for an airflow around a two dimensional square rib placed within a boundary-layer by means of a massive parallel computer consisting of 1024 processors arranged in a MIMD (Multi-Instructions Multi-Data) network. Since shared memory paral-

lelism is inapplicable due to a conflict in memory access, a network of loosely-coupled multiprocessors with each having its own memory was preferred. The result of their investigation confirm the fact that the local memory parallelism requires a great deal of data exchange between the processors. The efficiency of parallel computation is significantly affected by the amount of inter-processor communication. It is also necessary to take into account effects of granularity (ratio of calculation time to communication time for each processor). For a network of 512 processors the computational speed was boosted by a factor of 420 compared to that of a single processor, i.e. an efficiency of 82% (i.e $420/512 \times 100$) of parallel computation.

The future of parallel processing critically depends on resolving several key issues regarding the implementation on parallel architecture machines, development of numerical algorithm for the parallel CFD, performance evaluation and the necessary computer science involved in achieving Teraflops capability. Such a technology would be extremely useful in carrying out the DNS or LES simulation of turbulent flows past complex bluff body configurations.

As pointed out before, the precise numerical solution of a given problem can be obtained by solving the general time-dependent Navier-Stokes equations incorporating a suitable turbulence model. However, for realistic values of the Reynolds number, this demands enormous computational effort and cost. On the other hand, judicious modelling of the flow character can provide information of sufficient accuracy for all engineering design purposes with nominal computational tools and insignificant cost. To that end extension of the well developed panel code to multielement bluff bodies with moving surface boundary-layer control appears quite attractive. Numerical modelling of inviscid flows can be accomplished using the panel method. Over the past several decades, this approach has evolved to a sophisticated level where it can successfully tackle two and three dimensional geometries with flow separation, shock wave formation and unsteady aerodynamic phenomena. Even though the

panel method uses potential flow assumptions, various schemes have been devised to account for viscous dissipation, flow separation and existence of a finite wake.

In the classical paper by Hess and Smith [128], the authors describe the original panel method, which replaces the body surface by source type singularities to obtain a numerical solution of the governing Fredholm integral equation of the second kind. The method is quite general in the sense that it can be easily extended to realistic flow regimes past ensemble of bodies, with nonrigid surfaces, moving with respect to each other; internal flows; suction for boundary-layer control; etc.. Nevertheless, certain classes of potential flow problems like partially unknown location of boundaries (e.g. trailing-vortex wake of unknown position) are excluded [128].

Recently, Farassat and Brown [129] have applied a particular form of the integral representation of the velocity potential to study helicopter rotor and propeller induced noise during flight. Using a similar approach, Lee and Yang [130] have developed a panel formulation to handle complex geometries (e.g. rotors, propellers etc.) undergoing complicated motions.

Yon, Katz and Plotkin [131] have investigated the effect of trailing-edge thickness on the solution accuracy of a given panel method. The panel method under consideration uses a combination of source/doublet distribution with Dirichlet type boundary conditions. The results suggest that both the use of larger panels making a bigger angular separation at the trailing-edge or an alternate form of Kutta condition requiring the upper and lower trailing-edge velocities to be equal give much better results. The information obtained suggests the sensitivity of the solution to the size and distribution of panels. Kida et al. [132] discuss the accuracy of the panel method with distributed sources applied to two dimensional bluff bodies. Their investigation shows that the panel method with point sources is mathematically superior compared to that with linear sources. A panel method based on linear sources would diverge if the number of panels is even, which results in a singular coefficient matrix. Katz

and Plotkin [133] provide a good introduction to various panel methods and relevant computational details.

Mokhtarian [134] has used a type of panel method with boundary-layer correction technique to predict the separation point on an airfoil with moving surface boundary-layer control. It accounts for the wall confinement and involves replacement of the airfoil and wind tunnel walls with vorticity distribution in conjunction with appropriate constraint relations. Inclusion of a source within the contour of the airfoil models the wake when there is flow separation from the surface.

A finite difference boundary-layer scheme is used to introduce viscous corrections. The scheme employs potential flow pressure distribution results to calculate the boundary-layer characteristics at the top and bottom surfaces starting from the stagnation point until the point of separation.

The procedure uses the displacement thickness to construct an equivalent airfoil and then iterates between the potential flow and boundary-layer scheme to converge to the final pressure distribution. Thus the objective is to match the outer potential flow solution with the inner boundary-layer prediction. The thin shear layer approximations of the Navier-Stokes equations for steady, two dimensional, incompressible flow are used. The finite difference method employed for viscous corrections is due to Keller and Cebeci [135,136]. The eddy viscosity term is expressed as suggested by Cebeci and Smith [137] which treats the turbulent boundary-layer as a composite layer consisting of inner and outer regions with separate expressions for eddy viscosity in each region. The details of the formulation and the finite difference procedure followed are those given by Cebeci and Bradshaw [138]. Celik et al. [139] have reported a viscous-inviscid interaction method to calculate the mean flow past a smooth circular cylinder. The method is applicable to flows with a Reynolds number as high as 10^8.

To handle separated flow problems as well as other complications arising due

to geometry, flow characteristics and boundary conditions, many extensions of the basic panel method of Hess and Smith have been proposed. In the method developed by Maskew and Dvorak [140], the interface between the potential flow region and the trailing-vortex wake have been modelled as a simple shear layer. The enclosed wake region between the upper and lower free-vortex lines is interpreted as a potential flow region with a reduced total pressure. The model is essentially formulated as mixed boundary condition problem. On the active part of the solid surface the position of the boundary is known but the strength of the panel vorticity is unknown. On the 'free-vortex lines' the inverse is true: the vortex strength is a known constant but the position is an unknown. An iteration scheme is required to establish the wake shape, i.e. the position of the 'free-vortex lines' by integrating the induced velocity vectors. The particular advantage of the 'free vortex lines' model is that the low pressure in the separated zone can be calculated directly.

An insight to the problem of viscous separated flow involving dispersion of vorticity field in the wake was given by Pearcy et al. [141] based on experimental observation of various cylindrical bodies having different surface roughness. In an attempt to explain the movement of separation point from bodies having smooth contours, it was argued by the authors that a balance must be maintained between the rate at which the vorticity field is shed into the wake and its subsequent dispersion by diffusion, dissipation and cancellation among mutually opposite shear layers.

In the improved model of Ribaut [142], the vorticity field is allowed to dissipate along the 'free vortex lines'. The vorticity dissipation model thus indirectly accounts for the presence of viscosity. Applying this model to a flat plate and blunt trailing edge section, Ribaut demonstrated that extent of, and pressure in, the wake are essentially determined by the amount of viscous diffusion and dissipation of the vorticity. As a result a finite closed wake is obtained.

A numerical approach, based on the first-order panel method employing lin-

early varying vorticity plus a constant source strength distribution, has been developed by Mukherjea and Bandyopadhyay [143,144] to model the separated flow past a wedge configuration. The solution obtained by this method, using a linear model of vorticity dispersion in the wake, shows close agreement with the experimental results over a range of the wedge angle.

1.4 Scope of the Present Investigation

A rather brief review of the literature, more relevant to the present investigation, provides some understanding of the present state in the area of industrial aerodynamics. With that as background, a comprehensive program of study was formulated to explore the effect of Moving Surface Boundary-layer Control (MSBC) as applied to a family of slender as well as bluff bodies. The two-dimensional models used in the investigation include a symmetrical airfoil, a D-section and a set of rectangular prisms representing geometries of increasing bluffness. The focus is on the effect of the MSBC on the aerodynamics of the models when they are stationary, as well as their dynamical response during vortex resonance and galloping type of instabilities. The problem is approached using wind tunnel tests, numerical analysis and flow visualization thus providing better appreciation of the subject.

To begin with, details of the models used, wind tunnel test methodology, modified panel method approach and flow visualization procedure are described in Chapter 2. This is followed by the results and their discussion for the airfoil, D-section and rectangular prisms in Chapter 3, 4 and 5, respectively. As all the results (wind tunnel test, flow visualization, etc.) for the bluff body under study are presented together, the individual chapter tends to be essentially self-contained. Finally, Chapter 6 looks at the dynamical response of the D-section and rectangular prisms in vortex resonance and galloping with the MSBC. Miscellaneous supporting information is contained in Appendices. The thesis ends with a summary of important results, original contribu-

tions, and suggestions for future investigation which are likely to be informative as well as satisfying. Figure 1-11 presents outline of the project.

Aerodynamics and Dynamics of Bluff Bodies in Presence of Moving Surface Boundary-layer Control (MSBC)

Experimental Investigation

Flow Visualization Without and With MSBC

Numerical Approach

Airfoil, D-section, Rectangular and Square Prisms

Static Measurements in the Wind Tunnel

Dynamic Tests in the Wind Tunnel

Airfoil, D-section, and Rectangular Prisms

Panel Method and Numerical Code

Steady-state Pressure Distribution

Spectral Analysis of Unsteady Pressure Signals through FFT

Vibration Response during Vortex Resonance and Galloping

One-Element Model

Aerodynamic forces

Multi-Element Model

Determination of the Vortex Shedding Frequency and Strouhal Number

Vibration Suppression through MSBC

Pressure Distribution, Aerodynamic Forces

Figure 1-11 A schematic diagram showing the scope of the investigation.

2. EXPERIMENTAL INVESTIGATION AND NUMERICAL MODELLING

2.1 Preliminary Remarks

As pointed out before, the investigation has three distinct phases: wind tunnel tests, flow visualization and numerical simulation. A set of four two-dimensional bodies, representing increasing bluffness, was used during the study: Joukowski airfoil; D-section; rectangular prism; and square prism. Wind tunnel tests to assess aerodynamics and dynamics of the models are described first. This is followed by an explanation of the flow visualization study using a closed circuit water channel. Finally, numerical analysis of the problem using the simple panel method is touched upon.

2.2 Experimental Investigations

2.2.1 Bluff body shapes

The set of bluff body shapes investigated is shown in Figure 2-1.

Joukowski Airfoil

The Joukowski airfoil (Figure 2-1) is 16% thick with a chord length of 370 mm and is symmetric about the chord. The rotating cylinder diameter is 10% of the chord length and is located at the leading edge of the airfoil. It is driven by a 1/4 H.P., variable speed, A.C. motor. 42 pressure taps, 0.5 mm in diameter, are located at the top and bottom surfaces of the airfoil. The bluffness of the airfoil is a function of the angle of attack (α). At zero angle of attack the airfoil behaves as a streamlined body. As the angle of attack is increased the bluffness increases. Variation of the lift, drag and lift/drag ratio with the angle of attack in presence of the MSBC are of primary interest in this study. The details of the motor connection to the rotating cylinder are shown in Figure 2-2.

The measurement of pressure on the surface of a rotating cylinder posed a problem. It was overcome in the following manner. Five pressure transmission tubes were located inside circumferential grooves as shown in Figure 2-3. The tubes remained stationary when the cylinder rotated. Thus the pressure taps remained immersed in the boundary-layer and provided accurate estimate of the static pressure.

D-Section

The front face of the D-section is flat and normal to the free stream (at α = 0) whereas the afterbody is semi-circular. Rotating cylinders are located at the two corners of the D-section. The presence of the cylinders causes rounding of the corners, i.e. departure from a sharp edged bluff body. This in turn, affects the vortex shedding process and drag of the body. The diameter of each rotating cylinder is 21% of the D-section width. Pressure taps are provided around the contour of the D-section, including taps on the rotating portion. As before, the cylinders are driven by a 1/4 H.P., A.C. Motors, capable of very high rates of rotation (upto 22000 rpm).

The aspect ratio (as defined in the list of symbols) of the D-section is 0.5. The D-section is likely to exhibit vortex resonance, galloping as well as autoration [145]. The present study is aimed at understanding of the D-section fluid dynamics and flow-induced instability in presence of the MSBC.

Rectangular Prisms

Two rectangular prisms selected for the study are also shown in Figure 2-1. The aspect ratios of the prisms are 1/2 (vertical rectangle) and 1 (square). The rotating cylinders are located at the two corners of the prism. The rotating cylinder diameter is 27% of the prism width. Pressure taps are provided around each model. The dynamics of a rectangular prism depends on its aspect ratio [19]. It is susceptible to both vortex resonance and galloping instabilities. The square prism, being a soft oscillator at all angles of attack, is particularly suitable for assessing the effectiveness of the MSBC in suppressing the vortex resonance and galloping vibrations. Note,

45

AR = 0.5

AR = 0.5

AR = 1.0

(AR = Aspect Ratio = Width / Height)
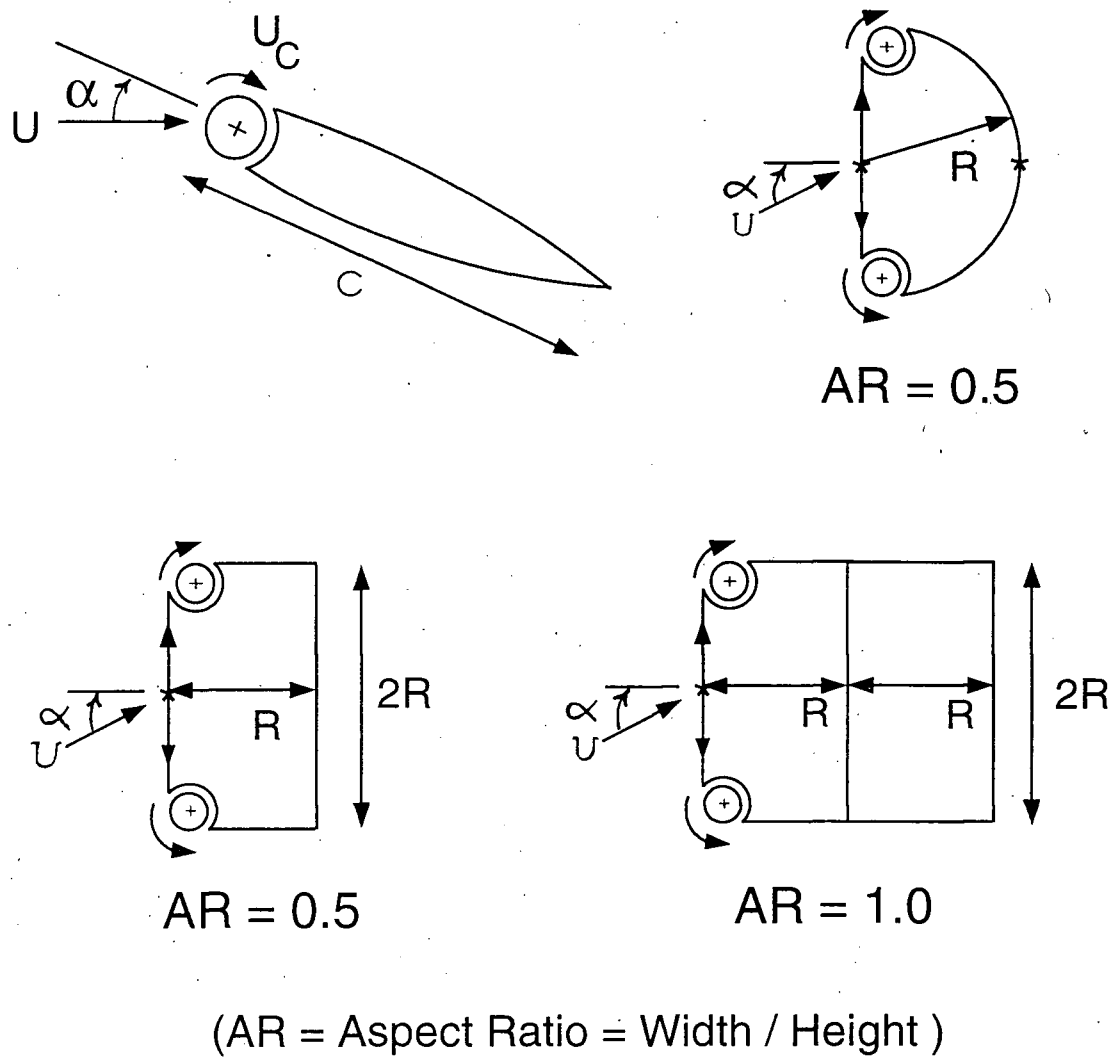
Figure 2-1   Bluff body geometries, without and with momentum injection, considered for investigation: (a) schematic diagrams.
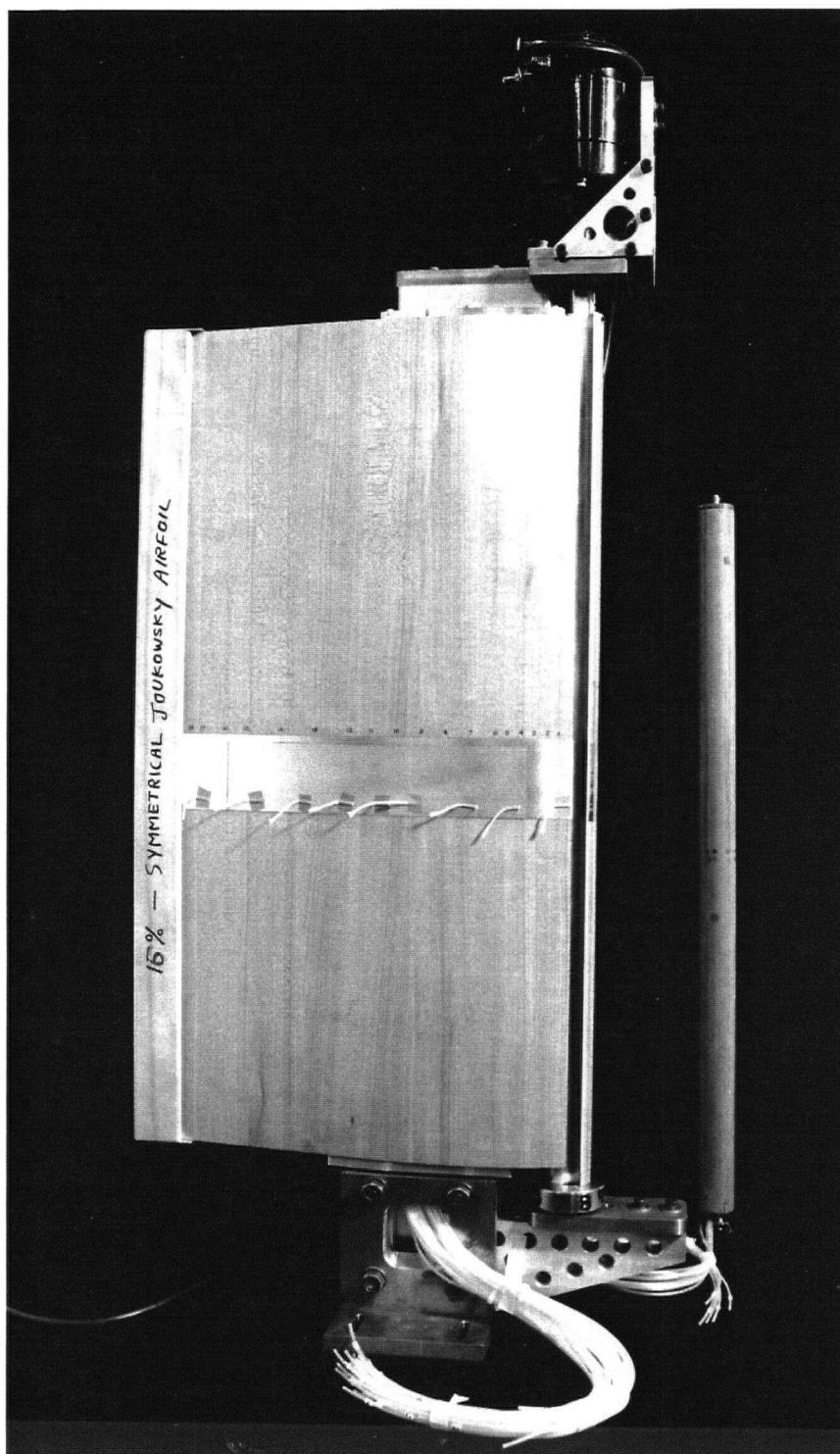
Figure 2-1(cont.) Bluff body geometries, without and with momentum injection, considered for investigation: (b₁) photograph of the Joukowski airfoil model.
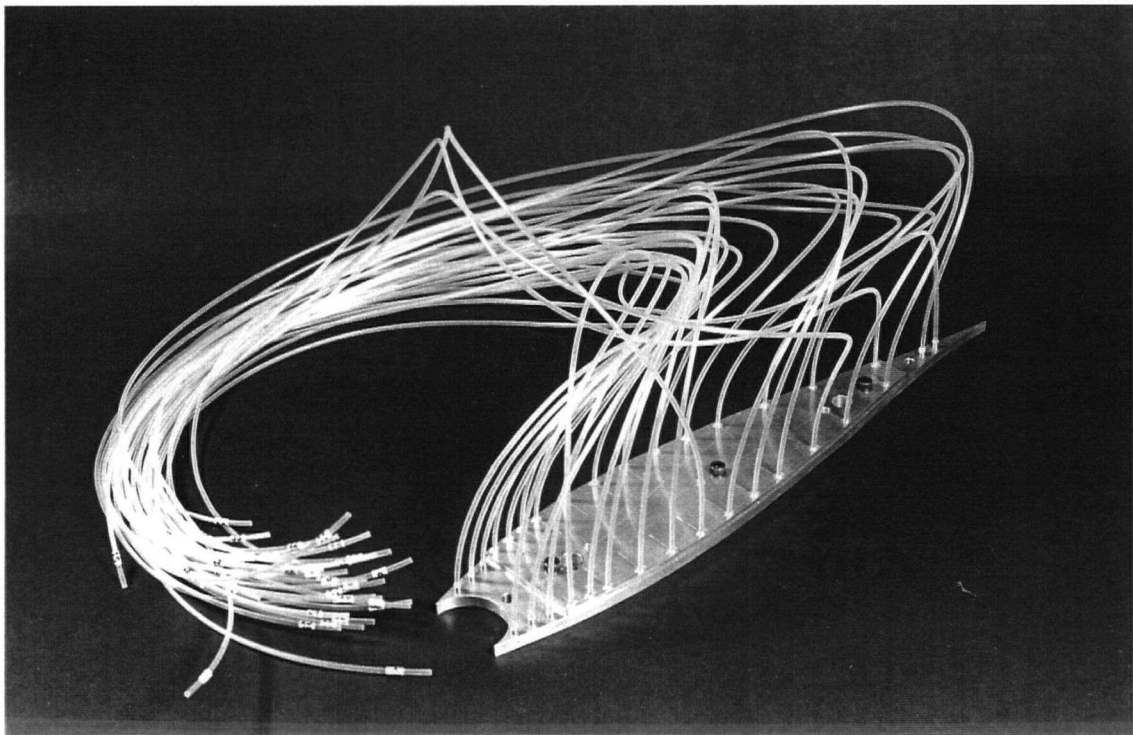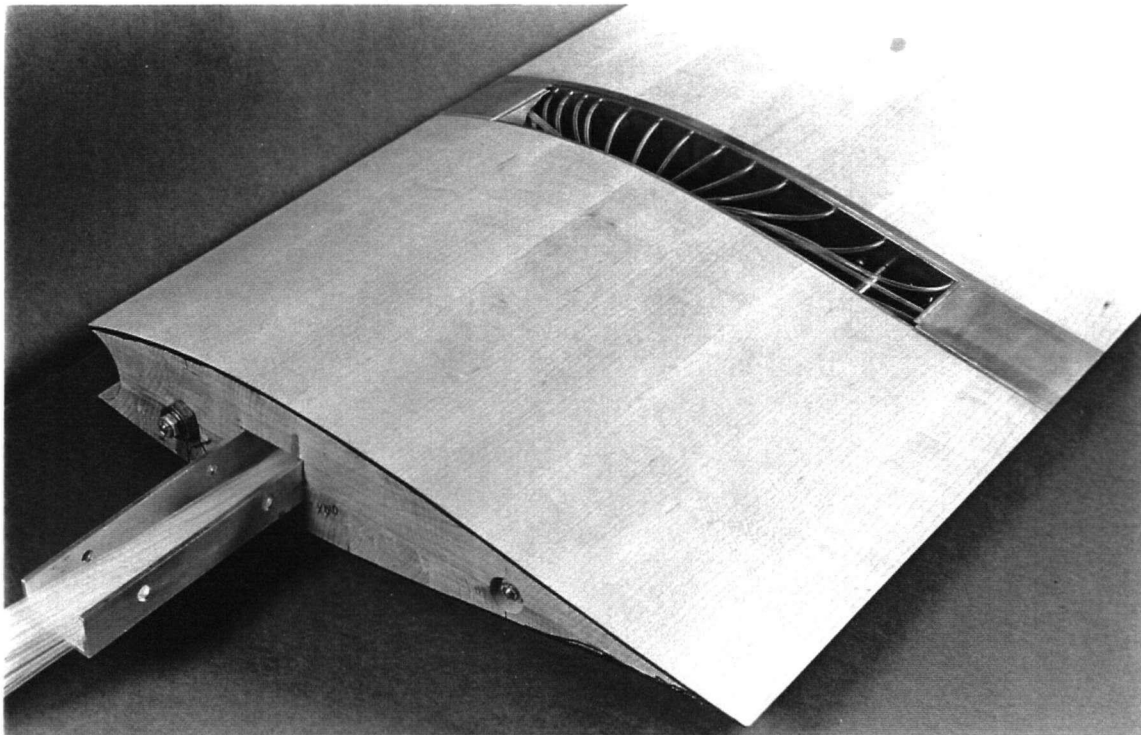
Figure 2-1(cont.) Bluff body geometries, without and with momentum injection, considered for investigation: (b₂) photograph showing details of the pressure taps and pressure conducting tubings.
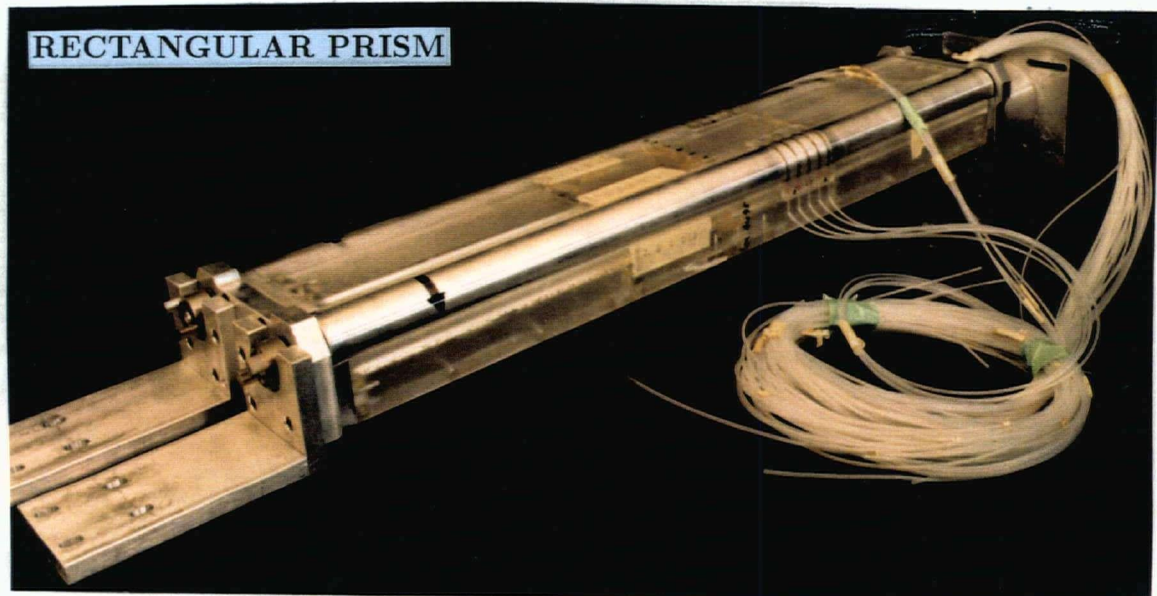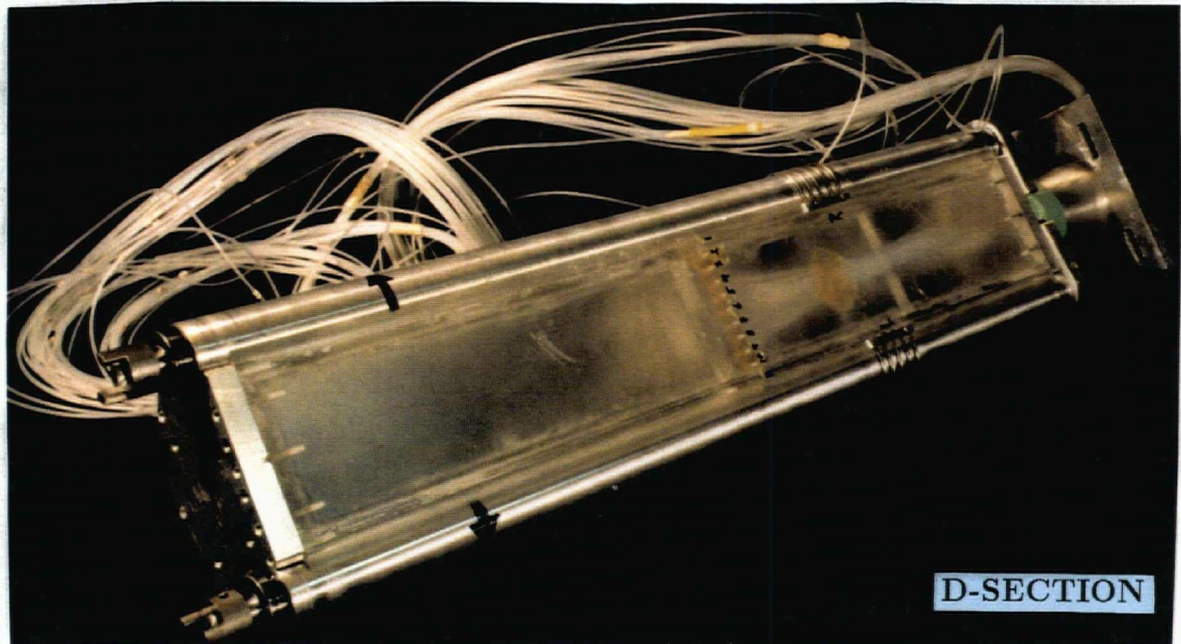
Figure 2-1(cont.) Bluff body geometries, without and with momentum injection, considered for investigation: (c) D-section and rectangular prism.
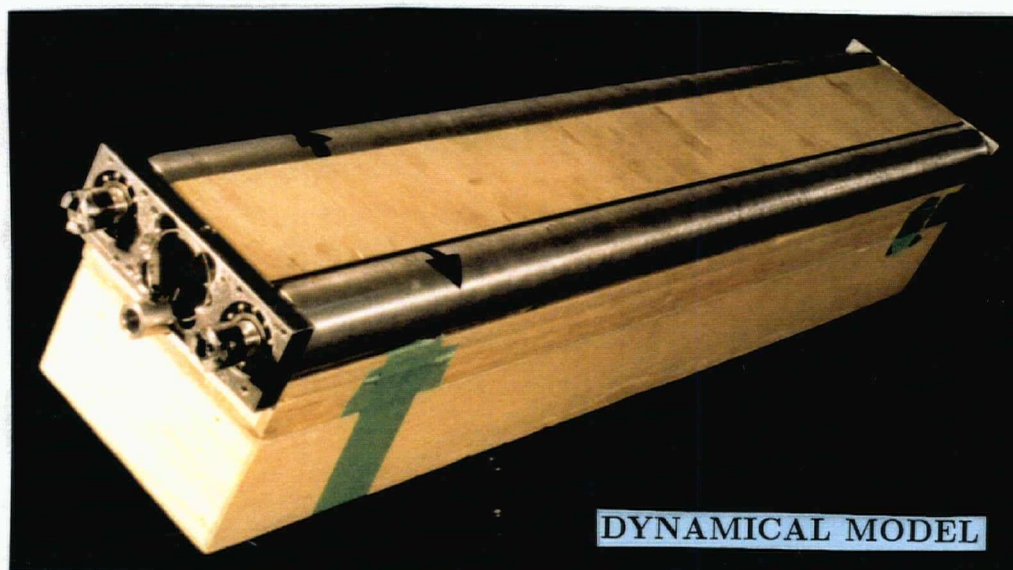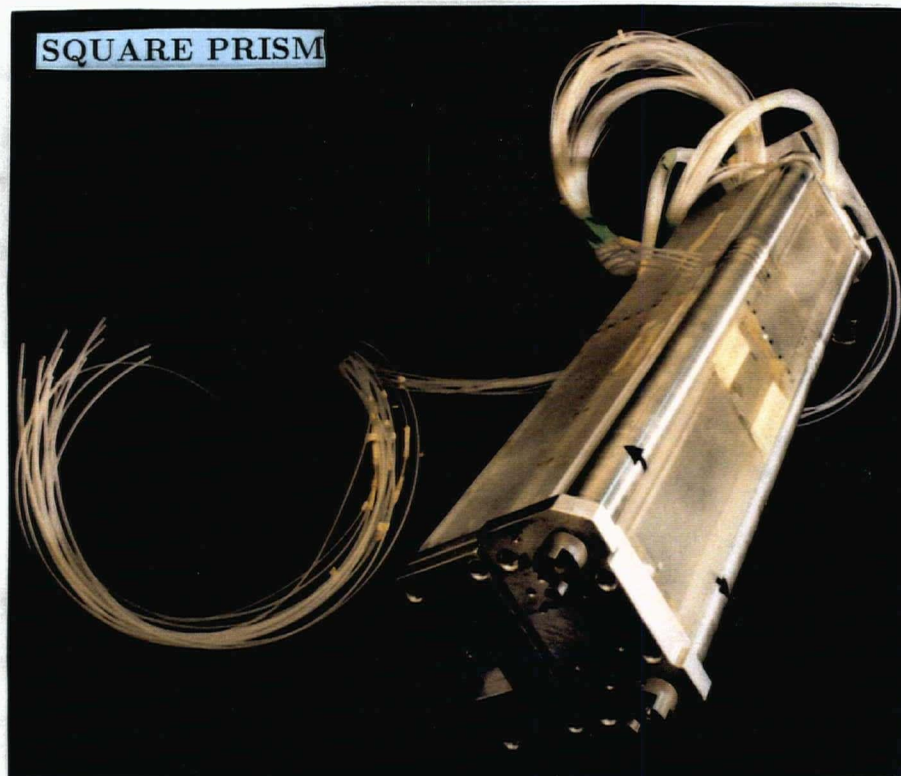
49

Figure 2-1(cont.) Bluff body geometries, without and with momentum injection, considered for investigation: (d) square prism and the dynamical test model.
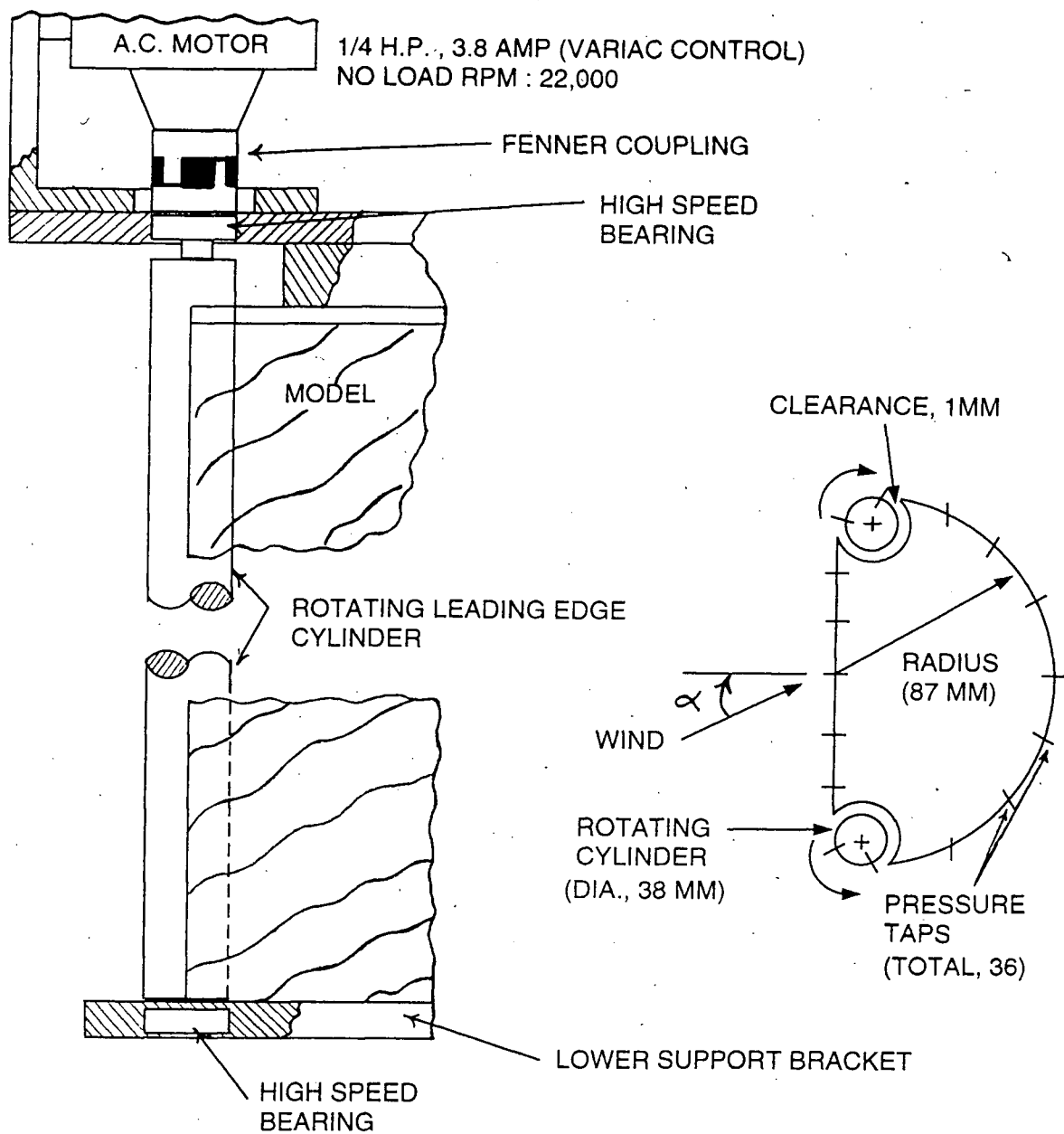
Figure 2-2   Detailed schematic of the rotating cylinder and drive mechanism.
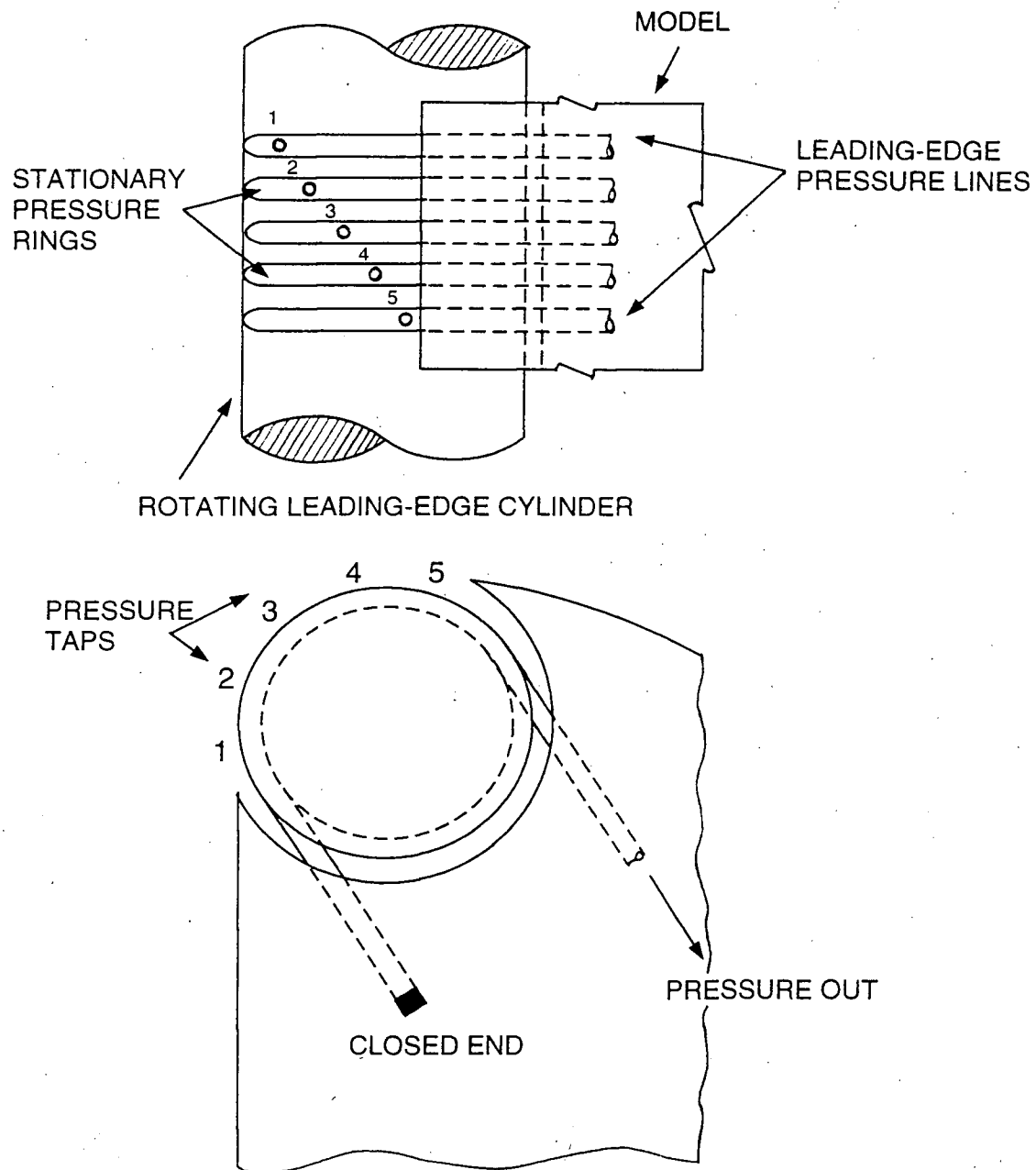
Figure 2-3   Schematic diagram showing details of the pressure taps near the
rotating element.

the vertical rectangular prism represents a transition between the D-section and the square prism, thus providing an important insight into the bluff body fluid dynamics.

2.2.2 Wind tunnel static experiments

During static wind tunnel tests the bluff body model is held stationary. The wind tunnel used in the test-program is shown in Figure 2-4. It is a closed circuit tunnel with a test-section of 0.914m × 0.686m × 2.6m. The test-section is provided with 45° corner fillets varying from 0.152m × 0.152m to 0.121m × 0.121m which compensate for the boundary-layer growth. The tunnel contraction ratio is 7:1.

The wind speed can be varied form 1 – 45 m/s. A wire screen at the inlet to the test-section ensures uniform velocity with a spatial variation of less than 0.25%. The intensity of turbulence in the test-section is less than 0.1%. The wind speed is calibrated using a Betz manometer which can read a variation of 0.2 mm of water. The wind tunnel is powered by a 230V, 57.2A, 15 H.P., D.C. motor driving a commercial axial-flow fan. A Ward-Leonard system is used for the speed control of the electric motor. A six component pyramidal force balance sits below the test-section and supports the model under test. The output of the force balance load cells are six electrical signals (one each for the lift, drag, and side forces; and the pitch, yaw and roll moments) which are transmitted to the computer based data acquisition system. Details of the instruments used during the experiments can be found in Appendix A.

2.2.3 Static test parameters

(a) The mean pressure distribution around the body was measured using pressure taps provided on the circumference of the model. The pressure taps were connected to a scanivalve pressure transducer system. The scanivalve has 48 pressure ports and is driven by a solenoid controller. The pressure conveying tubes had little effect on attenuation and phase response of the signal [79]. The output signal is directed to the signal conditioner, amplifier and finally to the computer through an analog to digital (A/D) interface card. The experimental set-up is shown in Figure 2-5. The pressure signals were sampled at a frequency of 100 Hz
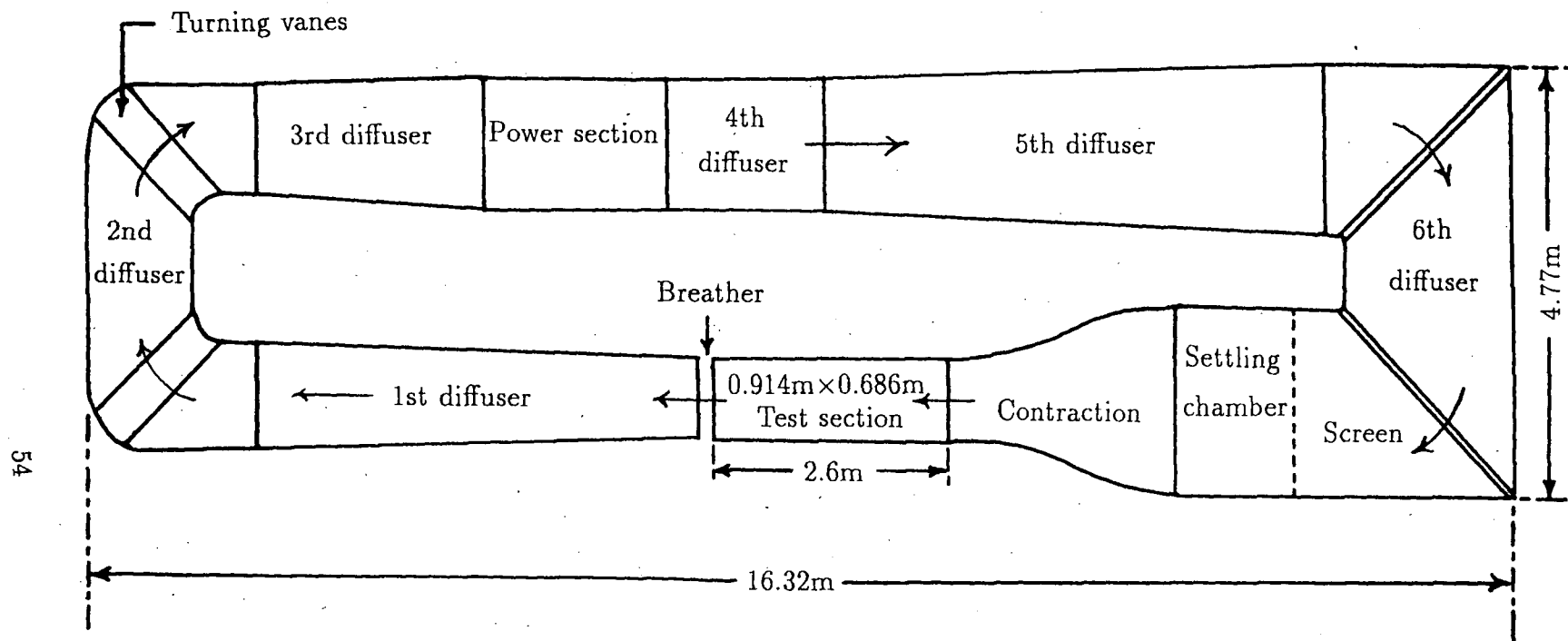
Figure 2-4 A schematic diagram of the low speed, low turbulence, closed circuit wind tunnel used in the test-program.

Model

U →

Wind
Tunnel

Model
Support

Pressure Tubes

Scanivalve Pressure Transducer

Signal Conditioner
and Amplifier

A/D Interface and
Data Bus

Data Acquisition, Processing and Analysis
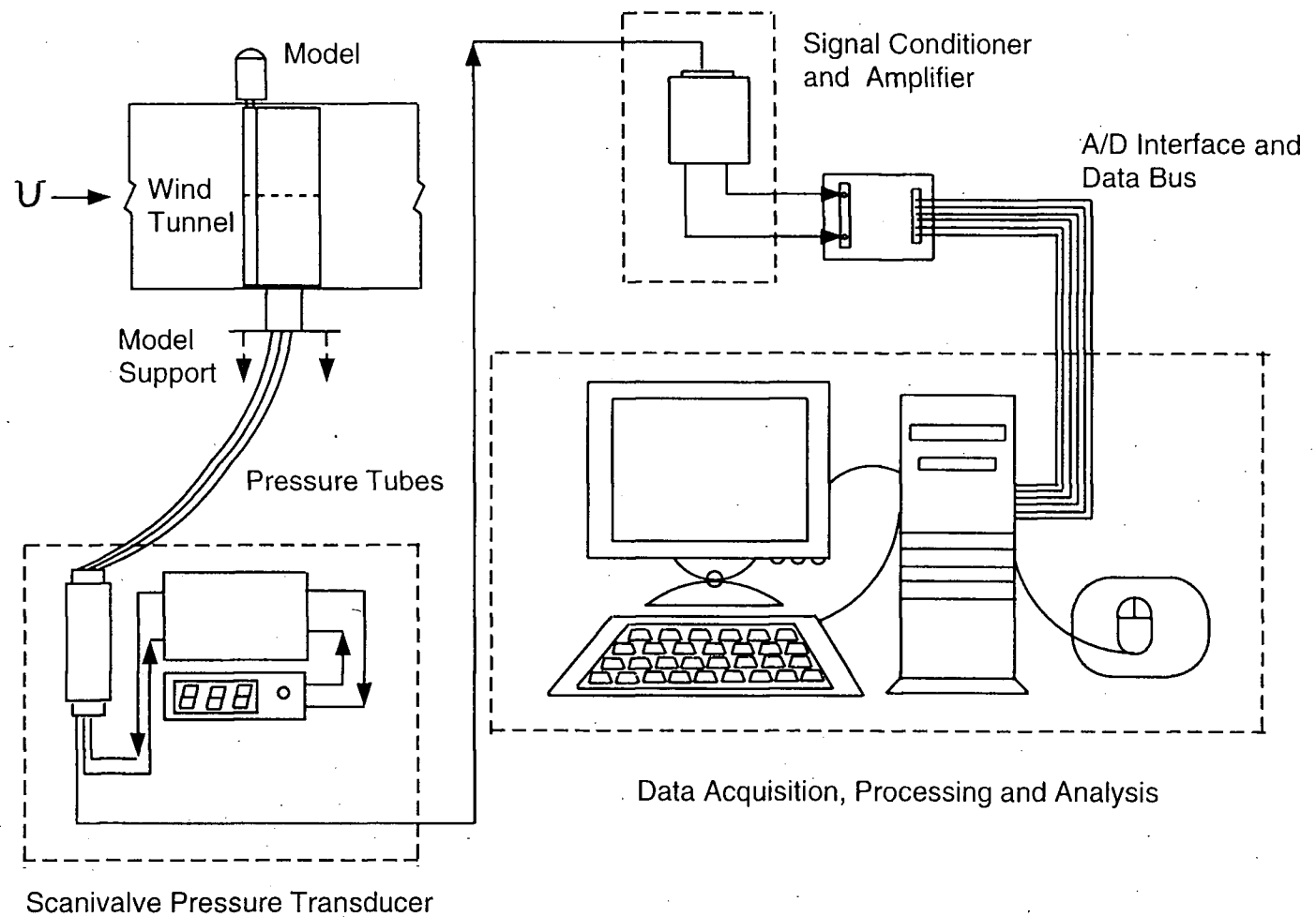
Figure 2-5   Experimental set-up for static aerodynamic investigation.

ing post processing, each signal is averaged to obtain the mean and rms (root mean square) components of the pressure. The mean pressure field around the surface of the body was integrated to obtain the aerodynamic force coefficients (the lift and drag).

(b) The fluctuating component of the pressure is obtained by calculating the rms value from the time dependent signal. The rms value of the pressure signal gives estimation of the unsteadiness in the flow field in presence of a bluff body.

(c) As the flow separates around the corners of a bluff body, a vortex is formed and is subsequently shed in the wake. This vortex creates suction pressure field which can be detected by pressure taps lying in its vicinity. By performing Fast Fourier Transform (FFT) analysis on the pressure against time signals, a spectrum of frequencies is obtained, with a dominant peak at the vortex shedding frequency. At times, due to weak strength of the vortex, none of the pressure taps could capture the vortex shedding frequency. In that case, a disk probe was inserted in the wake close to the body to determine the vortex shedding frequency. The geometry and calibration charts for the disk probe as well as the test set-up are shown in Figures 2-6 and 2-7, respectively. The Strouhal number (St) was calculated from the vortex shedding frequency.

(d) The experiments were performed in the angle of attack range 0-180°. Important changes in the flow character occur as the angle of attack is increased from zero. It was anticipated that as the angle of attack approaches 45° - 60° range, reversal in the direction of momentum injection of the upstream cylinder would become necessary. Similarly, beyond $\alpha = 90°$ the afterbody faces upstream and the forebody turns towards the downstream flow direction. Again this necessitates changes in the direction of momentum injection.

(e) The momentum injection parameter (U_c/U) was varied from 0 to 4 in steps of one unit.

DRILL 0.25

6.35

25.4

0.914

R 0.457

57

$-C_p$

α_y

α_p

α_y

α_p

V

0.3

0.2

0.1

0

-20°   -10°   0° α 10°   20°

$-C_p$

$\alpha_p = \alpha_y = 0°$

0.15

0.05

0   6.1   12.2   18.3   24.4

V, m/sec
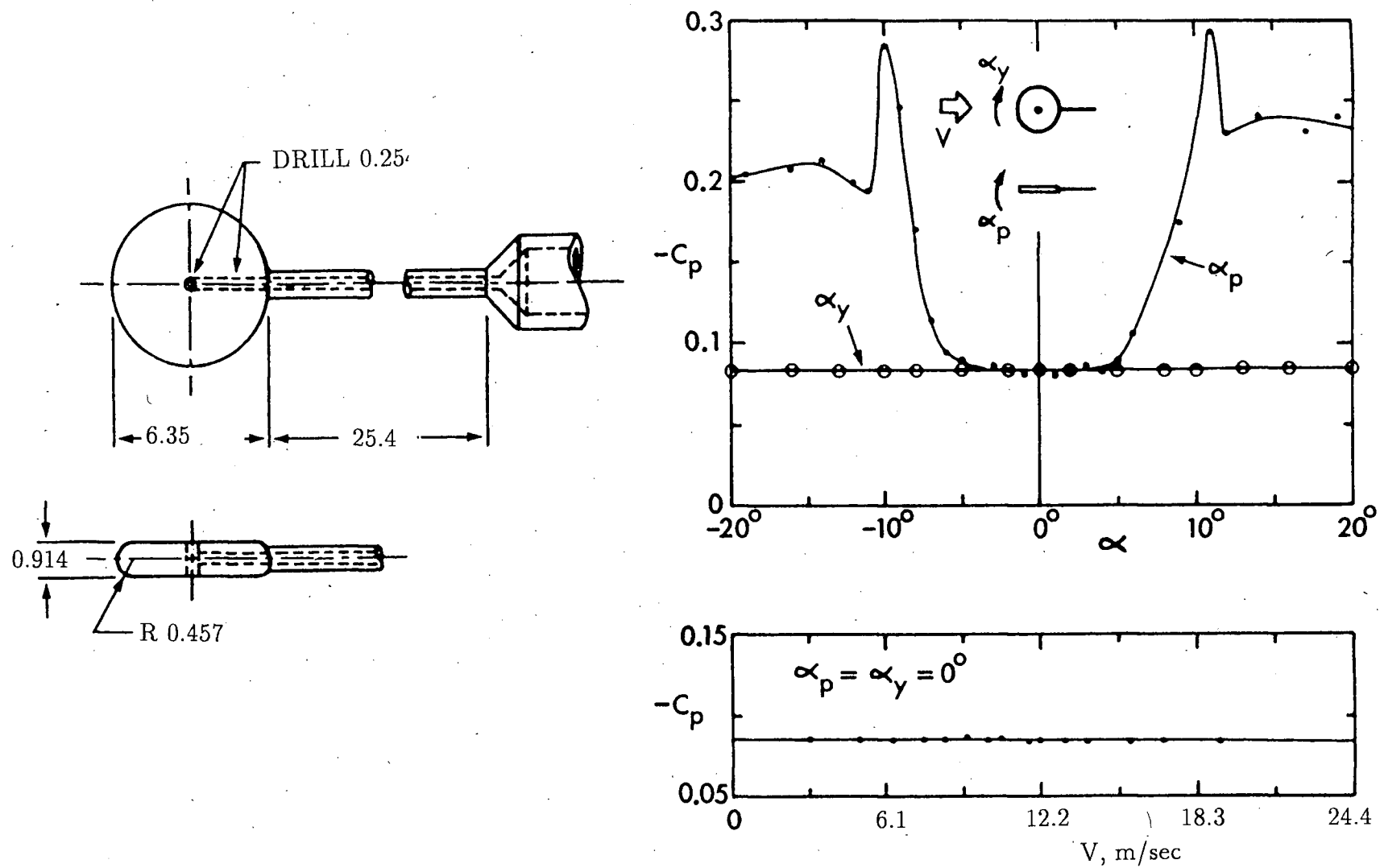
Figure 2-6   Constructional details and calibration plots of the disc probe.
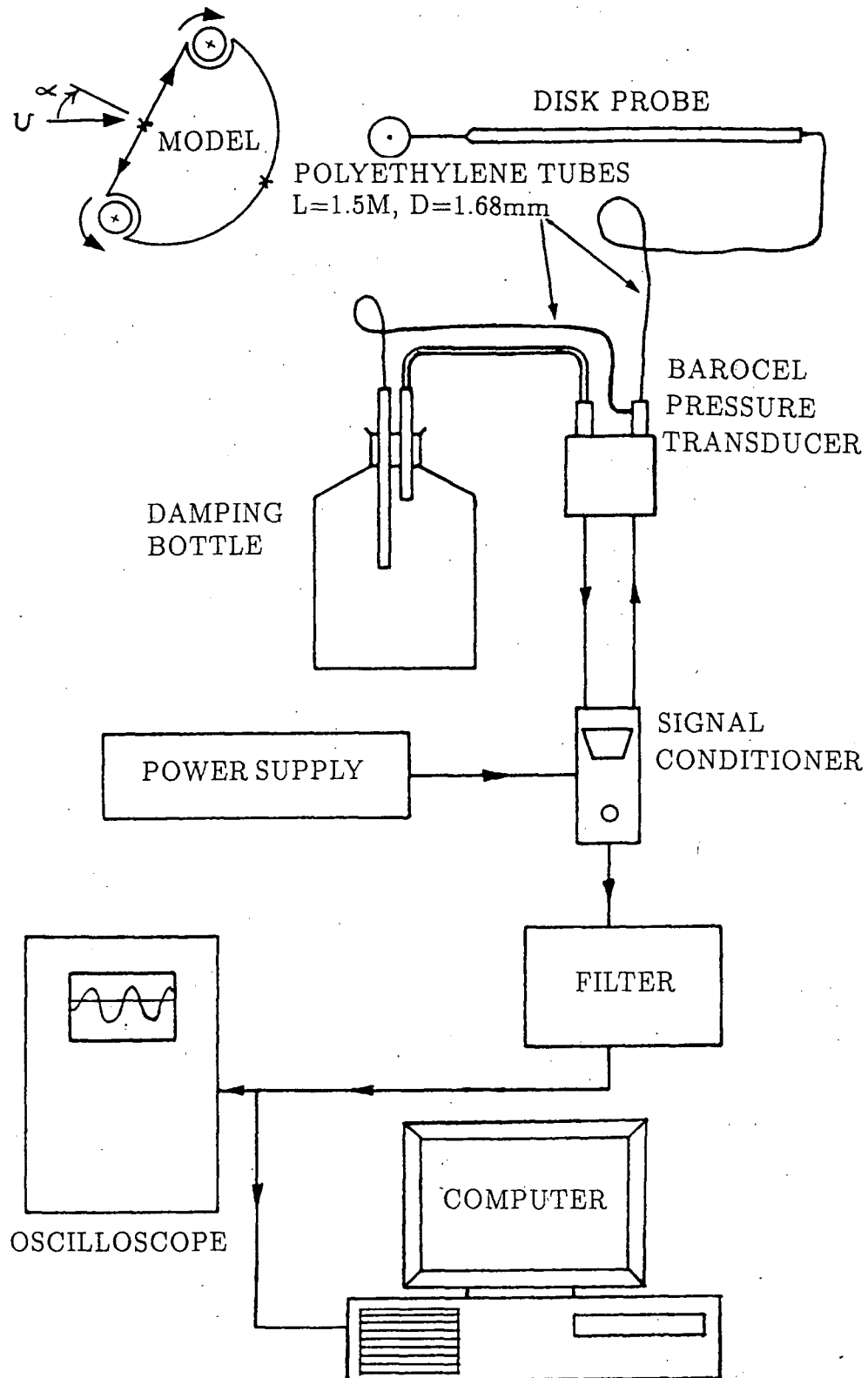
Figure 2-7   Instrumentation layout for vortex shedding frequency and fluctuating pressure measurement.

58

(f) For the Joukowski airfoil and the D-section prism, the effect of roughness of the cylinder surface on efficiency of the momentum injection process was also investigated. Rotating cylinders with three different surface roughness were fabricated. The baseline case is the cylinder with smooth surface. The splined cylinder has 10 axially parallel surface grooves. The depth of these grooves is about 5% of the cylinder diameter. The third cylinder is characterized by roughness elements (5% thick, 18% wide and 55% long - based on cylinder diameter). The three types of rotating cylinders are shown in Figure 2-8. The longitudinal and circumferential grooves act as tiny vortex generators and it was anticipated that this would increase effectiveness of the momentum injection process.

2.2.4   Dynamical experiments in the wind tunnel

The study of vortex resonance and galloping instability of a bluff body involved wind tunnel experiments simulating the dynamic response of a body. The wind tunnel utilized for static tests was also used for the dynamic experiments. The model was suspended on a dynamic test-rig with an arrangement allowing transverse oscillations (Figure 2-9).

The rig is constructed of thick steel frame, on which two pairs of air bearings are fixed on the top and bottom support members as shown in the figure. Each air bearing was pressurized to around 40 N/cm^2. The support frame is positioned in such a way that the the model is located inside the test-section of the wind tunnel. The model can oscillate transverse to the freestream direction. The desired stiffness is provided by four springs attached between the model and the supporting structure. The controlled damping is provided by four eddy current dampers. The damping is proportional to the current level in the damper. The vibration amplitude of the model is measured by a displacement transducer. The time dependent signal also provides frequency of the response through spectrum analysis.

The bluff body model design was similar to that in the static experiments, except

59

SMOOTH CYLINDER   ROUGH CYLINDER   SPLINED CYLINDER
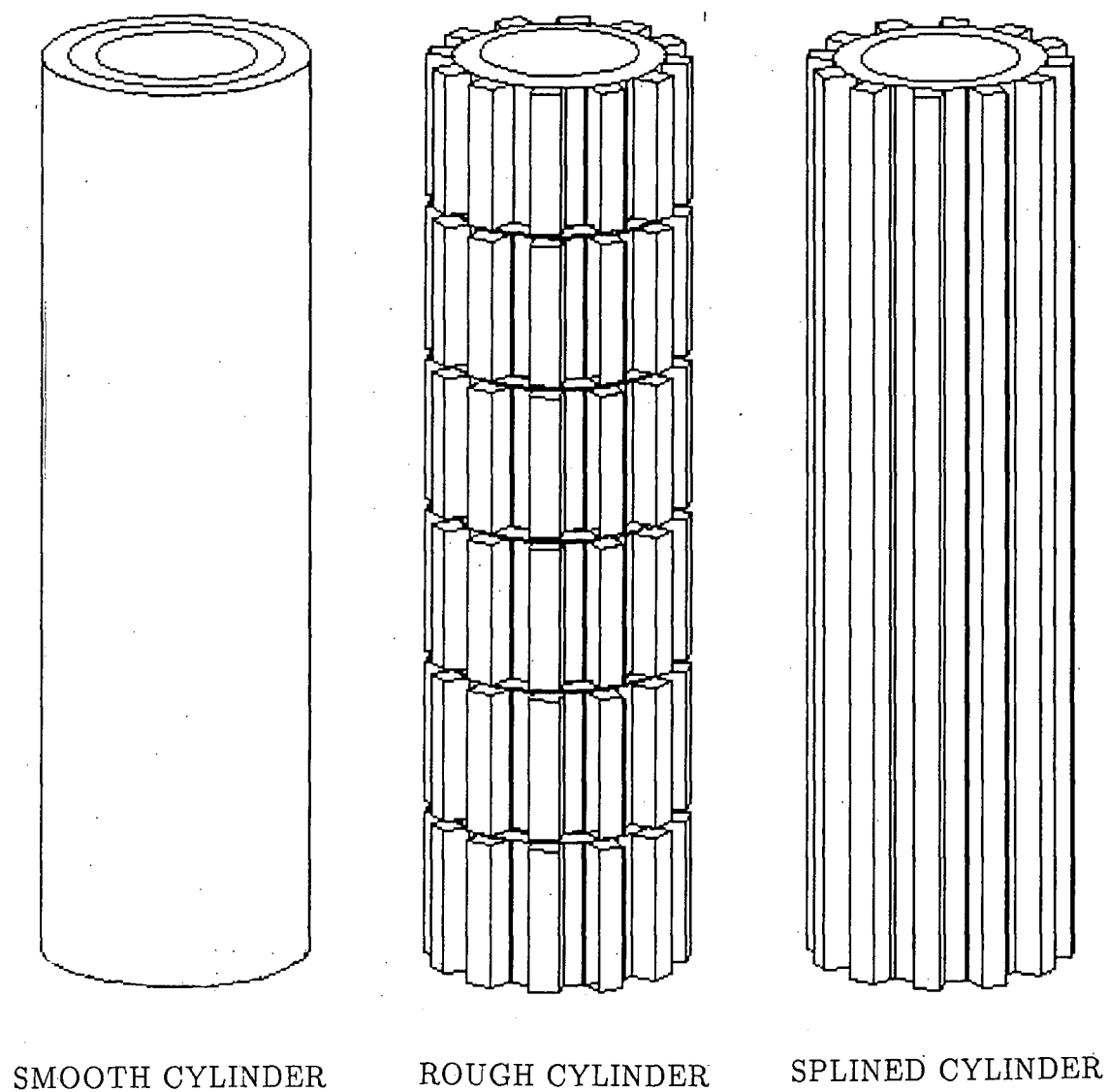
Figure 2-8   Rotating cylinders, with three different types of surface conditions, used in the test program: (a) schematic diagram.
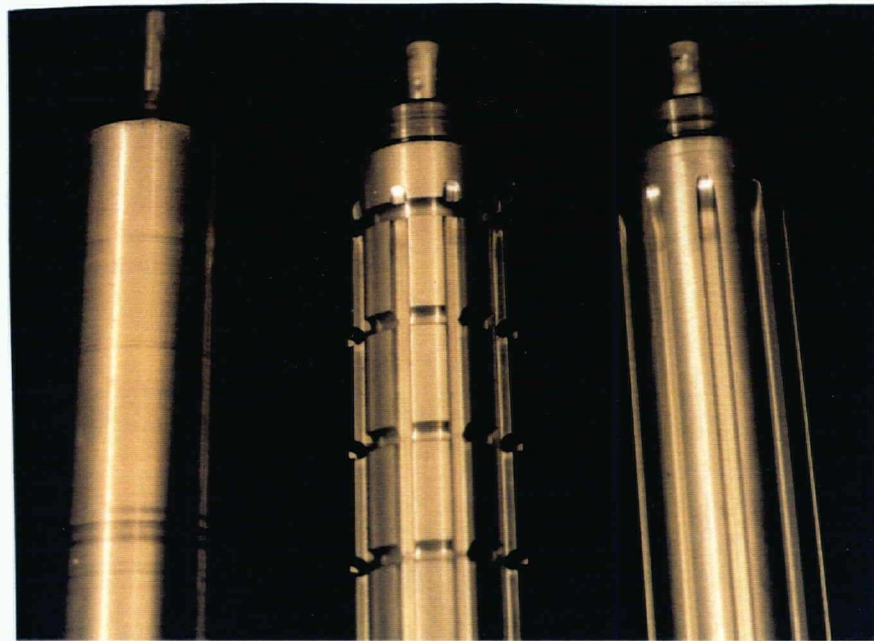
SMOOTH   ROUGH   SPLINED

Figure 2-8(cont.) Rotating cylinders, with three different types of surface conditions, used in the test program: (b) photographs showing details.

STEEL FRAME

AIR BEARINGS

SLIDING BAR

HELICAL TENSION
SPRING

MODEL

CROSS SECTION OF
THE WIND TUNNEL
TEST-SECTION

SPECTRAL
ANALYSIS

AMPLITUDE,
FREQUENCY
MEASUREMENTS

A/D INTERFACE AND
DATA BUS

DISPLACEMENT
TRANSDUCER

COMPUTER DATA ACQUISITION SYSTEM
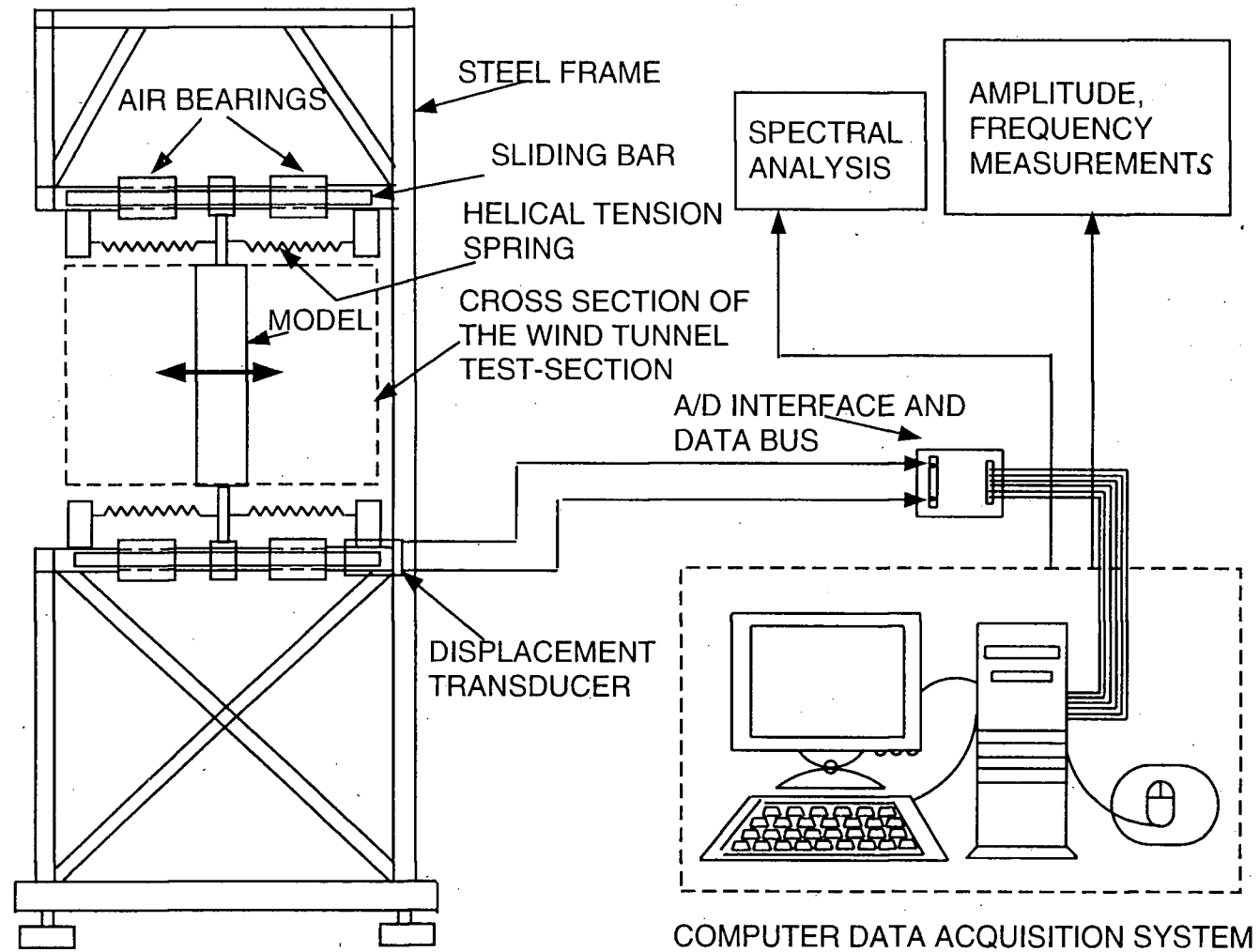
Figure 2-9   A schematic diagram of the dynamic experiment set-up involving the
wind tunnel, test-rig and data acquisition system.
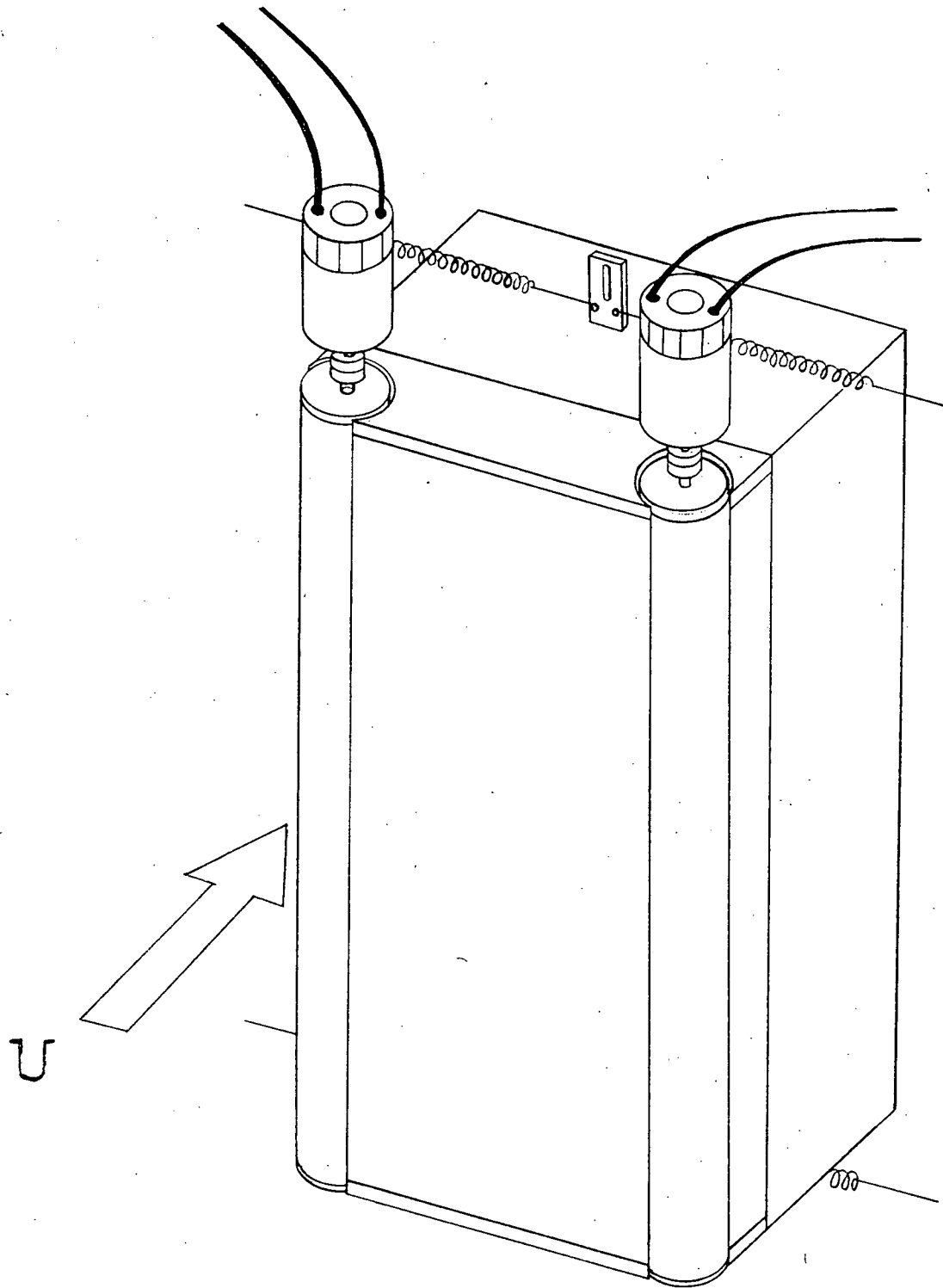
Figure 2-10 A three dimensional view of the light weight balsa wood model utilized for dynamic experiments.

for the pressure taps. The model was constructed from balsa wood to conserve weight (Figure 2-10). The photograph of the balsa wood model is given in Figure 2-1. The electric motors were mounted on top of the model and are coupled directly to the rotating cylinders. The rotating cylinders were constructed from hollow aluminium to keep the system light.

2.2.5 Dynamic test parameters

(a) As mentioned above, the amplitude of vibration was measured by a displacement transducer. To identify regions of vortex resonance and galloping it was necessary to plot the vibration amplitude as a function of wind speed. Effect of momentum injection on the dynamical characteristics of the system was assessed by analyzing the amplitude versus wind speed plots at various speeds of the rotating cylinders.

(b) Frequency of the vibration was obtained directly through the spectrum analyzer and also through FFT analysis of the amplitude versus time signal.

(c) A disk probe, inserted in the wake downstream of the body, was used to measure the vortex shedding frequency. This is further described in Section 2.3.3.

(d) The experiments were performed at zero angle of attack.

(e) The rate of momentum injection was varied from 0–4 in steps of one unit.

(f) Rotating cylinders were located at the leading (upstream) edges of each bluff body model (Figure 2-1d). Instead of rotating both the cylinders, it was decided to activate only one of them in order to investigate the effect of asymmetric momentum injection.

2.2.6 Flow visualization

Flow visualization represents a powerful tool in the study of fluid dynamical problems as it provides physical appreciation of the complex character of the flow. Flow visualization pictures and video movie of the fluid dynamics of bluff bodies in presence of the MSBC were taken. The tests were conducted by the author using the facility at the Kanto Gakuin University, Japan.
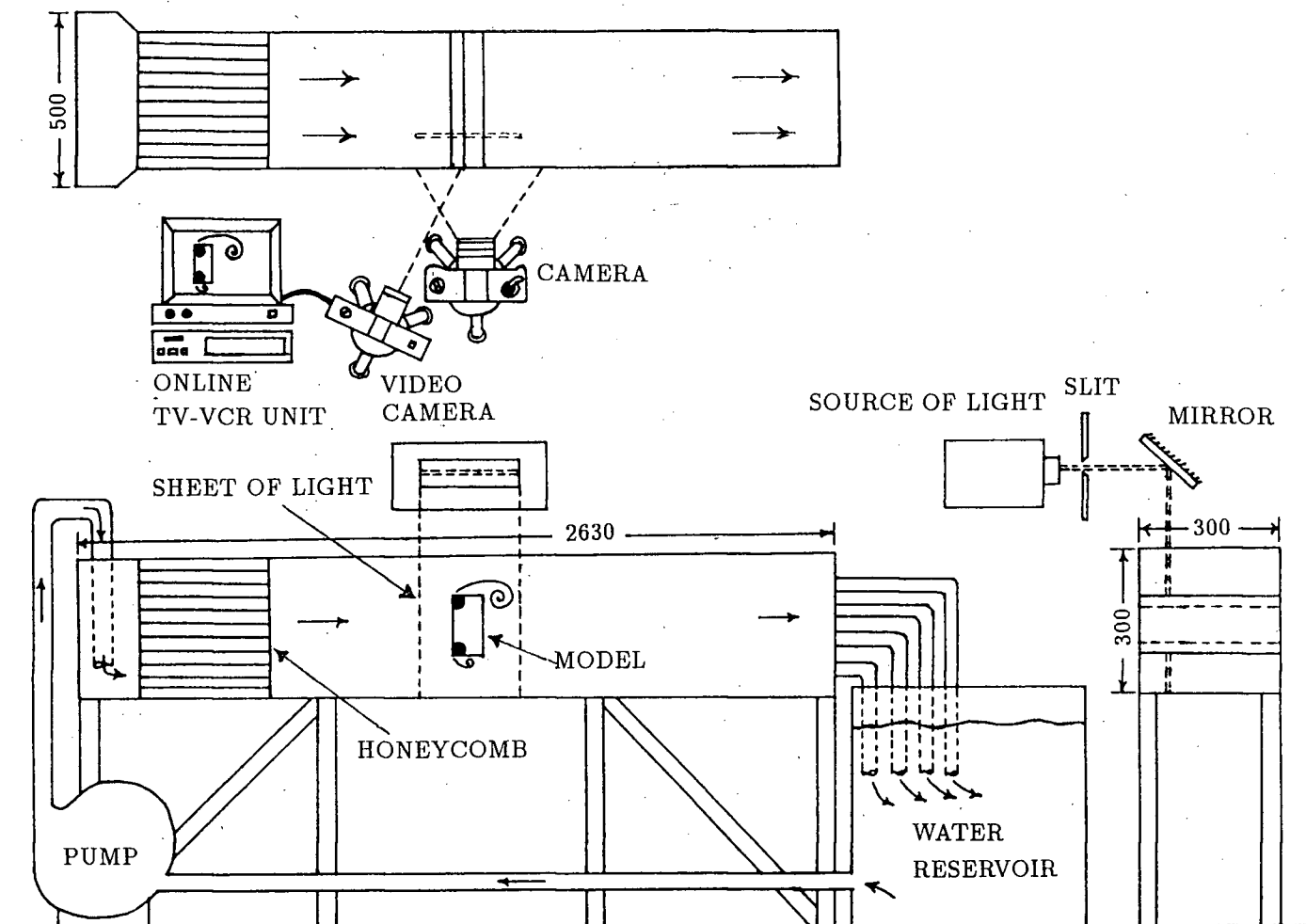
Figure 2-11 A schematic diagram of the closed circuit water channel facility used in the flow visualization study. Slit lighting was used to minimize distortion due to three dimensional character of the flow. Long exposure provided path-lines with ployvinyl chloride particles serving as tracers. The dimensions are in mm.

The flow visualization setup used is shown in Figure 2-11. The experiments were carried out in a closed circuit water channel. Bluff body plexiglass model fitted with rotating cylinders was placed in the water channel. The water was seeded with fine polyvinyl chloride (PVC) powder. The PVC particles are almost neutrally buoyant in the flow and hence do not rise or fall as they move in the water channel. As shown in the figure, a slit lighting arrangement was used to illuminate a very thin plane of the test-section. The steady flow of PVC particles resulted in streaklines which were viewed from the front of the test-section. The flow velocity in most cases was fixed at 0.3 m/s. The experiments were carried out in a dark room resulting in a sharp contrast between the bright streaklines and a dark background. A series of long exposure photographs dramatically captured the streaklines, showing formation and subsequent dissipation of alternate vortex shedding process. A video was also taken to assess time evolution of the process. A sensitive CCD (charged coupled device) video camera was utilized for the purpose.

2.3 Numerical Analysis

2.3.1 Formulation of the problem

The numerical approach is based on the well-established vortex panel method. The surface of a given body is descretized into a large number of panels with vortex and source type singularities distributed on each panel. The overall flow at any point in the domain is a result of elemental contributions from each panel. Simulation of the rotating cylinder integral to a bluff body poses a problem. As a first approximation the rotating cylinder and the rest of the body can be considered a single object and is descretized into panels accordingly. This formulation is referred to as the "single element configuration". In reality, the rotating cylinder is separate from the rest of the bluff body, with the presence of a gap. In the multi-element panel method, the rotating cylinder and the rest of the body are treated as two distinct physical objects.

66

The details of both the formulations are described below.

The general two dimensional Navier-Stokes equation is given by [146]

$$\frac{\partial \vec{V}}{\partial t} + (\vec{V} \cdot \nabla)\vec{V} = \frac{-1}{\rho}\nabla p + \nu \nabla^2 \vec{V}, \qquad (2.1)$$

where: $\vec{V}$ = fluid velocity at any given point;

p = pressure;

ν = kinematic viscosity of the fluid;

ρ = density of the fluid.

The continuity equation for an incompressible fluid is

$$\nabla \cdot \vec{V} = 0. \qquad (2.2)$$

All body forces (e.g. gravity) have been assumed conservative and their potentials have been absorbed in the pressure term. For the potential flow situation the viscous terms vanish and the above set of equations reduces to Euler's equation

$$\frac{\partial \vec{V}}{\partial t} + (\vec{V} \cdot \nabla)\vec{V} = \frac{-1}{\rho}\nabla p. \qquad (2.3)$$

The general fluid dynamic problem under consideration is characterized by a known boundary surface and the normal components of fluid velocity are prescribed on these boundaries. The boundary condition is

$$\vec{V} \cdot \vec{n}\Big|_s = 0, \qquad (2.4)$$

where $\vec{n}$ is the outward normal from the surface 'S'. The set of equations (2.2) and (2.3) do not define the potential flow. To obtain potential form of the equation the condition of irrotationality is invoked. Let $\vec{V} = \vec{V}_\infty + \vec{v}$, where: $\vec{V}_\infty$ = freestream velocity, satisfies continuity equation; $\vec{v}$ = perturbation velocity field due to the presence of the boundary, satisfies irrotationality condition, $\vec{v} = -\nabla\phi$; and ϕ =

disturbance velocity potential. Recognizing that $\nabla \cdot \vec{v} = 0$ gives

$$\nabla^2 \phi = 0. \tag{2.5}$$

This is a linear, elliptic second order partial differential equation. Now $\vec{V} = \vec{V}_\infty - \nabla \phi$, and the boundary condition takes the form

$$(\vec{V}_\infty - \nabla \phi) \cdot \vec{n}|_s = 0,$$

$$\frac{\partial \phi}{\partial n} = \vec{V}_\infty \cdot \vec{n}|_s, \tag{2.6}$$

with $|\nabla \phi| \rightarrow 0$ at infinity. The set of equations (2.5), (2.6) represents a well-posed elliptic boundary value problem with Neumann-type velocity boundary condition. Once the velocity field is obtained, the pressure is calculated by intergrating equation (2.3) to give Bernoulli's equation

$$\frac{p}{\rho} = P(t) - \frac{1}{2}|\vec{V}_\infty|^2 + \frac{\partial \phi}{\partial t}, \tag{2.7}$$

where p and $\vec{V}_\infty$ are the free-stream pressure and velocity, respectively.

Reduction of the problem into an integral equation with singularity distribution on the body surface is carried out as follows. Consider an arbitrary body as sketched in Figure 2-12. It shows a combination of unit source and a unit vortex singularity at a point $q(x_q, z_q)$. The potential at any point P(x,z) is given by

$$\phi = \ln r(p, q) + \theta(p, q), \tag{2.8}$$

where: $r(p,q) = \sqrt{(x - x_q)^2 + (z - z_q)^2}$; $\quad \theta(p,q) = tan^{-1}[(z - z_q)/(x - x_q)]$.

In case of a continuous distribution of the singularities, the total potential at any point P(x,z) is a linear combination of such contributions. For a constant source strength (σ) and linearly varying vorticity strength (γ) distributed on the contour of
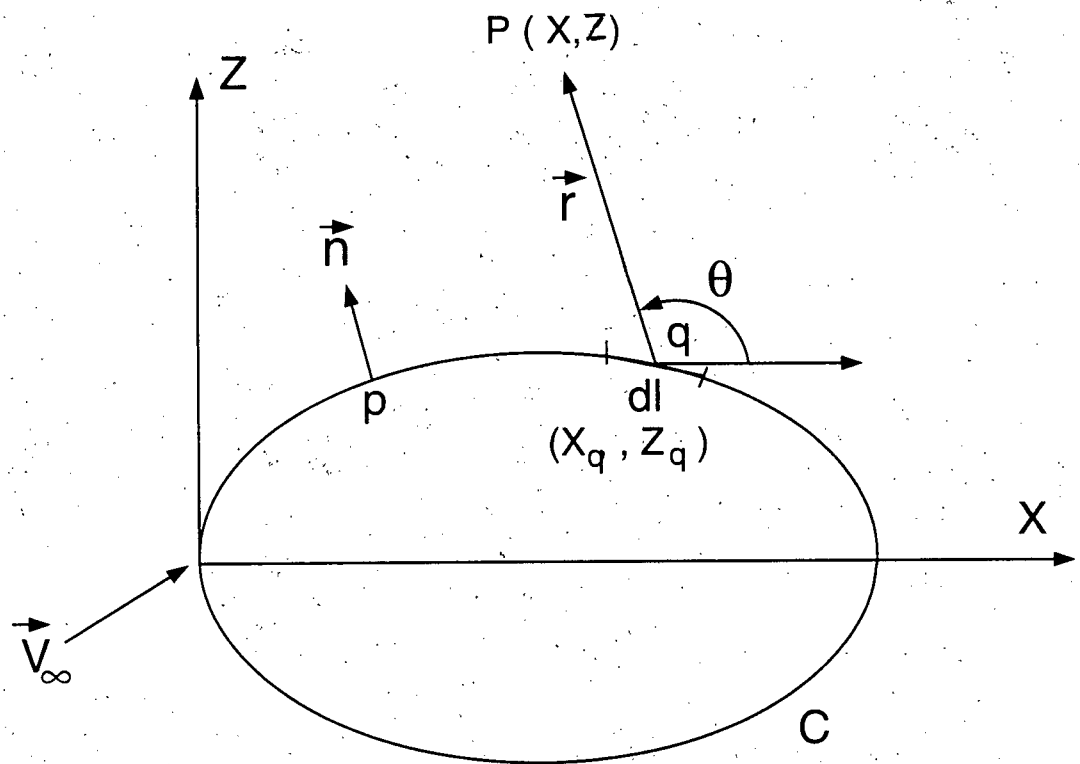
Figure 2-12   An arbitrary two dimensional body.

the body surface, the perturbation potential can be written as

$$\phi = \oint_C \Big[\sigma(q) \cdot \ln r(p,q) + \gamma(q) \cdot \theta(p,q) \Big] dl. \tag{2.9}$$

Applying the boundary conditions and rearranging the terms gives [128],

$$\underbrace{2\pi \Big[\sigma(p) + \gamma(p) \Big]}_{(i)} - \oint_C \underbrace{\frac{\partial}{\partial n} \Big[\sigma(q) \cdot \ln r(p,q) + \gamma(q) \cdot \theta(p,q) \Big] dl}_{(ii)} = -\vec{n}(p) \cdot \vec{V}_\infty. \tag{2.10}$$

This is a Fredholm integral equation of the second kind where:(i) represents contribution of the singularity obtained through the limiting process [147]; (ii) is the kernel of the integral equation.

The solution of the integral equation is obtained by approximating it as a set of linear algebraic equations. The body contour is descretized into a large number of line elements (panels), whose characteristic dimensions are small compared to those of the body. Over each panel a distribution of unknown singularities is prescribed. Thus the problem reduces to that of obtaining a finite number of singularity strengths, one for each panel. The form of the singularity distribution over each panel is a known geometric function and hence integration can be performed. Application of normal velocity boundary condition on each panel results in a set of linear algebraic equations relating unknown singularity strengths. The coefficient matrix consists of normal velocities induced by the panels at each collocation point for unit value of the singularity strength. Once the linear equations are solved, the flow velocities and pressures are evaluated readily.

2.3.2 Single element configuration

In the single element panel formulation, the rotating cylinder and the rest of the bluff body are treated as a single physical object. The numerical formulation is described here using the airfoil as a bluff body model (Figure 2-13a). The body surface is descretized into a large number (N) of panel elements. Each element is a

70

combination of linearly varying vortex strength (γ) and a constant source strength (σ). The end points of any panel are known as nodes, whereas the mid-point of a panel is called the collocation point. The collocation point on a given panel serves as a convenient reference to evaluate velocity and pressure after implementing the boundary conditions. On an i-th panel, the nodal vortex strength varies from (γ_i) to (γ_{i+1}) in a linear fashion. The source strength (σ) remains constant over all the panels. The source distribution on each panel prevents leakage of the fluid across the panel. For a total of N panels, there are (N+1) unknown vortex strengths and an unknown source strength, making a total of (N+2) unknowns.

Modelling of the 'Free Vortex Sheets'

As shown in Figure 2-13(a), the separated flow is represented by the upper and lower 'free vortex sheets' issuing from the separation points. They are also descretized in to a large number (M) of panels. However, the vorticity strength in the wake does not constitute an additional unknown. At the beginning of the 'free vortex sheet', the vorticity strength equals that at the point of separation. If the shed vortex strength is taken to remain constant as it is convected along the 'free vortex sheet', an infinitely long wake would result with a constant wake pressure. Realistically, the wake is finite and closed, with a gradual rise in pressure. This can be attributed to the presence of viscosity in the flow. To account for this effect, the shed vortex is allowed to dissipate as it is convected downstream along the 'free vortex sheet'. The rate of dissipation is an empirical input to the program. Originally this idea was proposed by Ribaut [142]. The Kutta condition requires zero net shedding of vorticity in the wake. Thus as we move along the panels on the 'free vortex sheets', the upper and lower shed vorticities remain equal and opposite in strength at all time. If a linear variation of vorticity dissipation is assumed, then the vorticity strength on the 'free vortex sheets' can be obtaining in terms of the vortex strength at the upper and lower separation

(a)

(b)
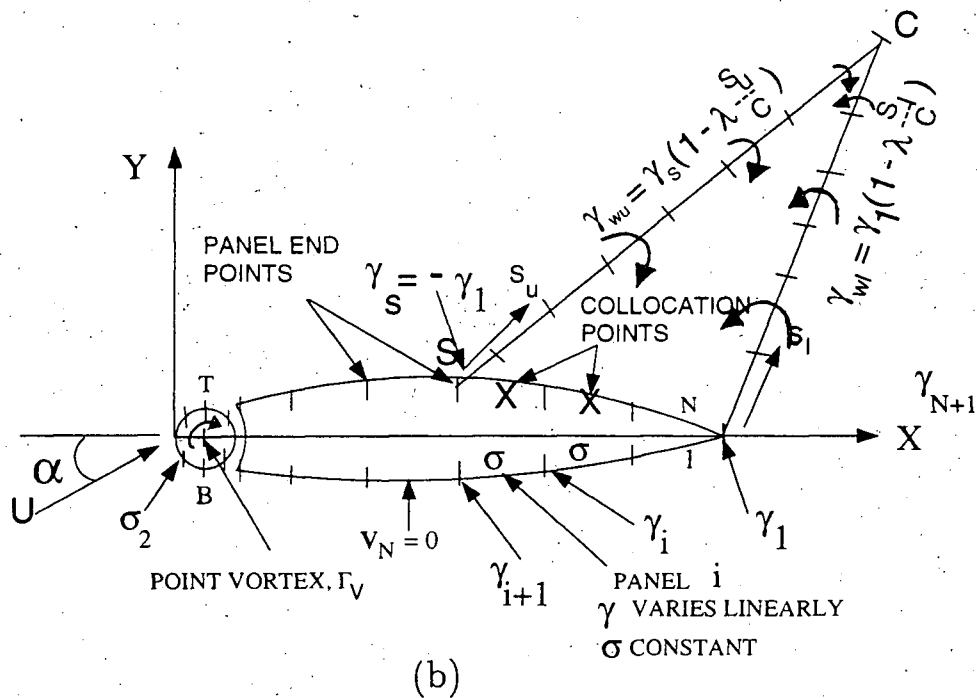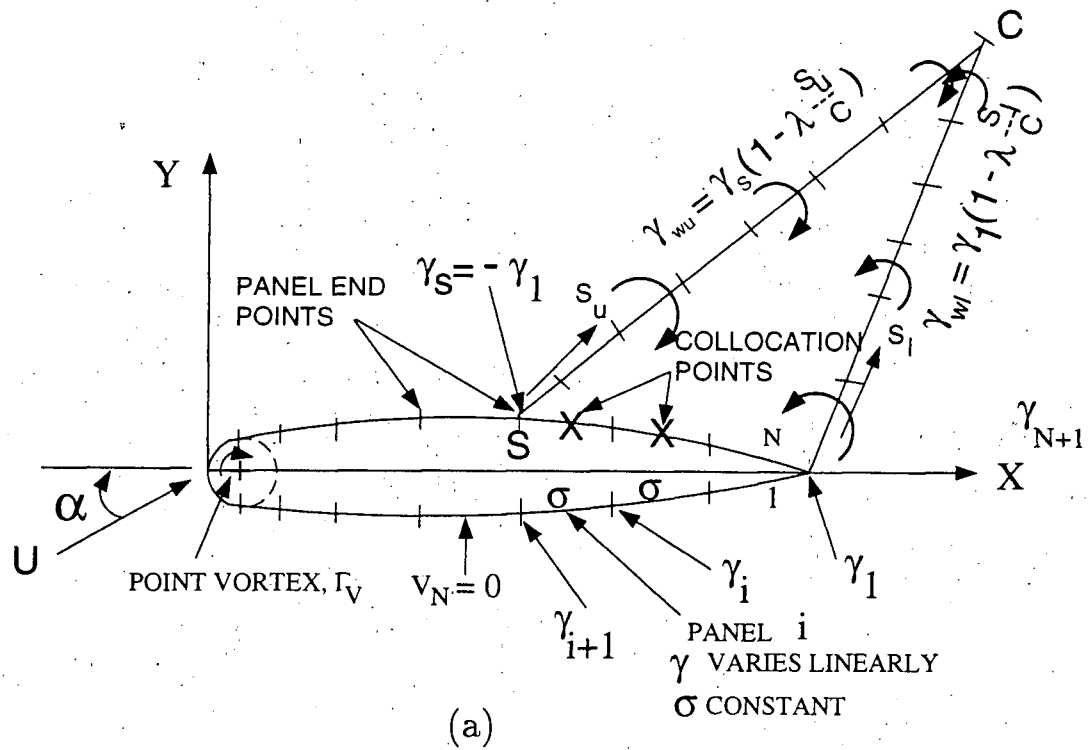
Figure 2-13 Numerical panel formulation describing, (a) single element configuration and, (b) multi-element configuration. Note, 'S' is obtained from the experimental results.

points. Mathematically it can be expressed as

$$\gamma_C = \gamma_1(1 - \lambda\frac{S_U}{c}) + \gamma_{N+1}(1 - \lambda\frac{S_L}{c}) = 0, \qquad (2.11)$$

where λ is the vorticity dissipation ratio, and S_U and S_L are the distances along the upper and lower 'free vortex sheets' from the separation points.

The perturbation velocity components can be calculated by taking the effects of surface singularities together with contribution from panels on the 'free vortex sheets' as:

$$u_j = \sum_{i=1}^{N+1} A_{ji}\gamma_i + \sigma\sum_{i=1}^{N} C_{ji} + \sum_{i=1}^{M} E_{ji}\gamma'_{wu} + \sum_{i=1}^{M} E_{ji}\gamma'_{wl}; \qquad (2.12)$$

$$w_j = \sum_{i=1}^{N+1} B_{ji}\gamma_i + \sigma\sum_{i=1}^{N} D_{ji} + \sum_{i=1}^{M} F_{ji}\gamma'_{wl} + \sum_{i=1}^{M} F_{ji}\gamma'_{wl}. \qquad (2.13)$$

For N number of panels on the airfoil contour, the (N+2) unknowns are obtained by satisfying the boundary condition of zero normal velocity in eq.(2.14) at N collocation points together with two auxiliary conditions. The condition of zero normal velocity at the j-th collocation point on the airfoil surface can be written as

$$w_j - u_j\frac{dz}{dx}\Big|_j = U\cos\alpha\frac{dz}{dx}\Big|_j - U\sin\alpha \qquad (2.14)$$

Satisfying the boundary condition at the mid-points of N panels gives N linear algebraic equations involving (N+2) unknown singularity strengths. The other two equations are obtained as follows. The Kutta condition of zero net shedding of vorticity in the wake is satisfied by setting the vorticity values at the upper and lower surfaces the same (and equal to the value of the 'free vortex sheet'). Mathematically, this can be expressed as:

$$\gamma_S = -\gamma_1; \qquad (2.15)$$

$$\gamma_{N+1} = 0; \qquad (2.16)$$

$$\gamma'_{wu} = \gamma_S; \qquad (2.17)$$

73

$$\gamma'_{wl} = \gamma_1; \qquad\qquad (2.18)$$

where γ_S is the vorticity strength at the upper separation point and γ'_{wu} and γ'_{wl} are the vorticity strengths on the upper and lower wake panels, respectively. Once the solution is obtained, the perturbation velocity components may be reobtained from equations (2.12) and (2.13). In the case of the D-section the auxiliary conditions are $\gamma_1 = \gamma_{N+1}$ and $\gamma'_{wu} = \gamma'_{wl}$.

The total velocity can be obtained from

$$q_j = \sqrt{(u_j + U\cos\alpha)^2 + (w_j + U\sin\alpha)^2}, \qquad\qquad (2.19)$$

and the pressure coefficient is given by

$$C_{p_j} = 1 - (q_j/U)^2. \qquad\qquad (2.20)$$

Geometry of the Wake

Since both the shape and the strength of the 'free vortex sheet' are unknown, the solution of the problem formulated above is obtained by an iterative procedure. The wake shape is initially assumed to be a straight line inclined at an angle $\alpha/2$, the mean angle at which the separation vortices are convected. Once the solution is obtained based on this assumed wake shape, velocities are recalculated at the mid-points of the panels on the wake. The new wake shape is then determined by piece-wise integration starting at the upper and lower separation points. At each iteration, the wake influence coefficients only need to be calculated. The computation is terminated when a convergence accuracy of 10^{-6} is achieved. This is usually accomplished within 50-60 iterations.

Wake Pressure

The pressure in the wake was calculated using the procedure outlined by Mukherjea and Bandyopadhyay [143]. The base pressure coefficients in the separated

74

region can be calculated directly from the Bernoulli equation as

$$C_p = \frac{(p - p_\infty)}{\frac{1}{2}\rho U^2},$$

$$= 1 - \frac{q_{inner}^2}{U^2} - \frac{\Delta H}{\frac{1}{2}\rho U^2}, \tag{2.21}$$

where q_{inner} is the velocity inside the separated zone and ΔH is the decrease in the total pressure from that at infinity. Since q_{inner} is small, C_p can be written as

$$C_p = 1 - \frac{\Delta H}{\frac{1}{2}\rho U^2}. \tag{2.22}$$

The jump in the total pressure across the free shear layer can be calculated by assuming zero static pressure drop across it. If the average velocity along the free shear layer is denoted by

$$q_{av} = \frac{1}{2}(q_{outer} + q_{inner}), \tag{2.23}$$

then, for upper shear layer:

$$q_{outer} = q_{av} + \frac{\gamma'_{wu}}{2}; \tag{2.24}$$

$$q_{inner} = q_{av} - \frac{\gamma'_{wu}}{2}. \tag{2.25}$$

Since the vorticity γ'_{wu} on the upper shear layer is

$$\gamma'_{wu} = q_{outer} - q_{inner}, \tag{2.26}$$

ΔH can now be calculated as

$$\Delta H = H_{outer} - H_{inner},$$

$$= \left[p_{outer} + \frac{1}{2}\rho(q_{av} + \frac{1}{2}\gamma'_{wu})^2\right] -$$

$$\left[p_{inner} + \frac{1}{2}\rho(q_{av} - \frac{1}{2}\gamma'_{wu})^2\right],$$

$$= \rho q_{av}\gamma'_{wu}. \tag{2.27}$$

Using eqs. (2.25) and (2.27), the coefficient of pressure in the separated region can

be calculated as

$$C_p = 1 - \frac{\rho(q_{inner} + \frac{1}{2}\gamma'_{wu})\gamma'_{wu}}{\frac{1}{2}\rho U^2},$$

$$= 1 - (\gamma'_{wu}/U)^2,$$

$$= 1 - (\gamma_S/U)^2. \qquad\qquad (2.28)$$

Modelling of the Vorticity Dissipation

The wake in the present model is finite and its extension is primarily dependent upon viscous dissipation λ. From eq. (2.27),

$$\Delta H = \rho q_{av}\gamma'_{wu} = \rho(q_{outer} - \frac{\gamma'_{wu}}{2})(1 - \lambda\frac{s_u}{c})\gamma_S. \qquad (2.29)$$

At the closure of the wake, its width becomes zero, i.e.

$$s_u = S_u = c/\lambda. \qquad\qquad (2.30)$$

With decreased dissipation, i.e. with reduction in λ, the wake length increases. The wake becomes infinite in the case of ideal fluid when $\lambda = 0$.

Numerical Simulation of the Rotating Cylinder

The effect of the rotating cylinder can be mathematically simulated either by a line vortex (Figure 2-14) at the center of the cylinder or by line vortices distributed over the discretized cylinder surface. The strength of the line vortex can be related, by a simple analogy, to the surface velocity and diameter of the cylinder. Mathematically the total circulation around an arbitrary body is defined as

$$\Gamma = \oint \vec{u} \cdot \vec{dl}, \qquad\qquad (2.31)$$

where: $|\vec{u}| = |U_C| =$constant; $|\vec{dl}| = |r \cdot d\theta|$. Thus:

$$\Gamma = U_C \cdot r \oint_0^{\pi/3} d\theta,$$

76
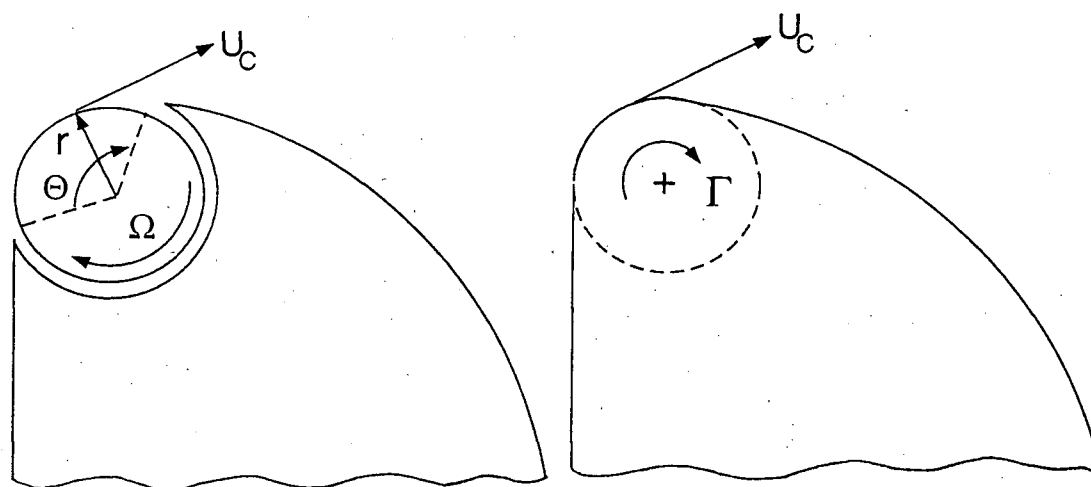
A bluff body with a rotating cylinder   Numerical Idealization

U_C = cylinder surface speed Θ = exposed portion of
                                              the cylinder surface
r = cylinder radius Ω = angular velocity of
Γ = equivalent point vortex   the cylinder

Figure 2-14   Numerical modelling of a rotating cylinder using a line vortex.

$$= \tfrac{2\pi}{3} r \cdot U_C ,$$

$$= \tfrac{\pi}{3} d \cdot U_C . \qquad (2.32)$$

wherex d=2r. This circulation can be mathematically simulated by a line vortex of strength Γ. The effect of the moving wall can now be incorporated in a simple manner through the boundary condition by modifying the right hand side of eq. (2.11) for upper surface collocation points as

$$w_j - u_j \frac{dz}{dx}\bigg|_j = (u_c + U\cos\alpha)\frac{dz}{dx}\bigg|_j - (w_c + U\sin\alpha), \qquad (2.33)$$

where u_c, w_c are the velocity components due to the line vortex of strength Γ situated at the centre of the cylinder. In this way it is possible to directly relate the circulation strength Γ to the speed ratio (U_c/U) through eq. (2.32).

2.3.3 Multi-element configuration

The next logical step is to develop a model for the moving wall problem based on the multi-element configuration by incorporating the effects of separation from both the cylinder and rear airfoil surface. This model, as before, involves distribution of linearly varying vorticity and sources on $(N_1 + N_2)$ number of panels descretizing the multi-element configuration (Figure 2-13b). Flow is assumed to separate from the cylinder surface at top (T) and bottom (B), and pass over the airfoil surface. Flow within the gap is assumed to be local with no effect on the external flow field. On the airfoil, the flow separates at point S on the upper surface and at the trailing edge (point 1) on the lower surface. The vortex sheets separating from the cylinder are assumed to undergo dissipation so that the vorticity strengths $(\gamma_{wu}, \gamma_{wl})$ become zero at points S and 1. This results in different dissipation ratios for upper and lower separation panels given by:

$$\lambda_u = c/S_u; \qquad (2.34)$$

$$\lambda_l = c/S_l; \qquad (2.35)$$

78

where S_u, S_l are the upper and lower wake lengths from the cylinder top and bottom separation points to points S and 1 on the airfoil surface, respectively.

For a flow separating from the airfoil surface, 'free vortex sheets' emanate from separation points S and 1. The vorticity strengths of the upper and lower separation panels can be obtained, as before, in terms of γ_S and γ_1 through eqs. (2.15)-(2.18). However, since the shape of the separating panels are not known 'a priori', an iterative procedure, similar to the one described in Section 2.3.2, is adopted. The perturbation velocity components, in this case, may be expressed as:

$$u_j = \sum_{i=1}^{N_1+N_2+2} A_{ji}\gamma_i + \sigma_1 \sum_{i=1}^{N_1} C_{ji} + \sigma_2 \sum_{i=1}^{N_2} C_{ji} + \sum_{i=1}^{N_{wu}} E_{ji}\gamma_{wu}$$
$$+ \sum_{i=1}^{N_{wl}} E_{ji}\gamma_{wl} + \sum_{i=1}^{M} E_{ji}\gamma'_{wu} + \sum_{i=1}^{M} E_{ji}\gamma'_{wl}; \tag{2.36}$$

$$w_j = \sum_{i=1}^{N_1+N_2+2} B_{ji}\gamma_i + \sigma_1 \sum_{i=1}^{N_1} D_{ji} + \sigma_2 \sum_{i=1}^{N_2} D_{ji} + \sum_{i=1}^{N_{wu}} F_{ji}\gamma_{wu}$$
$$+ \sum_{i=1}^{N_{wl}} F_{ji}\gamma_{wl} + \sum_{i=1}^{M} F_{ji}\gamma'_{wu} + \sum_{i=1}^{M} F_{ji}\gamma'_{wl}. \tag{2.37}$$

Using eqs. (2.36) and (2.37), boundary condition of zero normal flow can be satisfied at (N_1+N_2) collocation points on the multi-element configuration surface giving (N_1+N_2) equations. To obtain (N_1+N_2+4) unknowns, auxiliary relations, pertaining to flow separation and Kutta condition, are used. For the cylinder surface, these conditions require the vorticity strengths just upstream and downstream of the top and bottom separation points be zero. Furthermore, $\gamma_{(N_1+2)} = \gamma_{(N_1+N_2+2)} = 0$. For the airfoil surface, these conditions require that vorticity strengths at the separation points be equal and opposite to the strength of the separating vortex sheets. Also, vorticity strengths just downstream of top separation point and upstream of lower separation point are taken to be zero.

Numerical solution can be obtained, as before, by an iterative scheme starting

with an assumed wake shape. Once the convergence is achieved, velocity and pressure can be calculated using eqs. (2.19), (2.20), (2.36), and (2.37).

2.3.4 Computer implementation

Computer codes for single and multi-element configurations were developed using FORTRAN 77. The programs can allow for zero and non-zero dissipation rate, desired cylinder rotation speed, angle of attack, etc. The total number of panels varies between 100-200 depending upon the configuration used. The infinite wake in case of zero vorticity dissipation is fixed at 150 times the airfoil chord. The programs require about 50-60 iterations to achieve a convergence accuracy of about 10^{-6}, and take about 15 minutes on a SUN SPARC 2 work station. A flowchart outlining the panel method is described in Figure 2-15. Details of the mathematical expressions for calculating the influence coefficients are given in the Appendix B.
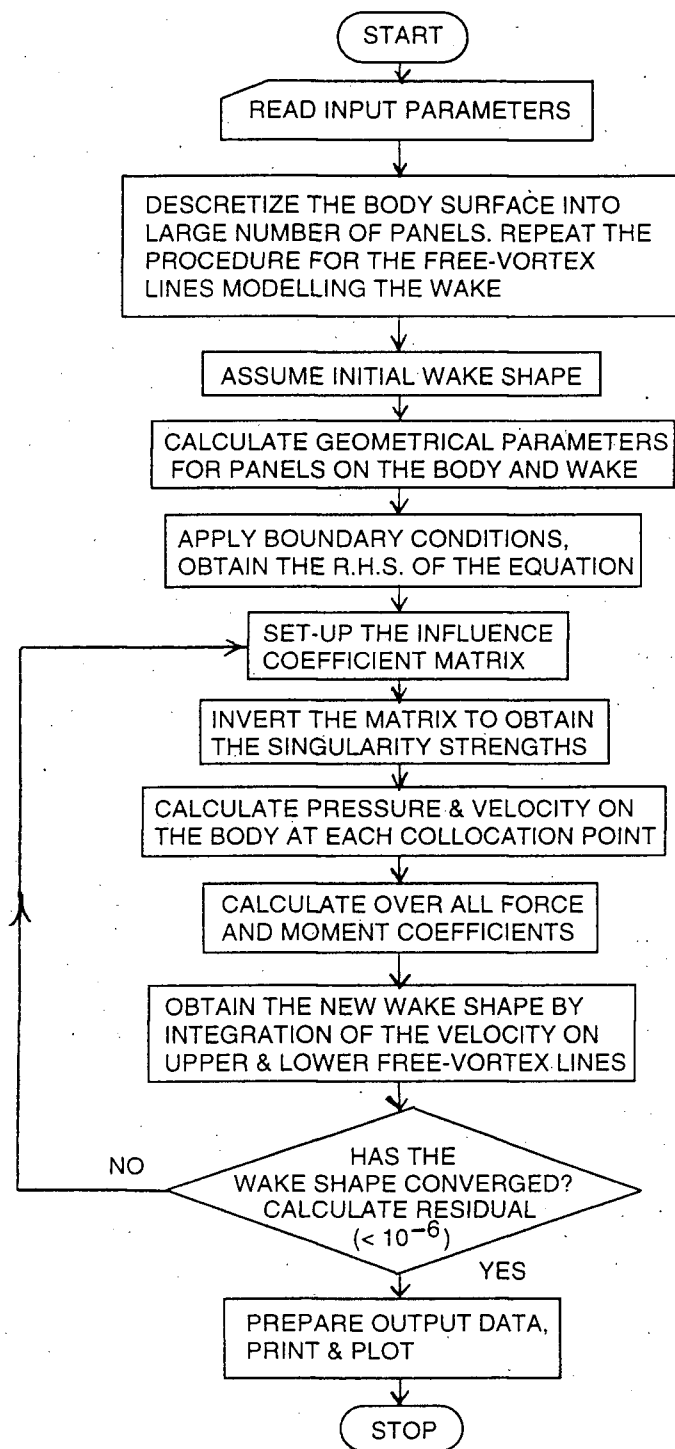
Figure 2-15   Numerical algorithm for the panel method.

3. AERODYNAMICS OF AN AIRFOIL WITH MOMENTUM INJECTION

3.1 Preliminary Remarks

The Moving Surface Boundary-layer Control (MSBC) was applied to a two-dimensional symmetric airfoil. The leading-edge of the Joukowski airfoil was replaced by a rotating cylinder, which injects momentum into the boundary-layer on the upper surface of the airfoil. Cylinders with smooth, splined (axial grooves) or rough (axial and circumferential grooves) surface were tested to assess their relative performance. To begin with wind tunnel results are presented. Effect of various flow parameters on the aerodynamic coefficients is discussed to emphasize physical changes in the flow brought about by application of the MSBC. Next, the numerical simulation results are presented and compared with the experimental data. Results of single and two element panel configurations with attached or separated flow model are presented and their relative accuracy is compared. The wake shape iterations and the effect of number of panels on the convergence accuracy of the numerical scheme are also discussed. Finally, the flow visualization photographs are presented which clearly demonstrate effectiveness of the MSBC in delaying the flow separation.

3.2 Wind Tunnel Investigation

3.2.1 Lift and drag characteristics

Variations in the lift coefficient with the angle of attack for smooth, rough and splined rotating cylinders are presented in Figure 3-1. The airfoil with a smooth leading edge cylinder is the benchmark case (Figure 3-1a) and all other results are compared with it. In absence of cylinder rotation ($U_C/U = 0$), the airfoil stalls at around $\alpha = 10^o$ regardless of the type of rotating cylinder employed. In case of the smooth cylinder (Figure 3-1a), as the cylinder rotation speed is increased from $U_C/U = 0$ to 4, the stall is delayed progressively to higher angles of attack: 15° at

$U_C/U = 1$; 25° at $U_C/U = 2$; and 30°–35° at $U_C/U = 3$–4. There is a corresponding increase in the lift coefficient (C_L) with α. For a momentum injection rate in the range $U_C/U = 3$–4, the $C_{L,max}$ of 1.84 for the smooth cylinder represents an increase of around 160%! The corresponding gain with the splined cylinder surface was equally impressive at 210% ($C_{L,max} = 2.2$). As α is increased beyond 35°, C_L decreases, but the stall is very gradual (i.e. it does not fit the nominal definition of a stall, since a rapid loss in lift is avoided). Even for α as high as 50°, C_L is about 1.48 (smooth cylinder), which is quite significant. The rate of change in C_L with α can be estimated from the slope $dC_L/d\alpha$. There is no significant change in the slope of the lift curve with the smooth rotating cylinder case. However, with the rough and splined rotating cylinders, there is a small rise in $dC_L/d\alpha$ with an increase in the momentum injection. Note, there is no appreciable further benefit in terms of an increase in lift when the momentum injection is raised from $U_C/U = 3$ to 4. This indicates a practical limit to the beneficial influence of the momentum injection.

Compared to the smooth surface rotating cylinder, the rough cylinder has inferior performance (Figure 3-1b). The maximum C_L is about 1.52 at $\alpha = 30°$ which is lower than that obtained with a smooth cylinder ($C_{L,max} = 1.84$). The axial grooves on the splined cylinder scoop the incoming fluid, and thereby improve momentum injection in the boundary-layer. In the case of the rough surface cylinder, the axial splines are supplemented by circumferential grooves (Figure 2-8), which seem to disrupt the effective scooping mechanism. The axial splines extend along the axis of the rotating cylinder from end to end, maintaining a two-dimensional flow. On the otherhand, the circumferential grooves introduce three-dimensional disturbances upstream of the two-dimensional airfoil, resulting in a deteriorated performance. Table 3.1 lists $C_{L,max}$ and stall values for the three different cylinder surface conditions. In Table 3.2, average values of the slope $dC_L/d\alpha$ are listed. It is apparent that the performance of the spline surface cylinder is relatively superior.
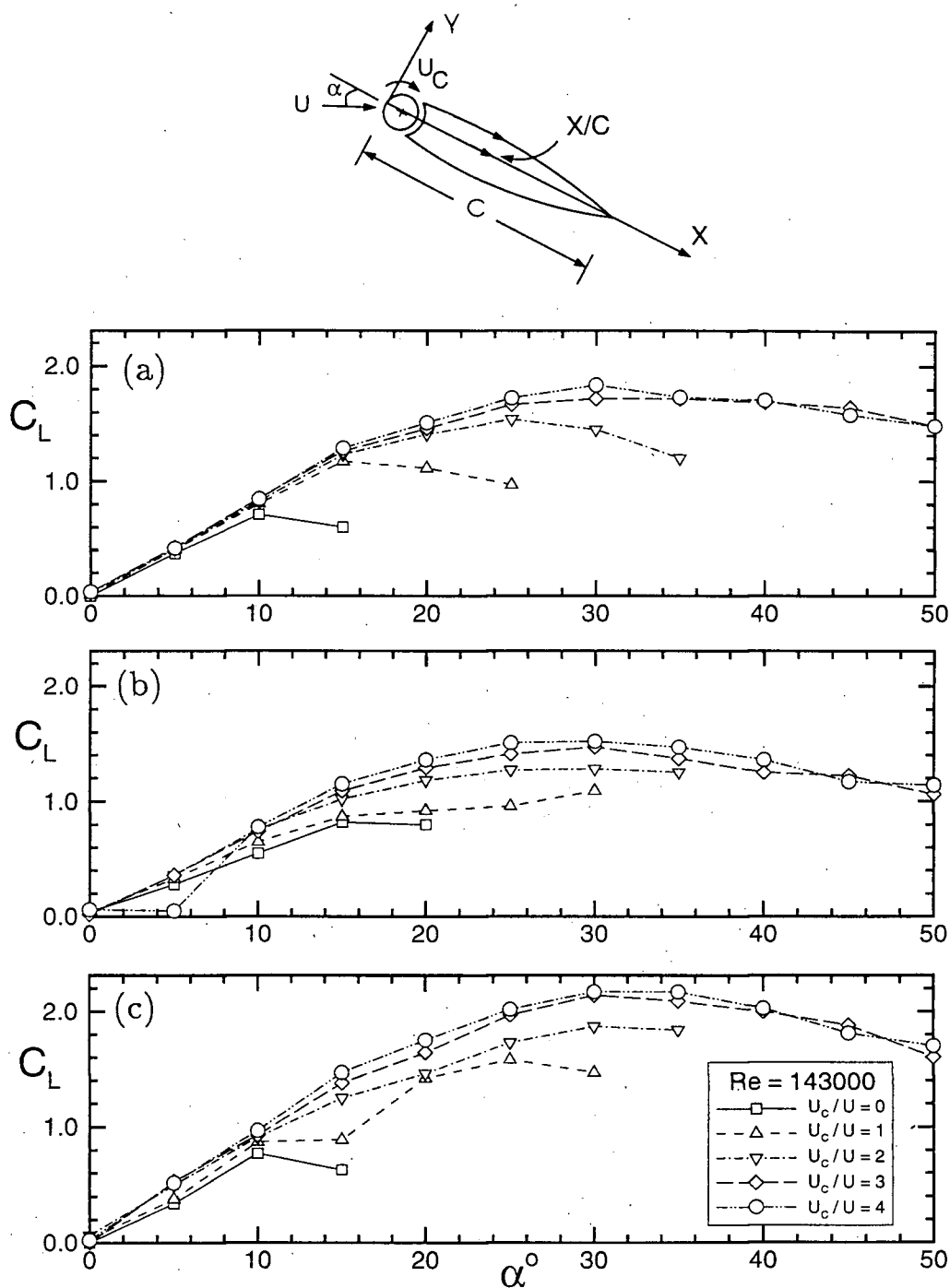
Figure 3-1   Experimentally obtained lift coefficient for the Joukowski airfoil in presence of momentum injection: (a) smooth leading-edge rotating cylinder; (b) rough cylinder; (c) splined cylinder.

Table 3.1 Comparative performance of the three rotating cylinders in terms of the maximum lift coefficient and the stall angle for $U_C/U = 3$ and 4.

Cylinder Surface	$U_C/U = 0$		$U_C/U = 3,4$	
	α_{stall}	$C_{L_{max}}$	α_{stall}	$C_{L_{max}}$
smooth	10°	0.70	35°	1.75
rough	15°	0.80	30°	1.50
splined	10°	0.75	35°	2.15

Table 3.2 Average values of $dC_L/d\alpha$ for three rotating cylinders ($d\alpha$ in radian).

Range of α, deg.	Smooth Cylinder	Rough Cylinder	Splined Cylinder
$0 - 20^o$	4.30	3.87	5.01
$0 - 30^o$	3.44	2.87	4.11
$30 - 50^o$	-0.86	-1.15	-1.29

The corresponding drag characteristics for the airfoil are shown in Figure 3-2. There is an almost linear rise in the drag coefficient (C_D) with α for all the three cases. For the Joukowski airfoil with splined cylinder (Figure 3-2c), C_D remains quite small for $\alpha \leq 15^o$. It attains a maximum value of around 2.5 at $\alpha = 50^o$ for the airfoil with smooth or rough cylinder. On the other hand, maximum C_D is about 1.95 in the case of the splined cylinder. The lower drag coupled with a higher lift in case of the airfoil with a splined cylinder appears quite promising for practical aerodynamic applications. In Table 3.3, the slope $dC_D/d\alpha$ is listed for $U_C/U = 0$ and 4. Note, by application of the momentum injection, flow separation near the leading edge is avoided and the local pressure on the upper surface remains much lower compared to that at the lower surface of the airfoil. This results in a large normal force acting perpendicular to the airfoil. Since the drag of an airfoil is proportional to the sine component (i.e. $C_D \propto sin\alpha$) of this normal force, it contributes more to C_D as α is increased. The rate of momentum injection increases the slope $dC_D/d\alpha$ in all three cases (Table 3.3).

Table 3.3   Average values of $dC_D/d\alpha$ as affected by the cylinder surface condition and rate of momentum injection.

Type of Cylinder	$U_C/U = 0 \ (0 \leq \alpha \leq 10^o)$	$U_C/U = 4 \ (0 \leq \alpha \leq 50^o)$
Smooth	0.997	2.865
Rough	0.229	2.865
Splined	0.516	2.292

The lift to drag ratio (C_L/C_D) for the airfoil with three different cylinder geometries is plotted in Figure 3-3. The C_L/C_D has a peak in the range $0 \leq \alpha \leq 10^o$, before stall. In the case of splined cylinder, large values of C_L/C_D are achieved, resulting from a combination of high lift and low drag coefficients. Beyond stall, the C_L/C_D ratio drops off rapidly and there is only little effect of momentum injection. At high angles of attack ($\alpha \geq 20^o$), both the lift and the drag coefficients show an increase keeping the C_L/C_D ratio low. Further appreciation in this regard can be obtained by examining C_L vs. C_D plots for the three cases (Figure 3-4). For the splined cylinder, the steep gradient of the plot suggests a favourable performance. In Figure 3-5, variation of both C_L as well as C_L/C_D with α are plotted for the three cases. These results clearly establish significant changes brought about by the surface condition of a momentum injecting rotating cylinder.

Results in Figure 3-6 focus on the variation of C_L with α beyond the nominal stall angle of 10° (reference case), as affected by the surface roughness of the rotating element and U_C/U. For the smooth cylinder case, as expected, the lift coefficient first dips at stall followed by a monotonic rise with an increase in the angle of attack in the range tested ($\alpha \leq 50^o$), in absence of the momentum injection. The effect of U_C/U is to delay the stall to around 35° for $U_C/U = 4$ with an increase in C_L by $\approx 160\%$ as mentioned before. Now the discontinuity in the C_L vs. α plot at the stall is eliminated. Note, the flat peak suggests onset of a gradual stall, a desirable feature. The presence of the splined surface accentuates this behaviour resulting in
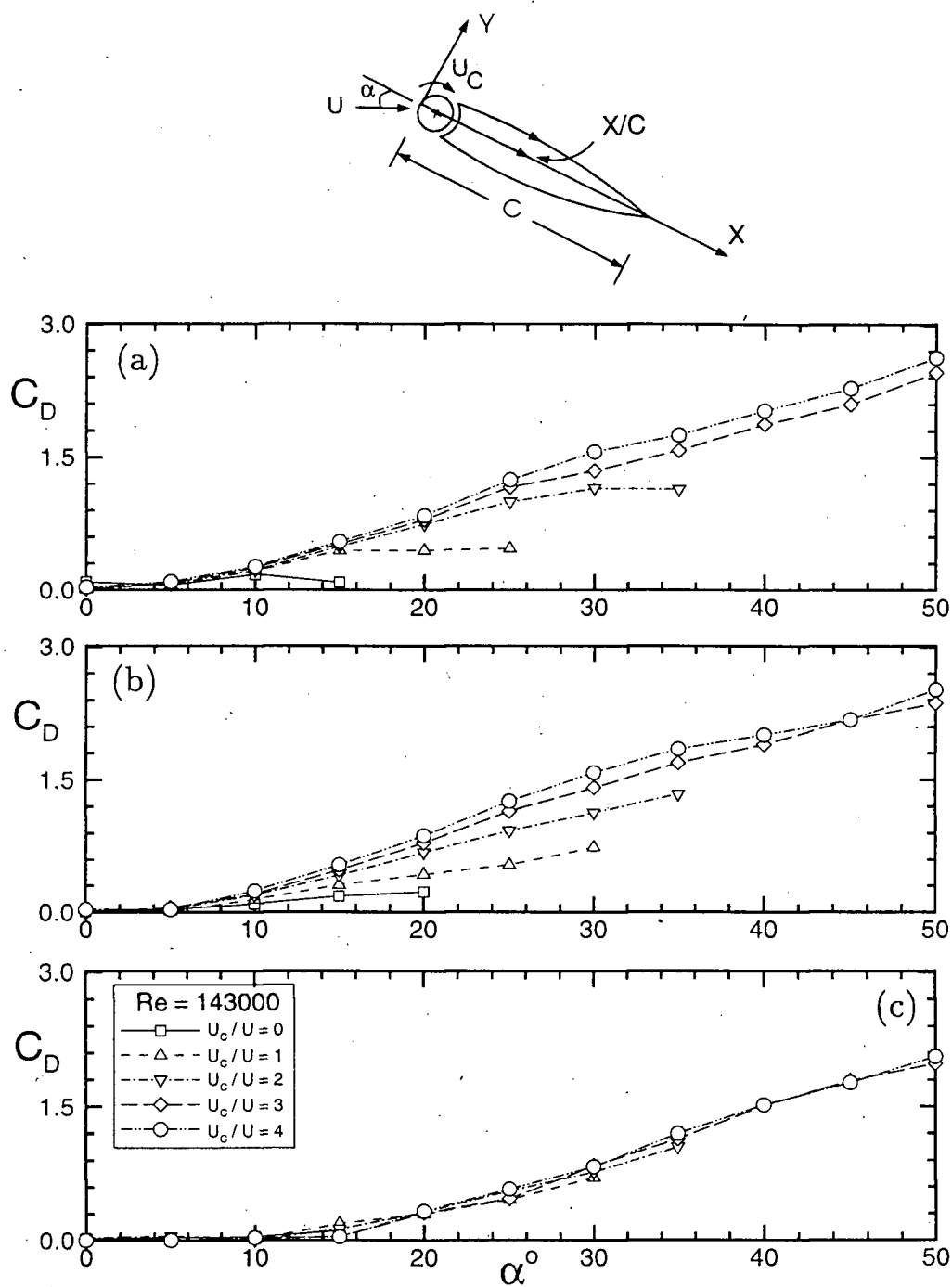
Figure 3-2   Experimentally obtained drag coefficient for the Joukowski airfoil in
presence of momentum injection: (a) smooth leading-edge rotating
cylinder; (b) rough cylinder; (c) splined cylinder.
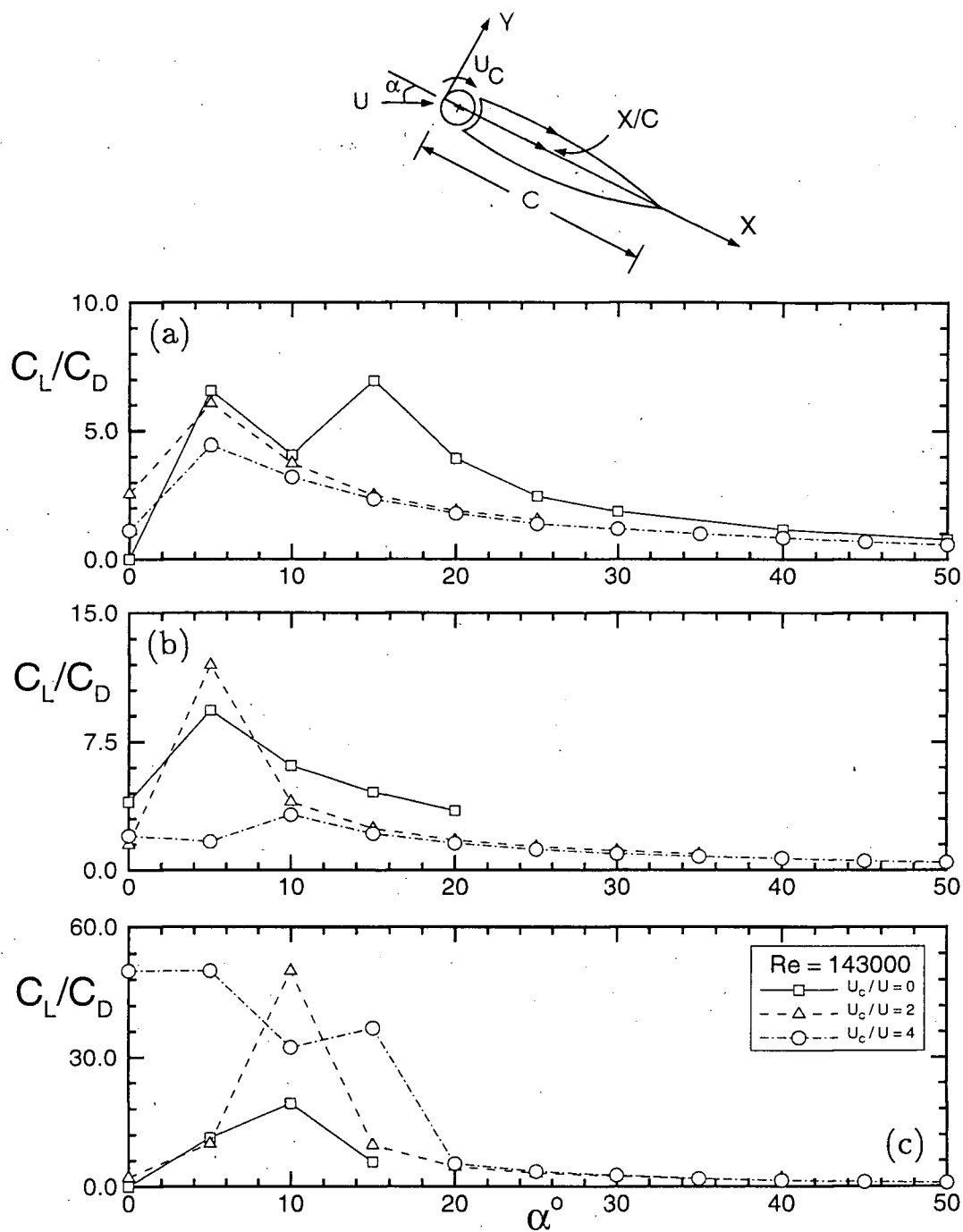
Figure 3-3   Experimentally obtained lift/drag ratio of the Joukowski airfoil in presence of momentum injection: (a) smooth cylinder; (b) rough cylinder; (c) splined cylinder.
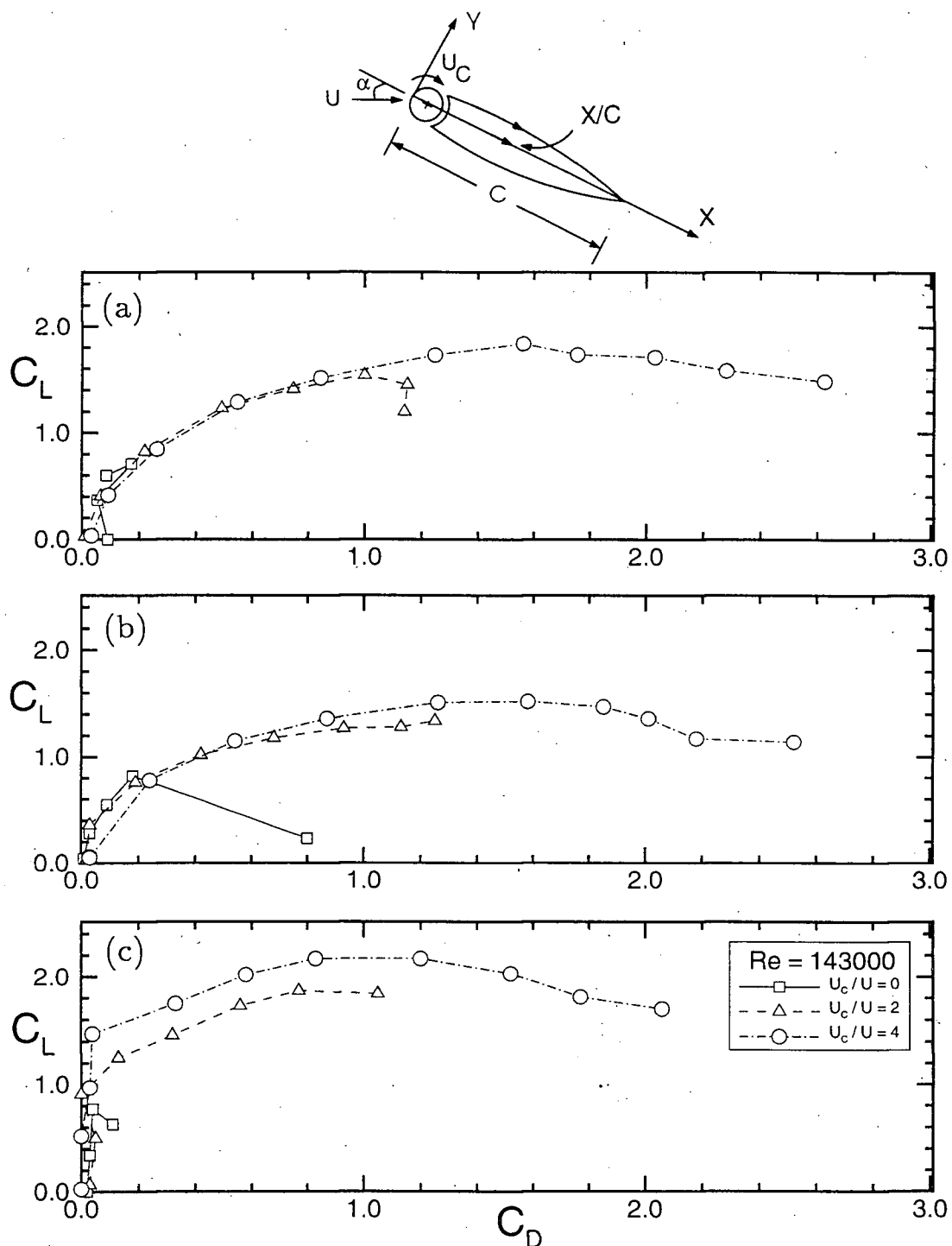
Figure 3-4   Variation of C_L with C_D for the Joukowski airfoil in presence of momentum injection: (a) smooth cylinder; (b) rough cylinder; (c) splined cylinder.
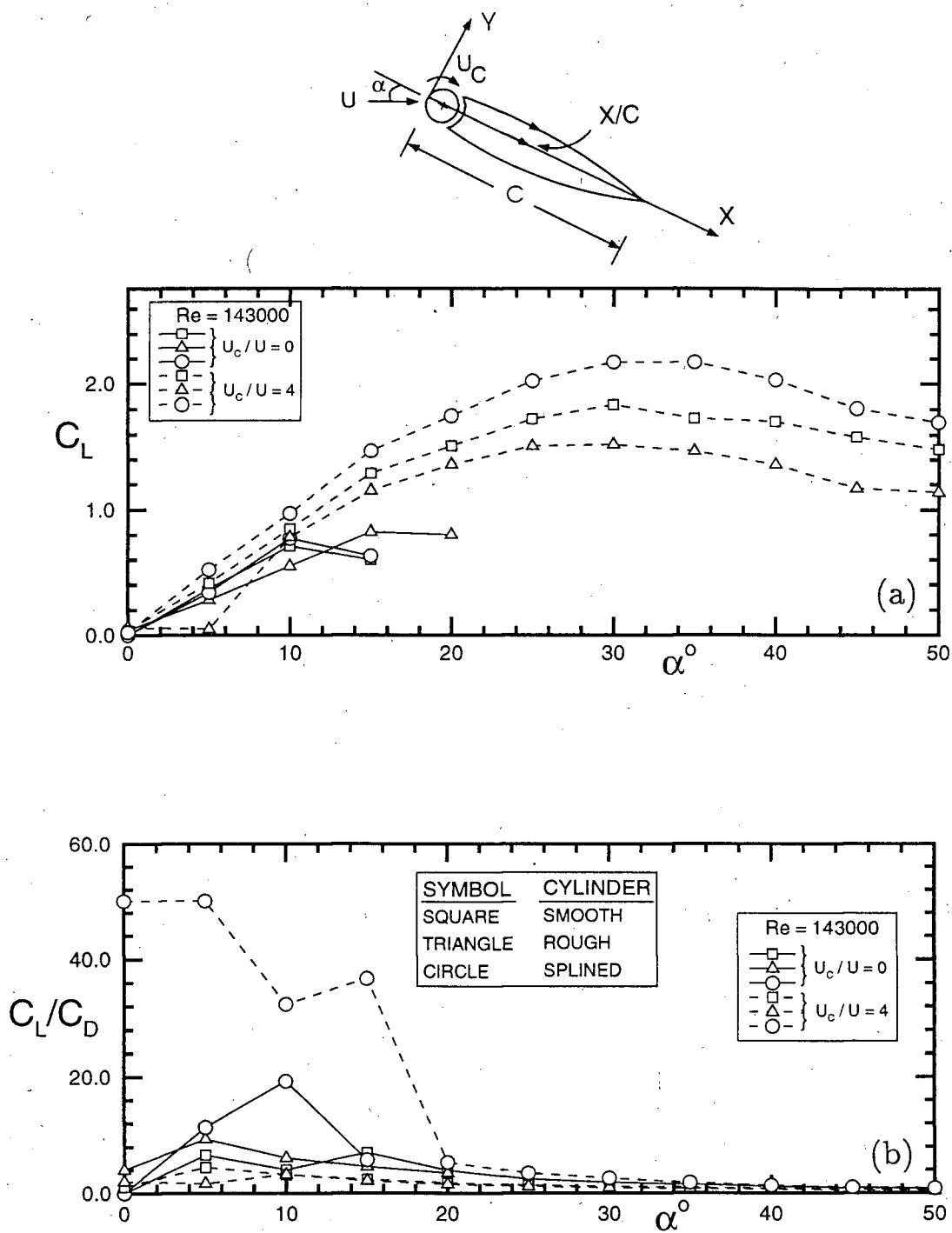
Figure 3-5   A comparative study showing the effect of cylinder surface during momentum injection on the variation of: (a) C_L with α; (b) C_L/C_D with α.

90
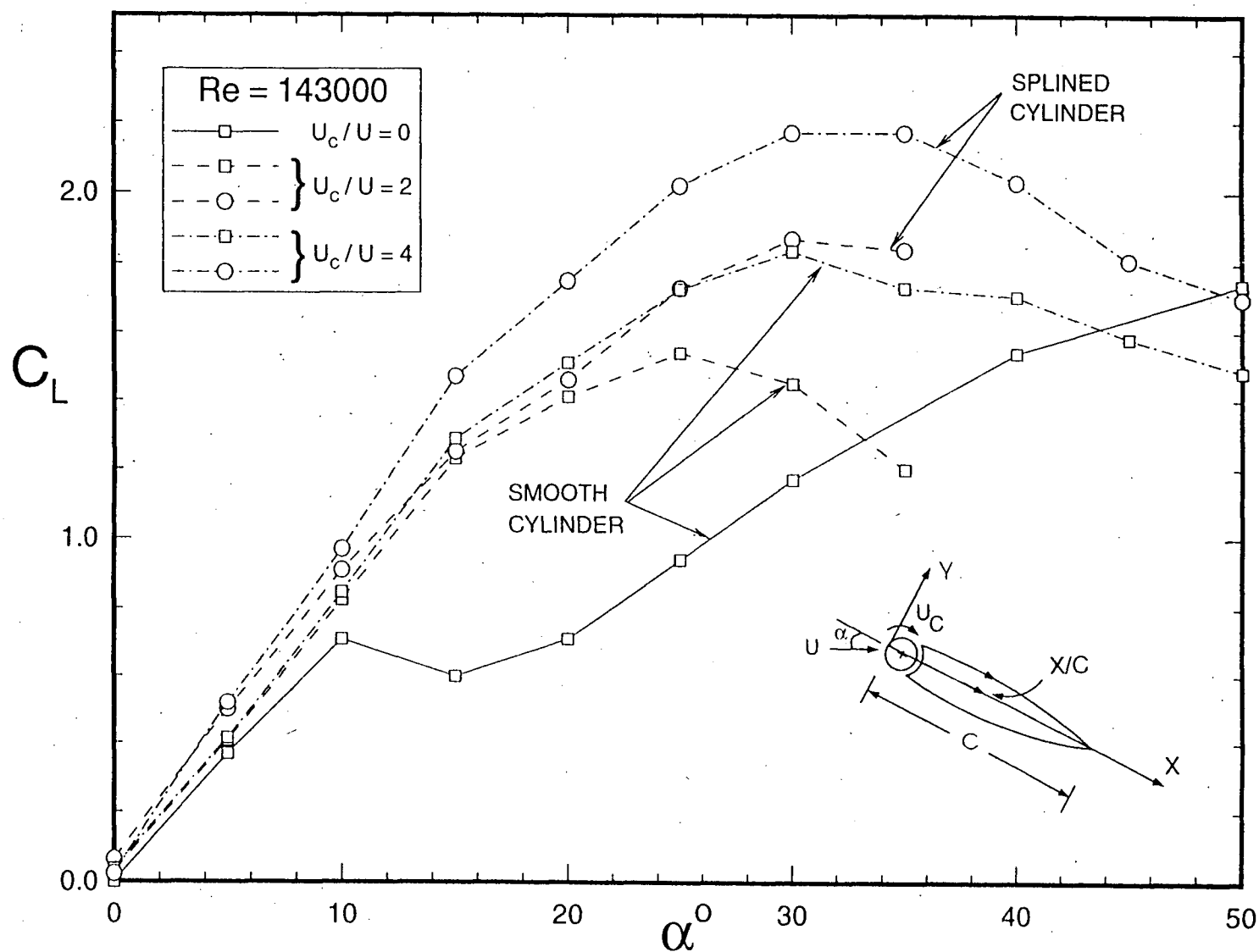
Figure 3-6   A comparative study showing the effect of surface roughness and momentum injection on the lift coefficient at high angles of attack.

higher slope of the lift curve, increased $C_{L,max}$ and slightly further delay in the onset of stall ($\approx 32^o$), which continues to be gradual. The corresponding plots for the C_D variation are presented in Figure 3-7. The relatively small increase in the drag for the splined cylinder case suggests effectiveness of the MSBC even at moderately high angles of attack. At an angle of attack of 30°, a reduction in the drag coefficient from $C_D \approx 1.6$ for the smooth cylinder case in absence of momentum injection to $C_D \approx 0.7$ for the airfoil with a splined cylinder at $U_C/U = 2$ is indeed impressive. It amounts to 56%.

3.2.2 Pressure distribution

Extensive wind tunnel tests provided a wealth of information in terms of the pressure distribution with respect to different flow parameters. Some typical results for the smooth and splined surface cylinders are presented in Figure 3-8 to explain the physical effects of momentum injection on the flow past the airfoil. As mentioned earlier, the airfoil is symmetric about its chord and hence has similar pressure distribution on the top and bottom surfaces resulting in a zero lift at $\alpha = 0$. At $\alpha = 5^o$ (Figure 3-8a), the pressure on the top surface of the airfoil is lower compared to that on the bottom surface. As α is increased further, the pressure on the top surface becomes even lower (Figure 3-8b). On the other hand, there is no change in the pressure distribution on the bottom surface. Also note the presence of a near stagnation value ($C_P \approx 0.9$) at the bottom of the leading edge. The airfoil has not yet stalled at $\alpha = 10^o$. Introduction of the momentum injection does not bring about any noticeable changes in the pressure distribution, as the flow is not separated. With a further increase in the angle of attack ($\alpha = 15^o$), the airfoil stalls completely in absence of the momentum injection ($U_C/U = 0$). As the momentum injection is increased from $U_C/U = 0$ to 4, the flow separation on the top surface is eliminated completely. The pressure coefficient (C_P) reaches a minimum value of -4.0 near the upper leading edge. Similar trend persists when α is further increased upto 40° (Fig-
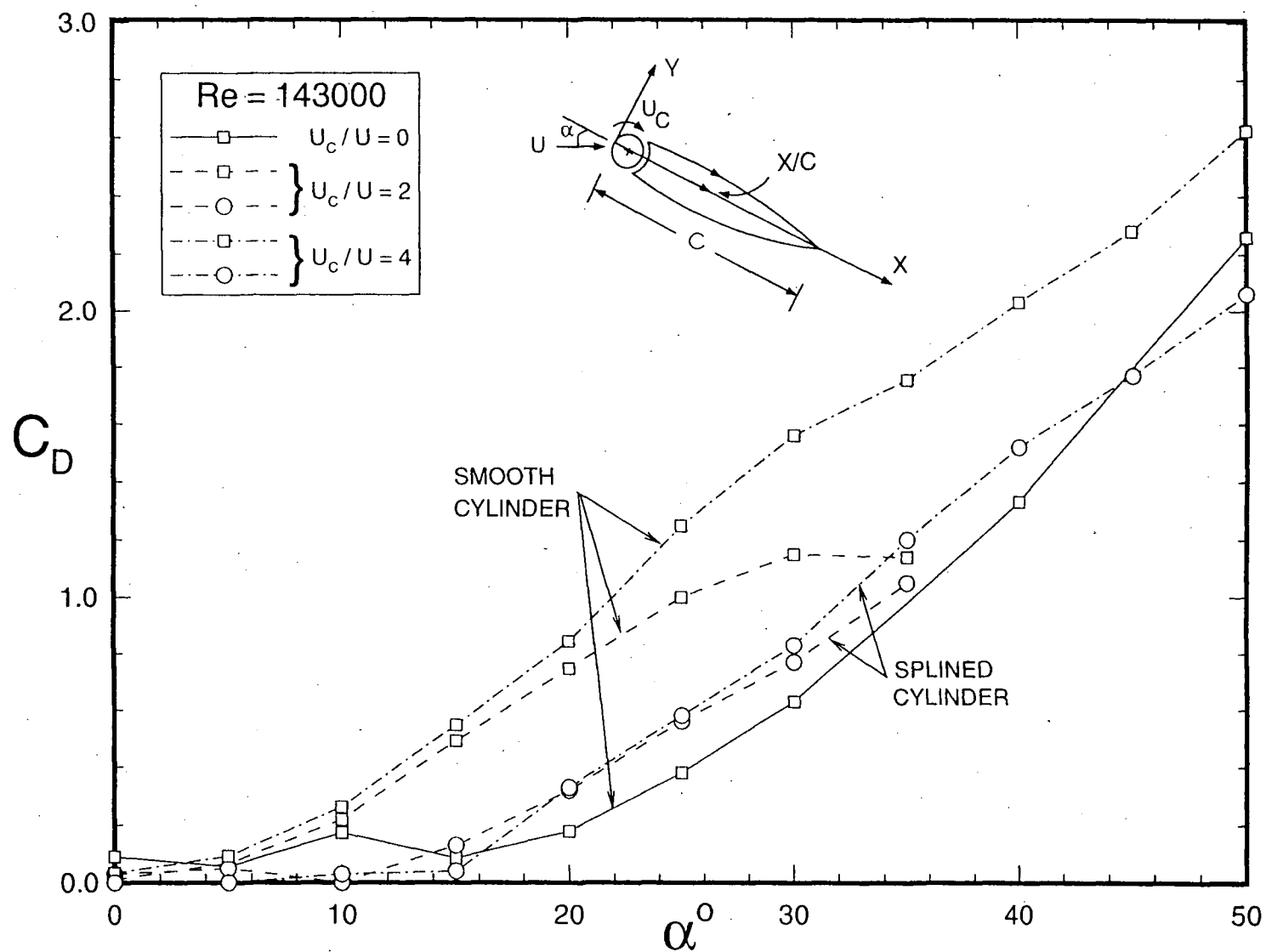
Figure 3-7   Effect of momentum injection with the splined surface cylinder on the variation of C_D with α. The smooth cylinder results are also presented to serve as reference.

ure 3-8d to 3-8f). The peak negative C_P is about −6.0 at the top face of the rotating cylinder ($U_C/U = 4$), which significantly contributes to a large increase in the lift. As expected, in presence of the momentum injection, the point of separation on the top surface moves toward the trailing edge with an increase in the cylinder rotation speed.

3.3 Numerical Simulation

3.3.1 Pressure distribution

Figure 3-9 compares pressure distribution plots on the surface of the airfoil obtained through the numerical scheme and wind tunnel tests. The experimental data pertain to the case of the Joukowski airfoil with smooth cylinder. The wind tunnel test Reynolds number based on the airfoil chord was 143,000. The numerical results were obtained using the two element panel configuration as described earlier.

At $\alpha = 5^o$ and in absence of momentum injection ($U_C/U = 0$), there is a good agreement between the theory and experimental data (Figure 3-9a). However, at a higher rate of momentum injection ($U_C/U = 4$), the numerical scheme somewhat overpredicts the negative pressure on the top surface of the airfoil. On the other hand, presence of a large suction peak at the rotating cylinder is successfully captured by the numerical scheme. Due to limited number of pressure taps on the surface of the rotating cylinder, the suction peak could be captured only partially during the experiment, though a tendency towards large negative C_P is evident. Overall, there is a satisfactory agreement between the numerical and experimental pressure distribution plots over the complete airfoil. An increase in α to 10° (Figure 3-9b), makes the suction peak even more pronounced. Close to the trailing edge the flow is almost separated at $U_C/U = 0$, indicating a tendency to stall. The complete stall at still higher angles of attack ($\alpha = 15^o$) is accurately captured by the numerical scheme. In presence of momentum injection ($U_C/U = 4$), the point of separation is pushed

94
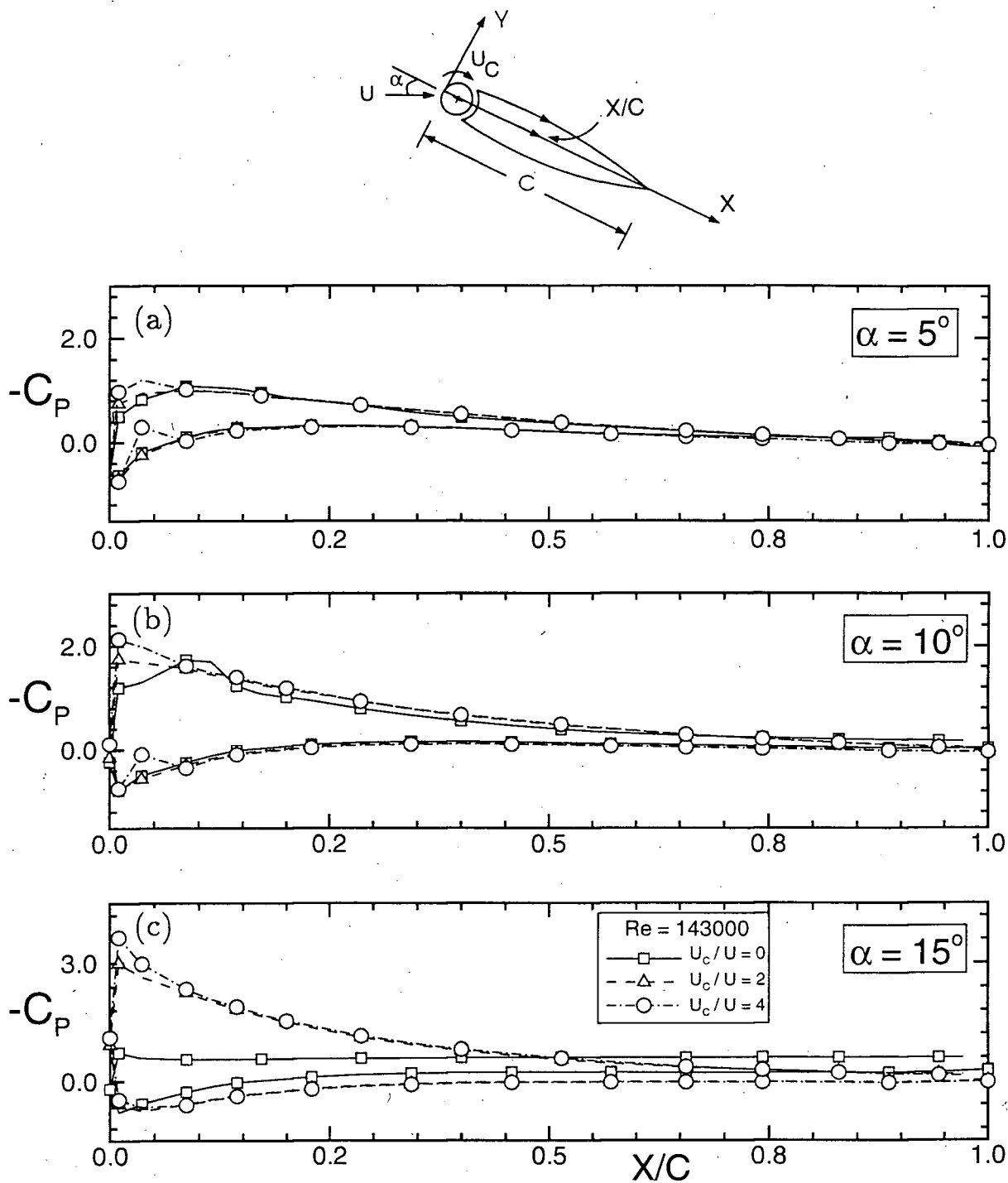
Figure 3-8   Experimentally obtained pressure distribution for the Joukowski airfoil with the MSBC provided by a smooth surface cylinder: (a) $\alpha = 5°$; (b) $\alpha = 10°$; (c) $\alpha = 15°$.
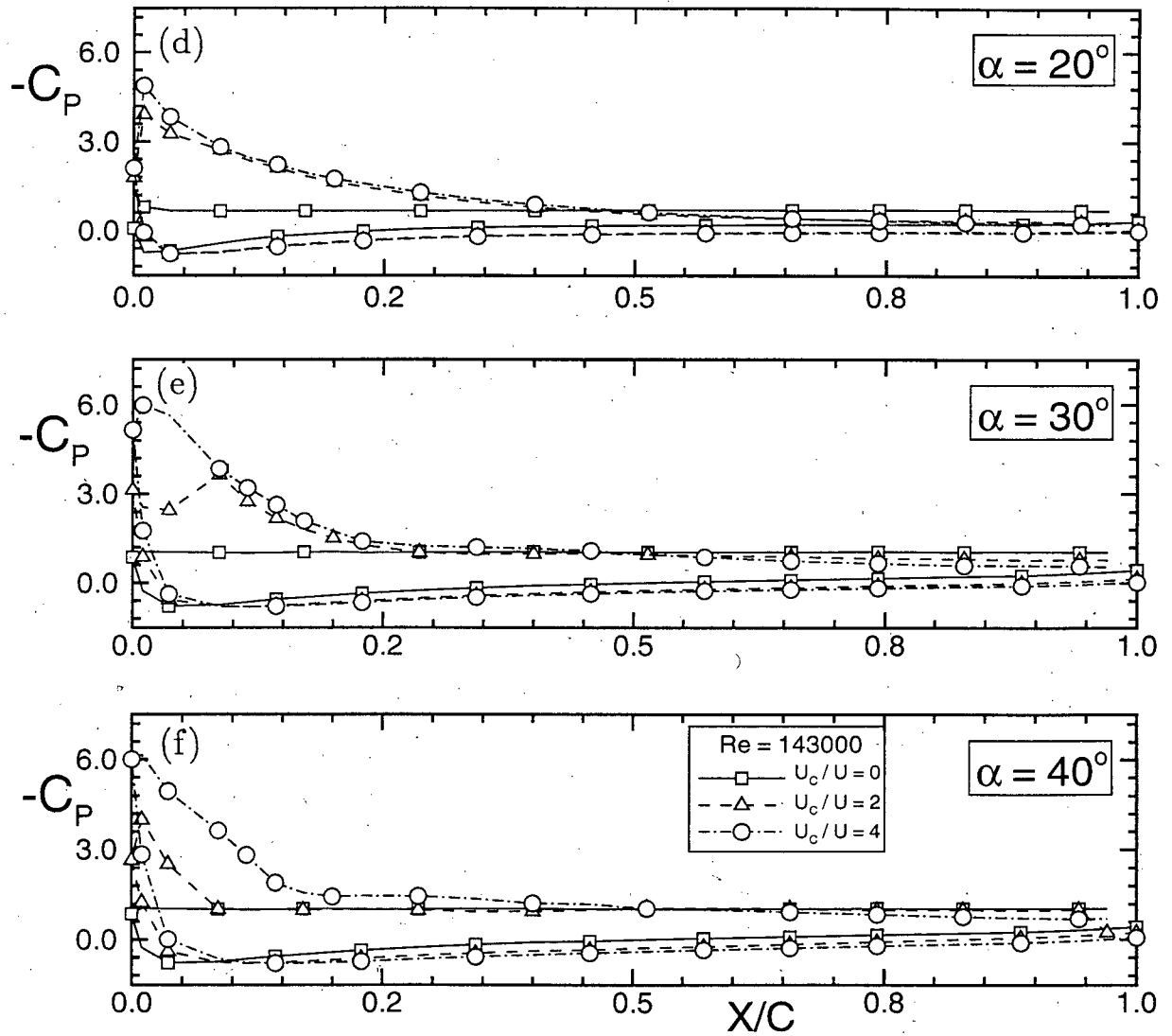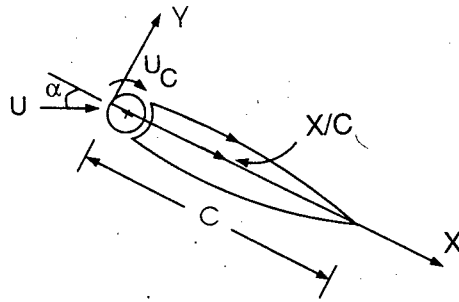
Figure 3-8(cont.) Experimentally obtained pressure distribution for the Joukowski airfoil with the MSBC: (d) $\alpha = 20°$; (e) $\alpha = 30°$; (f) $\alpha = 40°$.

96

further downstream ($X/C \approx 0.6$). The effect of the momentum injection diminishes as X/C increases and becomes negligible beyond $X/C \approx 0.6$, which is expected due to the vorticity dispersion and dissipation effects.

3.3.2 Comparison of the various numerical schemes

Figures 3-10 to 3-12 present comparison of results obtained using the various numerical schemes described in Section 2.3.

Numerically obtained pressure plots using a single and two element panel formulations with the attached flow model are shown in Figure 3-10. The results are essentially similar except for the suction peak, which is larger for the two element case. Figure 3-11(a) shows comparison between attached and separated flow solutions for the single element configuration. As expected, the separated flow solution agrees better with the experimental data since it is more realistic. The suction peak near the leading edge diminishes due to flow separation. The discrepancy near the trailing edge (Figure 3-10) is also eliminated. In Figure 3-11(b), the results for the single element airfoil are compared with those obtained using the two element model. Note, the prediction by the two element case shows a slight improvement. The spike in the suction peak (which is physically unlikely) is replaced by a smooth curve indicating a gradual change in the pressure. Figure 3-12 presents results at $\alpha = 20^{o}$ for the two element airfoil with attached and separated flow models. As can be expected, there is a significant improvement in prediction with the separated flow model. The unrealistically high suction peak predicted by the attached flow model is now substantially reduced. The modelling of flow separation near the leading edge agrees more closely with the actual physical process. The discrepancies between the numerical and experimental pressure values near the leading and the trailing edges are also eliminated.

3.3.3 Prediction of the lift coefficient

In Figure 3-13, the numerically obtained lift coefficient is compared with that
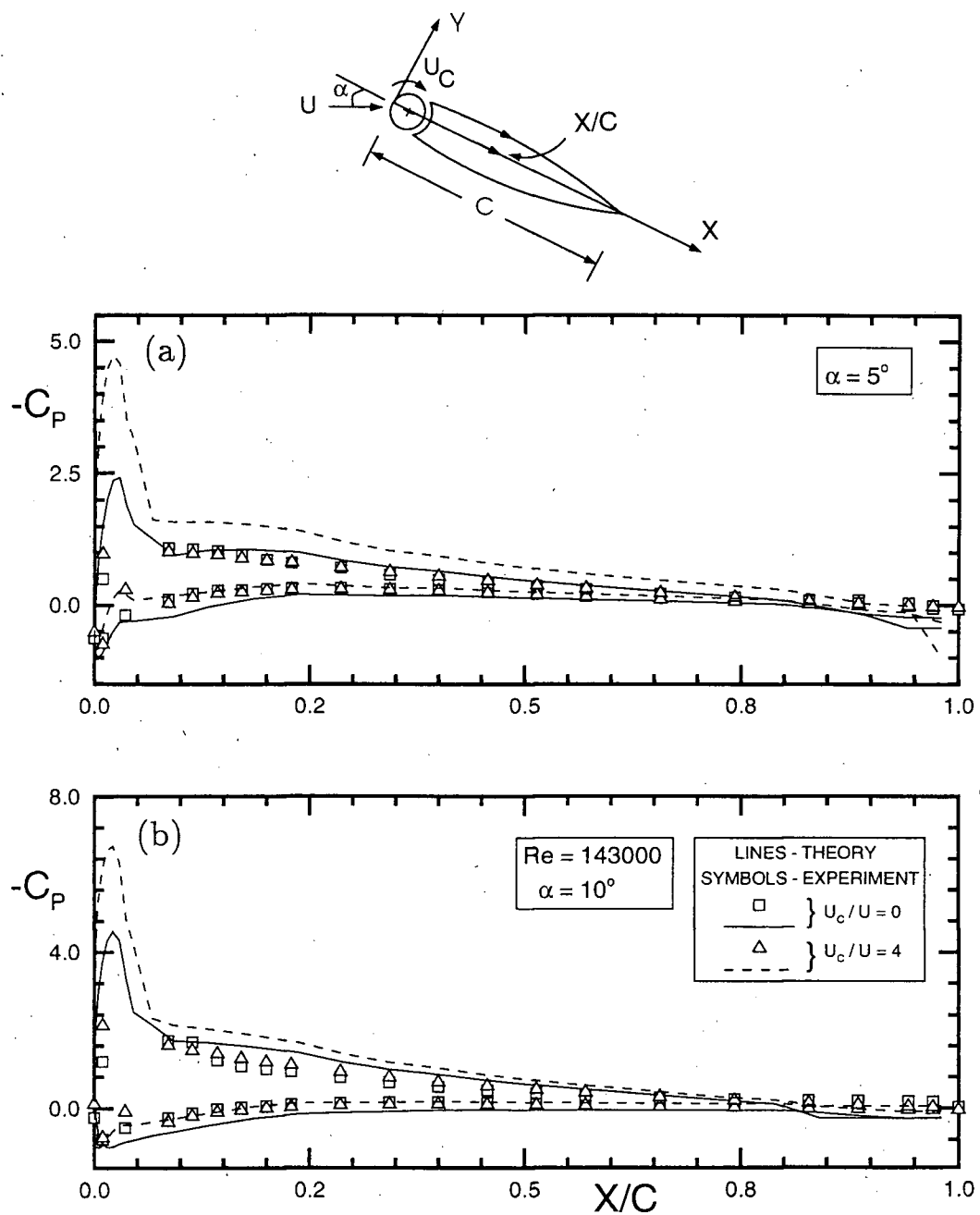
Figure 3-9 Comparison of the numerically obtained pressure distribution with the experimental data for a Joukowski airfoil with the MSBC: (a) α = 5° ; (b) α = 10°.
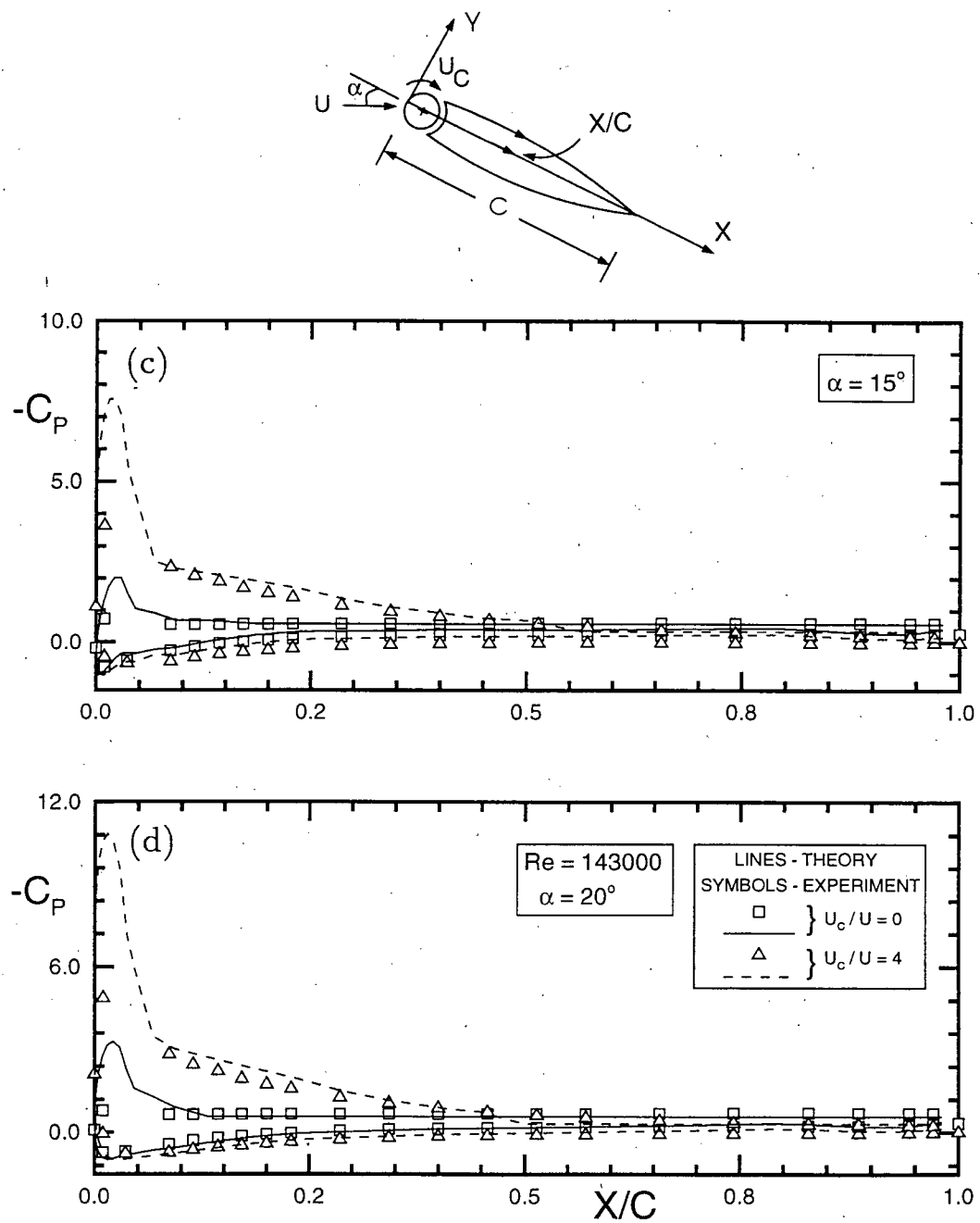
Figure 3-9(cont.) Comparison of the numerically obtained pressure distribution with the experimental data for a Joukowski airfoil with the MSBC: (c) $\alpha = 15^{\circ}$; (d) $\alpha = 20^{\circ}$.
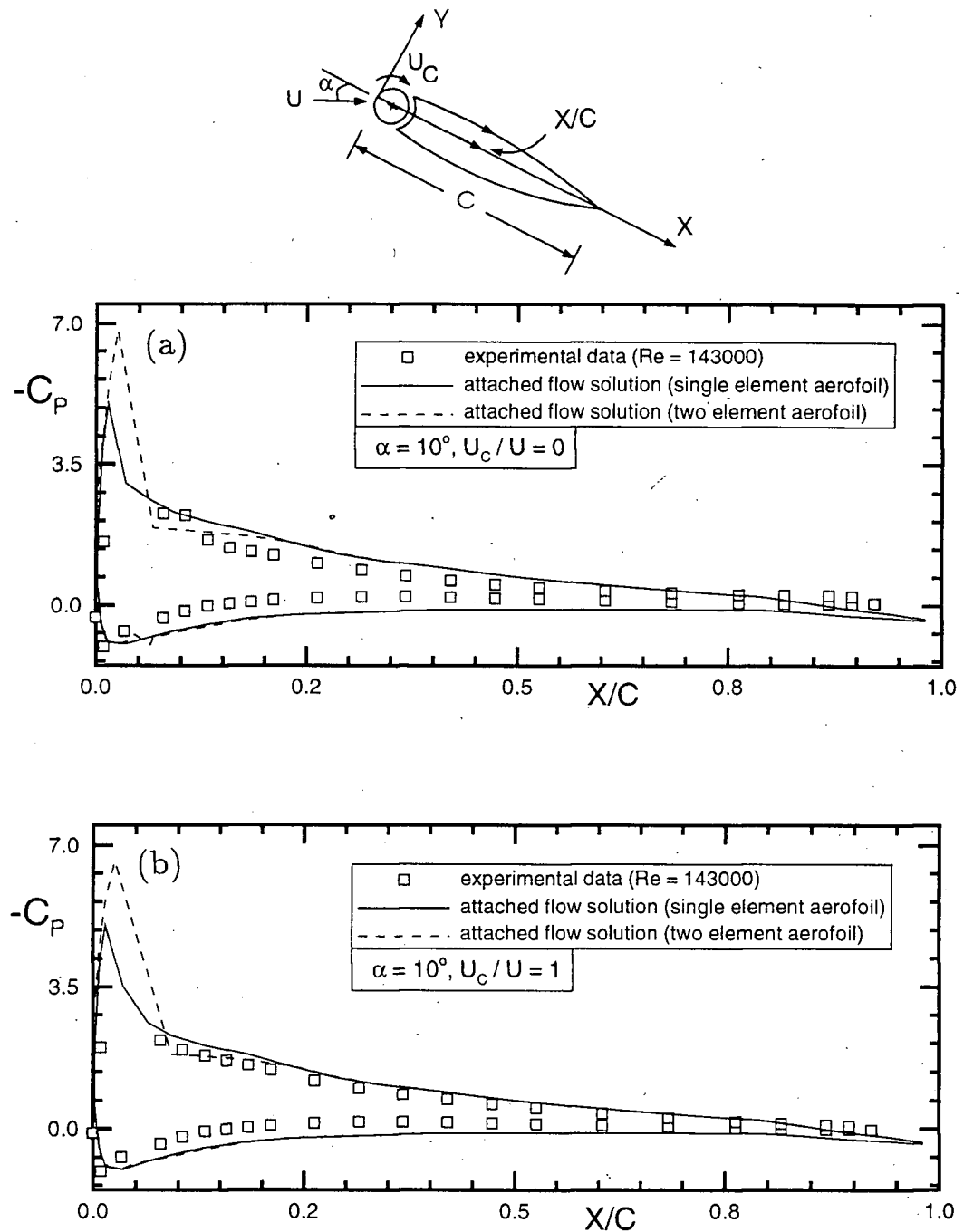
Figure 3-10   Comparison between the results obtained through the single and two
element numerical panel formulations in presence of the MSBC: (a)
$\alpha = 10^\circ, U_C/U = 0$; (b) $\alpha = 10^\circ$, $U_C/U = 1$. The experimental data
are also included.

100
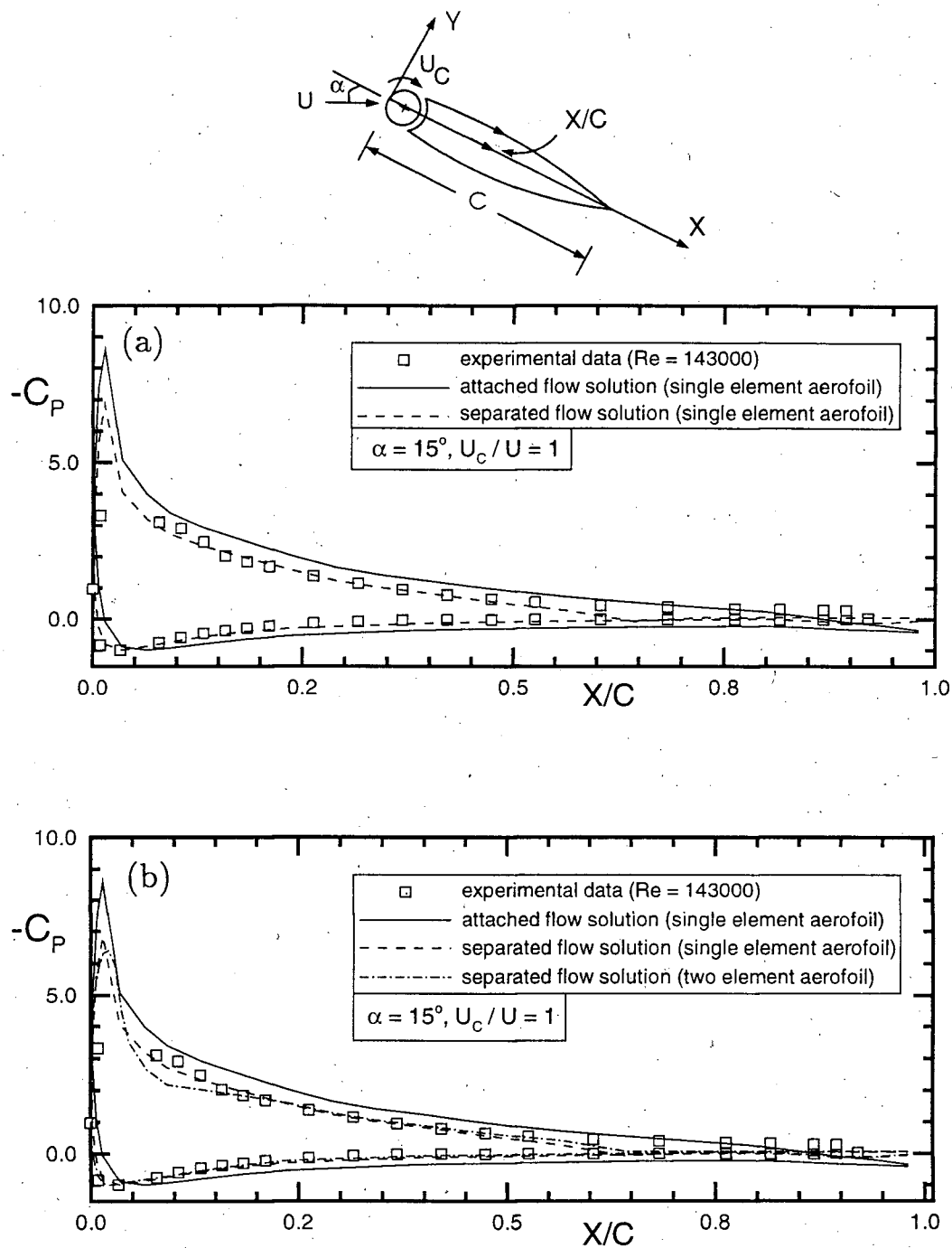
Figure 3-11 Comparative studies of pressure plots in presence of the MSBC: (a) attached versus separated flow solutions for a single element formulation; (b) corresponding results for the two element airfoil. The experimental data are also included.

101
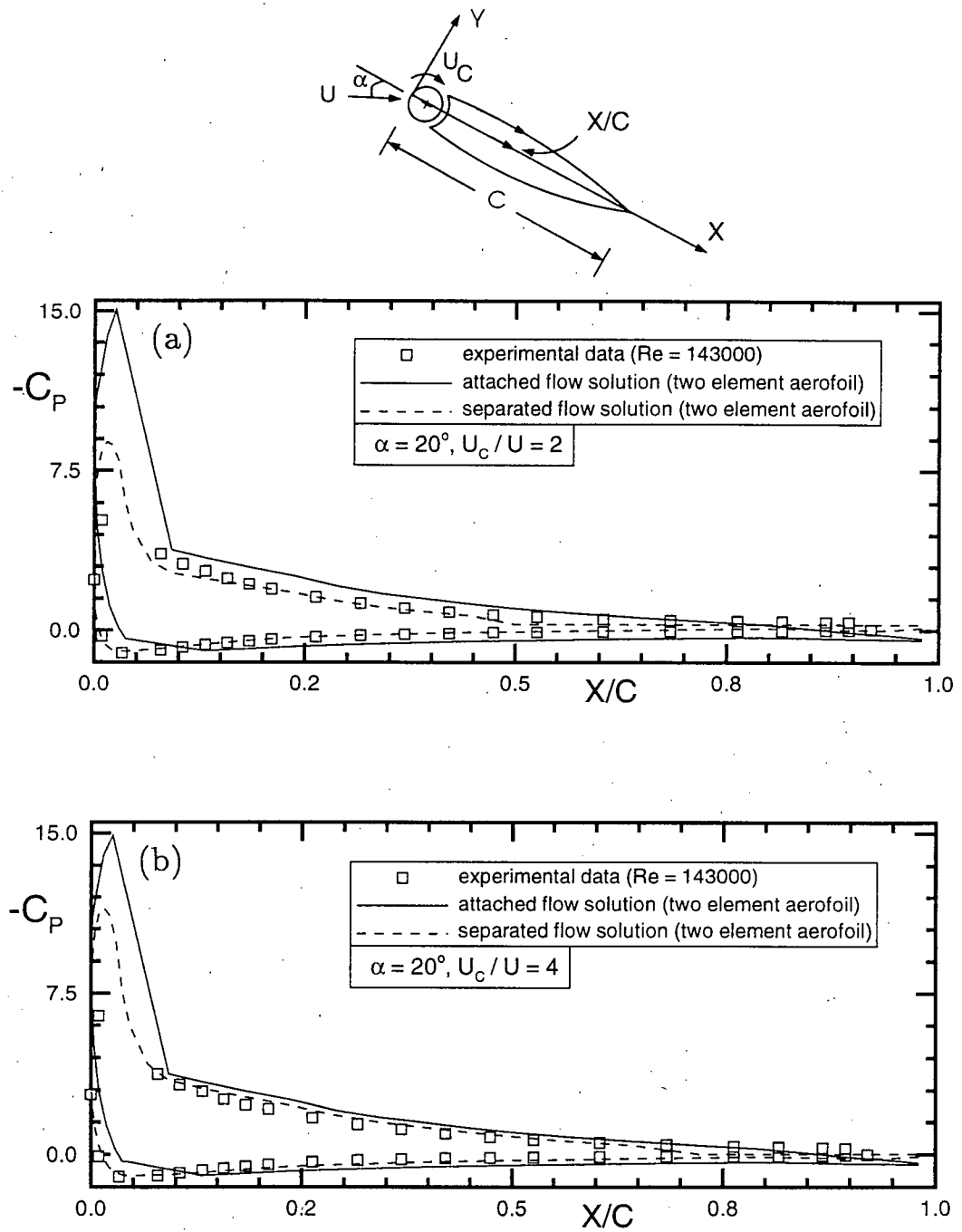
Figure 3-12 Relative performance of the attached and separated flow models as applied to the two element airfoil:(a) $\alpha = 20°$, $U_C/U = 2$; (b) $\alpha = 20°$, $U_C/U = 4$.

from the wind tunnel tests. The C_L against α curve agrees closely with the experimental results, especially at low and moderate angles of attack ($\alpha \leq 20^o$). The airfoil stall around $\alpha = 10^o$ is also captured by the numerical scheme accurately. However, for $\alpha \geq 30^o$ the numerical results start to diverge from the experimental data. This can be expected due to relatively complex character of the flow. It indicates a need for improvement in the 'free vortex layer' model of the wake at very high angles of attack.

3.3.4 Iteration characteristic and the wake shape

The iteration character of the numerical scheme is indicated in Figure 3-14. The results are for the two element airfoil with separated flow model in presence of momentum injection ($\alpha = 15^o$, $U_C/U = 1$). The lift coefficient converges quite rapidly to its final value in less than 15 iterations, which is considered very good. Each iteration cycle affects the shape of the wake. Initially, the flow is represented by parallel upper and lower 'free vortex layers' emanating from the separation points. This is shown in the inset box. If the wake vorticity dissipation rate (λ) is considered zero then an infinite wake is obtained, which is unrealistic. In case of the nonzero dissipation rate ($\lambda = 0.62$), the 'free vortex layers' converge to a closed wake in about 15 iterations. This takes about 2 minutes on a SUN SPARC 2 workstation.

The effect of number of panels on the convergence of the numerical scheme was also investigated (Figure 3-15). With just 57 panels (airfoil + wake) the residual (i.e. the maximum difference in wake shape between the two consecutive iterations) is about 10^{-2} when a cyclic variation sets in. If the number of panels is increased to 104, the accuracy is improved to 10^{-5}. Finally, with 204 panels, an accuracy of the order of 10^{-6} is achieved in 100 iterations which is sufficient for all engineering purposes. This suggests sensitivity of the solution to the distribution of panels.
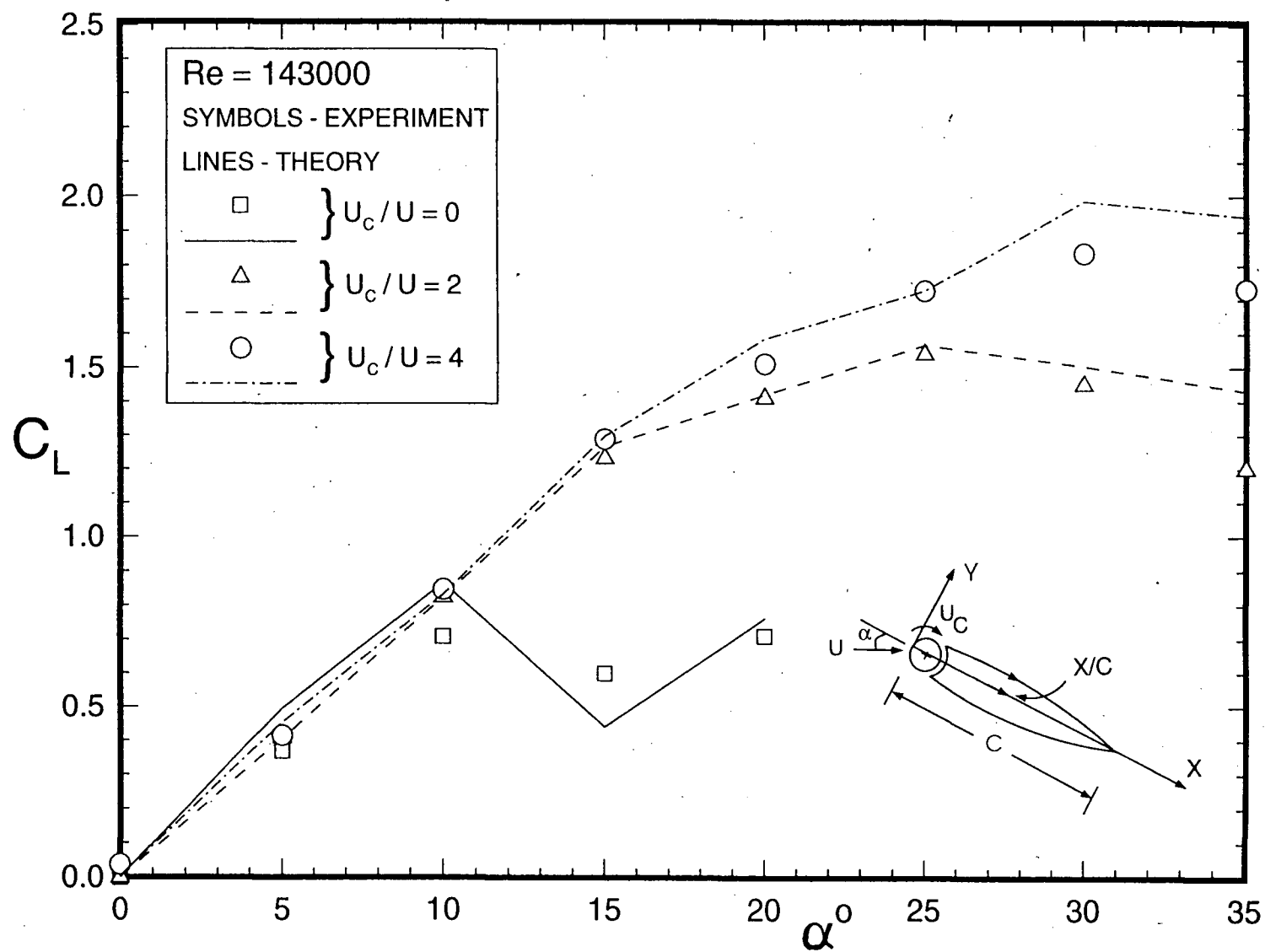
Figure 3-13 Numerically obtained lift coefficient as compared to the experimental data for a Joukowski airfoil in presence of the MSBC.
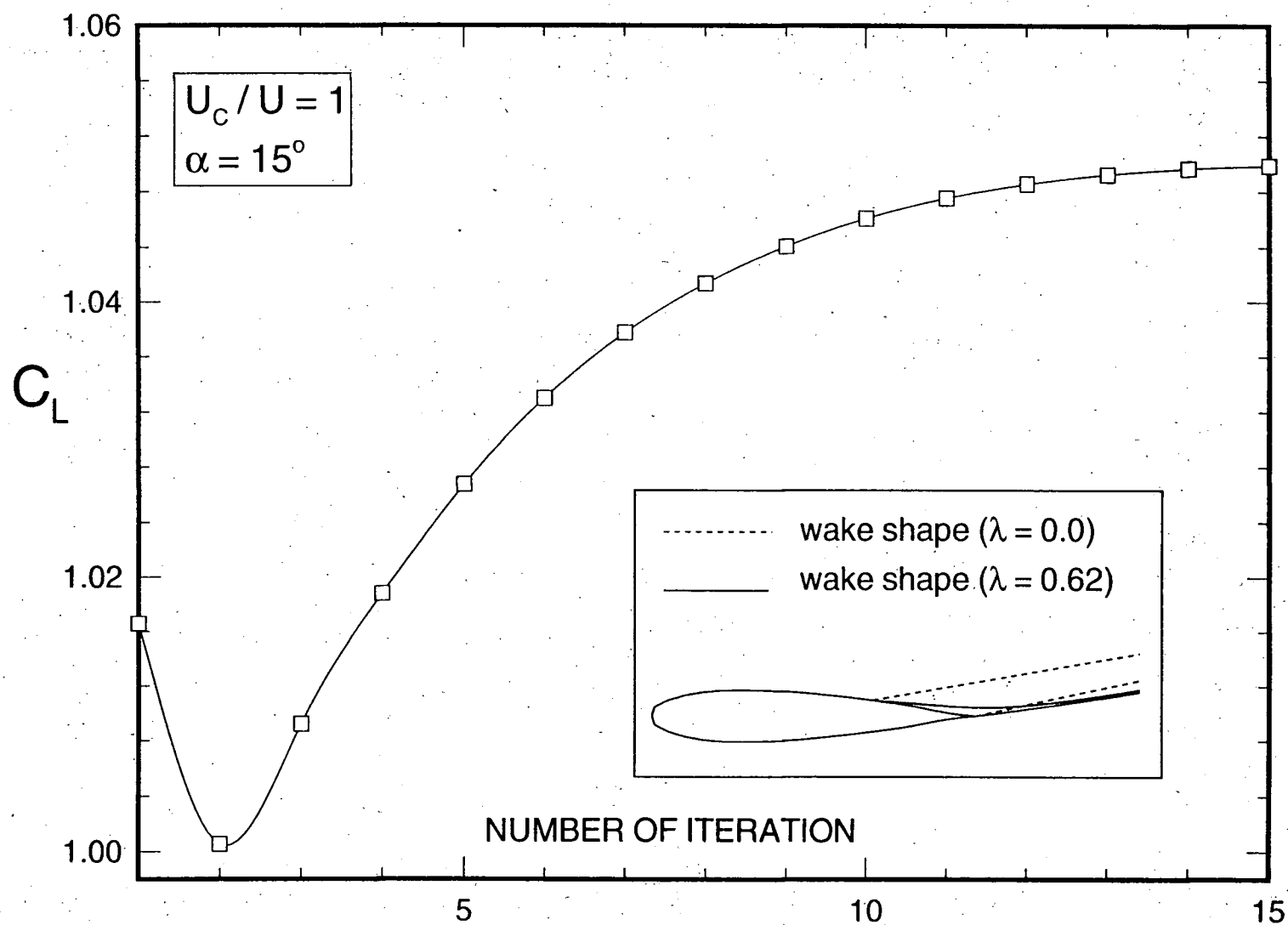
Figure 3-14 Iteration characteristic and convergence of the wake shape for a flow past the Joukowski aerofoil in presence of the MSBC. The results were obtained using the two element separated flow numerical model.
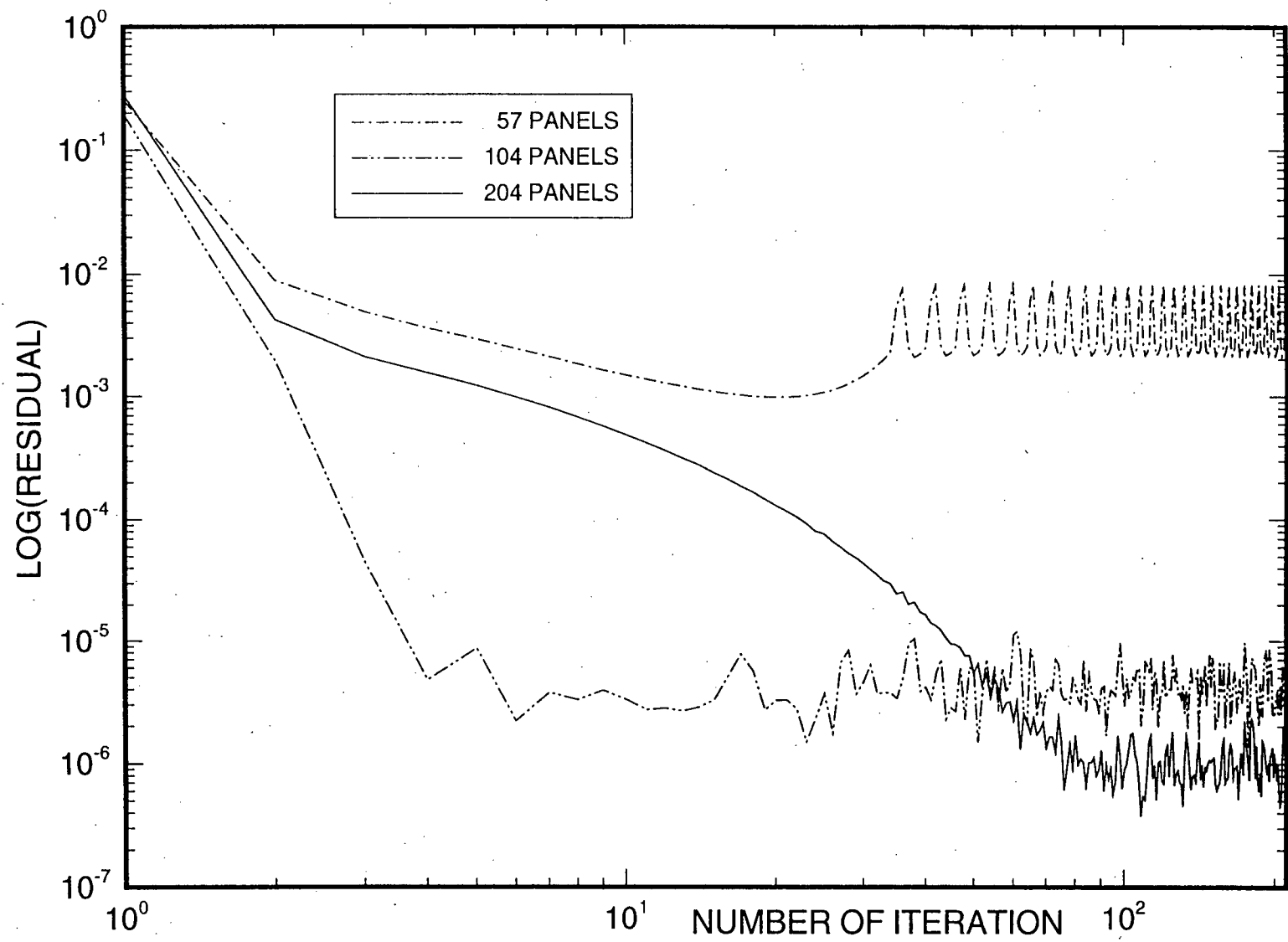
Figure 3-15   Effect of number of panels on the convergence accuracy of the numerical scheme.

3.4 Flow Visualization

To get better appreciation as to the physical character of the complex flow field as affected by the angle of attack and momentum injection parameters, extensive flow visualization study was undertaken. It also gave useful information about relative importance of the various system parameters and hence assisted in planning of the experiments as well as the numerical analysis.

The study showed, rather dramatically, effectiveness of this form of boundary-layer control (Figure 3-16). For the leading edge smooth cylinder at $\alpha = 15°$ (Re = 29,400) and in absence of the cylinder rotation, a well-defined early separation, almost at the leading edge, results in a wide wake with large-scale vortices sweeping away downstream (Figure 3-16a). As the momentum injection is increased to $U_C/U = 1$, there is flow reattachment of the separated shear-layer at about $X/C \approx 0.6$ forming a large bubble with recirculating flow. However, the momentum injection is not sufficient to keep the flow attached and the flow separates again rather quickly, forming a well organized wake. Compared to the case of $U_C/U = 0$, the streamlines move closer on the upper surface of the airfoil, diminishing the wake width considerably ($\approx 0.48C$). At $U_C/U = 2$, the streamlines are very close to the upper surface and the wake is quite small ($\approx 0.3C$). The separation bubble has disappeared completely. Note the presence of a stagnation point near the leading edge on the bottom surface of the airfoil. The separation point is further pushed towards the trailing edge. At $U_C/U = 4$, an essentially attached flow is established over most of the upper surface of the airfoil, even at such a high angle of attack, considerably beyond the nominal stall angle of around 10°. Similar trends persists even at $\alpha = 45°$ (Figure 3-16b).

The flow pattern in the wake of the airfoil was found to be quite unsteady with the vortex layer separating and forming a bubble on reattachment, the whole structure drifting downstream, diffusing, and regrouping at different scales of vortices. Ultimately the flow sheds large as well as small vortices. This unsteady character of the

107
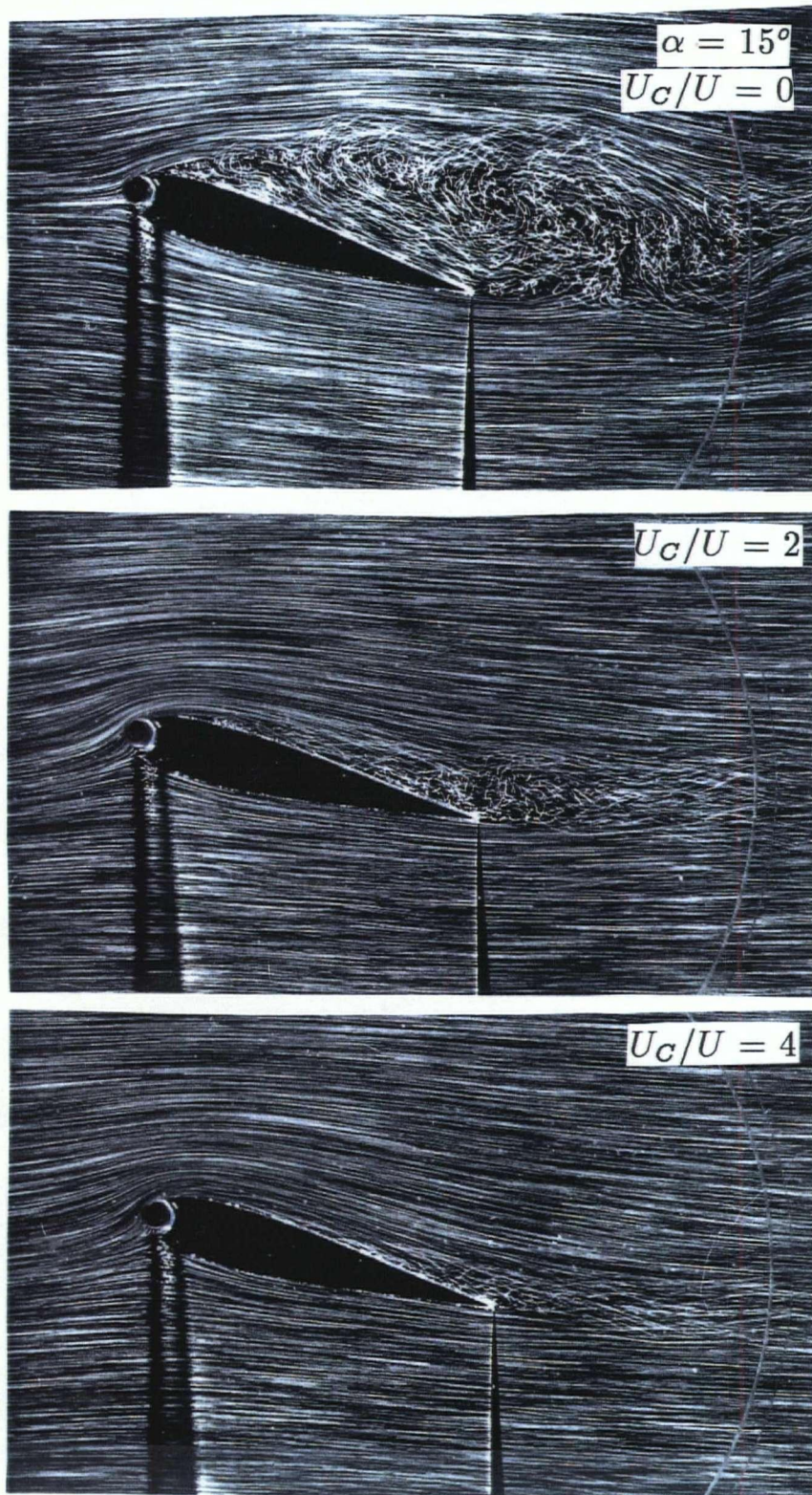
Figure 3-16 Representative flow visualization pictures showing, rather dramatically, effectiveness of the boundary-layer control through momentum injection. The observed results compare well with the delay in separation predicted by the panel code: (a) $\alpha = 15°$.
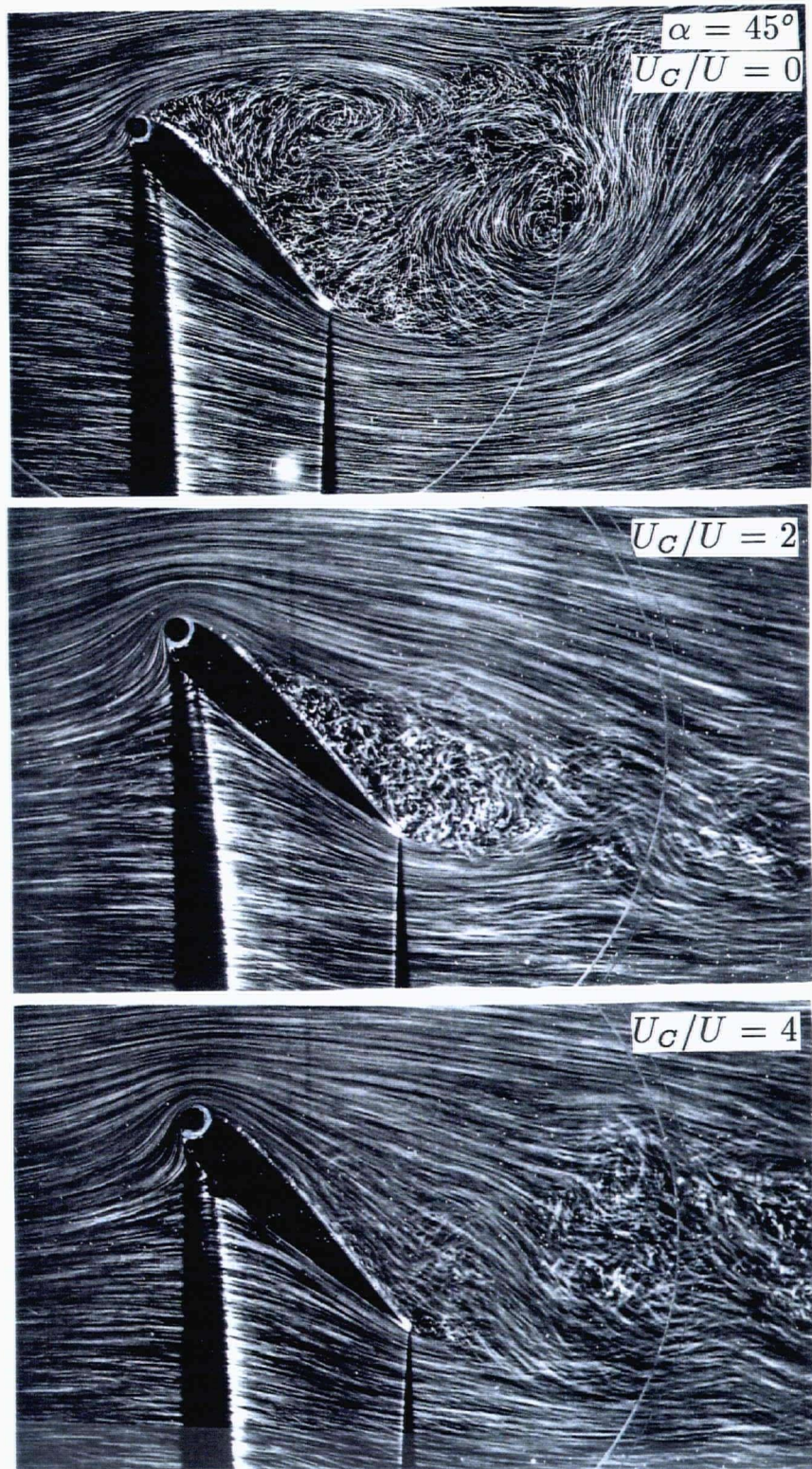
Figure 3-16(cont.) Representative flow visualization pictures showing, rather dramatically, effectiveness of the boundary-layer control through momentum injection. The observed results compare well with the delay in separation predicted by the panel code: (b) $\alpha = 45^o$.

109

separating shear layer and the wake is clearly evident in the flow visualization video. Thus the flow character indicated by the experimentally obtained time-averaged plots appear to be a fair description of the process.

3.5 Summary

Based on the wind tunnel, numerical and flow visualization results it can be concluded that significant improvement in the lift coefficient as well as delay in the stall angle could be achieved by judiciously selecting the rate of the momentum injection, and the cylinder surface geometry. Among the three different surface roughness conditions studied, the cylinder with axial splines was found to be the most effective. In presence of the MSBC the stall becomes gradual and could be delayed to $50°$. The numerical scheme provides good approximation of the actual fluid dynamics of the MSBC as applied to an airfoil at high angles of attack. The flow visualization results dramatically confirm the effectiveness of the MSBC in delaying separation.

4. FLOW PAST A D-SECTION WITH MOMENTUM INJECTION

4.1 Preliminary Remarks

Over the years, considerable attention has been directed towards the aerodynamics and dynamics of circular cylinders and rectangular prisms. On the other hand, the D-section has received, relatively, less attention. This is surprising because it does exhibit behaviour of importance to design engineers. The D-section has a frontal flat face and a semicircular afterbody. An interesting toy known as "Lanchesters's aerial tourbillion" [148] has a D-shaped cross-section and exhibits autorotation [145]. The D-section is susceptible to both the vortex resonance and galloping instabilities. Being a hard oscillator due to nonlinear character of the system, the D-section would not gallop from rest, but requires an initial threshold disturbance at a given freestream speed, to execute transverse vibrations. Dynamics of ice-covered transmission lines exposed to wind has been studied by employing the D-section as the likely model [149, 150]. In fact, Prince hotel in Otsu, Japan, around 135 m tall, has a cross-section of a D-geometry (Figure 4-1).

With this as background, the present study focuses on:

(i)   Wind tunnel tests with a two-dimensional model of the D-section to assess its aerodynamics as affected by the angle of attack and momentum injection. Results show the MSBC to be effective in delaying the boundary-layer separation resulting in a significant reduction in the drag, a desirable feature from the structural design consideration. It also proves to be quite successful in suppressing the vortex shedding even with a small amount of momentum injection.

(ii)   Numerical simulation of the fluid dynamics of the D-section, in presence of momentum injection, using an extension of the vortex panel method. Results

111

琵琶湖畔に美しい半円形のフォルム。
超高層38階、大津プリンスホテル。

万葉の時代より幾多の歌人、旅人のロマンをかきたててきた湖都、大津。その大津のシンボルともいえる琵琶湖のほとりに、風景と調和してたたずむ超高層38階の大津プリンスホテル。設計は、赤坂プリンスホテル新館を手がけた建築家、丹下健三氏。540の客室はすべて琵琶湖に面し、四季折々の表情をみせる湖面を眺めながらゆったりとご滞在いただけます。また、京都駅へJR線で20分、京都の観光拠点としても絶好のホテルです。バラエティー豊かな6つのレストラン、1,200㎡をこえる主宴会場「プリンスホール」をはじめ、ご婚礼や各種宴会に幅広くご利用いただけます。

ホテル

新宴会場
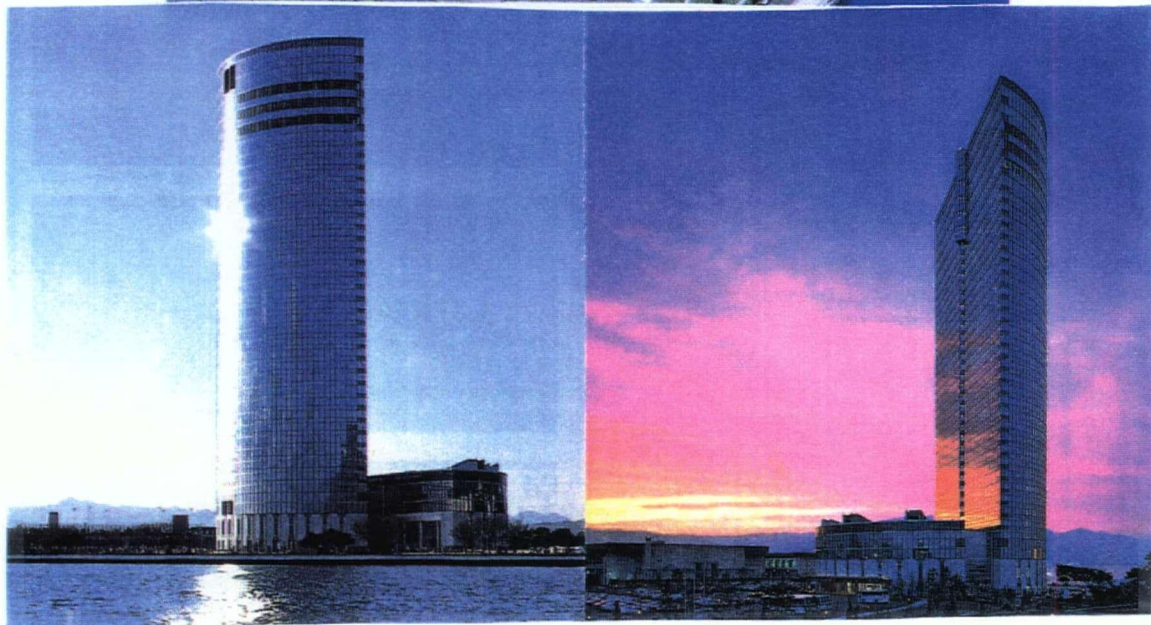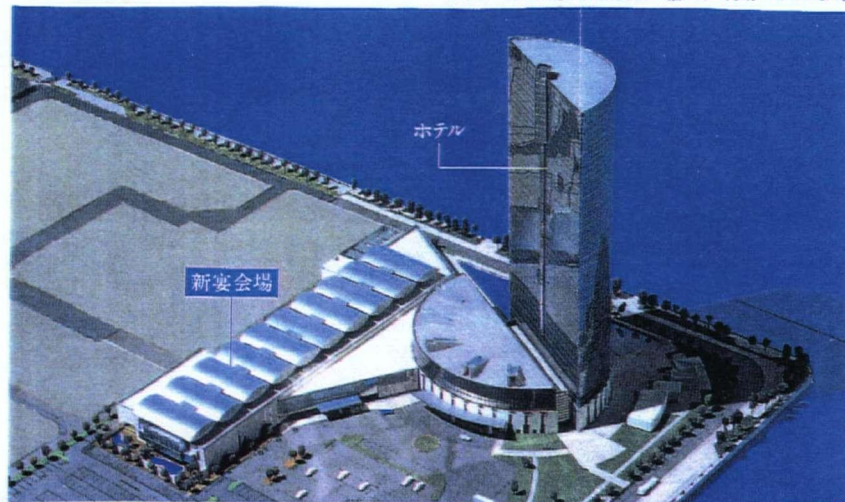
Figure 4-1 The 38 storey Prince Hotel in Otsu, Japan; height 137 m.

compare well with the experimental data promising considerable saving in time, effort and cost associated with wind tunnel tests.

(iii)   Extensive flow visualization study in a closed circuit water channel using slit lighting in conjunction with polyvinyl chloride tracer particles. It shows, rather dramatically, effectiveness of the MSBC as applied to the D-section.

4.2   Wind Tunnel Investigation

Here results are presented for a D-section with smooth rotating cylinders, which also serve as the benchmark case for comparison with the numerical data.

4.2.1   Pressure distribution

Experimentally obtained pressure distribution around the D-section is presented for a complete range of angle of attack (0-180°) in Figure 4-2. Experiments were carried out for the rate of momentum injection ranging from $U_C/U = 0$ to 4 in steps of one unit, however, for clarity, results are presented for $U_C/U = 0$, 2 and 4.

At $\alpha = 0$, the pressure distribution is symmetrical about the stagnation point as expected. The stagnation point is located midway on the front flat face of the D-section. The D-section has rounded corners due to the presence of rotating cylinders. The pressure starts decreasing gradually as the flow approaches the corners and finally it separates near the rotating cylinders in absence of momentum injection ($U_C/U = 0$). The semicircular afterbody lies completely in the wake with a negative pressure coefficient, which is constant everywhere on the afterbody. This indicates presence of a large wake, which is responsible for a higher drag ($C_D = 1.3$) experienced by the D-section. As the momentum injection is increased ($U_C/U = 0 \rightarrow 4$) the pressure distribution is altered substantially. The rotating cylinders have a small effect on the upstream flow, except that the fluid is accelerated towards the rotating cylinder resulting in a slightly lower pressure. As seen from the pressure plot for $\alpha = 0$, large
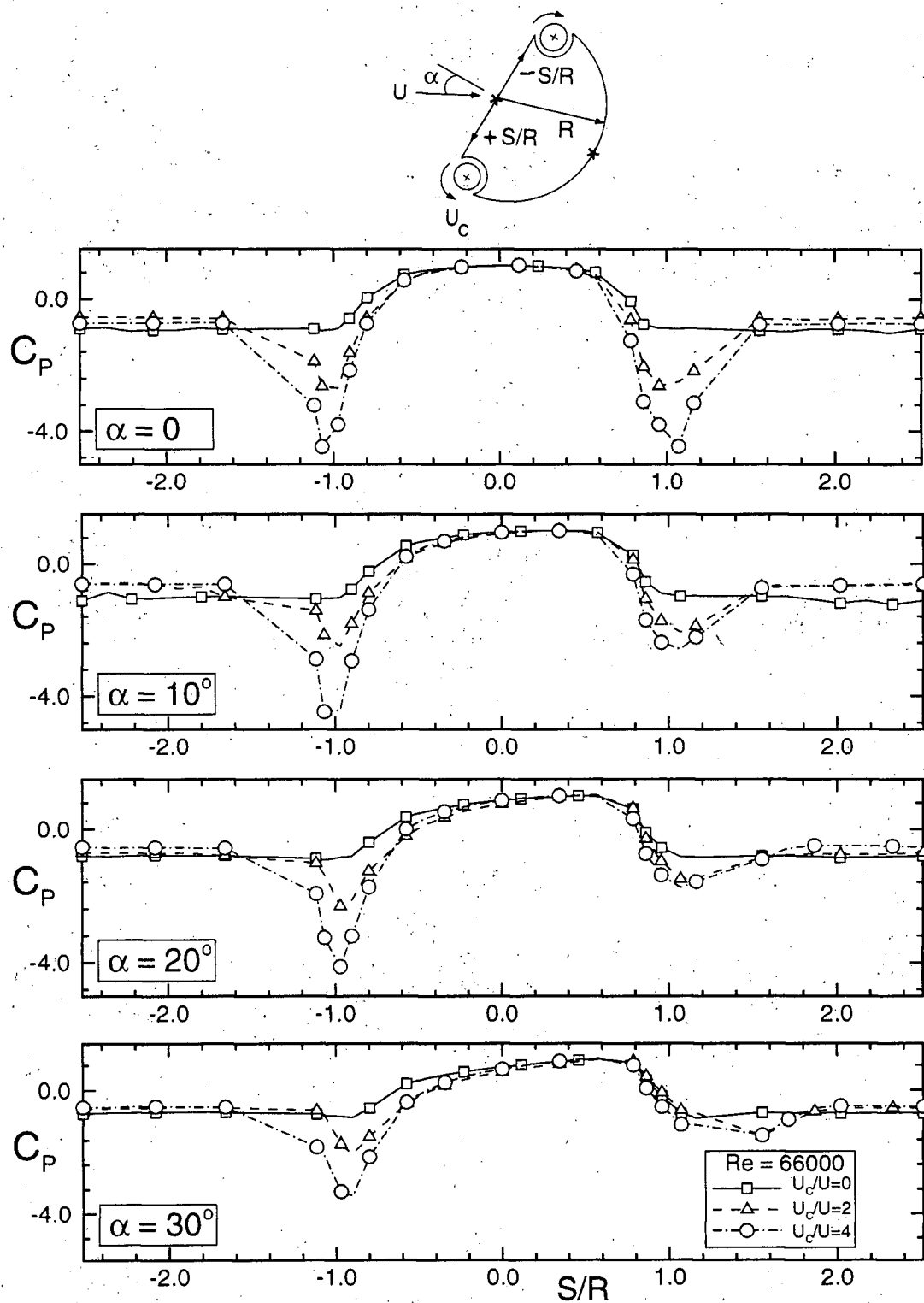
Figure 4-2   Surface pressure plots for the D-section showing effects of the angle of attack and momentum injection ($\alpha = 0$–$30°$).
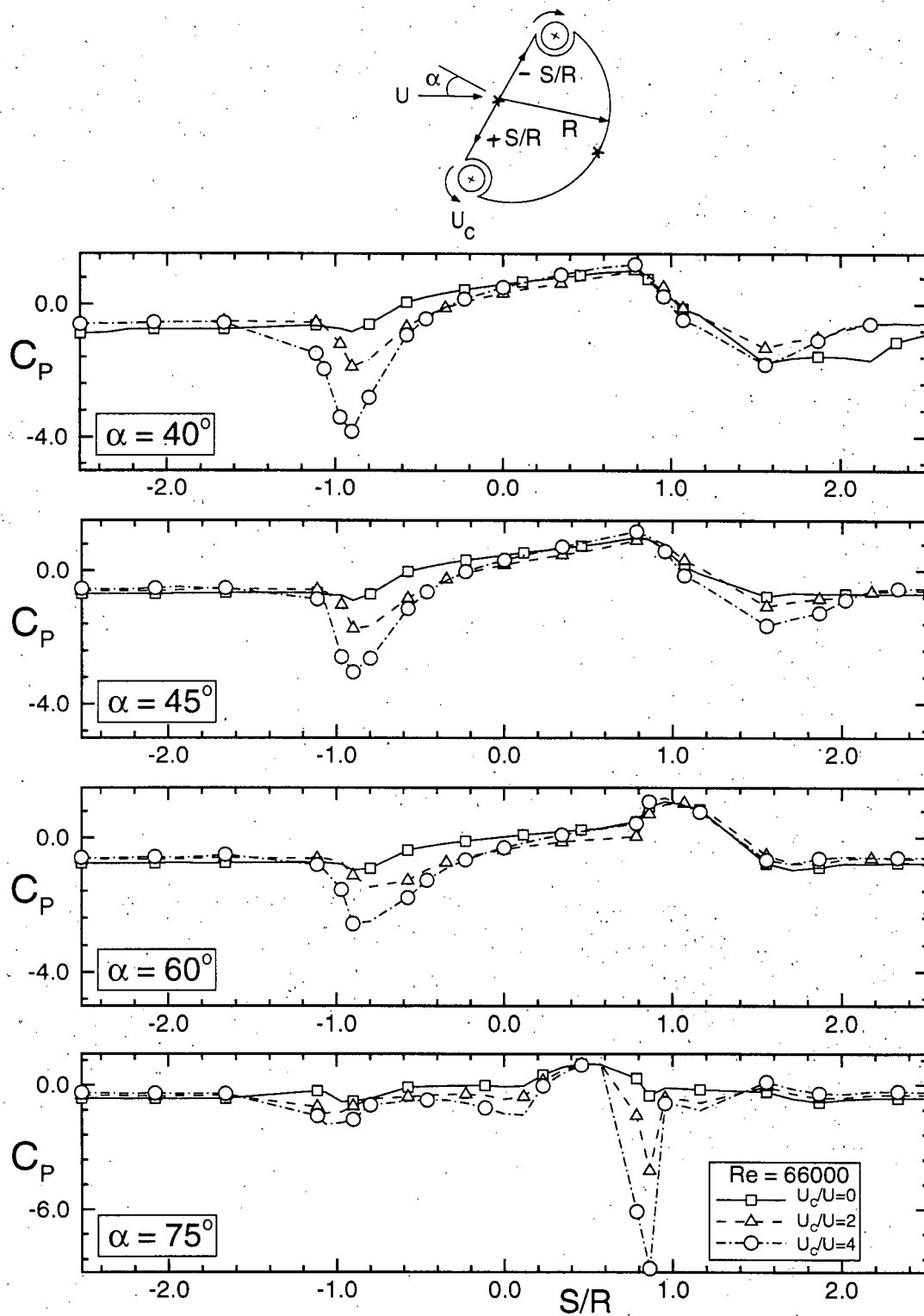
Figure 4-2(cont.) Surface pressure plots for the D-section showing effects of the angle of attack and momentum injection ($\alpha = 40^\circ$–75°).
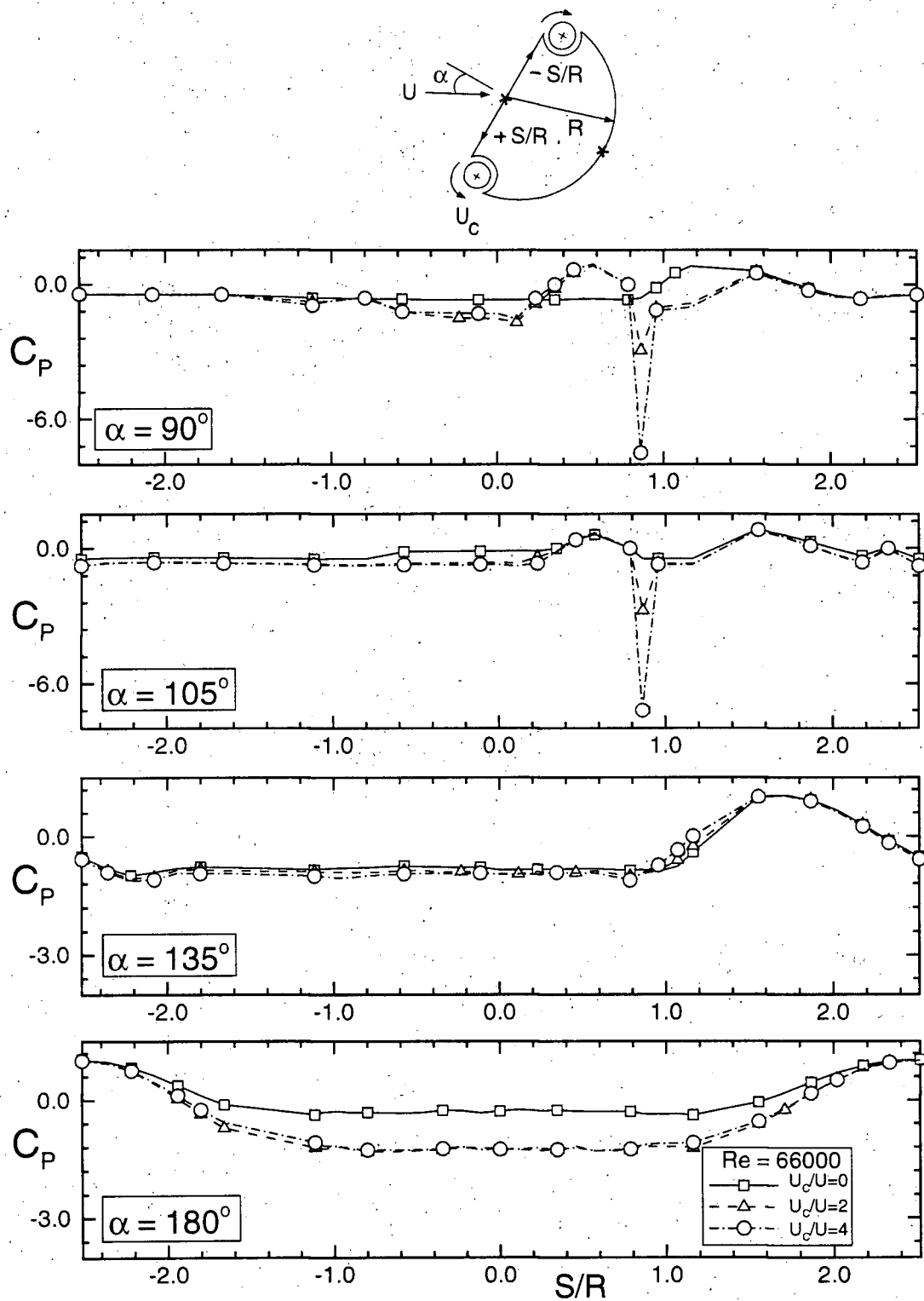
115

Figure 4-2(cont.) Surface pressure plots for the D-section showing effects of the angle of attack and momentum injection ($\alpha = 90°-180°$).

suction peaks appear on the surface of the rotating cylinders. The strength of the suction peak grows with an increase in the rate of momentum injection. A part of the suction peak is located towards the front of the D-section, which also contributes to the drag reduction. The injection of momentum also results in a higher wake, pressure, i.e. the pressure at the base of the afterbody lying in the wake. In absence of momentum injection, the wake pressure coefficient $C_{PB} \approx -0.90$, whereas at U_C/U =4, $C_{PB} \approx -0.74$, i.e. a rise of about 22%, which is significant.

As the angle of attack is increased from zero, the symmetry in the pressure distribution is disturbed. The stagnation point no longer remains at the center of the front face. It gradually shifts towards the rotating cylinder facing upstream. The asymmetry in the flow field results in an adjustment of pressure distribution over the whole body including the wake. As a result, the suction peaks on the rotating cylinders are no longer of equal strength. The upstream suction peak is diminished while the downstream suction peak remains almost unaffected at low angles of attack ($\alpha < 30^{\circ}$). Thus the movement of the stagnation point has important consequences on the overall pressure distribution. At $\alpha = 40^{\circ}$, the stagnation point has moved close to the upstream corner, merging with the original location of the suction peak. Note, now the suction peak is no longer visible on the upstream rotating cylinder, even at the highest rate of momentum injection used during the experiment ($U_C/U = 4$). But the wake pressure still shows a positive increase in presence of the momentum injection. The suction peak on the downstream rotating cylinder progressively diminishes. An increase in α upto 60° produces no further changes in the overall pressure distribution. For $75^{\circ} \leq \alpha \leq 105^{\circ}$, a large suction peak reappears at the upstream rotating cylinder due to local acceleration of the flow. The rest of the body lies completely in the wake on either side of the stagnation point. At $\alpha = 90^{\circ}$, there is no rise in the wake pressure with momentum injection. In fact, at $\alpha = 105^{\circ}$, the wake pressure becomes more negative due to adverse effect of upstream cylinder rotation, and the resulting

drag is higher. This indicates that for $\alpha > 90°$, the direction of upstream cylinder rotation needs to be reversed.

At $\alpha = 180°$ the semicircular afterbody of the D-section faces upstream and the flat face turns towards the downstream direction. This situation is of some interest, since at $\alpha = 180°$, the D-section has no afterbody lying in the wake. The rotating cylinders are now located at the trailing edges as against at the leading edge. Note, the front portion of the D-section behaves like a circular cylinder. The original scheme of cylinder rotation is obviously detrimental and a large decrease in the wake pressure coupled with a very high drag (160% increase) is observed.

As seen earlier, $\alpha = 90°$ represents a special case. The flat face is now aligned with the flow. The upstream rotating cylinder encounters the flow first. By examining the schematic of the D-section (Figure 4-3), it is apparent that the upstream cylinder should be rotated clockwise so as not to oppose the incoming flow. It was decided to assess the effect of both clockwise and counter-clockwise rotation of the upstream cylinder. In addition, a third case involving reversal in the direction of the downstream cylinder was also studied. The results are presented in Figure 4-3. The reversal in the downstream cylinder rotation has virtually no effect since it already operates in a separated flow environment (upstream cylinder rotation counter-clockwise). The other two cases had little effect on the overall pressure distribution, though a small drag reduction was achieved for both the cases. Thus, for $\alpha = 90°$, the results suggest that the D-section has essentially reached the minimum drag value and the injection of momentum has little effect on further reduction of C_D.

4.2.2 Wake pressure and vortex shedding

The fluid in the wake is separated from the main flow by a thin layer of vorticity which originate on the body and detaches at the separation points. These surfaces of discontinuity represent a jump in the velocity and could be idealized as "free vortex lines" in two-dimensions. In reality, the demarcation between the wake and the outer
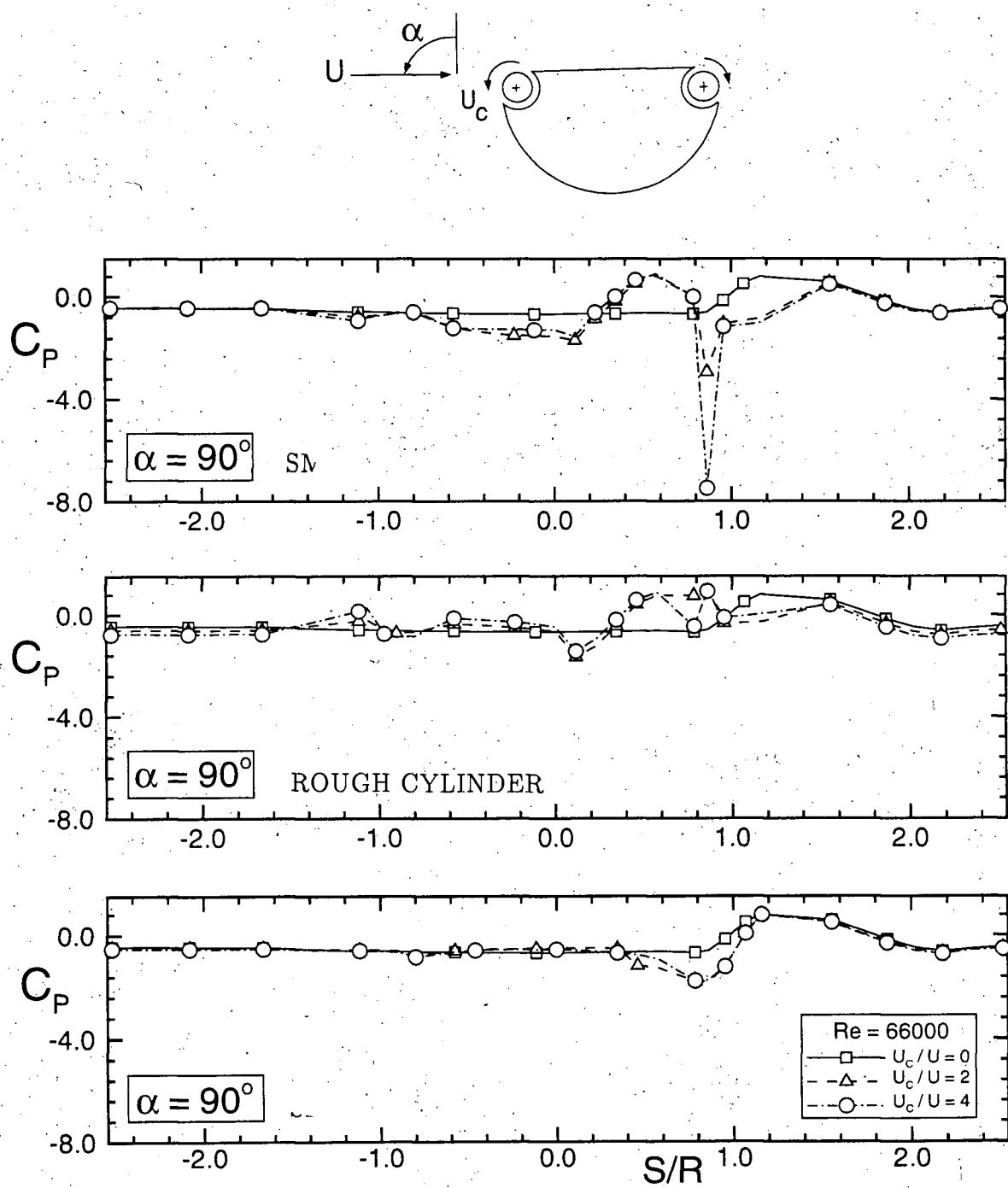
Figure 4-3   Effect of three different modes of momentum injection on the surface pressure distribution at $\alpha = 90°$.

119

potential flow is not so sharp as the viscosity and turbulence smear this boundary. The mean freestream velocity at separation (U_B) can be approximated as [16]

$$U_B{}^2 = U^2(1 - C_{PB}),\qquad(4.1)$$

where C_{PB} = base pressure in the wake and U = free stream velocity. Thus the two shear layers, carrying opposite sign of vorticity, are responsible for vortex shedding. The presence of a bluff body merely modifies the process by allowing a feedback mechanism between the wake and the shedding of circulation at the separation points [16].

The rate at which the circulation (Γ) is shedded at the separation points can be approximated as [16]

$$\frac{d\Gamma}{dt} = \frac{U_B^2}{2}.\qquad(4.2)$$

It is also known that vortex formation involves mixing of flows of oppositely signed vorticity [96]. The strengths of individual wake vortices will be less than the total circulation shed from one side of a bluff body during a shedding cycle. Hence the fraction of the original circulation that survives vortex formation is [16]

$$\delta = \frac{2St\Gamma_V}{UD}(1 - C_{PB})^{-1},\qquad(4.3)$$

where St = Strouhal number, Γ_V = strength of a wake vortex, and D = characteristic dimension of the body.

The value of δ has been determined mostly through experiment and range from 0.2 to 0.6 for different bluff body shapes [6, 16, 151-153]. Even for a given bluff shape, value of δ is not consistent [16]. The set of equations (4.1) to (4.3) emphasize the strong link that exists between the vortex shedding and base pressure in the wake. A higher base pressure, in general, would correspond to a lower rate of shedding. This fact could be inferred qualitatively from the present experiments with momentum injection. Though no quantitative estimates were sought, it was obvious

that momentum injection disrupts the vortex shedding process and, at a sufficiently high rate, it completely suppresses it.

Variation of the base pressure as affected by the angle of attack and momentum injection is shown in Figure 4-4. Upto $\alpha = 105°$, pressure tap A (as shown in the schematic of the D-section) was found to lie in the wake. For $\alpha = 135°$ and $180°$, pressure tap B was used for the purpose. The results show that the base pressure is much lower than the freestream value ($C_{PB} < 0$), and increases significantly due to momentum injection. On average, almost 30% rise in the base pressure was achieved for $0 < \alpha < 90°$. At $\alpha = 90°$, the rise in base pressure was about 8%. For $\alpha > 90°$, the wake pressure reduces, indicating a need for the reversal in the direction of rotation of the upstream cylinder. For $\alpha \geq 135°$, it becomes necessary to reverse the direction of both the rotating cylinders (i.e. inward mode of rotation). This raises the wake pressure by $10 - 25$ %.

In Figure 4-4(b), variation in the Strouhal number is plotted against the angle of attack. The Strouhal number remains essentially unchanged except in the range $60° \leq \alpha \leq 105°$, with a peak at $\alpha = 90°$. The flat face of the D-section is now aligned with the flow thus making the body relatively streamlined and causing a jump in the vortex shedding frequency. As the momentum injection is increased from $U_C/U = 0 - 4$, a dramatic change occurs in the wake. At a low rate of momentum injection ($U_C/U \approx 1$), the vortex shedding process was extremely weak and hence no clear frequency could be identified through spectral analysis of pressure signal from the surface of the body. Even a disk probe (Section 2.2.3) in conjunction with an extremely sensitive Barocel pressure transducer (resolution 10^{-6} lb/in^2, 6.9×10^{-5} N/M^2) as well as a hot wire anemometer system (DISA Elektronik, Denmark), both traversing the wake to identify discernible signals, failed to detect a coherent vortex shedding frequency. Perhaps the small amount of vorticity shed was quickly dissipated in the turbulent wake (Re $\approx$ 66,000). Of course, with the momentum
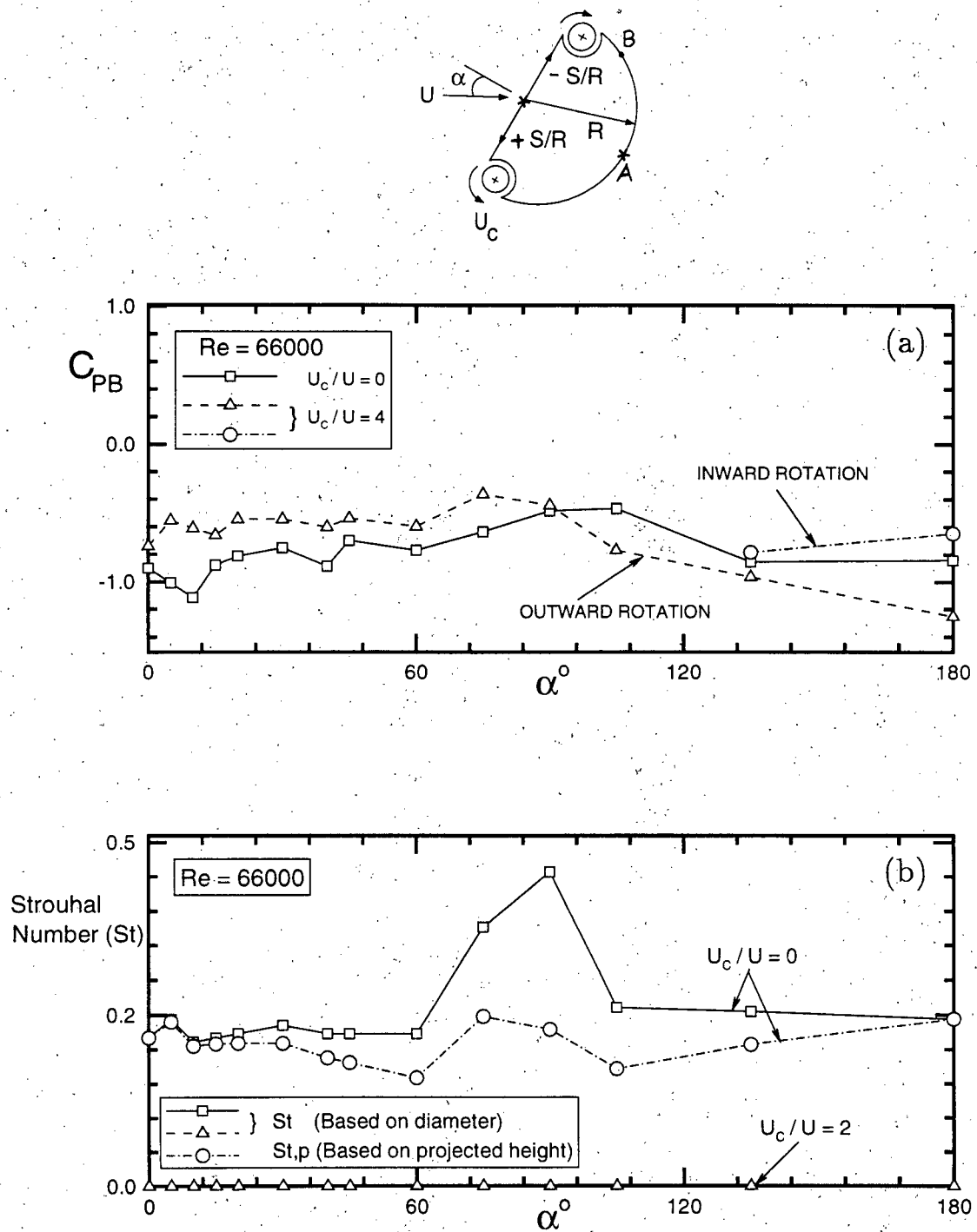
Figure 4-4   Wake pressure and the Strouhal number for the D-section as affected
             by the momentum injection.

injection, the shed vorticity diminishes in strength, and for $U_C/U \geq 2$ it was virtually eliminated with the Strouhal number designated as zero (Figure 4-4). The changes in the wake brought about by momentum injection can be better appreciated through flow visualization photographs, which are presented later in this chapter.

The elimination of vortex shedding is also indicated by a higher base pressure in the wake. An increase in the base pressure can be attributed to a smaller width of the wake and a lower drag coefficient. The rise in the base pressure is similar to that obtained when a splitter plate of appropriate length is placed behind a circular cylinder at a suitable location [151]. The momentum injection is responsible for delaying and even suppressing the boundary-layer separation.

4.2.3 Aerodynamic coefficients

Variations in the drag and lift coefficients with the angle of attack are shown in Figure 4-5. The net drag reduction is summarized in Table 4.1. The drag reduction ($\%\Delta C_D$) is defined as

$$\%\Delta C_D = \frac{C_{D(U_C/U=0)} - C_{D(U_C/U=4)}}{C_{D(U_C/U=0)}} \times 100. \qquad (4.4)$$

The direction of rotation is kept fixed as at $\alpha = 0$ throughout.

Table 4.1   Drag reduction with momentum injection for various α

α^o	$C_D(U_C/U = 0)$	$\%\Delta C_D\ (U_C/U = 4)$
0	1.293	42
30	0.997	19
45	0.806	22
60	0.583	29
90	0.209	75
105	0.306	-13
180	0.130	-158

The drag coefficient reduces with the angle of attack and reaches a minimum at $\alpha = 90^o$. In presence of momentum injection the drag coefficient is lowered considerably. The drag reduction continues for $0 \leq \alpha \leq 105^o$. Beyond $\alpha \geq 105^o$, the

need for reversal in the direction of cylinder rotation is clearly indicated. Note, the minimum drag coefficient at $\alpha = 90^\circ$ is also coupled with the highest vortex shedding frequency (Figure 4-4). The decrease in drag by as much as 75% ($\alpha = 90^\circ$) is indeed impressive.

The absolute change in the lift coefficient by itself is of little significance for a bluff body like a D-section, but the rate of change of lift coefficient, $dC_L/d\alpha$, is quite important in determining the susceptibility to flow-induced vibrations. A negative $dC_L/d\alpha$ indicates a likelyhood for galloping instability at low angles of attack [154]. Figure 4-5 clearly shows $dC_L/d\alpha < 0$ at $U_C/U = 0$, but becomes positive for $U_C/U \geq 2$ indicating that the stability is restored. This results are discussed in more detail in Chapter 6 in connection with dynamic experiments.

At $\alpha = 0$ and 180°, the D-section is symmetric with respect to the flow direction and the lift coefficient is zero. In the range $\alpha = 40^\circ - 45^\circ$, the lift coefficient is negative but large in value ($C_L \approx -1.0$) in absence of momentum injection. However, with $U_C/U = 4$, the lift coefficient is increased substantially ($C_L \approx -0.55$, i.e. the absolute value is reduced). Thus in general, momentum injection reduces transverse load on the structure. This could be used to advantage in their design.

Figure 4-6 shows effect of various strategies of cylinder rotation on the drag coefficient. As pointed out earlier, for $\alpha \leq 105^\circ$, the outward rotation mode is most effective in reducing the drag. For $\alpha = 135^\circ$, the direction of rotation of the upstream cylinder needs to be reversed (i.e. the downstream rotation mode). For $\alpha \geq 135^\circ$, both the cylinders are affected (i.e. inward rotation mode) to obtain drag reduction. In practice, for a tall building , this can be accomplished quite readily through a microprocessor based switching actuator operating in conjunction with a wind direction transducer.

4.3 Numerical Simulation

A comparison between numerically and experimentally obtained pressure plots,
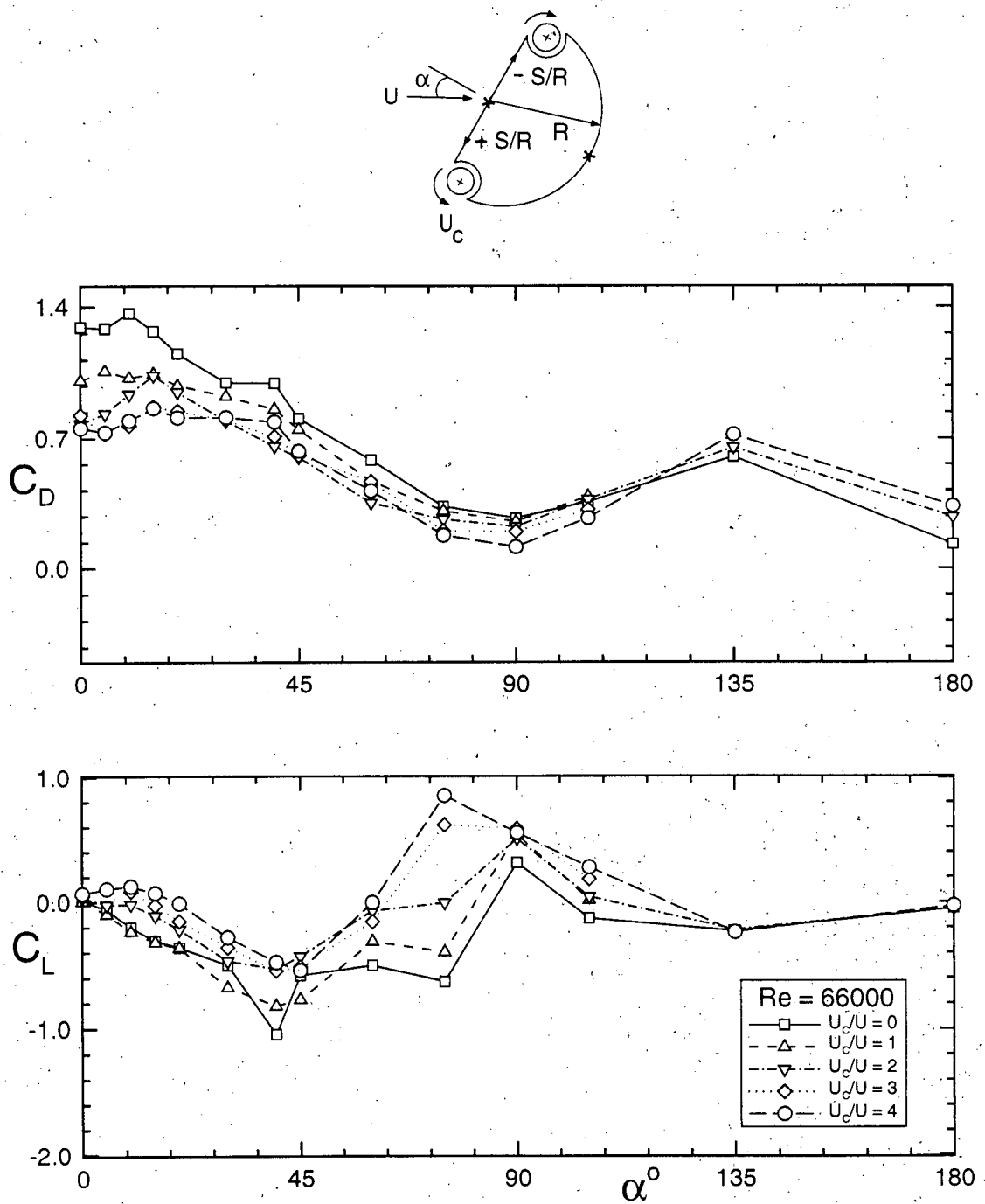
Figure 4-5   Drag and lift characteristics of the D-section as affected by the momentum injection

OUTWARD ROTATION

DOWNSTREAM ROTATION

Re = 66000
$U_c / U = 0$
$\left.\begin{array}{c} \\ \\ \end{array}\right\} U_c / U = 4$

C_D

INWARD
ROTATION

OUTWARD
ROTATION

DOWNSTREAM
ROTATION

α°

INWARD ROTATION
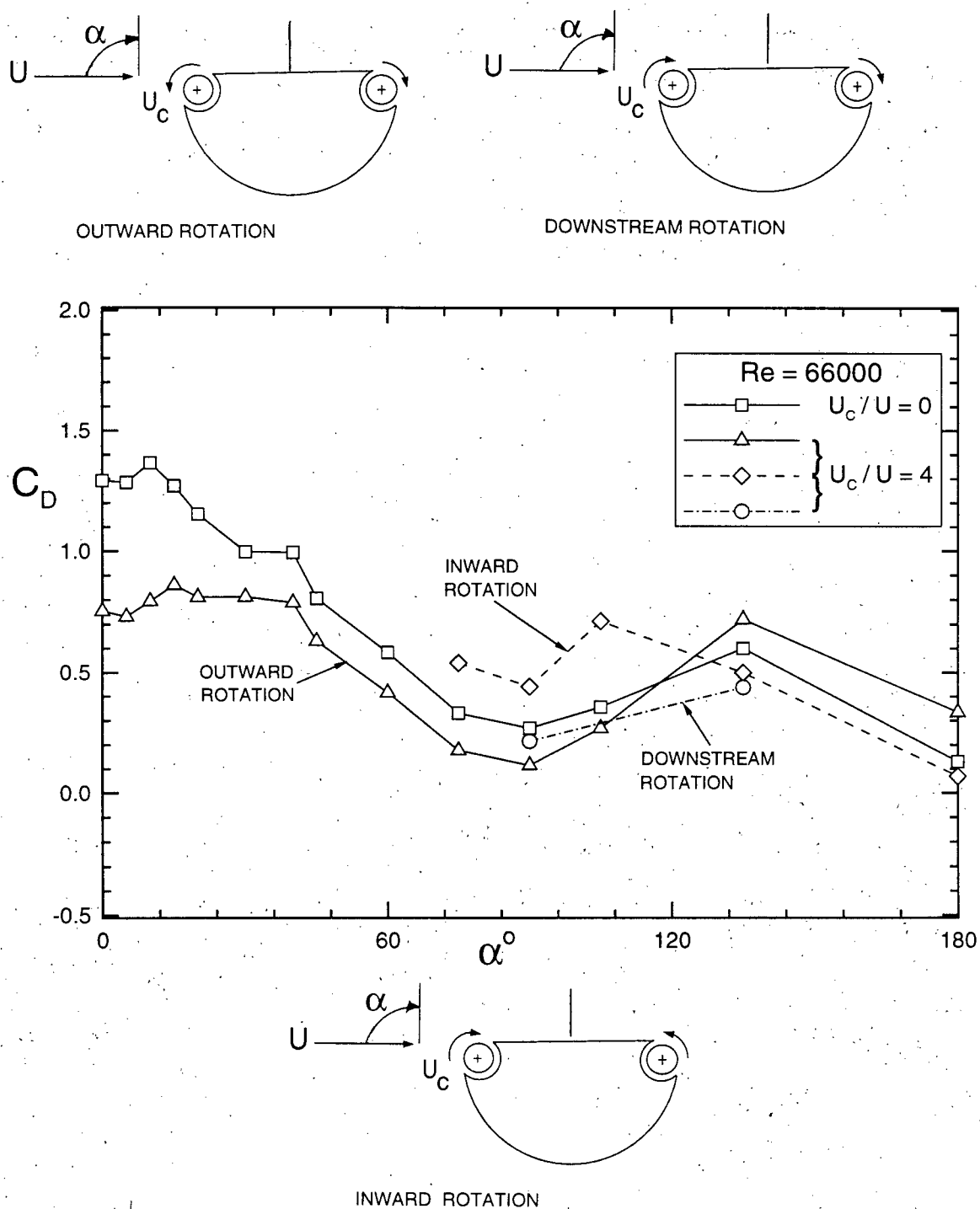
Figure 4-6   The effect of three different modes of momentum injection on the drag coefficient of the D-section as a function of angle of attack.

126

as presented in Figure 4-7, shows good agreement. At $\alpha = 0$, the numerical scheme predicts separation at the corners and a constant pressure wake. It successfully captures the existence of suction peaks, and predicts a rise in the base pressure in presence of momentum injection. For $\alpha > 0$, an asymmetric pressure distribution coupled with the movement of the stagnation point matches with that obtained from the wind tunnel tests. At higher α, the pressure distribution on the upstream face of the D-section agrees more closely with the wind tunnel results, whereas in the wake, the difference between the theory and experiments is relatively higher, though the trend is quite similar. This, of course, is understandable due to potential character of the panel method.

Figure 4-8(a) compares the corresponding drag data. The numerical scheme accurately predicts drag reduction in presence of momentum injection. The comparison was extended upto $\alpha = 40^o$ to assess the limit of applicability of the panel method used here. For $\alpha \geq 30^o$, discrepancy between the theory and the experiment is detected. This suggests that, at high angles of attack, the panel method needs an improved model for the wake. Figure 4-8(b) shows numerically obtained wake geometry at $\alpha = 0$. In absence of momentum injection, a wide wake results. It should be pointed out that only the near wake region (upto $X/R = 10$) is shown here. The actual wake continues for many diameters downstream, with the 'free vortex lines' drawing near each other and eventually closing. A finite wake is obtained due to the dissipation of the vorticity modelled in the panel code. The vorticity dissipation factor determines the wake length and is an empirical input to the program. The value of the base pressure in the wake was found to be a function of the vorticity dissipation factor. As the momentum injection is increased from zero, the "free vortex lines" converge toward each other resulting in a smaller wake width. This feature of the numerically obtained wake shape is in good qualitative agreement with the flow visualization results.
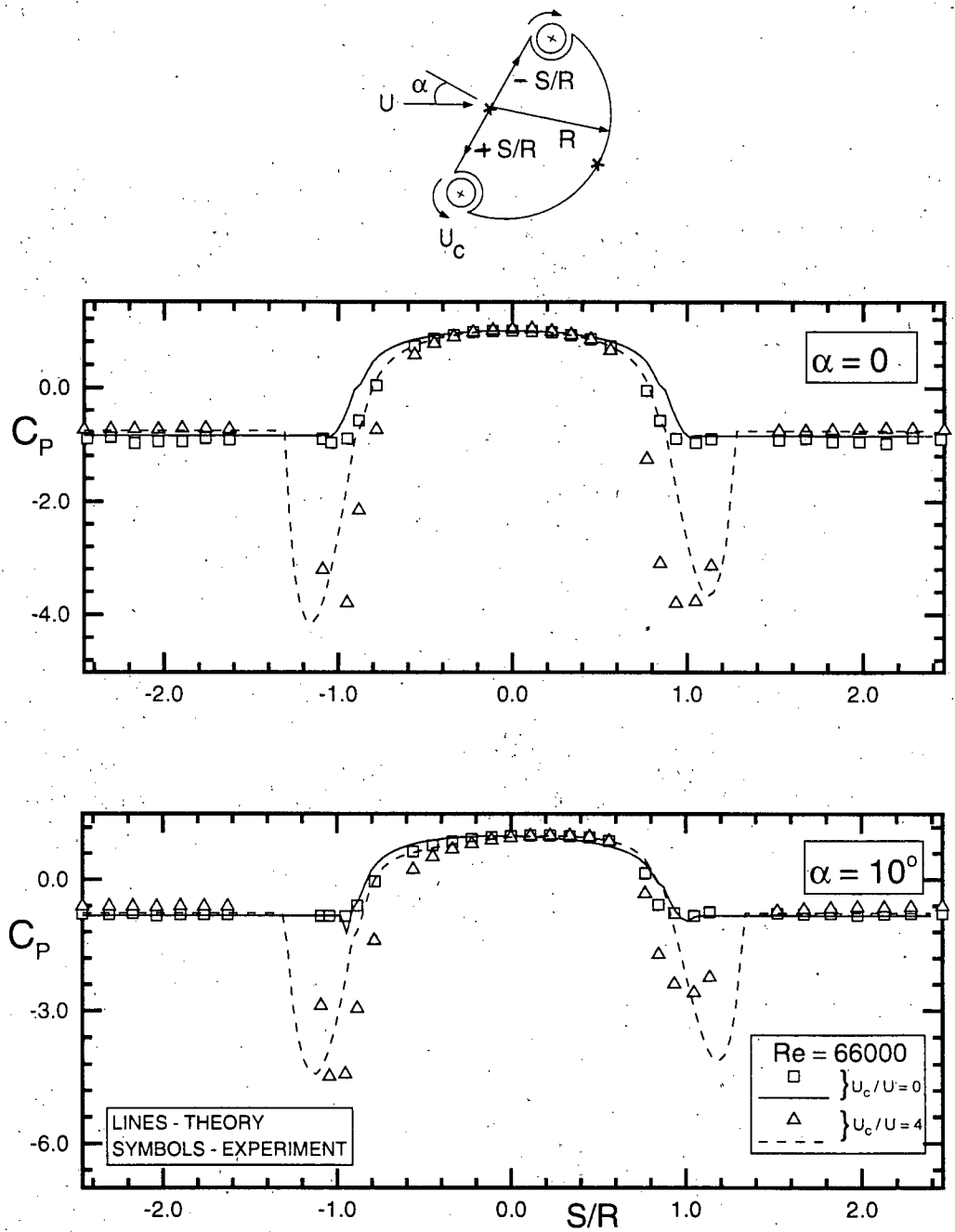
Figure 4-7   Comparison between the numerically and experimentally obtained pressure plots for the D-section. Note, the numerical scheme accurately predicts presence of large suction peaks, as well as rise in the wake pressure in presence of momentum injection ($\alpha = 0, 10°$).
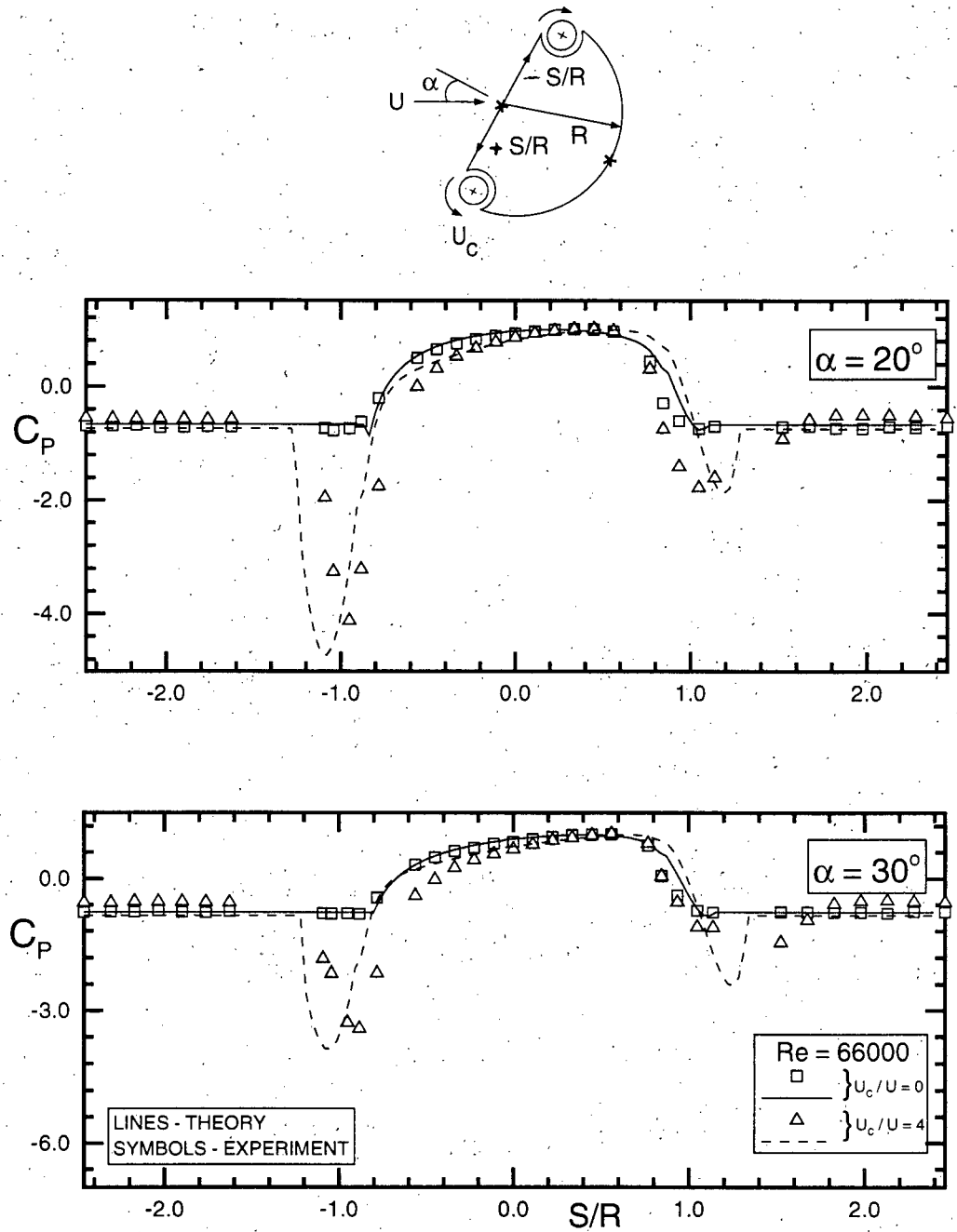
Figure 4-7(cont.) Comparison between the numerically and experimentally obtained pressure plots for the D-section. Note, the numerical scheme accurately predicts presence of large suction peaks, as well as rise in wake pressure in presence of momentum injection ($\alpha = 20°, 30°$).

129
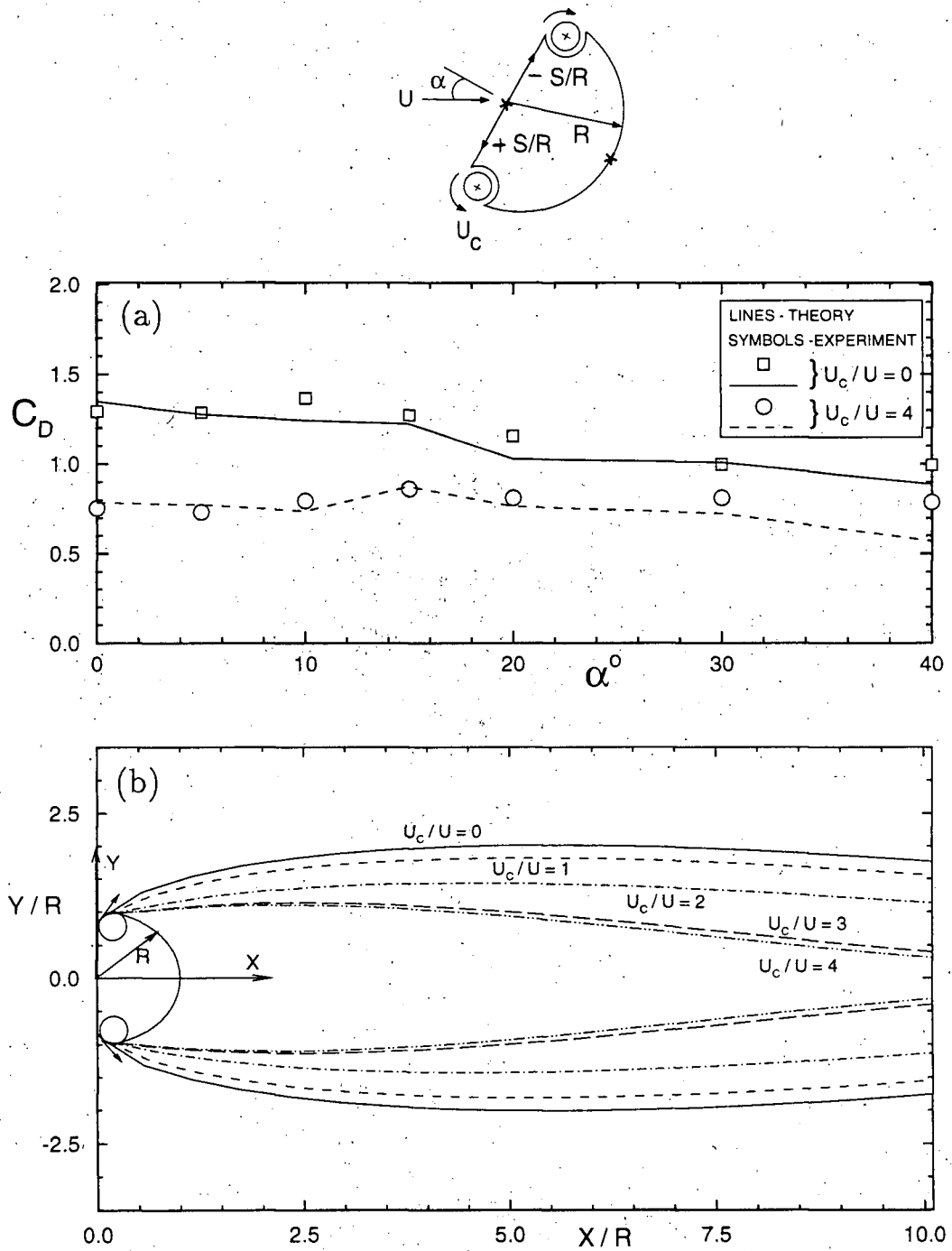
Figure 4-8 Numerical simulation data showing the effect of momentum injection: (a) drag coefficient; (b) wake geometry as represented by the 'free vortex lines'.

Thus even a simple panel code in conjunction with vorticity dissipation gives surprisingly good results, even for such a complex flow phenomena as represented by a bluff body with momentum injection.

4.4   Effect of Surface Condition of a Rotating Cylinder

A change in the surface conditions of the rotating cylinder could result in important benefits in terms of more efficient momentum injection. As described in Chapter 3, a splined rotating cylinder was found most effective in increasing the lift of an airfoil. Hence it was decided to assess the relative performance of cylinders with different surface conditions (smooth, rough and splined).

Figures 4-9 and 4-10 present relative performance of the three different rotating cylinders in terms of the drag and lift coefficients, lift/drag ratio and the base pressure coefficient. In absence of momentum injection ($U_C/U = 0$), the splined and rough rotating cylinder have a higher drag due to wider wake caused by early separation. However, the surface roughness does improve efficiency of the momentum injection process resulting in further decrease in the drag and increase in the base pressure (compared to the smooth cylinder case), particularly for $\alpha \leq 20^o$ (Figure 4-9). On the other hand, so far as the lift is concerned, the cylinder surface roughness has little effect even upto α as large as 30° (Figure 4-10). However, beyond that there are some discernible differences which can be better understood by referring to the pressure distribution plots (Figure 4-11). At $\alpha = 0$, in absence of momentum injection, the base pressure is lower for the rough and splined rotating cylinders, which explains the measured higher drag coefficient. However, with $U_C/U = 4$, the wake pressure rise is more for splined and rough cylinders, and strength of the suction peak is slightly diminished (S/R=1). The resultant effect is the decrease in drag. At $\alpha = 45^o$, the strength of the suction peak at $S/R = -1$ is significantly increased with the momentum injection leading to a higher C_L.
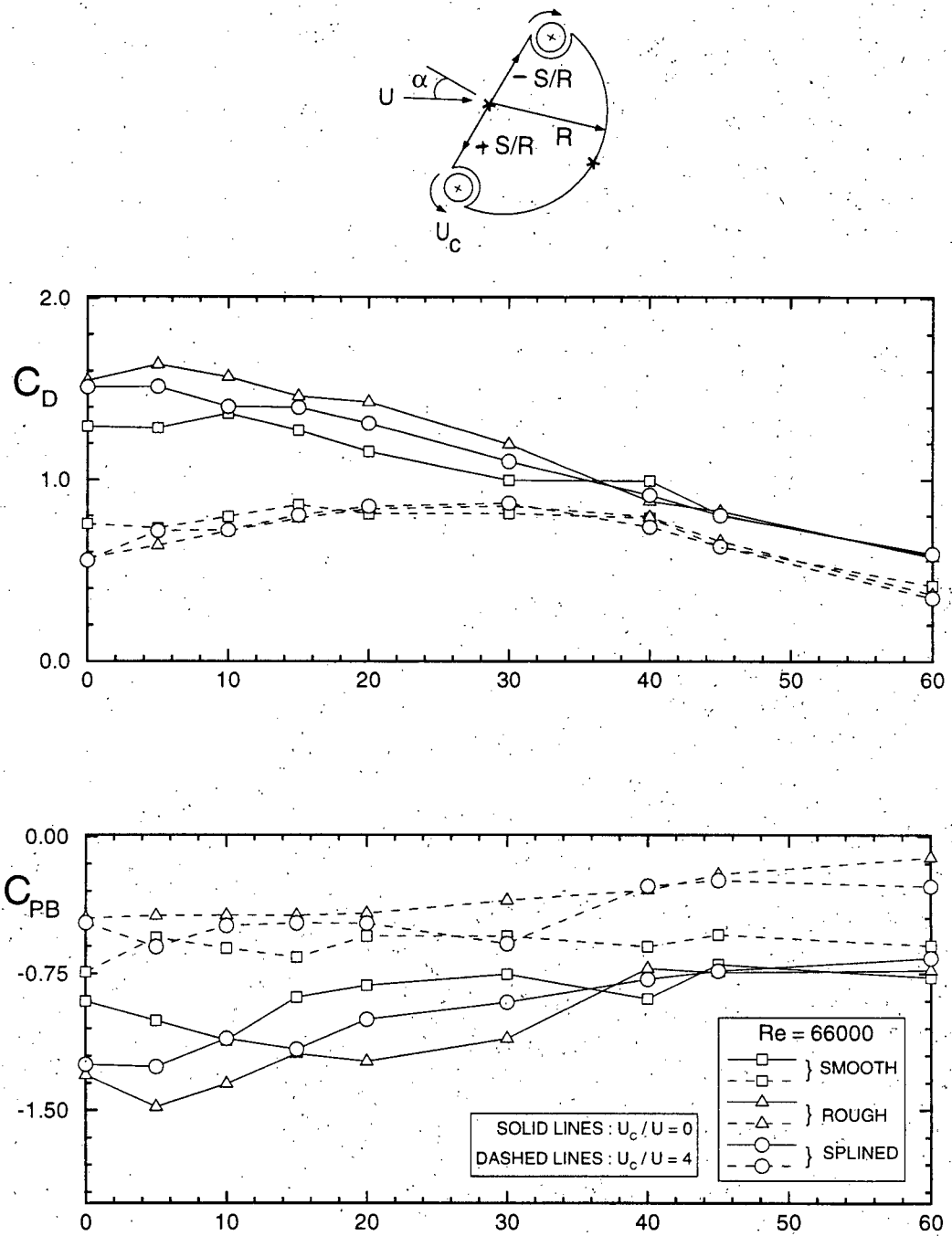
Figure 4-9   Effect of cylinder surface condition on: (a) drag coefficient; (b) wake pressure.
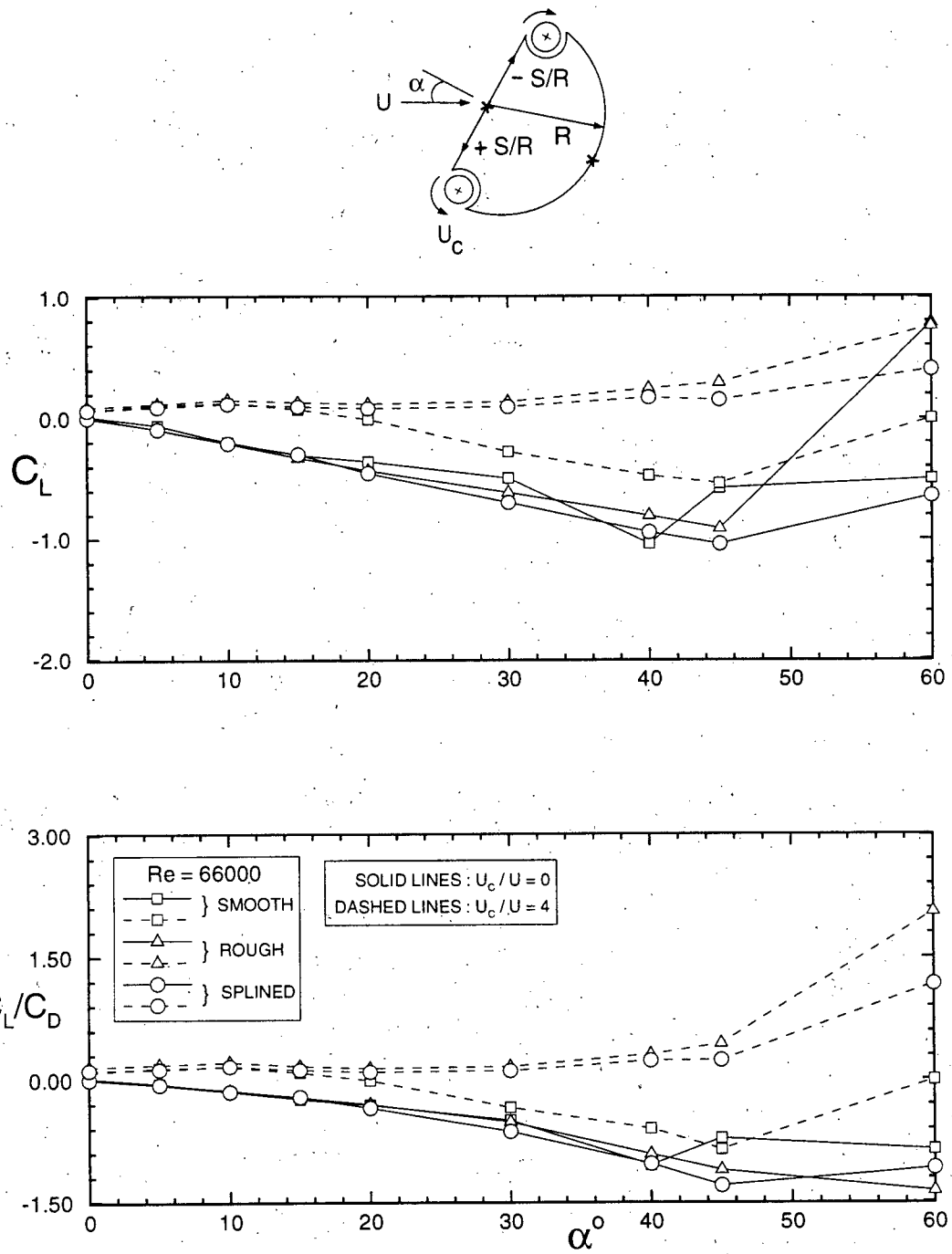
Figure 4-10   Effect of cylinder surface roughness on:(a) lift coefficient; (b) lift/drag ratio.
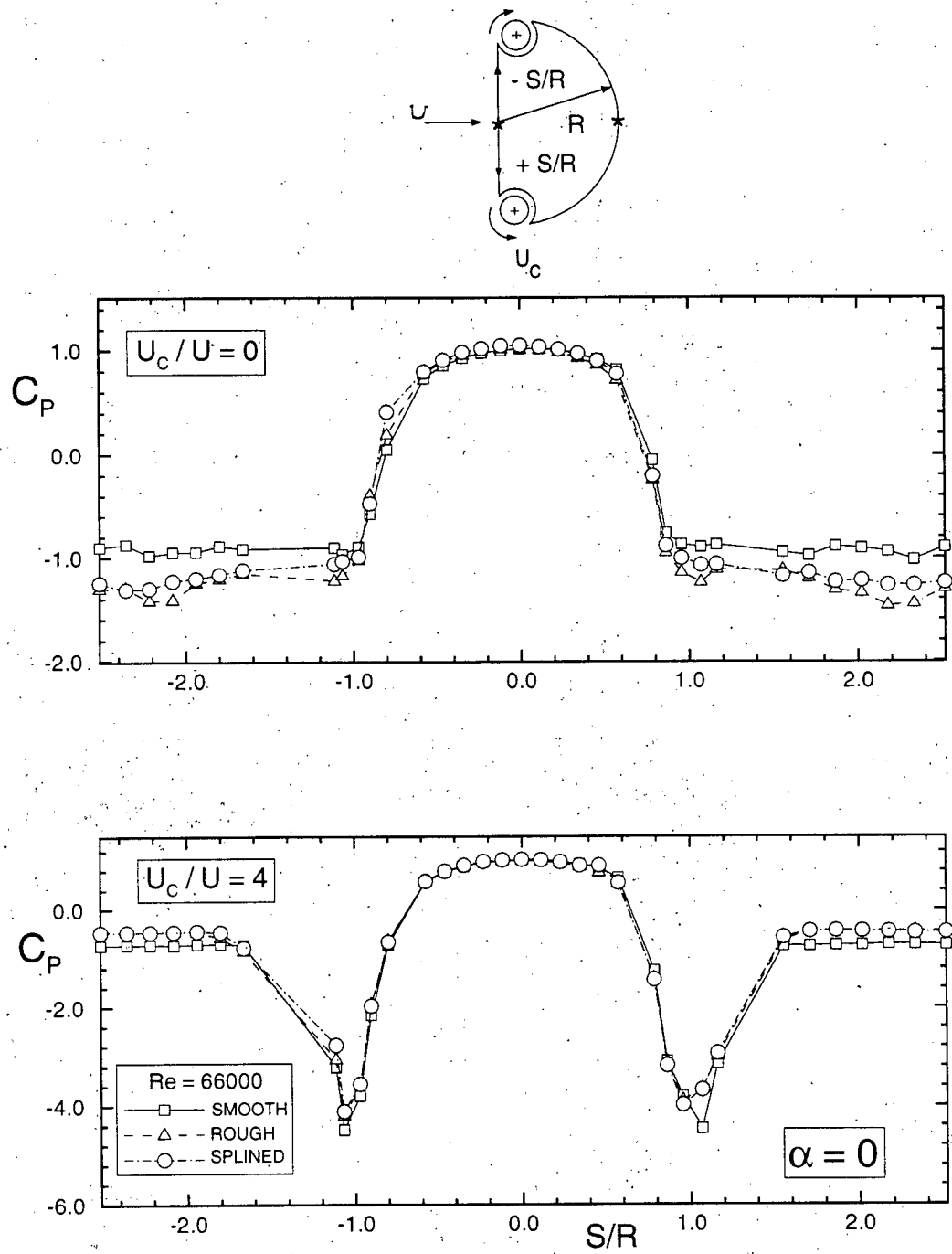
Figure 4-11 Effect of cylinder surface characteristic on pressure distribution over the D-section:(a) $\alpha = 0$.

134
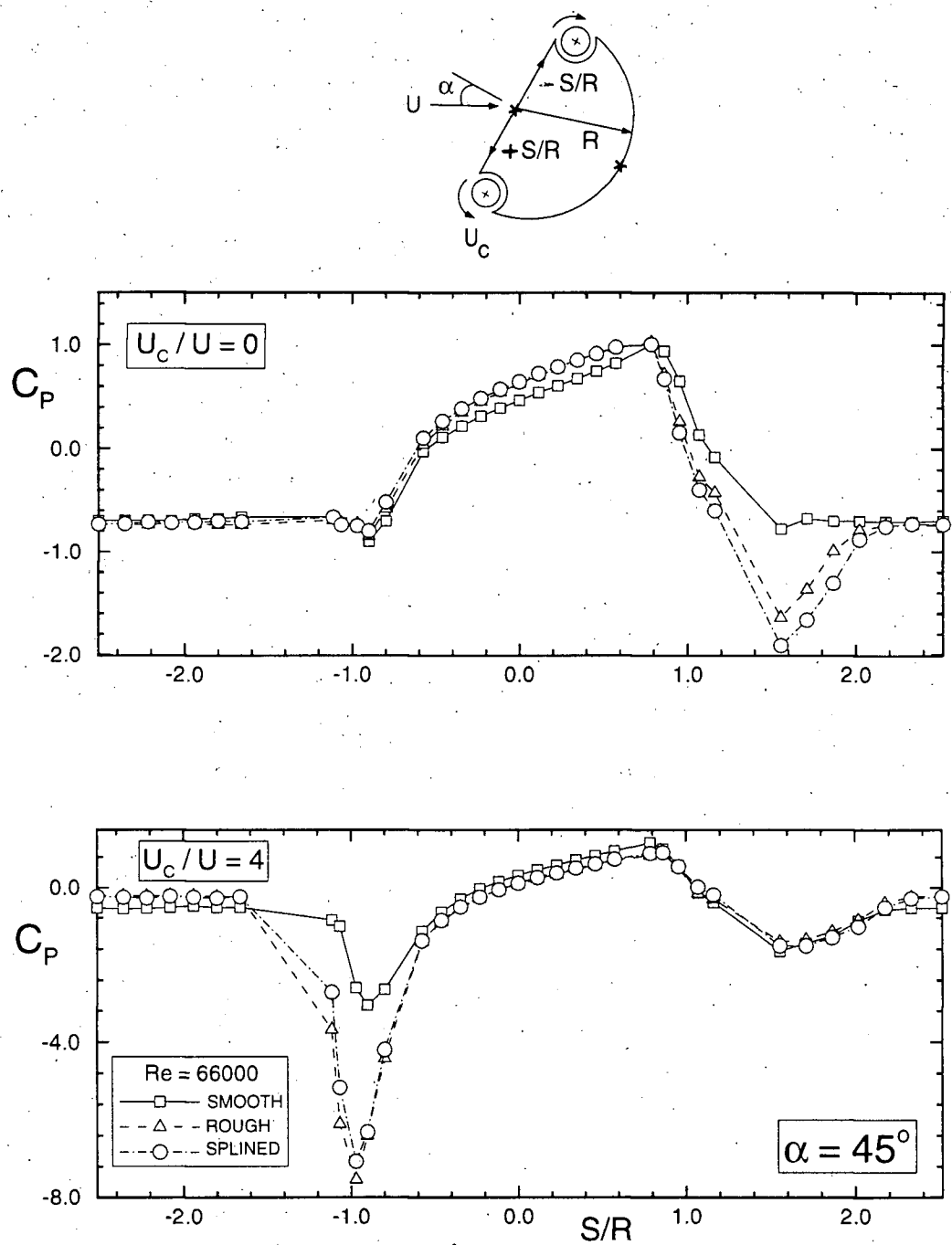
Figure 4-11(cont.) Effect of cylinder surface characteristic on pressure distribution over the D-section: (b)$\alpha = 45^o$.

4.5 Flow Visualization

Flow visualization has always been a powerful tool in studying complex fluid dynamics phenomena. A set of revealing photographs can convey important information about the physical character of the flow, at least qualitatively. Thus it helps in understanding of possible mechanisms at work that characterize the flow field. Depending on the accuracy of the flow visualization process and parameters of interest, even quantitative information can be obtained through analysis of photographs and video movies. The details of flow visualization procedure adopted was described in Section 2.2.6. Here, results for the D-section are presented (Figures 4-12 and 4-13).

At $\alpha = 0$ and in absence of momentum injection, the first thing that captures the attention is the existence of a wide wake behind the D-section (Figure 4-12). Note, the wake is significantly wider than the diameter of the D-section. The Reynolds number was 20,000 and the boundary-layer at separation is turbulent. The wake vortex structure displays considerable turbulence, with associated mixing and dissipation. Immediately behind the D-section, there is a small region of essentially stagnant fluid. The separating shear layer from the top has a sinusoidal character and divides the wake into well-defined pockets of diffused vorticity, generated from the viscous dissipation of the shed vortices. The overall configuration of the wake reverses itself in an alternate manner in phase with the vortex shedding process. The video revealed considerable unsteadiness of the wake, oscillating from side to side due to the low pressure region associated with the nascent vortex. At a given instant, the wake is slightly asymmetric (Figures 4-12 and 4-13). The shed vortices grow rapidly as they are convected downstream, diffusing vorticity in the surrounding fluid at a faster rate.

With an increase in the momentum injection from $U_C/U = 0 \rightarrow 4$, the wake becomes progressively narrower, turning into a small bubble at $U_C/U = 4$. This suggests considerable influence of the momentum injection on the inclination of the

136
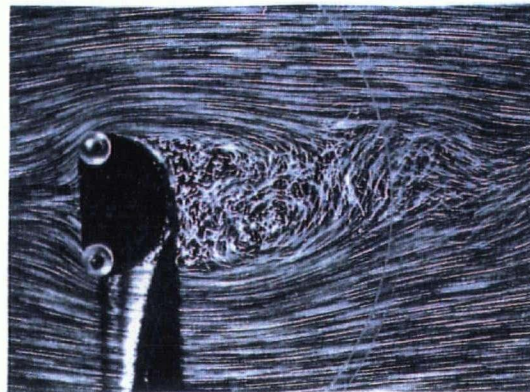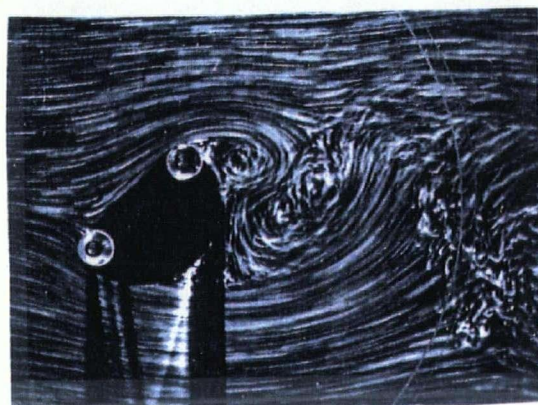
Figure 4-12   Flow visualization photographs showing effectiveness of the Moving Surface Boundary-layer Control (MSBC) as applied to the D-section. Note, at $U_C/U = 4$, the fluid motion tends to approach the potential character.

$U_C/U = 0$

D-SECTION SEPARATED SHEAR LAYER

RAPIDLY DIFFUSING VORTEX

GROWING VORTEX

A CLOSED WAKE
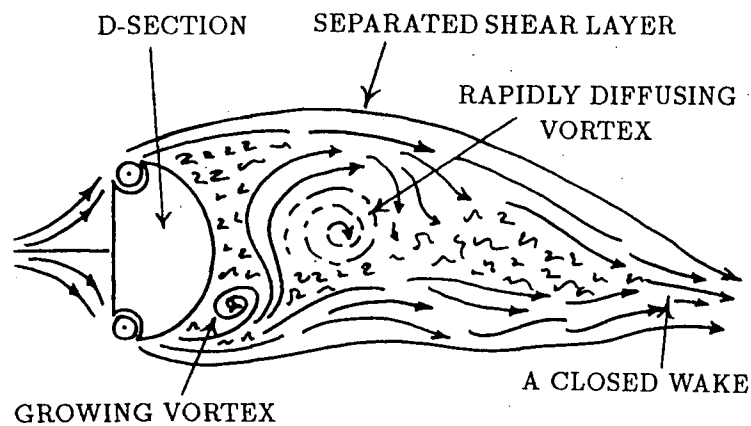
$U_C/U = 0$
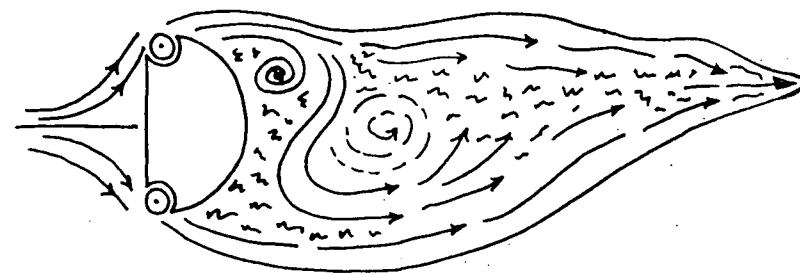
MOMENTUM INJECTION ELEMENT
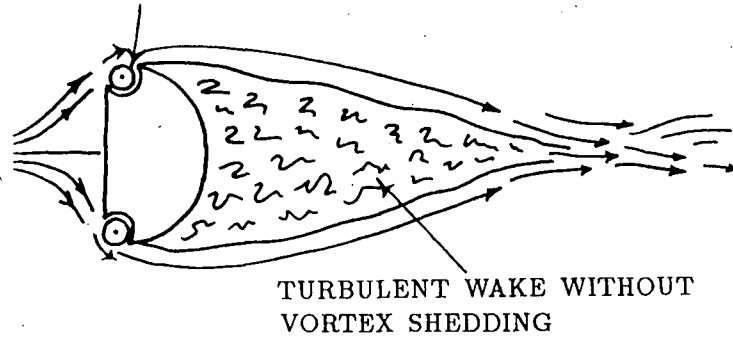
RELATIVELY SMALL WAKE BUBBLE

TURBULENT WAKE WITHOUT VORTEX SHEDDING

$U_C/U = 2$

$U_C/U = 4$

138
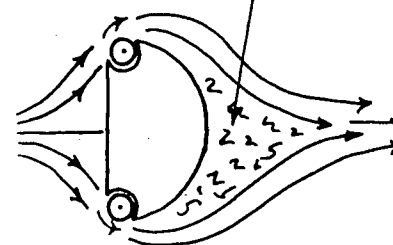
Figure 4-13 Effect of momentum injection on the characteristic features of the wake and the shed vortex system, as inferred from the flow visualization study.

separating shear layers. For example, the separation angle at the top corner of the D-section is around 10° at $U_C/U = 0$ (measured counter-clockwise with respect to the flow direction), changes to $\approx -10^o$ at $U_C/U = 2$ and reaches a value of approximately -35° at $U_C/U = 4$ thus resulting in a progressively smaller cavity in the wake. The oscillatory behaviour of the wake manifests itself in a much weaker form further downstream. At low rates of momentum injection ($U_C/U \leq 1$), the video clearly showed a significant increase in the vortex shedding frequency. However, at sufficiently high rates of momentum injection ($U_C/U \geq 2$), vortex shedding is suppressed completely and the fluid motion approaches the potential flow character. Since the "bluffness" of a body and the width of the wake are related, a reduction in the wake-width implies, effectively, a more streamlined body with an associated reduction in the drag.

Number of researchers [153, 155, 156] have pointed out the discrepancy between the experimentally observed vortex spacing ratio b/a (i.e. transverse to longitudinal spacing of a staggered row of vortices) and that predicted by Karman's stability analysis (b/a $\approx$ 0.281). A close scrutiny of a large number of flow visualization photographs revealed considerable scatter (b/a = 0.23–0.58 for $U_C/U = 0$ and depending on α) away from the value predicted by Karman. The Reynolds number being sufficiently high ($\approx$ 20,000), the separation is turbulent. This could introduce intermittency and randomness in the vortex formation. Three dimensional effects are also known to alter the vortex spacing ratio.

At $\alpha = 45^o$ (Figure 4-12) the essential features of the wake remain similar. Even at $U_C/U = 0$, the wake is narrower compared to that for the $\alpha = 0$ case, and this explains the lower drag coefficient. In presence of momentum injection the bubble containing separated recirculating fluid is nearly eliminated. Note, the freestream leaves the body at an angle due to the momentum injection.

4.6 Summary

The D-section in presence of momentum injection shows significant decrease

in drag as revealed from the wind tunnel, numerical and flow visualization results. The angle of attack beyond a certain range necessitates reversal in the direction of the momentum injection for one or both the cylinders. The reversal in the direction of momentum injection is governed primarily by the location of the upstream stagnation point. A small increase in the drag reduction can be achieved by changing the cylinder surface condition. Vortex shedding is completely eliminated even at a moderate rate of momentum injection ($U_C/U \geq 2$). A reduction in the drag as well as the lift coefficient in presence of momentum injection coupled with the dynamically more stable configuration, free from vortex resonance and galloping, are features quite attractive to design engineers.

5. FLOW PAST RECTANGULAR PRISMS WITH MOMENTUM INJECTION

5.1   Preliminary Remarks

Rectangular prisms represent a family of two-dimensional bluff bodies defined by a non-dimensional parameter called the aspect ratio (length to height ratio abbreviated as AR). This is not the case with a circular cylinder or a D-section, the geometries which remain unaffected by changes in their dimensions. By varying the aspect ratio of a rectangular prism, a variety of aerodynamic phenomena, like complete flow separation (AR $\leq$ 3), reattachment (AR $\geq$ 3), galloping instability (0.8 $\leq$ AR $\leq$ 2.5) and vortex resonance (AR $>$ 0) can be studied. A rectangular prism with AR $\approx$ 0 is the familiar normal flat plate, while AR $\rightarrow$ ∞ (i.e. for very large values of aspect ratio, say 20) results in a flat plate aligned with the flow. Rectangular shapes are encountered frequently in actual engineering practice, e.g. cross-sectional shapes of majority of tall buildings and ground vehicles (tractor-trailer trucks; buses and trains). From the structural dynamics point of view, a varying aspect ratio implies changes in the stiffness (longitudinal, transverse and torsional); natural vibrational frequency; load bearing capacity and internal damping.

Though much attention has been directed towards the basic fluid mechanics of rectangular prisms, their performance in presence of the MSBC has received little attention. Important questions regarding the effectiveness of momentum injection in terms of the overall drag reduction, suppression of vortex shedding, susceptibility to galloping type of wind-induced instability as well as effect on the wake structure, remain unanswered.

Two representative rectangular bluff body models, a vertical rectangle (AR = 0.5) and a square prism (AR = 1.0), were subjected to extensive wind tunnel investigation. The rectangular prism at $\alpha = 90^o$ is aligned with the flow and has AR = 2.0. The wind tunnel results in terms of pressure distribution, drag and lift

coefficients, wake pressure and the Strouhal number are discussed as affected by the angle of attack and the rate of momentum injection. The aerodynamic coefficients are also utilized for quasi-steady analysis to assess susceptibility of the prisms to galloping type of instability. An attempt is made to arrive at a universal Strouhal number. The chapter ends with flow visualization results which reveal intricate character of the flow field and the effect of momentum injection on it.

5.2   Wind Tunnel Investigation

5.2.1   Pressure distribution

The surface pressure distribution results as affected by the angle of attack and rate of momentum injection are presented in Figures 5-1 and 5-2 for the rectangular and the square prisms, respectively. The angle of attack (α) was varied from 0 to 180° for the rectangular prism and from 0 to 105° for the square prism. Experiments were carried out for the rate of momentum injection ranging from $U_C/U = 0$ to 4 in steps of one unit as before. Only some typical results useful in establishing trends are presented here for conciseness and clarity.

At $\alpha = 0$, the pressure distribution is symmetric about the stagnation point. The entire front faces of the prisms are stagnation zones. Note, both the prisms have rounded upstream corners due to presence of the rotating cylinders. The pressure starts decreasing, at first gradually, as one moves away from the mid-point, followed by a rapid reduction on the surface of the rotating cylinder resulting in large suction peaks. In absence of momentum injection, the flow separates near the corners and the rest of the afterbody lies in the wake. The pressure coefficient (C_P) in the wake is negative and remains nearly constant on the surface of the afterbody. The presence of a large wake is primarily responsible for the high drag coefficient ($C_D \approx 1.2$) experienced by both the rectangular and the square prisms. Note that the pressure plots for the rectangular and the square prisms at $\alpha = 0$ are almost identical indicating

142
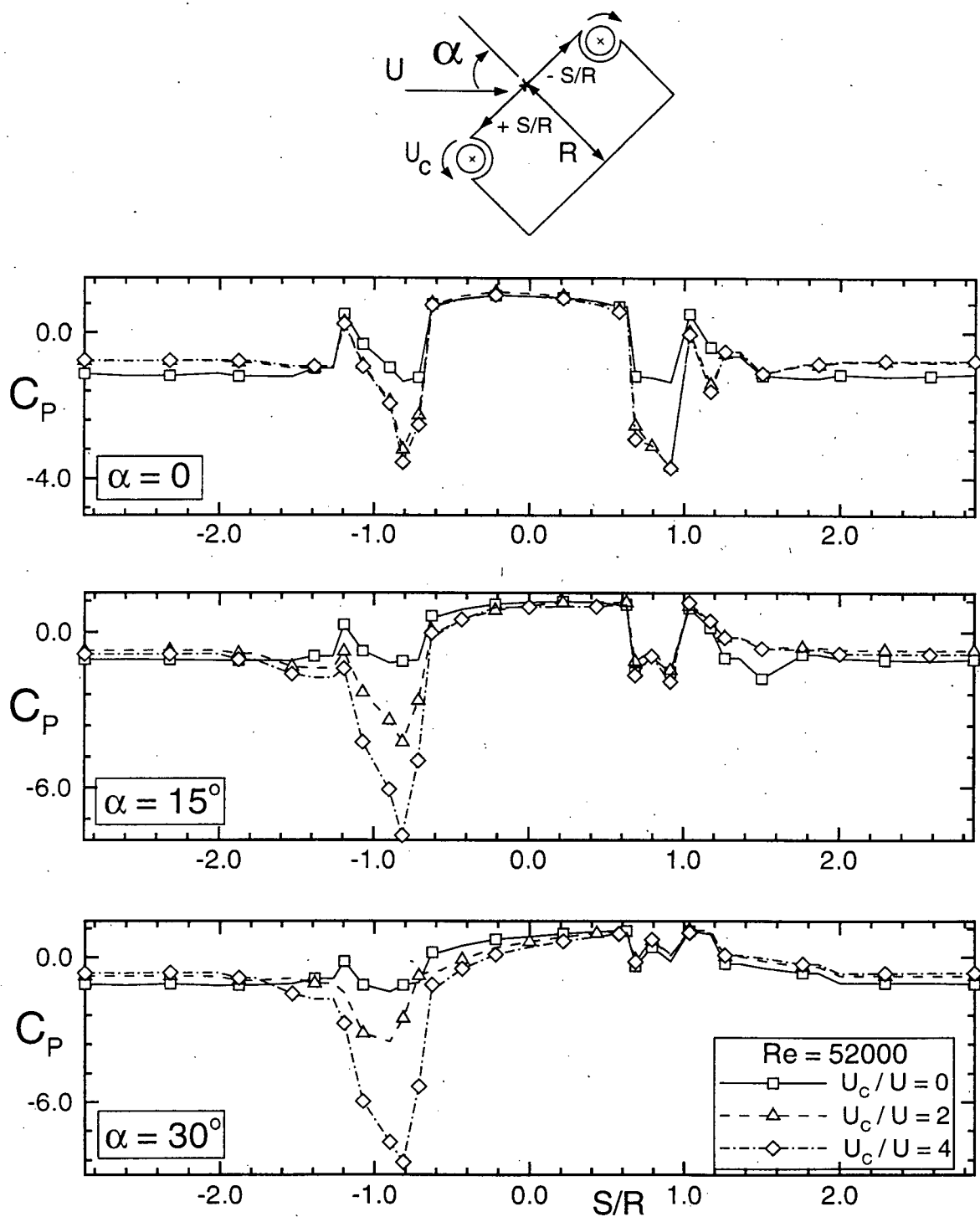
Figure 5-1 Surface pressure plots for the rectangular prism showing effects of the angle of attack and momentum injection: $\alpha = 0, 15°, 30°$.
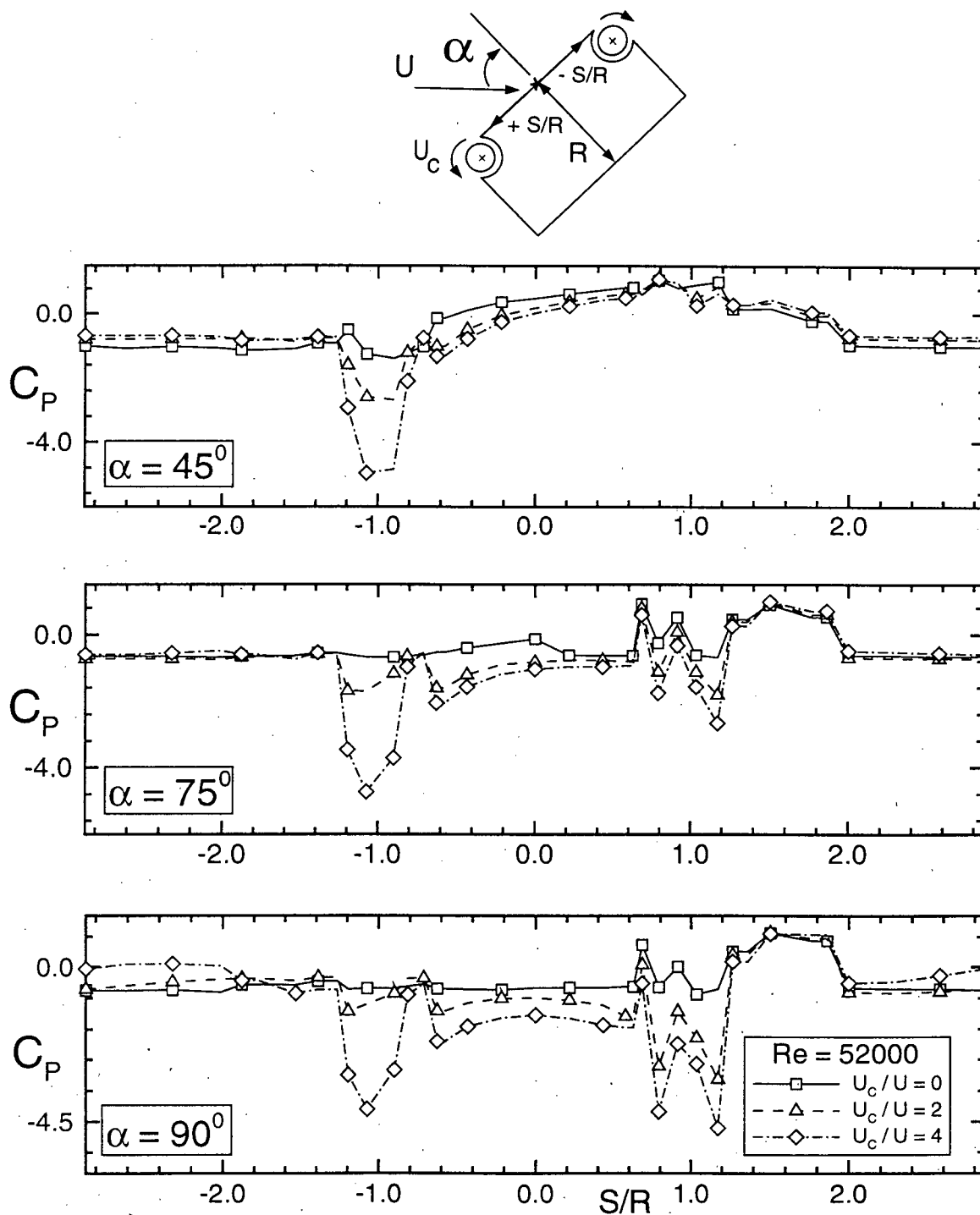
Figure 5-1(cont.) Surface pressure plots for the rectangular prism showing effects of the angle of attack and momentum injection: $\alpha = 45,^o$ 75°, 90°.
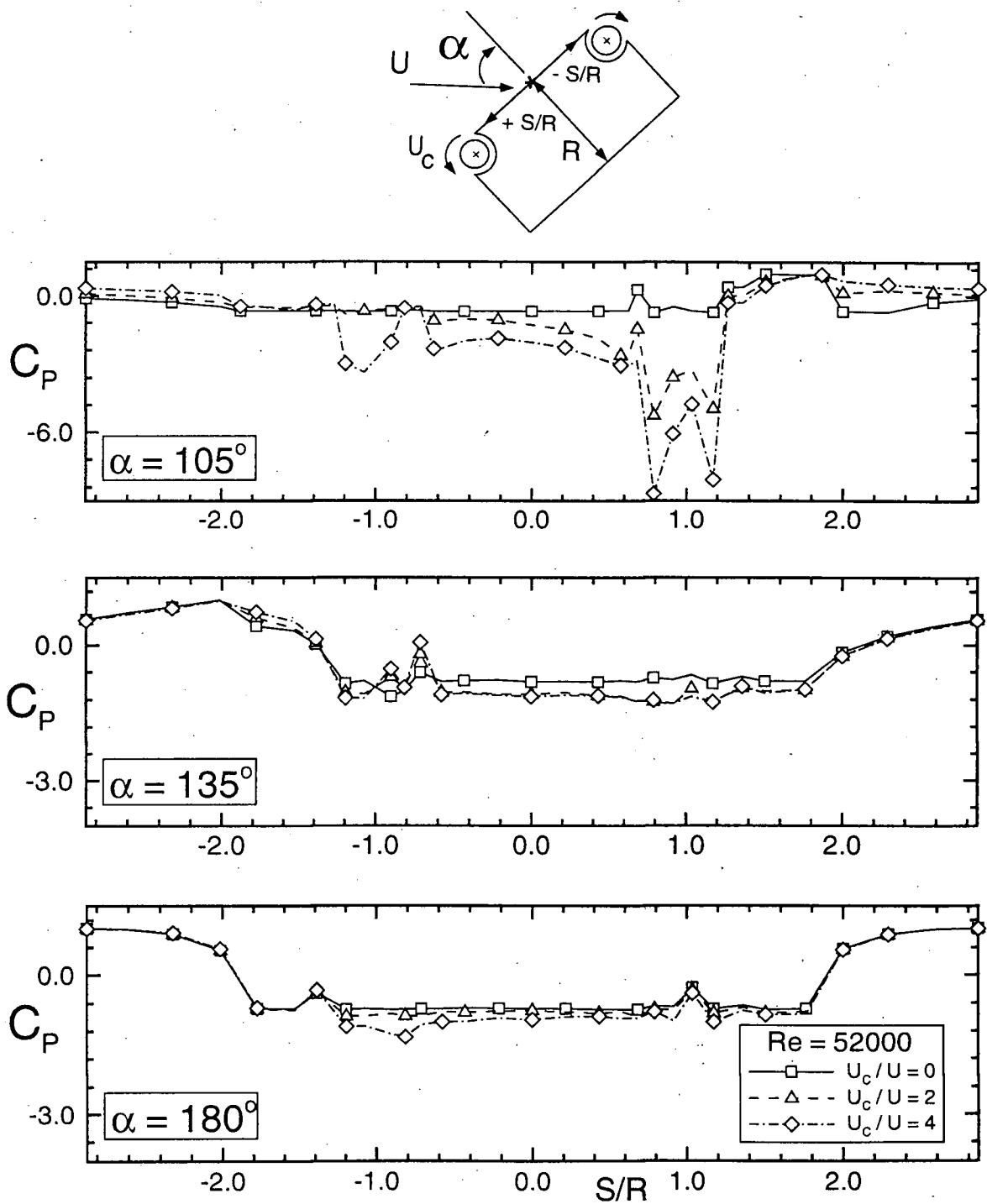
144

Figure 5-1(cont.) Surface pressure plots for the rectangular prism showing effects of the angle of attack and momentum injection: $\alpha = 105^\circ$, 135°, 180°.

that in absence of reattachment, it is frontal geometry that primarily determines the aerodynamics of a bluff body.

As the momentum injection is increased from $U_C/U = 0 \to 4$, the pressure distribution is altered substantially. The rotating cylinder has a negligible effect in the upstream direction (i.e. on the stagnation zone), except for the acceleration experienced by the fluid in its vicinity. The strength of the suction peak grows with an increase in the rate of momentum injection. A part of the suction peak located towards the front of the prism may also contribute to the drag reduction. Of course, as can be expected, injection of the momentum by the rotating cylinders results in a higher near wake pressure, i.e. the pressure on the base of the afterbody in the wake. At $\alpha = 0$, the rise in the wake pressure is about 33% and 20% ($U_C/U = 4$) for the rectangular and square prism, respectively. This rise in the wake pressure was reflected in the lower drag coefficients for both the prisms.

As the angle of attack is increased from zero, the symmetry in the pressure distribution is no longer present. The stagnation point starts moving towards the rotating cylinder facing upstream. The asymmetry in the flow demands an adjustment in the pressure distribution over the whole body. The suction peaks on the rotating cylinders are no longer of equal strength: the one on the upstream rotating cylinder is weaker while the downstream suction peak becomes more pronounced ($0 \le \alpha \le 30°$). Thus the movement of the stagnation point has important consequences on the overall pressure distribution. For $\alpha \approx 15° - 20°$, there are two small stagnation regions, on either side of the rotating cylinder, for both the rectangular and the square prisms. In case of the rectangular prism this phenomena persists upto $\alpha = 45°$. For $\alpha \ge 20°$, the stagnation point moves very close to the upstream rotating cylinder and merges with the suction peak, causing the upstream suction peak to disappear even at the highest rate of momentum injection ($U_C/U = 4$). For $20° \le \alpha \le 40°$, a significant difference develops between the surface pressure character of the rectangular and square prisms.
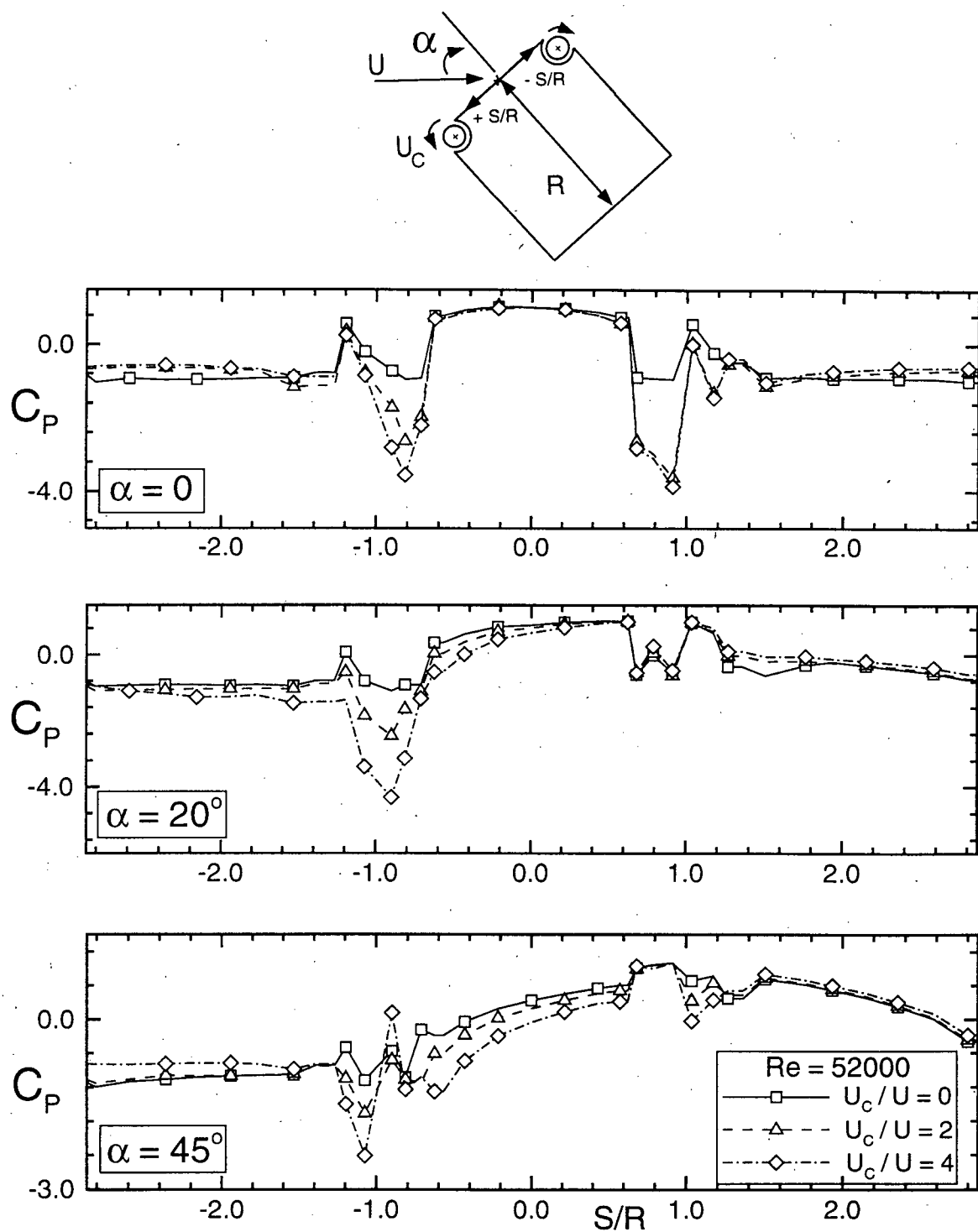
Figure 5-2 Surface pressure plots for the square prism as affected by the angle of attack and momentum injection: $\alpha = 0, 20^{\circ}, 45^{\circ}$.
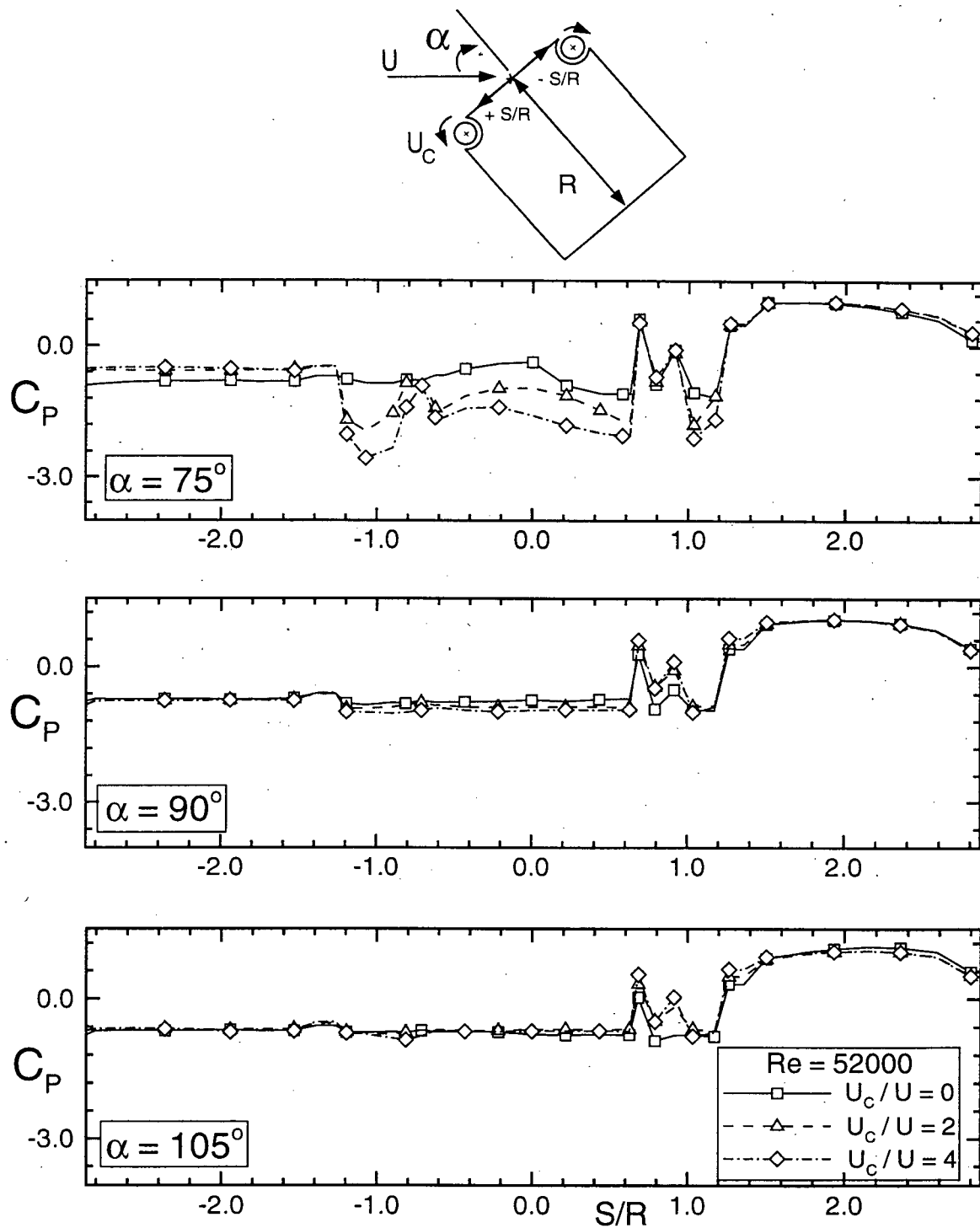
Figure 5-2(cont.) Surface pressure plots for the square prism as affected by the angle of attack and momentum injection: $\alpha = 75°$, $90°$, $105°$.
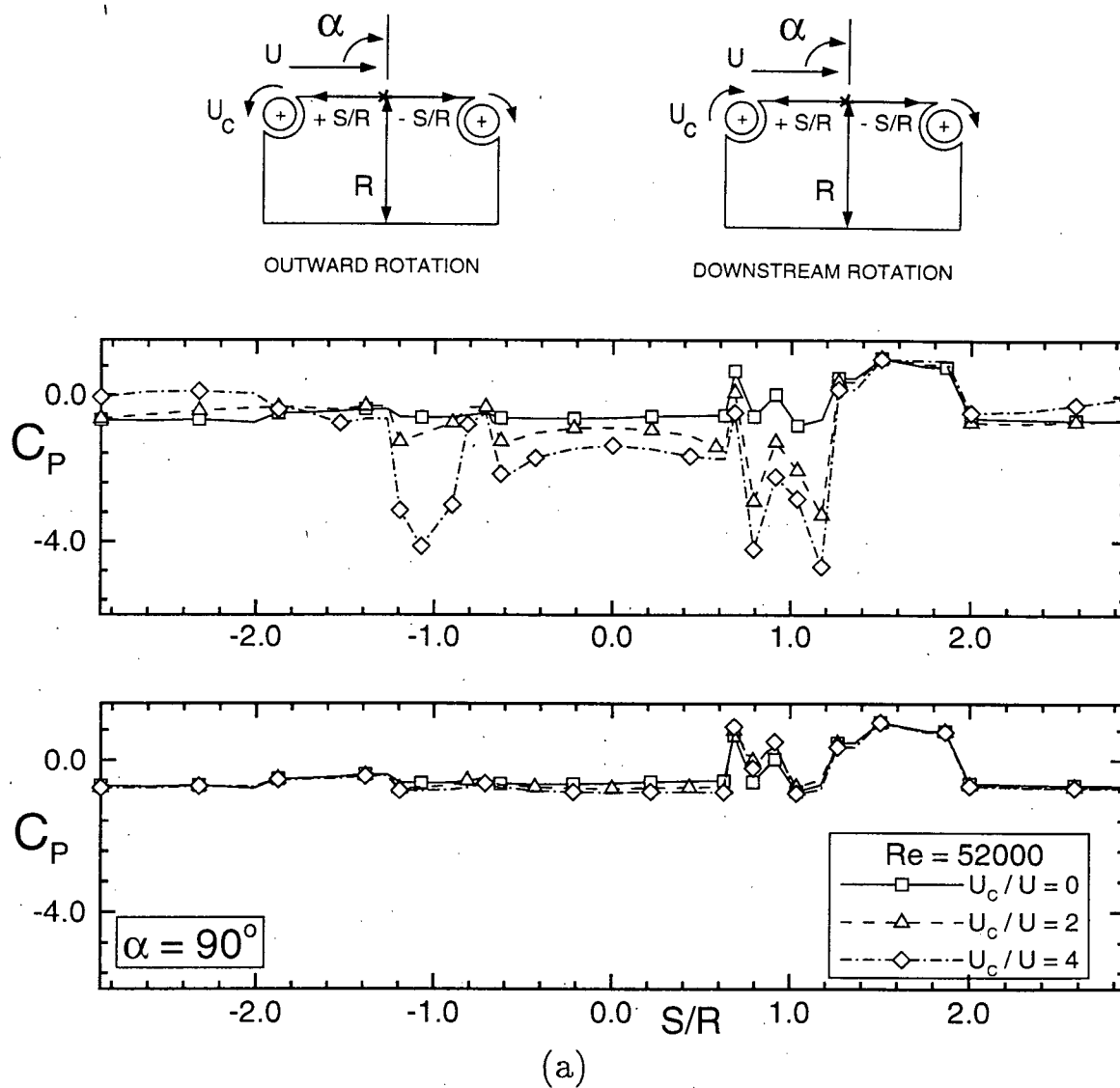
Figure 5-3   Effect of reversing the direction of upstream cylinder on the surface pressure distribution at $\alpha = 90^o$: (a) rectangular prism.
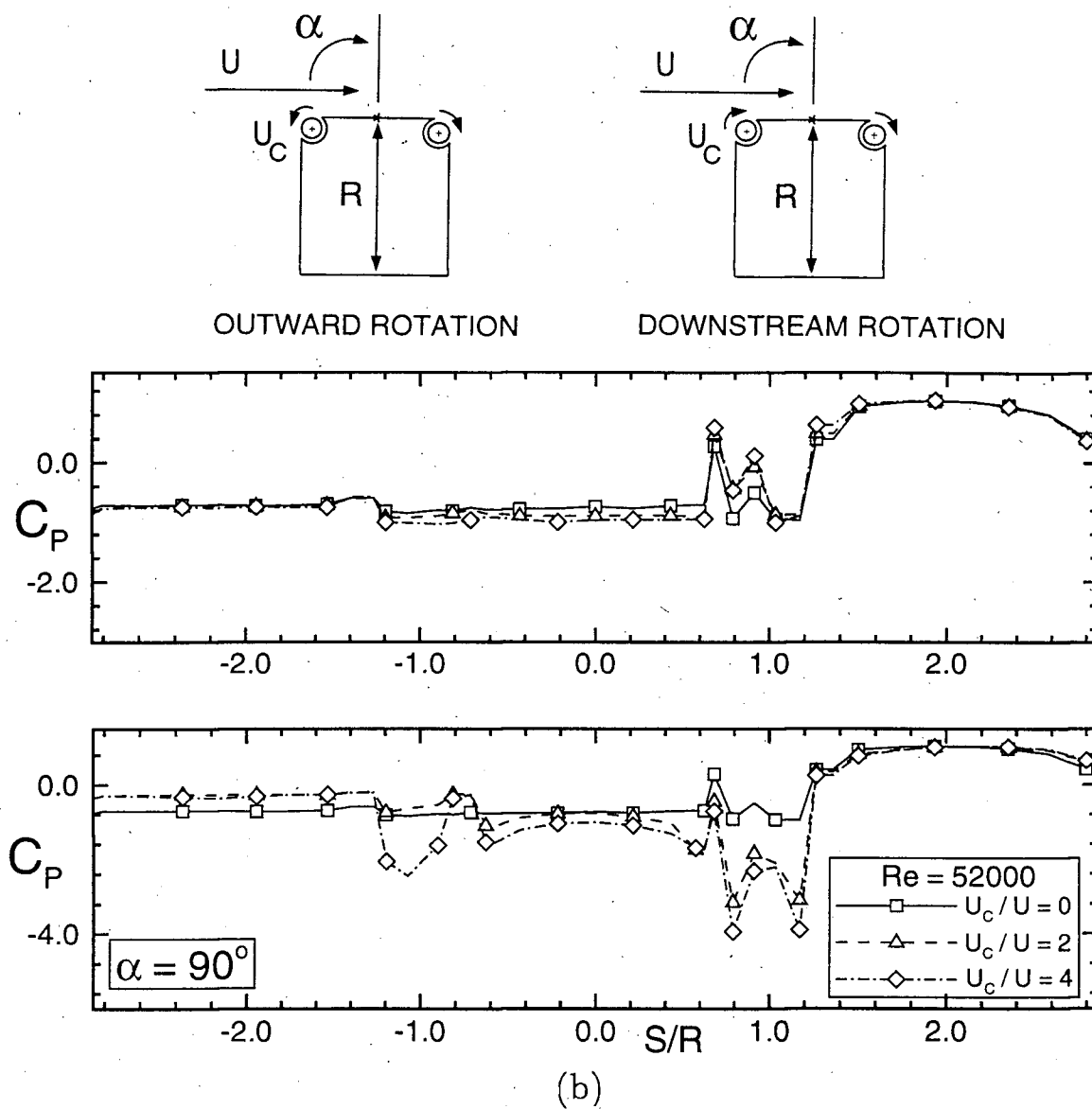
Figure 5-3(cont.) Effect of reversing the direction of upstream cylinder on the surface pressure distribution at $\alpha = 90°$: (b) square prism.

As against the rectangular prism where the wake pressure rose uniformly for $U_C/U \geq 0$, with the square prism, the wake pressure rises only on the upstream side (S/R $\geq$ 0) and becomes lower on the downstream side (S/R $\leq$ 0). This is reflected in the minimum reduction in the drag of $\approx 21\%$ compared to the average drag reduction of $\approx 36\%$ ($0 \leq \alpha \leq 75^o$) for the square prism. For $\alpha \geq 45^o$, the situation near the upstream rotating cylinder becomes quite complicated. The stagnation point has clearly moved to the side face for both the rectangular and the square prisms. Also, multiple regions of primary and secondary separations as well as partial reattachment are present, as indicated by the irregular pressure plots. Similar trend persists in presence of the momentum injection, except for variations in the magnitude. In case of the rectangular prism, the suction peak on the downstream rotating cylinder maintains itself even at α as high as 90°, however, this is not the case for the square prism.

For $\alpha = 90^o$ and 105°, almost the entire body lies in the wake and rotating the cylinders in the original direction does not make any difference. Note, the pressure distribution on the square prism at $\alpha = 90^o$ is quite similar to that at $\alpha = 0$ in absence of momentum injection, except for a shift of the stagnation point to the upstream facing side. It is of interest to recognize that, at $\alpha = 90^o$, the upstream cylinder is rotating in the opposite sense to the direction of the flow. This suggests a need for reversal in the direction of rotation. Figure 5-1 also shows pressure results for the rectangular prism in the range $\alpha \geq 135^o$. Clearly by not reversing the direction of momentum inection there is an adverse effect on the overall pressure distribution. The pressure in the wake becomes even more negative in presence of the momentum injection. This causes a large increase in the drag coefficient. Direction of rotation of both the cylinders should now be reversed in order for the momentum injection to be effective.

The $\alpha = 90^o$ is a special case. The face carrying the rotating elements is now

aligned with the flow. Note, the aspect ratio of the rectangular prism is now 2. It is apparent that the upstream cylinder should be rotated clockwise in order not to oppose the incoming flow. It was decided to test both the clockwise and counterclockwise rotation of the upstream cylinder. The results are shown in Figure 5-3. It is of interest to point out that reversal in the downstream cylinder rotation had virtually no effect, since it is submerged in the separated flow field. For both the prisms, the pressure distribution is altered in such a way that a net drag reduction is achieved by reversing the upstream cylinder rotation.

5.2.2 Aerodynamic coefficients

Variation in the drag and the lift coefficients with the angle of attack and rate of momentum injection are shown in Figures 5-4 and 5-5 for the rectangular and the square prisms, respectively. The net changes in the drag (ΔC_D) and the lift (ΔC_L) are given in Tables 5.1–5.4 for both the rectangular and square prisms. Note, the % ΔC_D and % ΔC_L are defined as:

$$\% \Delta C_D = \frac{C_{D(U_C/U=0)} - C_{D(U_C/U=4)}}{C_{D(U_C/U=0)}} \times 100; \qquad (5.1)$$

$$\% \Delta C_L = \frac{C_{L(U_C/U=0)} - C_{L(U_C/U=4)}}{C_{L(U_C/U=0)}} \times 100. \qquad (5.2)$$

Table 5.1 Drag reduction for the rectangular prism with the momentum injection at various α.

α^o	$C_D(U_C/U = 0)$	$\% \Delta C_D(U_C/U = 4)$
0	1.234	61
30	1.528	46
45	1.436	27
60	1.143	25
75	0.527	18
90	0.334	-15
135	0.540	-24
180	1.551	-17

Table 5.2   Change in the lift of the rectangular prism with the momentum injection at various α.

α^o	$C_L(U_C/U = 0)$	$\%\Delta C_L(U_C/U = 4)$
0	0.0	0
30	-0.310	542
45	-0.415	260
60	-0.539	232
75	-0.221	270
90	-0.113	143
135	-0.751	-1
180	0.0	0

Table 5.3   Drag reduction for the square prism with the momentum injection at various α.

α^o	$C_D(U_C/U = 0)$	$\%\Delta C_D(U_C/U = 4)$
0	1.201	61
30	1.755	24
45	1.846	26
60	1.568	40
75	1.272	26
90	1.231	-10
105	1.107	-1

Table 5.4   change in the lift of the square prism with the momentum injection at various α.

α^o	$C_L(U_C/U = 0)$	$\%\Delta C_L(U_C/U = 4)$
0	0.0	0
30	0.304	210
45	0.101	377
60	0.031	1213
75	0.093	1159
90	0.0	0
105	-0.709	-5

For $0 \leq \alpha \leq 75^o$, a significant decrease in drag is achieved for both the rectangular and the square prisms. The drag reduction was found to increase directly with the rate of momentum injection. As explained earlier, at $\alpha = 90^\circ$, it necessary to reverse the direction of the upstream rotating cylinder. The projected height of the rectangular prism is minimum at $\alpha = 90^o$ and the drag coefficient attains a minimum value (Figure 5-4a). In case of the square prism the projected height is maximum
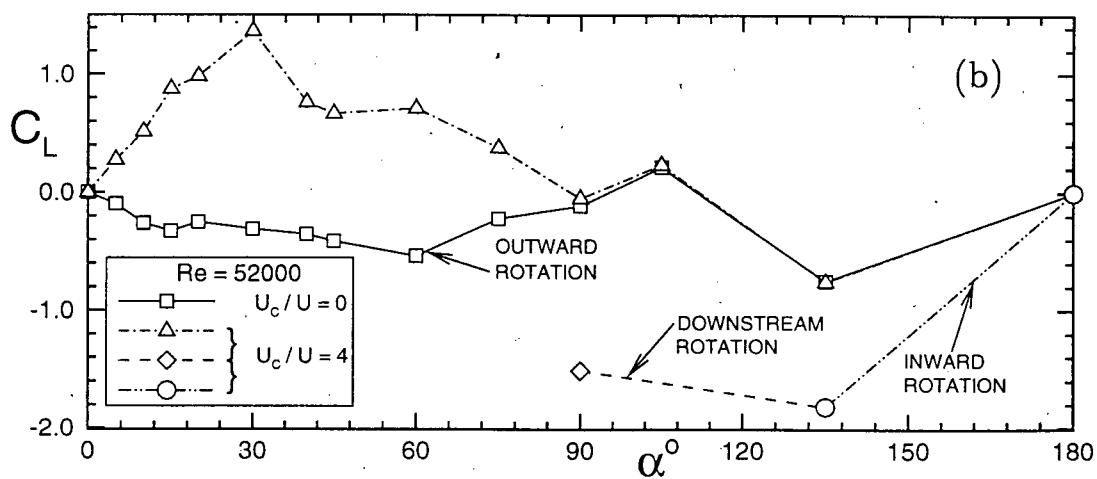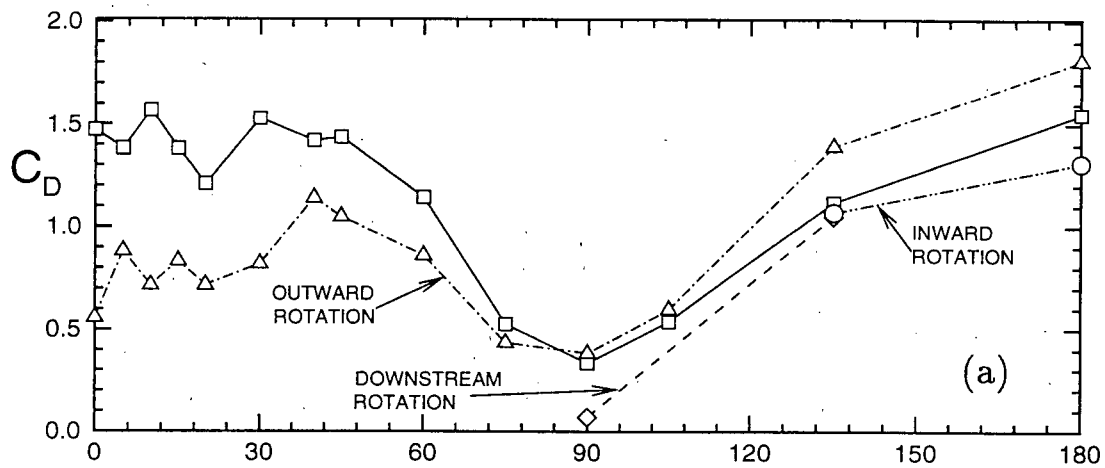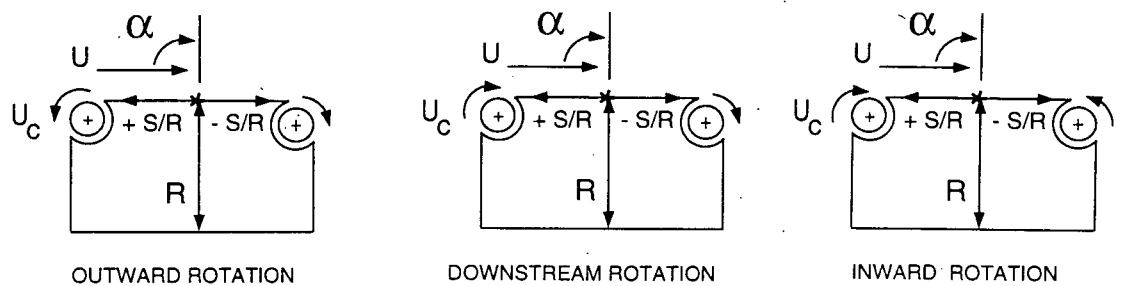
Figure 5-4 Drag and lift characteristics of the rectangular prism as affected by the momentum injection.
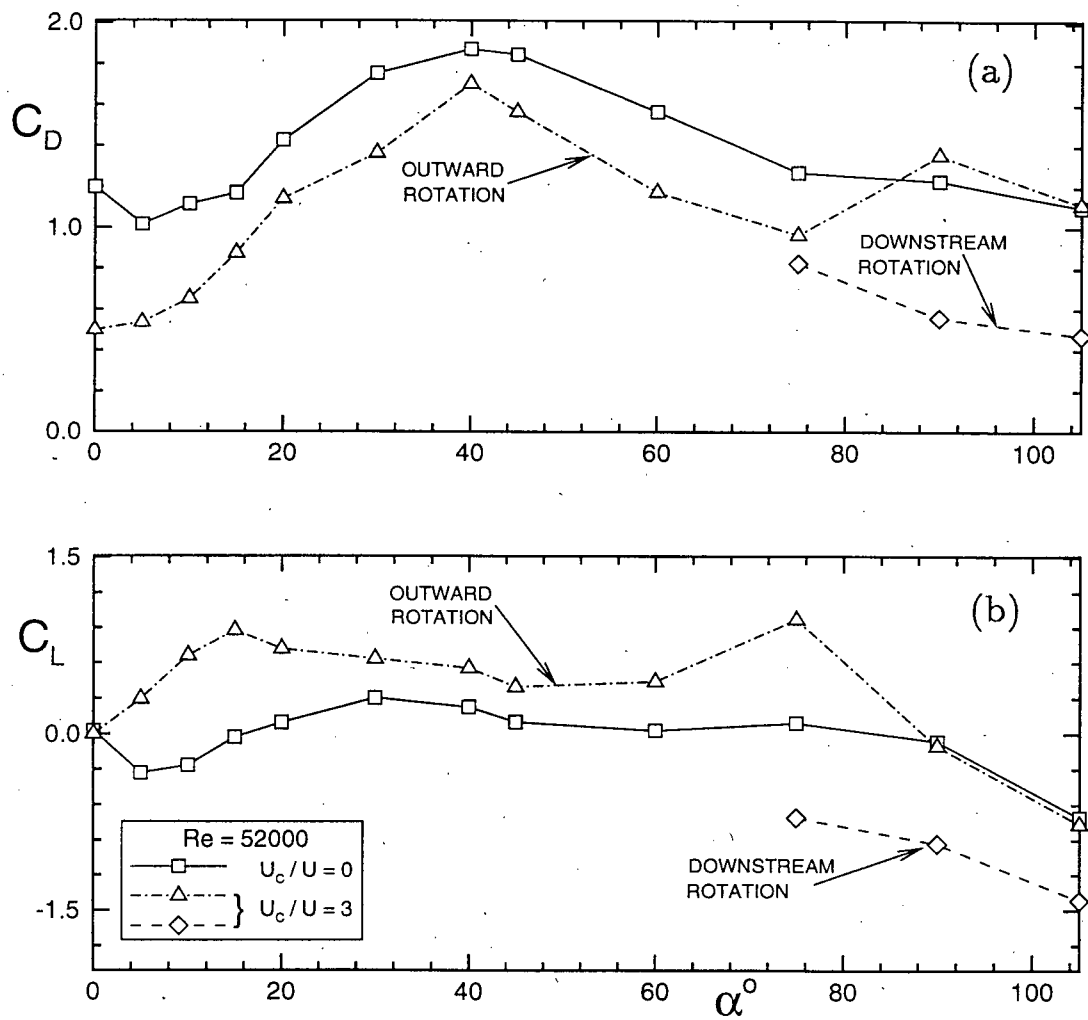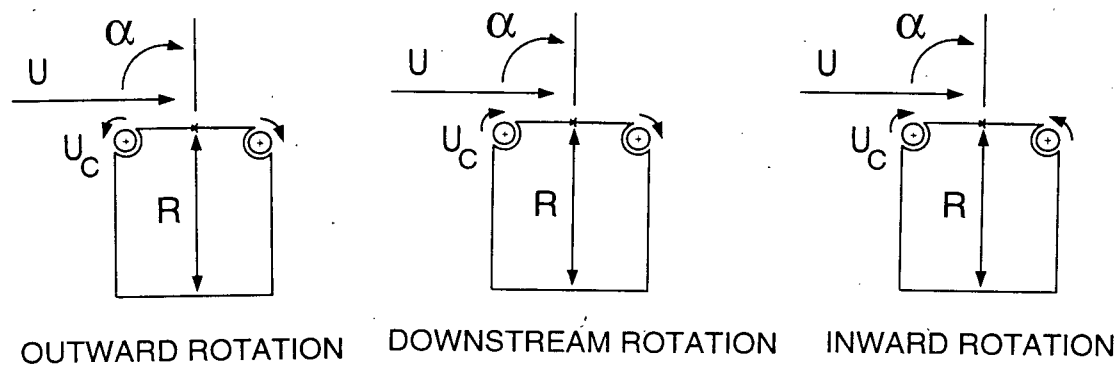
Figure 5-5   The drag and lift characteristics of the square prism as affected by momentum injection

at $\alpha = 40^{\circ}-45^{\circ}$, and the drag coefficient is the highest (Figure 5-5a). Also, the drag and the lift coefficients at $\alpha = 0$ and 90° remain essentially the same for the square prism as expected. For $0 \leq \alpha \leq 75^{\circ}$, an average reduction in drag was around 36% for both the rectangular and the square prisms, which is indeed remarkable. For $90^{\circ} \leq \alpha \leq 135^{\circ}$, introduction of the downstream rotation is necessary to establish a favourable condition for drag reduction. For $\alpha \geq 135^{\circ}$, the inward mode of rotation (i.e. reversal in the direction of rotation of both the upstream and downstream cylinders) is required to assure a decrease in drag.

For $\alpha = 0$, 90° and 180°, the rectangular and the square prism are symmetric with respect to the flow direction and the lift coefficient is zero. But for $0 \leq \alpha \leq 75^{\circ}$, a large increase in the lift is observed as the momentum injection is increased from $U_C/U = 0$ to 4 (Figure 5-4b and 5-5b). This is also evident from Tables 5.2 and 5.4. This means a substantial increase in the load acting transverse to the wind direction and should be taken into consideration while designing a real life structure. But the maximum value of $|C_L|$ at $U_C/U = 4$ is not greater than $|C_D|$ at $U_C/U = 0$ and the structure should be able to withstand the load. A negative $dC_L/d\alpha$ indicates a likelihood for galloping instability at small angles of attack. An explanation of the criterion for stability is described in Section 6.3.1. At small angles of attack ($\alpha \leq 20^{\circ}$), $dC_L/d\alpha \leq 0$ ($U_C/U = 0$) and becomes positive in presence of momentum injection ($U_C/U \geq = 2$) indicating that the stability is restored.

5.2.3 Wake pressure and Strouhal number

A strong link between the base pressure and the vortex shedding was emphasized in Section 4.2.2. Based on the experience gained through the study of D-section, it was expected that, for sufficiently high rates of momentum injection ($U_C/U \geq 2$), vortex shedding would be eliminated completely.

Dependence of the base pressure on the angle of attack and rate of momentum injection is shown in Figure 5-6 (rectangular prism) and Figure 5-7 (square prism).

Pressure tap - A was found to lie in the wake for $\alpha \leq 105°$ as shown in the schematic diagrams at the top of the figures. For $\alpha \geq 135°$, pressure tap - B was used for the purpose. In general, the wake pressure coefficient is much lower than the freestream value ($C_{PB} \leq 0$), and increases significantly in presence of the momentum injection. In case of the rectangular prism, an average increase of 24% in the wake pressure was observed for $0 \leq \alpha \leq 75°$ and $U_C/U = 4$. Similarly, for the square prism, the average rise in the wake pressure was around 23% under similar conditions. If one continues to rotate the upstream cylinder in the counter-clockwise direction, the wake pressure becomes lower in presence of momentum injection at $\alpha = 90°$. Obviously, this has an adversed effect on the drag of the body. By adopting the downstream rotation mode, the situation is improved significantly in the range of $75° \leq \alpha \leq 105°$ (Figures 5-6a and 5-7a).

Figures 5-6(b) and 5-7(b) show variation in the Strouhal number (St) for the rectangular and the square prisms, respectively. In case of the rectangular prism, an interesting feature is the sudden jump in the vortex shedding frequency at $\alpha = 90°$. In fact this is very similar to that observed for the D-section (Figure 4-3b). The D-section and the vertical rectangular prism have a measure of similarity in this configuration resulting in similar Strouhal number characteristics. At $\alpha = 90°$, the rectangular prism is aligned with the flow direction and behaves as a relatively streamlined body. Hence a jump in the vortex shedding frequency can be expected. The behaviour of the square prism is somewhat different. It shows several small peaks over a range of the angle of attack investigated ($0 \leq \alpha \leq 105°$). Since the rectangular and the square prisms have well defined side faces (unlike the D-section), it was easier to capture the vortex shedding frequency using the pressure taps located on the sides. As evident from the results, a small but consistent increase in the Strouhal number is detected in presence of the momentum injection ($U_C/U = 1$). But the amplitude of the dominant vortex shedding frequency is much smaller as obtained from the
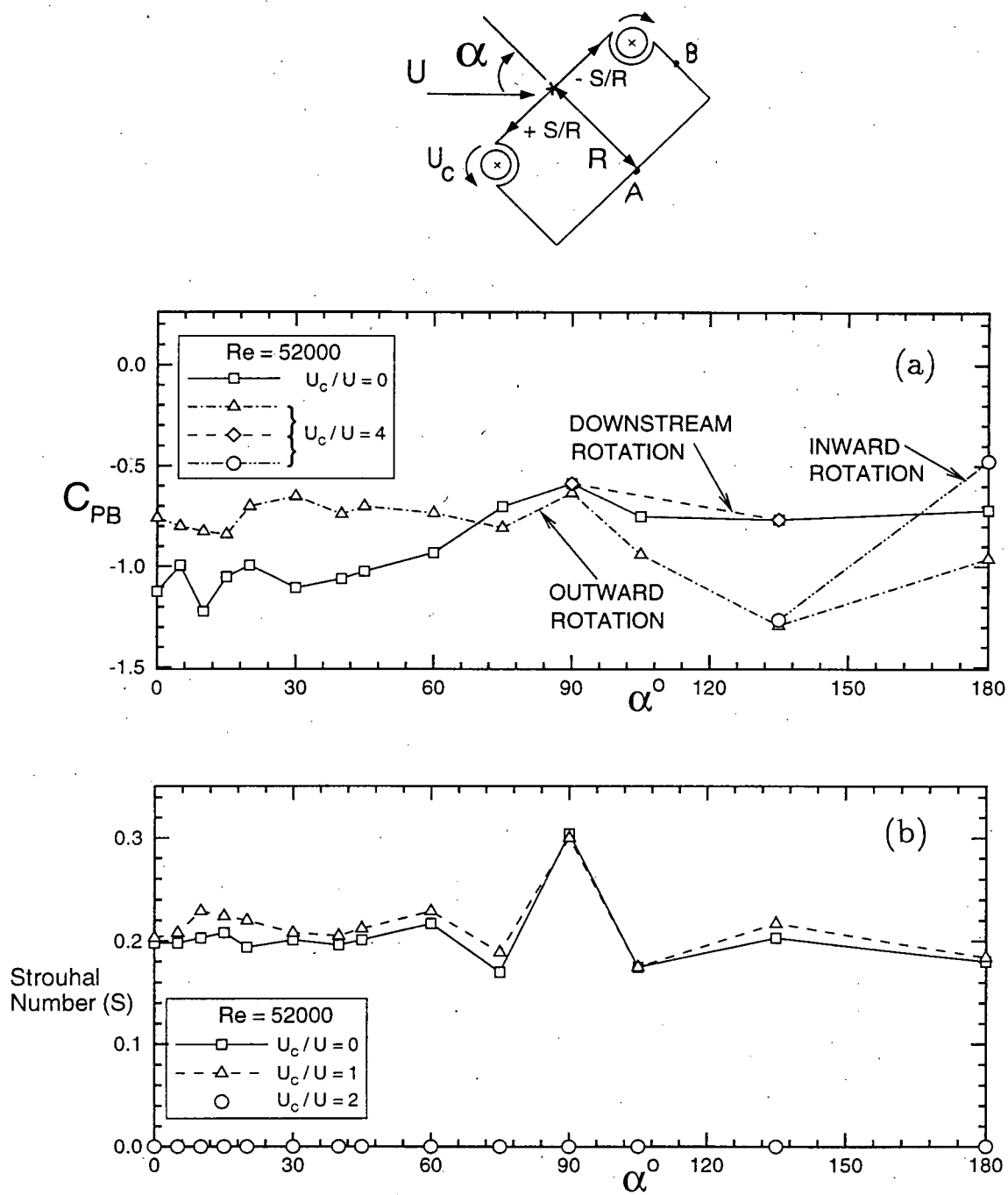
Figure 5-6   Effect of momentum injection on the wake pressure and Strouhal number of the rectangular prism.
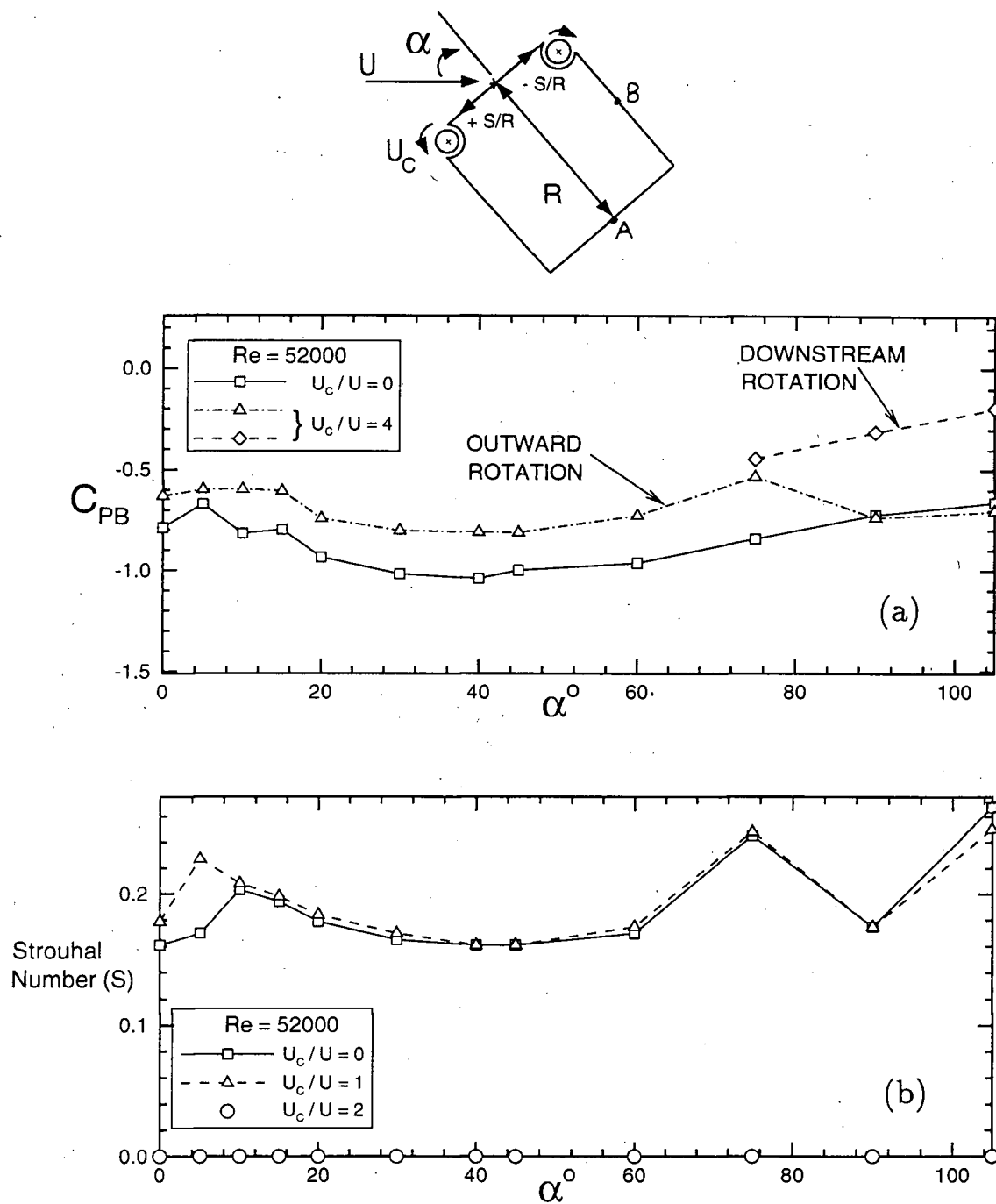
Figure 5-7   Variation in the wake pressure and Strouhal number for the square prism as affected by the momentum injection.

power spectral analysis. At $U_C/U = 2$, no vortex shedding could be detected. As confirmed from the flow visualization, at $U_C/U \geq 2$, the vortex shedding is completely eliminated.

5.3 Universal Strouhal Number

5.3.1 Correlation between some nondimensional numbers

The problem of flow past a bluff body has eluded complete theoretical treatment so far. Notable advances in this direction were made by Strouhal [1], Karman [3] and Roshko [69,151,158-159]. In recent times, the advent of numerical computation procedures have, to some extent, overshadowed the value of simple, elegant, carefully designed experiments. It is well known that all bluff bodies are characterized by wide wakes, vortex shedding and lower than freestream pressure in the wake. As remarked by Roshko [159], "the wake structure of different bluff bodies is similar. That is, the shape, or bluffness, of the body has no characteristic effect on the wake other than to determine its geometrical and velocity scales". As seen from the results of bluff bodies under study, the vortex shedding frequency and the wake pressure are functions of the angle of attack. Hence it is logical to look for a parameter which can be used to compare the wakes of different bluff bodies, or a single bluff body at different orientations. Furthermore, it would be of interest to assess the effect of momentum injection on such a parameter. Attempts to formulate a universal Strouhal number are not new. The present approach is based on the contributions by Roshko [159] and Bearman [155].

The wake of a given bluff body can be modelled as two shear layers, a distance h' apart with the velocity outside the layers equal to U_b, the velocity at the edge of the boundary layer at the point of separation. The frequency with which the vortices are formed can be considered proportional to U_b/h' and the 'Wake Strouhal Number',

Sr, can be defined as

$$Sr = \frac{f_V h'}{U_b}, \tag{5.1}$$

where f_V = frequency of vortex shedding. By applying Bernoulli's equation to the flow at the separation point, just outside the shear layer,

$$U_b = U\sqrt{[1 - C_{PB}]}, \tag{5.2}$$

where: U = free stream velocity; and C_{PB} = base pressure. Putting $k_1 = \sqrt{[1 - C_{PB}]}$, the base pressure parameter [158]

$$U_b = U k_1. \tag{5.3}$$

Now a new Strouhal number St is defined as

$$St = \frac{f_V D}{U}, \tag{5.4}$$

where D = characteristic diameter of the body. Then

$$Sr = \frac{(St)h'}{k_1 D}. \tag{5.5}$$

The value of h' was originally obtained by Roshko [159] using the notched hodograph theory. It gives the spacing of the shear layers when they become parallel. In general, it is difficult to apply the notched hodograph theory to complex bluff geometries. One alternative would be to solve, numerically, the Navier-Stokes equation, but this would require considerable effort and time. As a first approximation, one may replace the distance h' by h (the height of the bluff body projected normal to the flow). This is reasonable because the separation of the shear layers is directly related to the projected height of the bluff body. Also, h is a function of the angle of attack and can be evaluated quite readily. The Strouhal number based on the projected height (St_p) is defined as

$$St_p = \frac{f_V h}{U} = \frac{(St)h}{D}. \tag{5.6}$$

By introdcuing 'St_p' in equation (5.6), one can define a universal nondimensional parameter Su as

$$Su = \frac{St_P}{k_1} = \frac{f_V h}{U k_1}. \tag{5.7}$$

For a given bluff body the quantities f_V, h and k_1 are all functions of the angle of attack (α). Hence for a given wind speed (U),

$$Su = \frac{F(\alpha)}{G(\alpha)}. \tag{5.8}$$

The next step would be to assess sensitivity of the parameter Su to the angle of attack and geometry of the bluff body.

5.3.2 Experimental confirmation

Figure 5-8(a) shows variation of the universal Strouhal number, Su, with α for two distinct bluff bodies (rectangular and square prisms) in absence of momentum injection. It is apparent from the figure that the points show scatter around a representative Su of around 0.155. This suggests relative insensitivity of Su to changes in the geometry and angle of attack. For a circular cylinder, a flat plate and a 90° wedge Roshko [159] obtains a mean value of about 0.163. Similarly, Bearman [155] gave a value of 0.181 for a blunt trailing-edge body with either a splitter plate or base bleed. It should be pointed out that their definition of the universal parameter ($Su = f_V h'/U_b$) is somewhat different than the one used here. Figure 5-8(b) show effect of the momentum injection. A small increase in the mean value of Su is observed for the rectangular prism at $U_C/U = 1$. In case of the square prism, the universal Strouhal number is shifted to a higher value with a mean of 0.219.

For a bluff body at a given angle of attack, St_p is known from equation (5.6) and Su can be obtained from Figure 5-8. Now k_1, and hence the base pressure coefficient, can be calculated from equation (5.7). Similarly if the wake pressure is known then the Strouhal number can be obtained at a given angle of attack. Thus correlation between St_p and k_1 confirms the observation made by Roshko [159] that
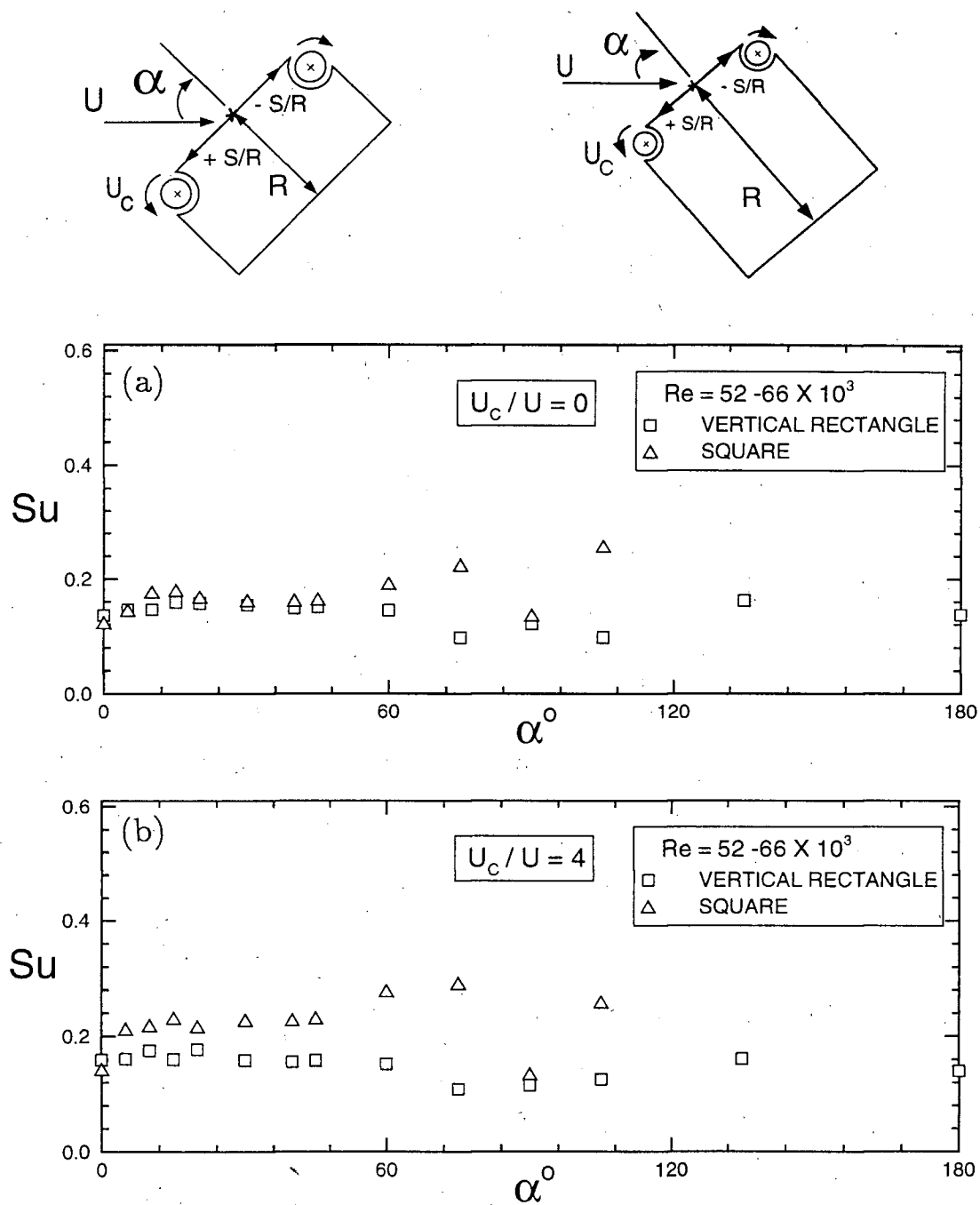
Figure 5-8   Effect of the angle of attack and bluff body geometries on the universal Strouhal number Su: (a) no momentum injection; (b) with momentum injection.

163

the wakes of various bluff bodies are similar except the changes in the geometric and velocity scales.

5.4 Flow Visualization

Figure 5-9 shows the effect of momentum injection on the wake of the rectangular prism (Re = 16,200). For $U_C/U = 0$, the wake is wider than the projected height (h) of the rectangular prism. In fact, measurements from the photographs show that the maximum wake width is around $2h$, and occurs, approximately, the distance 'h' downstream from the base of the body. The region immediately downstream of the body is also the scene of intense periodic pressure and velocity fluctuations caused by the alternately shed vortices. The size of the shed vortex (Figure 5-9a) is nearly comparable to the size of the body. The shed vortices undergo rapid dissipation due to the viscous action. As explained in Section 4.5, the overall wake displays considerable unsteadiness. Introduction of the momentum injection ($U_C/U > 0$) causes the wake to become progressively narrower until it becomes the same as the vertical face of the rectangular prism. Any further increase in the momentum injection beyond $U_C/U = 4$ does not have significant effect on the wake. The extent of the wake along the flow direction is also progressively reduced however, even at $U_C/U = 4$, the wake does not close completely. For sufficiently high rates of the momentum injection ($U_C/U \geq 2$) vortex shedding is completely eliminated, the wake becomes quite small and the overall fluid motion approaches the potential flow character. The reduction in the wake width implies drag reduction, which was confirmed by the wind tunnel tests results presented earlier.

The results for the square prism at $\alpha = 15°$ and $90°$ are shown in Figures 5-10 and 5-11, respectively (Re = 23,400). As seen in Figure 5-10(a), in absence of any momentum injection the top and bottom faces are immersed in a separated flow field. A large vortex can be seen in the process of formation. As U_C/U is increased, the separation at the top disappears completely and the vortex formation is suppressed.

There is an associated rise in the wake pressure which causes the drag coefficient to be lowered as seen before. Note, the stagnation point on the front face has moved away from the mid-point towards the bottom corner. In Figures 5-11 ($\alpha = 90°$), both the cylinders are rotating in the same direction (i.e. clockwise) to achieve a maximum benefit. For $U_C/U = 4$, the wake is nearly eliminated. Figure 5-11(c) shows that the fluid at the top is accelerated, where as at the bottom the speed remains essentially unchanged. A region of low pressure is created on the top of the square prism which explains a large increase in the lift coefficient (Figure 5-5b).

The flow visualization study brings to attention the fact that to obtain a further control of the flow separation, it is necessary to provide rotating elements at all four corners of the body. Figure 5-12 attempts to show, schematically, anticipated flow patterns for a rectangular prism as affected by the momentum injection and angle of attack. At $\alpha = 0$ it is necessary rotate at least cylinders A and B, but the wake does not close completely. To achieve the wake closure, it may be necessary to inject a small amount of momentum ($U_C/U = 1$ or 2) through rotation of cylinders C and D. For $0 \le \alpha \le 90°$, cylinders B, C and D are the most important ones to close the wake. Similarly at $\alpha = 90°$, cylinders A, B would have to rotate clockwise and the cylinders C, D in the counter-clockwise direction to eliminate the wake completely. Such a scheme can be easily implemented using a microprocessor controlled switching actuator in conjunction with a wind direction sensor.

5.5 Summary

The results from the wind tunnel tests and the flow visualization study confirm that application of the momentum injection to the rectangular and the square prisms lead to significant drag reduction. In addition, the vortex shedding is completely suppressed, thereby eliminating the problem of vortex resonance. The width and the length of the wake is reduced considerably, thereby reducing the interaction between the wake and the afterbody, which is primarily responsible for the galloping instability.
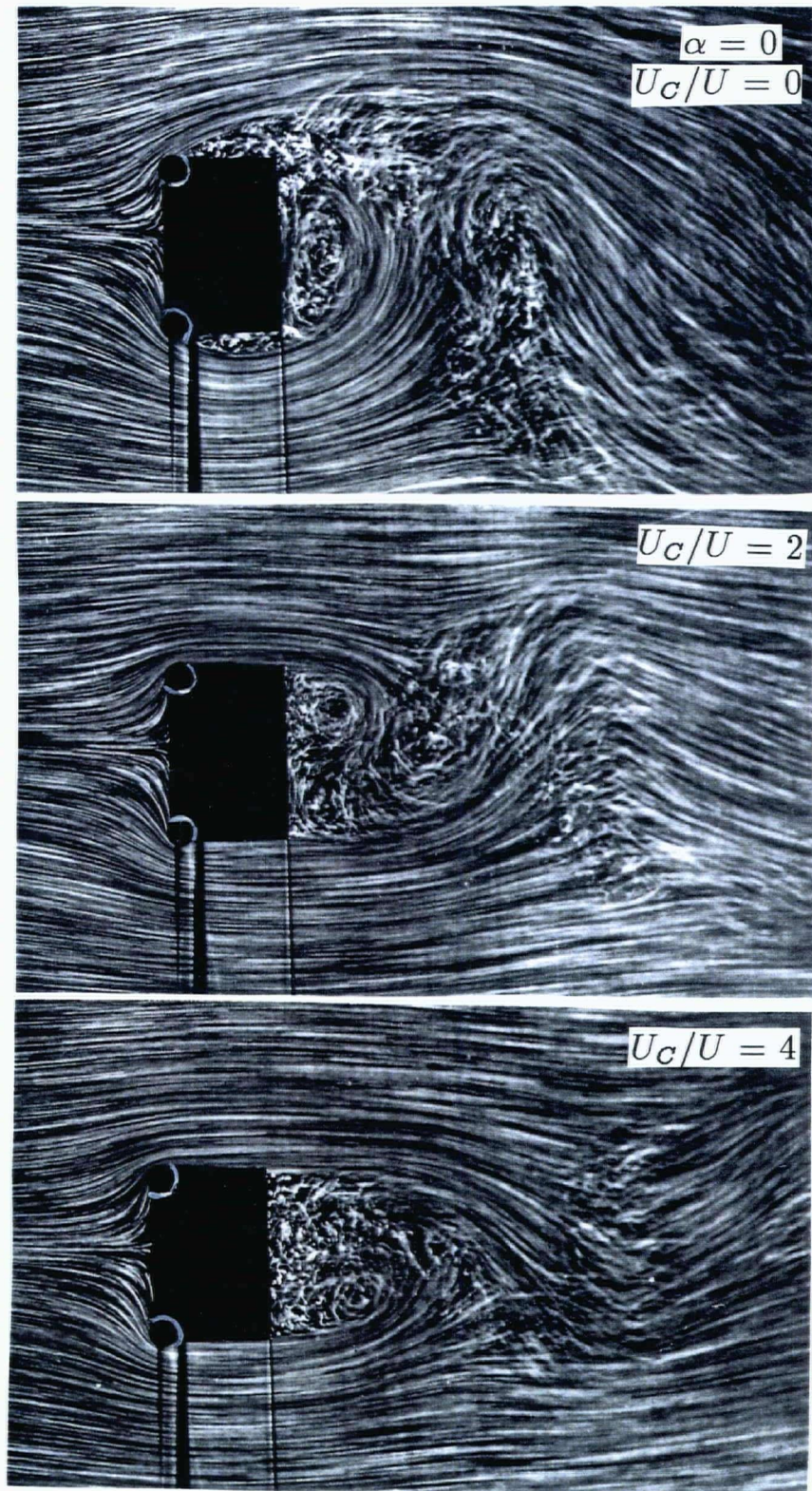
Figure 5-9   Effect of momentum injection on the characteristic features of the wake and the shed vortex system associated with the rectangular prism (AR = 0.5) as observed during the flow visualization study.
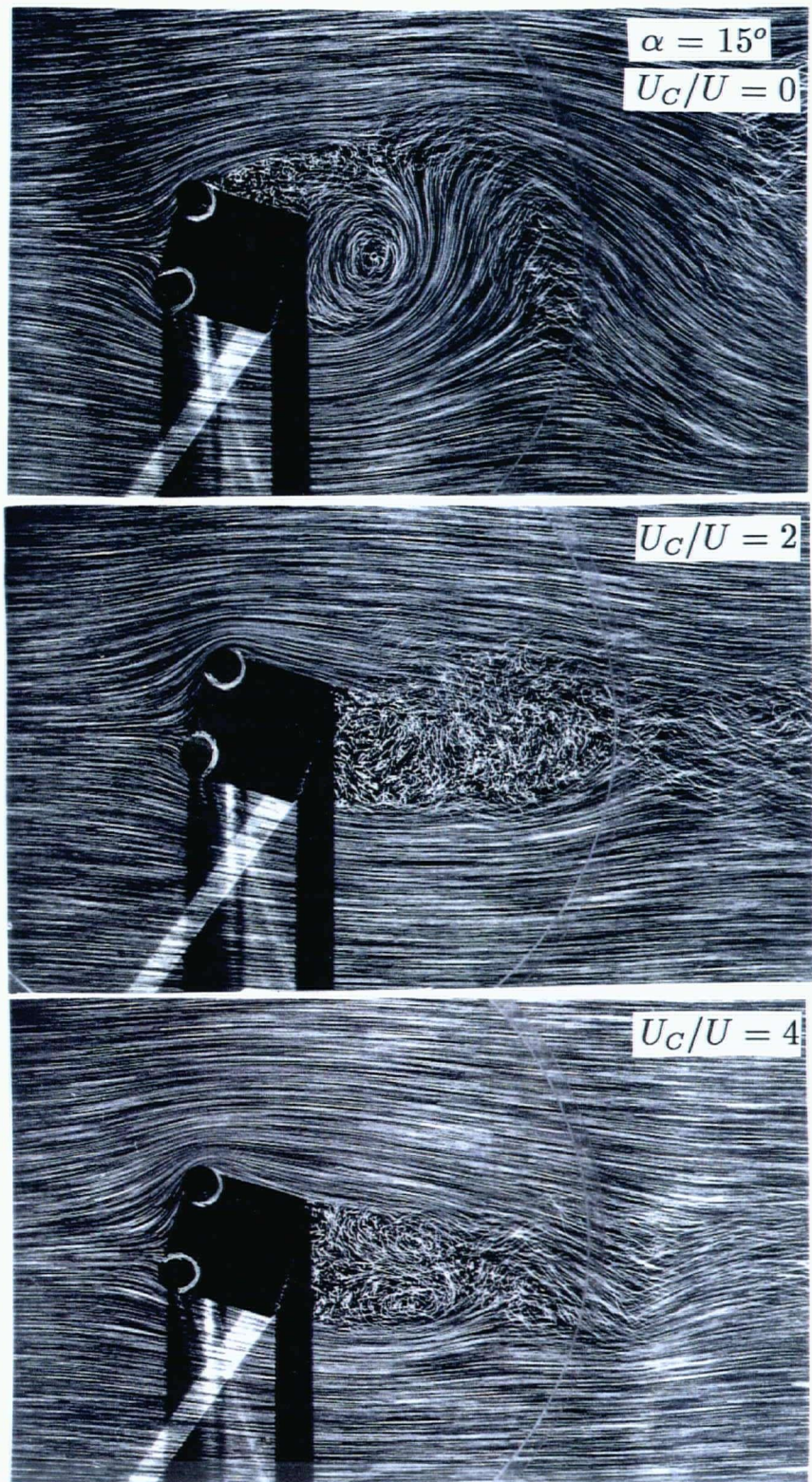
Figure 5-10   Flow visualization pictures showing effect of the momentum injection on the wake of the square prism at $\alpha = 15^\circ$.

167
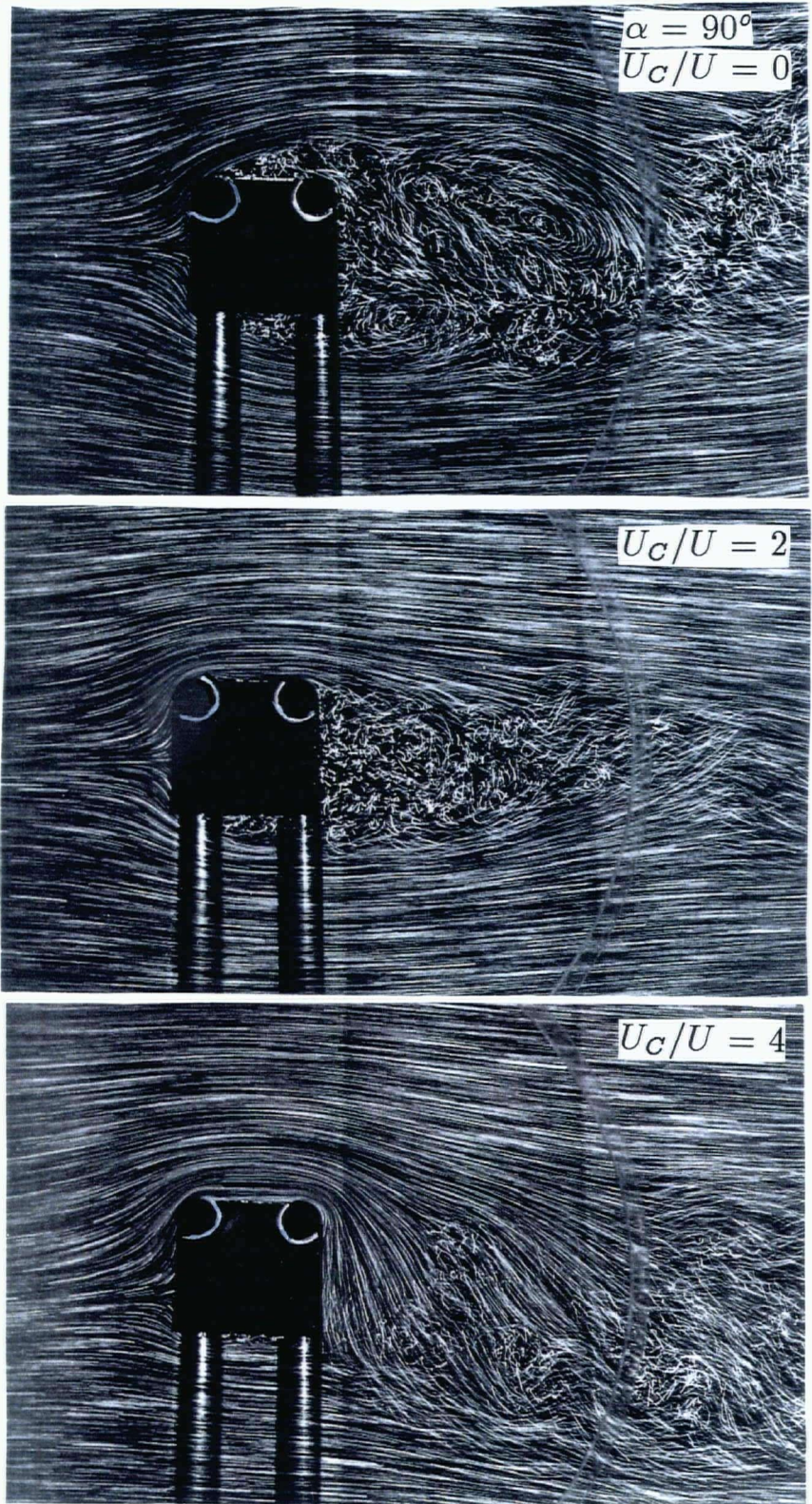
Figure 5-11   Flow visualization pictures for a square prism at $\alpha = 90°$.
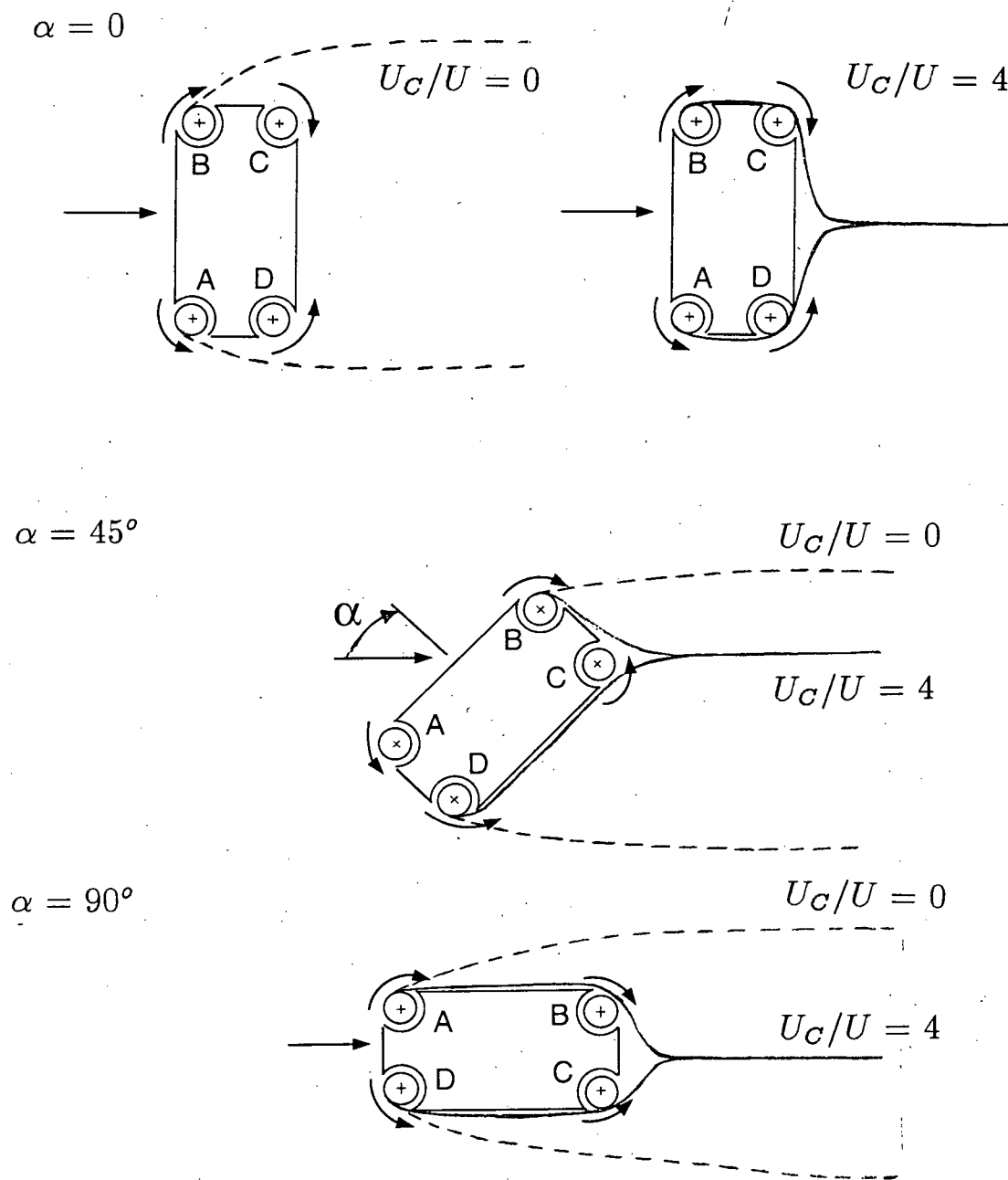
Figure 5-12 A schematic diagram showing possible strategies of momentum injection for a rectangular prism undergoing a change in the angle of attack.

169

A universal Strouhal number (Su), based on the St and the base pressure parameter k, is proposed. The results firmly establish effectiveness of the momentum injection to achieve boundary-layer control of rectangular prisms.

6. BLUFF BODY DYNAMICS IN PRESENCE OF MOMENTUM INJECTION

6.1 Preliminary Remarks

Fluid induced vibrations of bluff structures encountered in practice may be classified into three distinct categories: uncoupled vortex resonance and galloping instabilities, and coupled flutter vibrations. At times, such oscillations could have catastrophic consequences. One of the celebrated and disastrous case on record [160,161] is that of the Tacoma suspension bridge built across the Narrows at Puget Sound in the State of Washington, U.S.A. It had a central span of about 853 meters and a width of 12 meters. Based on several studies [162-164], it is believed that the bridge was destroyed by a combination of more than one type of vibratory phenomena. At the outset, the bridge was found to be prone to vertical oscillations (amplitude $\approx$ 1.27m, frequency $\approx$ 0.62 Hz). In less than five months after opening to the public (on July 1, 1940), the bridge collapsed on 7 November, 1940, in a strong gale of about 67 km/hr. Few hours before failure, torsional oscillations set-in, which eventually led to the collapse. The edges of the bridge had a maximum vertical displacement of about 8.5m with a $\pm45^o$ twist. The frequency of torsional vibrations was about 0.23 Hz. A rough estimate of the power supplied by the wind is about 4000 kW!

A steady wind blowing around a structure can pump energy continuously into the system. Such a fluid loading is nonconservative due to the presence of an energy source. Furthermore, the system dissipates energy through structural and external damping. For a nonconservative system the fluid force can not be derived from a potential function and the Hamiltonian is not a constant of the motion [165]. In the equations of motion describing a structure undergoing flow-induced vibrations, the energy source is normally modelled as a nonlinear function of the structural velocity in the form of negative damping. Such self-excited systems begin to vibrate spontaneously when subjected to a small disturbance, the amplitude increasing, until

a balance is struck between the rate at which the energy is introduced into system and the rate at which it is dissipated. In self-excited vibrations the force sustaining the motion exists because of the motion itself.

The governing equations of motion describing flow-induced vibrations are generally nonlinear and their solutions display a rich variety of physical phenomena generally not found in a linear system. Examples include frequency entrainment or lock-in during vortex resonance, hysterisis and jump in amplitude for galloping instability, as well as relaxation type oscillations due to velocity dependent friction, and others. The investigation reported in this chapter is mainly experimental. Accompanying discussion attempts to clarify the physical mechanism of the process and emphasize the challenge involved in modelling and controlling flow-induced vibrations in practice.

The phenomena of vortex-resonance is briefly touched upon to begin with. Next, the effect of momentum injection in suppressing vortex-resonance is discussed based on the vortex shedding frequency and vibration amplitude measurements. The basic equation of motion governing the galloping instability in plunging is outlined and a simple criterion useful in identifying regions of instability is explained. The criterion is applied using the wind tunnel static test data to predict the dynamic behaviour of bluff bodies (D-section, square and rectangular prisms). Finally, results are presented to demonstrate the effectiveness of momentum injection in suppressing wind induced instabilities, both vortex resonance and galloping. Effect of asymmetric rotation is also touched upon. The chapter concludes with a short summary.

6.2 Control of Vortex Resonance Type Vibrations

6.2.1 Mathematical description

In order to better appreciate how momentum injection affects the vortex-excitation response of a structure, a short description of the model describing vortex-

resonance would be appropriate. The vibrations are in the plane perpendicular to the incident flow under the action of oscillatory pressure loading created by the alternately shed vortices. Ideally, the governing equations for this problem are the dynamic equation of motion for the bluff body and the time-dependent Navier-Stokes equations for the fluid flow. Flow separation and vortex shedding would be the natural outcome of their solution, which would also provide the forcing function acting on the bluff body. This could be accomplished through an appropriate numerical scheme implemented on a computer. It, of course, would entail enormous amount of time and effort.

As a closed-form solution of the Navier-Stokes equations is not available, considerable efforts have been expended in developing simpler models based on physical considerations. Among others, the wake-oscillator model by Hartlen and Currie [166] and the Iwan-Blevins model [167,168] are quite well known. Consider the Iwan-Blevins model in brief. It utilizes a van der Pol type equation [169-171] with a 'hidden' flow variable to simulate the effect of the vortex shedding (Figure 6-1a). The governing equations are:

$$\frac{d^2z}{dt^2} + K'\frac{u_t}{U}\frac{U}{D}\omega_v z = (a_1' - a_4')\frac{U}{D}\left(\frac{dz}{dt}\right) - a_2'\frac{1}{UD}\left(\frac{dz}{dt}\right)^3 + a_3'\frac{d^2y}{dt^2} + a_4'\frac{U}{D}\frac{dy}{dt}; \quad (6.1)$$

$$\frac{d^2y}{dt^2} + 2\zeta_t\omega_n\frac{dy}{dt} + \omega_n^2 y = a_3''\frac{dz}{dt}\frac{U}{D} + a_4''z\frac{U}{D}; \quad (6.2)$$

where: $a_i'' = \rho D^2 a_i/(m + a_3\rho D^2), i = 3, 4;$ $\qquad a_i' = a_i/(a_0 + a_3), i = 1, 2, 3, 4;$

$\qquad \omega_n = \sqrt{k/m}/[1 + (a_3\rho D^2)/m]; \quad \zeta_t = [(\zeta\sqrt{k/m})/\omega_n + \zeta_f]/(1 + a_3\rho D^2/m);$

$\qquad \zeta_f = a_4\rho DU/(2m\omega_n);$

ζ = system damping ratio; ζ_t = total effective damping ratio; ζ_f = viscous fluid damping ratio; k = stiffness; m = structure mass per unit length; ρ = density of fluid; D = body characteristic dimension; ω_v = circular frequency of vortex shedding; ω_n =

system circular natural frequency; U= freestream velocity; u_t = translational velocity of the vortex street; $\dot{z}$ = 'hidden' fluid variable (dz/dt) which can be considered as the weighted average of the transverse component of the flow velocity within the control volume; y = coordinate describing transverse displacement, t = time; a_i = dimensionless constants; $K' = K / (a_0 + a_3)$, and K = proportionality constant.

Equation (6.1) describes an autonomous nonlinear fluid oscillator coupled with equation (6.2), which is a linear differential equation describing motion of the bluff body. The first term on the right-hand-side of equation (6.1) represents negative damping, meaning extraction of energy from the freestream fluid and delivering it to the structure in motion, which causes build-up of the vibrations. The second term on the right is cubic (in velocity) which eventually limits the amplitude of the vibrations. The terms on the left-hand-side of equation (6.1) represent the feedback between the wake and the boundary-layer on the bluff body. The terms on the right-hand side of equation (6.2) represent the excitation which couple the two equations.

The frequency of vortex shedding (f_V) varies proportionally as the wind speed is increased from zero. At some critical value of the wind speed, it coincides with the natural frequency (f_n) of the bluff structure resulting in resonance (Figure 6-1a). This can also be explained by employing the concepts of bifurcation and catastrophe as applicable to nonlinear dynamical systems in the phase space [172-179]. The change in behaviour as described by transition from stability to instability and vice versa due to variation in a given parameter is known as bifurcation. Mathematically, "Catastrophe" describes a point in some parameter space at which a dynamical system loses structural stability, so that its solutions change their topological type [174]. Nonelementary catastrophes have a more dynamic nature, one example being the Hopf bifurcation [179] to a limit cycle. For a real life bluff structure, generally all parameters (e.g. stiffness, mass, internal damping etc.) remain fixed, except the fluid velocity. If the fluid velocity is increased form zero, the solution in the phase space $(y, \dot{y}, t)$ in

174

$$\dot{z} = \frac{1}{a_O \rho D^2} \iint_A v\,dx\,dy$$

ρ = FLUID DENSITY

v = VERTICAL VELOCITY OF
   THE FLUID IN WAKE

a_0 = CONSTANT OF PROPORTIONALITY
   DETERMINED FROM THE EXPERIMENT

f_V = VORTEX SHEDDING FREQUENCY

f_n =   STURE NATURAL FREQUENCY

$f_V = f_n$ at resonance
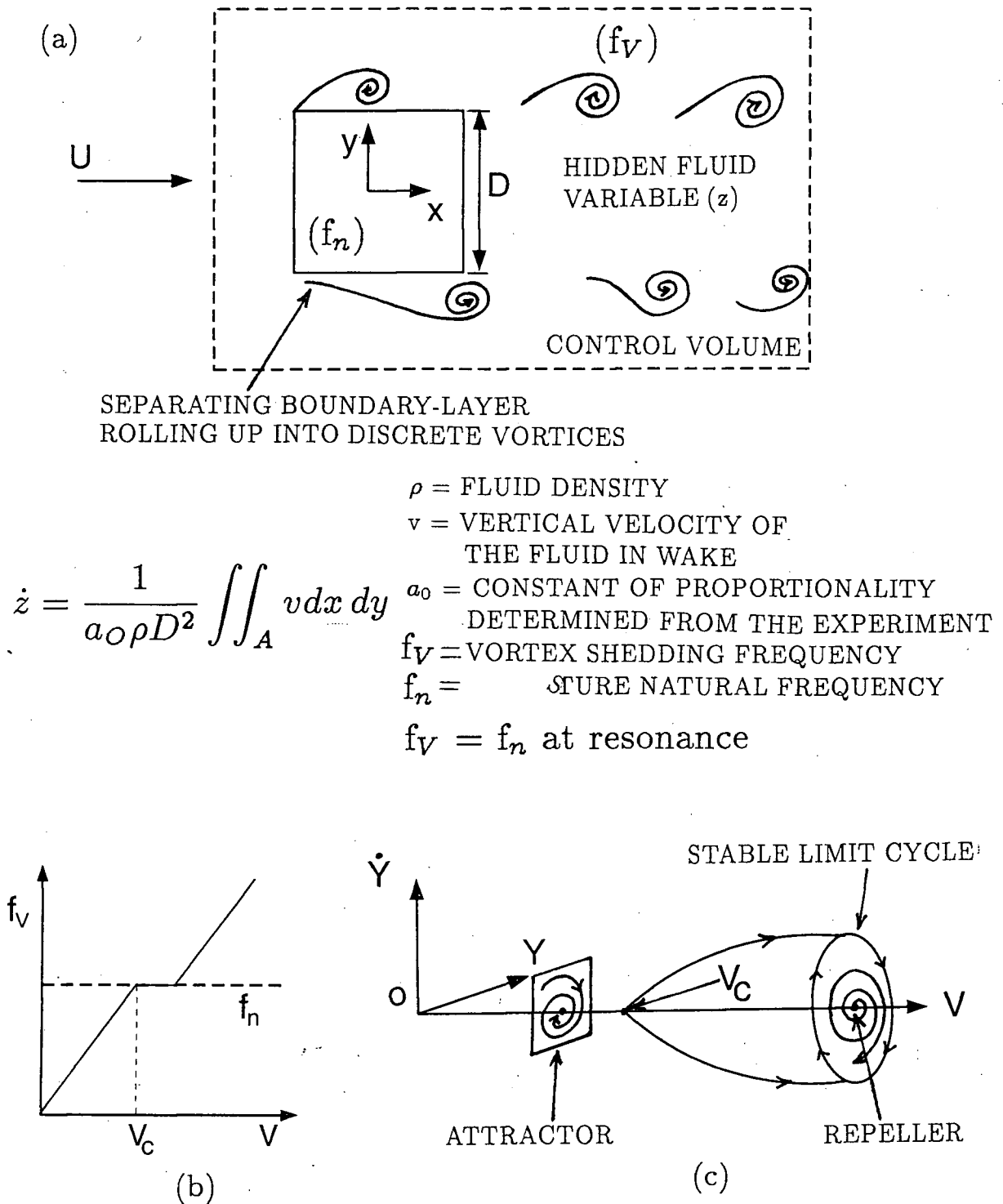
Figure 6-1   Schematic diagram showing a bluff structure experiencing vortex excitation: (a) physical model; (b) variation of vortex shedding frequency and resonance; (c) phase space representation of the dynamical model.

the form of a singularity at the origin (i.e. a stable focus representing the equilibrium position) can transform itself into a growing limit cycle (enclosing an unstable focus) at some critical velocity. An unstable focus under the action of small perturbations (e.g. a wind gust) gives rise to a limit cycle whose amplitude is a function of the fluid velocity. Figure 6-1(b) shows schematically the topological behaviour of a self-excited system. A stable focus/limit cycle acts as an attractor since all perturbations away from it are damped out. Similarly, an unstable focus/limit cycle acts as a repeller as all perturbations away from it tend to grow. The characteristic equation derived from the equation of motion has complex roots (eigenvalues) with positive real part in the region of instability [173]. This situation is the exact opposite of a damped linear oscillator (which has negative real roots). The model also successfully explains the entrainment of the vortex shedding frequency by the natural frequency of the system.

It is apparent that the vortex resonance vibrations arise out of the nonlinear interactions between the vortex wake and the bluff body. Unfortunately, the fluid dynamics during vortex shedding, especially in the near-wake region, is rather complex and no exact solution to the fluid-structure interaction problem has yet been found. Any attempt to control the vortex resonance could greatly benefit by preventing the very process of vortex formation. This is where momentum injection could prove useful. The control of boundary-layer separation and resulting suppression of alternate vortex shedding would mathematically imply vanishing of the hidden fluid variable dz/dt and hence an elimination of the forcing terms in equation (6.2).

6.2.2 Suppression of the vortex shedding

Figure 6-2 presents typical set of results showing the effect of the momentum injection on the vortex shedding for a D-section. Similar results were obtained for all the bluff bodies (D-section, square and rectangular prisms) at various angles of attack, without and with momentum injection. As described in Section 2.2.3, the vortex shedding frequency and the signal amplitude were obtained by performing
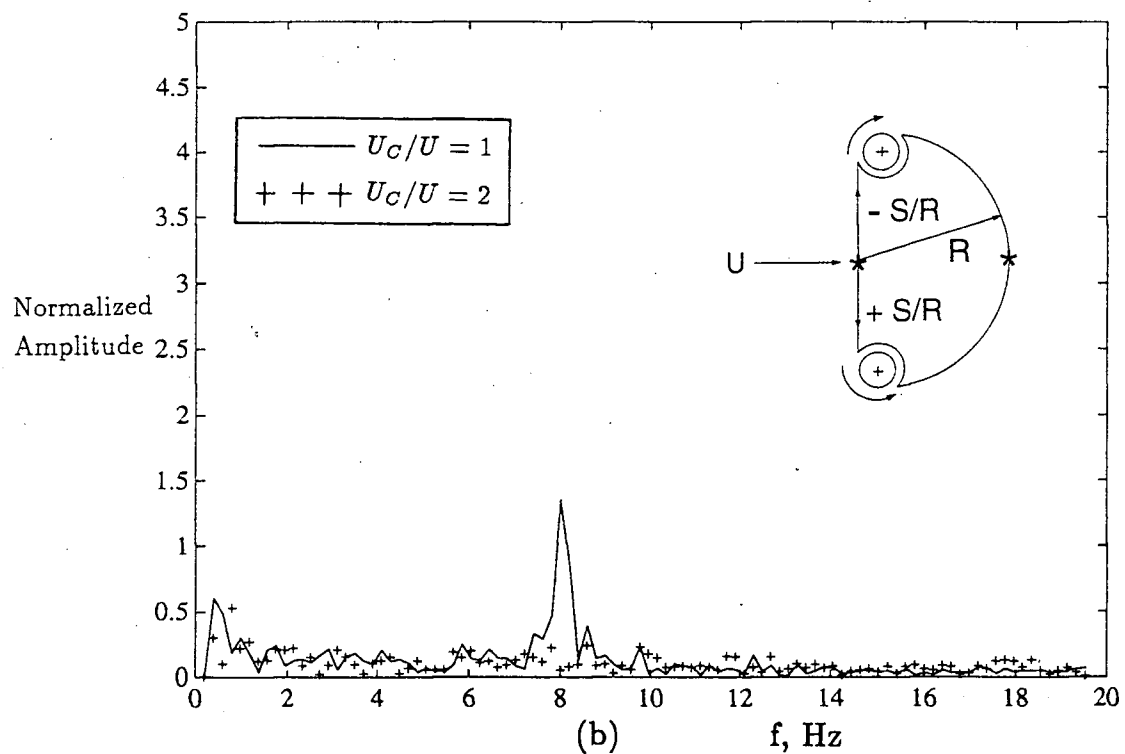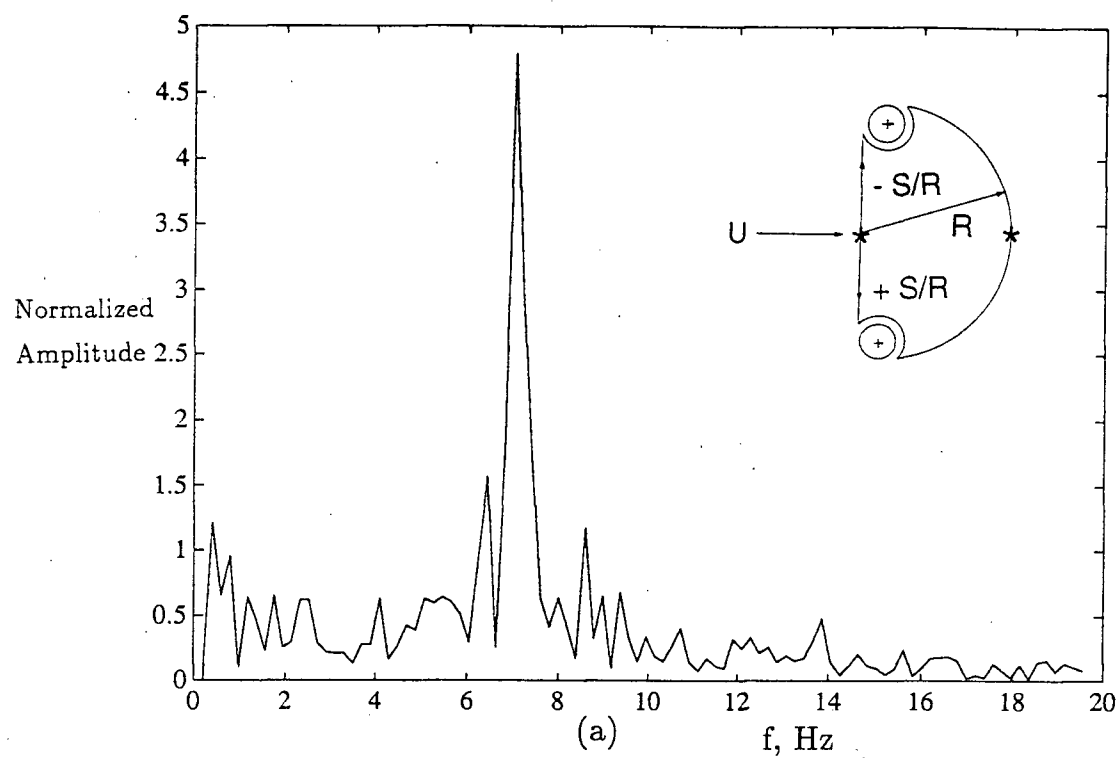
Figure 6-2   Power spectral representation of the wake pressure showing reduction in the strength of the shed vortex in presence of the momentum injection: (a) $U_C/U = 0$; (b) $U_C/U = 1, 2$.

the Fast Fourier Transform (FFT) analysis on the time dependent pressure signals, obtained through the data acquisition system. The trailing vortices cause pressure fluctuations as they are convected downstream in the wake. The dominant frequency in the pressure signal is the vortex shedding frequency. The amplitude of the signal is a measure of the strength of the shed vortex. In absence of momentum injection ($U_C/U = 0$), Figure 6-2(a) clearly shows the vortex shedding at $f_v = 7.0$ Hz, with a large signal amplitude. For a small amount of momentum injection ($U_C/U = 1$), the vortex shedding becomes much weaker as indicated by the drop in the signal strength (Figure 6-2b). Also, the frequency of vortex shedding has increased to about $f_v = 8.0$ Hz. The corresponding Strouhal number (St) increases from 0.208 ($U_C/U = 0$) to 0.237 ($U_C/U = 1$) suggesting a reduction in the effective bluffness. At $U_C/U = 2$, the vortex shedding is virtually eliminated since no pressure fluctuations could be detected. This fact is also confirmed by the flow visualization photographs and a video movie. The complete suppression of the vortex shedding in presence of momentum injection can be interpreted in terms of the interaction between the wake and the bluff body. The introduction of the momentum injection reduces the extent of the wake and delays the separation of the boundary-layer. Mathematically this amounts to setting z and dz/dt equal to zero in equations (6.1) and (6.2). The fluid in the wake no longer rolls-up into vortices. The momentum injection prevents transfer of the convective energy in the wake to the structure thus preventing growth of structural vibrations.

6.3 Control of Galloping Type of Instability

All bluff bodies with noncircular cross-sections are susceptible to self-excited oscillations referred to as galloping. Pure galloping is a single degree of freedom phenomena in which the body experiences plunging vibrations in a plane perpendicular to the direction of the flow. Because of the inherent difficulties in modelling unsteady

aerodynamics around a vibrating structure, it becomes necessary to invoke the concept of quasi-steady flow, i.e. the aerodynamic force on a bluff body in motion, having a certain instantaneous orientation, can be approximated by a force acting on a fixed body having the same angle of attack. Any changes in the aerodynamic force arising out of the unsteadiness in the flow are neglected. This assumption has proved generally valid as demonstrated by Parkinson and Brooks [180], Novak [84], and others. The quasi-steady analysis works well at higher fluid velocities in the range of $U/\omega_n D \geq 3$ where U = freestream velocity; ω_n = circular natural frequency of the structure; and D = characteristic dimension of the structure. For $U/\omega_n D \leq 3$, quasi-steady analysis is questionable due to the likelihood of vortex-resonance. The problem of galloping instability has received considerable attention in the past with important contributions from Parkinson [19], Novak [84,181], Richardson [182], Blevins [71], Lawson [183], and others. In the next section mathematical description of galloping instability is briefly reviewed to emphasize key parameters governing the vibrations [19,71, 84, 157, 181]. Further details pertaining to nonlinear dynamics of self-excited vibration can be found in references [172-179].

6.3.1 Criterion for determining the galloping instability

Consider a tall bluff structure with square cross-section undergoing galloping type of oscillations (Figure 6-3). The stiffness (k) and the internal damping (r_1) of the structure are assumed to be linear. By convention, the structural motion is considered positive (+y) downwards. The resultant fluid velocity ($-\dot{y}$) acts upwards. Please note that this transverse motion in reality lies in a horizontal plane. The instantaneous angle of attack (α) is given by

$$\alpha = tan^{-1}\frac{\dot{y}}{U},\tag{6.3}$$

where $\dot{y} = dy/dt$.

The lateral aerodynamic force ($-F_y$) is in the upward direction and opposes the motion. The absolute value of F_y is not of concern here, but its variation with respect

$$\alpha = tan^{-1}\left(\frac{\dot{y}}{U}\right)$$

CROSS-SECTION OF A BLUFF
STRUCTURE (MASS, $\dot{m}$)
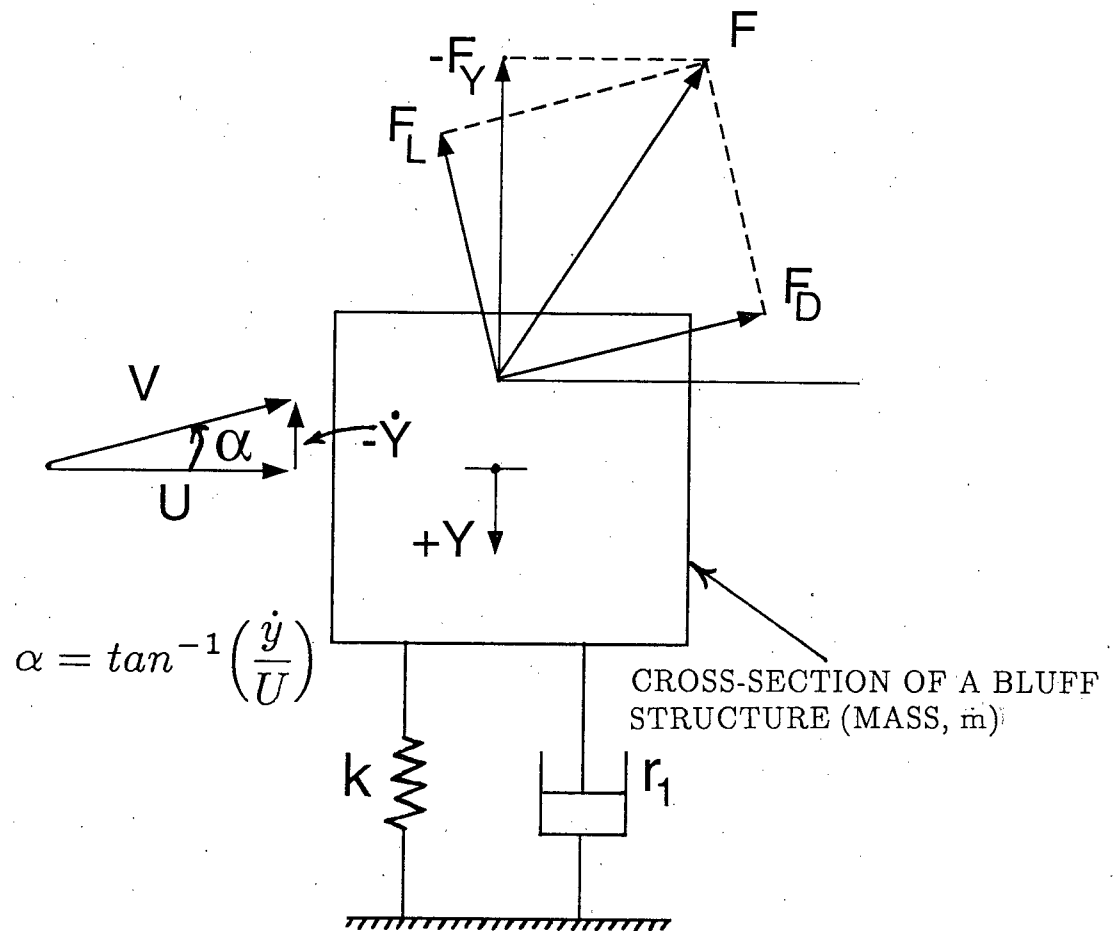
$$\frac{d(-F_Y)}{d\alpha} < 0 \Rightarrow \frac{dF_Y}{d\alpha} > 0 \qquad \text{FOR INSTABILITY}$$

$$m\ddot{y} + r_1\dot{y} + ky = -F_Y(\alpha)$$

Figure 6-3   A bluff structure experiencing galloping and the criterion for instability.

to α determines the stability of the structure. If F_y increases with α, then a sudden transverse motion (+y) of the structure (possibly caused by a wind gust) would increase α and hence decrease the aerodynamic force (-F_y) opposing the motion. This would leave the structure more vulnerable to further displacement. Such a situation is clearly unstable. For most aerodynamic shapes $dF_y/d\alpha < 0$, and the structure remains stable. But, for some rectangular geometries (0.75 ≤ AR ≤ 3) there is a likelihood of $dF_y/d\alpha$ to be negative in a certain range of α. The D-section is neutrally stable in a smooth flow ($dF_y/d\alpha = 0$) for $0 \leq \alpha \leq 30°$, but becomes unstable at $\alpha = 11°$ in a turbulent flow [184]. The criterion for instability is

$$\frac{dF_y}{d\alpha} > 0. \tag{6.4}$$

The aerodynamic forces are given as:

$$F_D = C_D \frac{1}{2}\rho h l V_1{}^2; \tag{6.5}$$

$$F_L = C_L \frac{1}{2}\rho h l V_1{}^2; \tag{6.6}$$

$$F_y = C_y \frac{1}{2}\rho h l U^2; \tag{6.7}$$

with

$$cos\alpha = \frac{U}{V_1}. \tag{6.8}$$

The lateral aerodynamic force can be expressed as

$$F_y = -(F_L cos\,\alpha + F_D sin\,\alpha). \tag{6.9}$$

Substituting the expressions for F_D and F_L in equation (6.9) and simplifying gives

$$C_y = -(C_L + C_D tan\,\alpha)sec\,\alpha. \tag{6.10}$$

Equation (6.11) can be used to evaluate the lateral force coefficient (C_y) from the drag and the lift coefficients obtained through static wind tunnel tests. At $\alpha = 0$, the

instability criterion becomes

$$\frac{dC_y}{d\alpha} = -\left[\frac{dC_L}{d\alpha} + C_D\right] > 0,$$
(6.11)

i.e.

$$\frac{dC_L}{d\alpha} + C_D < 0.$$
(6.12)

Equation (6.12) represents the Den Hartog criterion [154] for instability.

The equation of motion governing the vibrations is

$$m\ddot{y} + r_1\dot{y} + ky = F_y.$$
(6.13)

The lateral force coefficient (C_y) is a function of α, and therefore of $\tan\alpha = \dot{y}/U$. C_y can be approximated by a polynomial in $\dot{y}/U$ over the pertinent range of α. It is an odd function by the reason of symmetry, and requires at least a seventh degree polynomial for a close fit [18],

$$C_y(\alpha) = P_1\left(\frac{\dot{y}}{U}\right) - P_3\left(\frac{\dot{y}}{U}\right)^3 + P_5\left(\frac{\dot{y}}{U}\right)^5 - P_7\left(\frac{\dot{y}}{U}\right)^7.$$
(6.14)

The equation of motion now becomes

$$m\ddot{y} + r_1\dot{y} + ky = \frac{1}{2}\rho h l U^2 \left[P_1\left(\frac{\dot{y}}{U}\right) - P_3\left(\frac{\dot{y}}{U}\right)^3 + P_5\left(\frac{\dot{y}}{U}\right)^5 - P_7\left(\frac{\dot{y}}{U}\right)^7\right].$$
(6.15)

The P_i (i=1,3,5,7) are the coefficients of the expansion and can be obtained from the curve of C_y against α using the least square technique. Defining nondimensional variables as:

$$Y = y/h;\ \tau = \omega t;\ \omega^2 = k/m;\ V = U/(\omega h);\ n = \rho h^2 l/(2m);\ \beta = r/(2m\omega);$$

i.e.

$$\ddot{Y} + 2\beta\dot{Y} + Y = nV^2 C_Y,$$
(6.16)

i.e.

$$\ddot{Y} + Y = nP_1\left[\left(V - \frac{2\beta}{nP_1}\right)\dot{Y} - \left(\frac{P_3}{P_1V}\right)\dot{Y}^3 + \left(\frac{P_5}{P_1V^3}\right)\dot{Y}^5 - \left(\frac{P_7}{P_1V^5}\right)\dot{Y}^7\right], \quad (6.17)$$

where $\dot{Y} = dY/d\tau$. This is a nonlinear ordinary differential equation. As a first approximation, neglecting the third and higher degree terns in $\dot{Y}$ gives the total damping as

$$nP_1\left(V - \frac{2\beta}{nP_1}\right).$$

Here the term β represents the internal damping of the structure, which remains constant. As long as the fluid velocity $V < 2\beta/(nP_1)$, there is a net positive damping, i.e. dissipation of energy. At some critical velocity, $V_C = 2\beta/(nP_1)$, the total damping is zero and beyond that the damping becomes negative leading to the galloping instability. In general, for a given structure, the system parameters (e.g. stiffness, mass, internal damping, etc.) remain fixed, and the only control variable is the fluid velocity. The fluid in motion can pump energy into the system causing build-up of large, low frequency vibrations. The higher order terms in equation (6.17) eventually limit the amplitude of motion. The resultant oscillatory motion has a character of a limit cycle in the phase plane $(\dot{Y}, Y)$. As V increases from zero and crosses V_C, a stable focus (attractor) bifurcates into an unstable focus (repeller) with a growing limit cycle. In fact, as demonstrated by Parkinson and Smith [18], the characteristic equation representing the galloping motion is a cubic and its roots describe a family of stable and unstable limit cycles in the phase plane. In equation (6.17), the highest derivative being of the second order, it is not possible to observe a class of chaotic bifurcations known as strange attractors. To put it differently, the system loses structural stability (in some parameter space) so that the solution changes its topological character. With momentum injection the system has one additional control parameter, U_C/U. Section 6.4 discusses how an originally unstable bluff body $(V > V_C)$ can be stabilized by a systematic variation of U_C/U.

6.3.2   Instability prediction based on static aerodynamic tests

The plots of C_y vs. α for the D-section as well as the rectangular and square prisms are presented in Figure 6-4. As explained in Section 6.3.1, these results were obtained from the lift and drag data obtained through the wind tunnel tests. The test Reynolds number ranged form $52 \times 10^3 - 66 \times 10^3$. The D-section is neutrally stable (Figure 6-4a) as $dC_y/d\alpha = 0$ in the range $0 \leq \alpha \leq 20°$. The presence of rotating cylinders has the effect of rounding the corners of the D-section. Parkinson and Brooks [180] have reported stability study of a D-section with sharp corners. The results for the two cases (model with sharp corners and round corners) were found to be identical upto $\alpha = 20°$. As obvious from Figure 6-4, the stability of the D-section significantly improves $(dC_y/d\alpha < 0)$ in presence of the momentum injection $(U_C/U = 2, 4)$. In the range $20° < \alpha < 30°$, there is a mild tendency towards instability. The region of concern is $30° < \alpha < 40°$, where $dC_y/d\alpha = +2.1$ at $U_C/U = 0$, and the D-section would exhibit strong instability. The unstable behaviour of the D-section at around $40°$ has been reported by Parkinson and Brooks [180]. However, in presence of the momentum injection $(U_C/U = 4)$, the stability is restored completely. Overall, there is a marked improvement in the stability of the D-section with momentum injection.

Results for the rectangular prism (Figure 6-4b) show similar trends in the range $\alpha \leq 20°$, with the system maintaining neutral stability. This is expected due to similarity in their shapes. This is in accord with the results obtained by Parkinson and Brooks [180] for a rectangular prism with sharp edges. In presence of momentum injection $(U_C/U = 4)$, there is a marked improvement in the stability as $dC_y/d\alpha \approx -3.7$. Even in absence of momentum injection $(U_C/U = 0)$, the rectangular prism is stable in the range $20° < \alpha < 45°$ $(dC_y/d\alpha \approx -2.7)$. In presence of the momentum injection, $dC_y/d\alpha$ becomes more negative (≈ -3.0) suggesting further increase in stability.

184
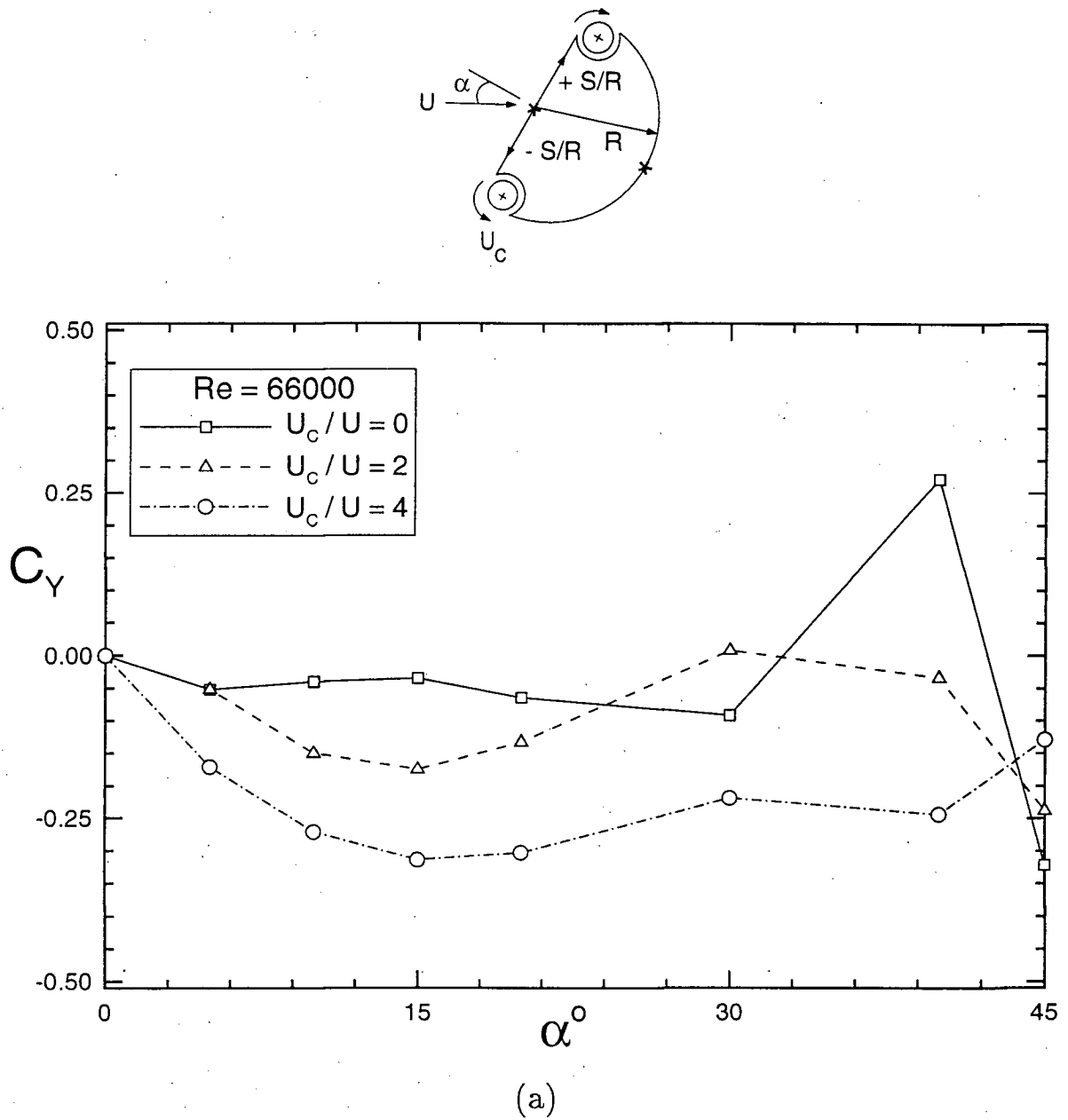
Figure 6-4(a) Influence of the momentum injection on the lateral force coefficient for the D-section. The criterion for galloping instability is $dC_y/d\alpha > 0$. Note a marked improvement in the stability with the momentum injection ($U_C/U = 4$).

(b)
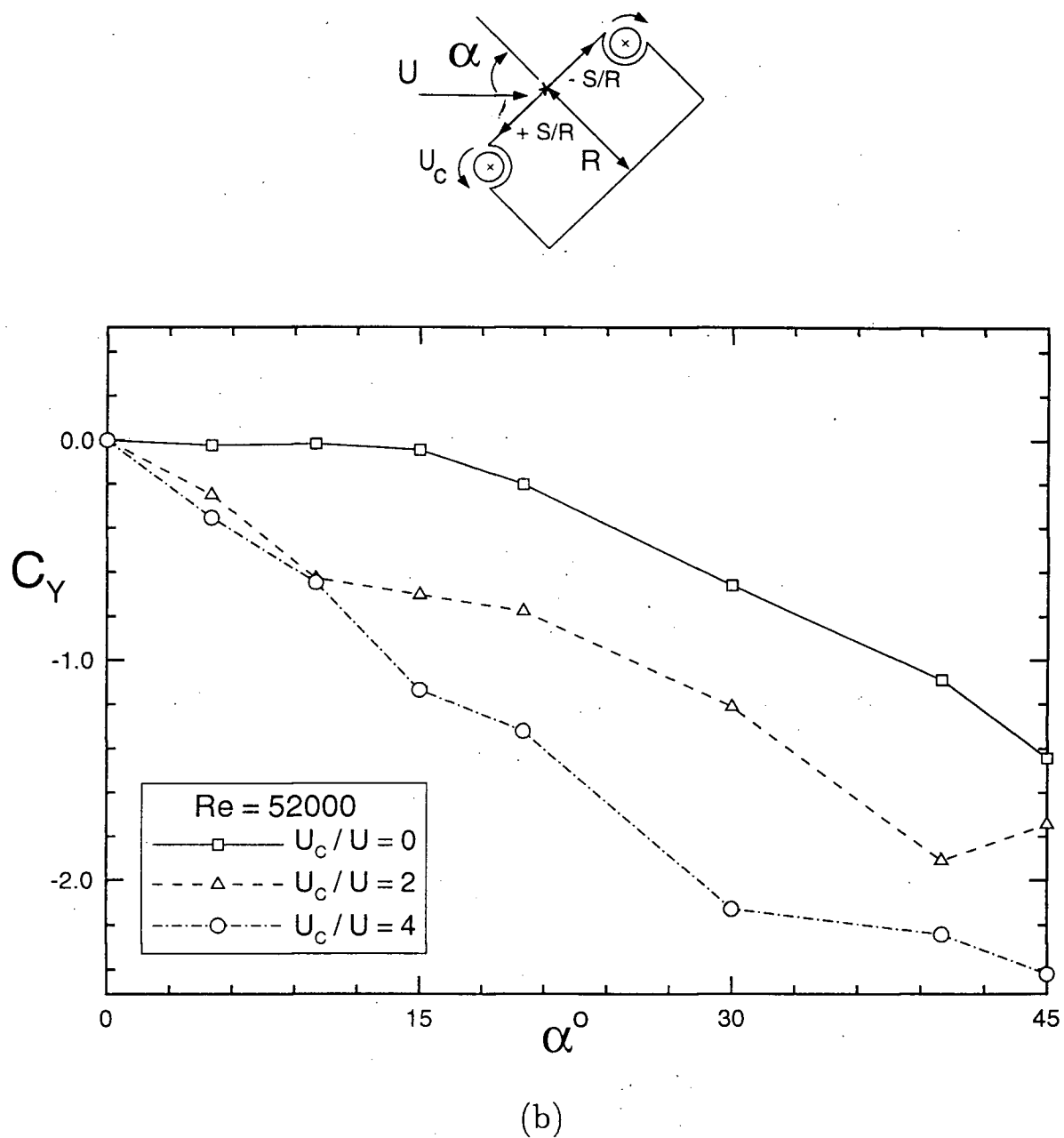
Figure 6-4(b) The rectangular prism is neutrally stable $(dC_y/d\alpha = 0)$ for $\alpha \leq$ 20° in absence of momentum injection $(U_C/U = 0)$. The stability is significantly improved $(dC_y/d\alpha < 0)$ with the cylinder rotation $(U_C/U = 2, 4)$.
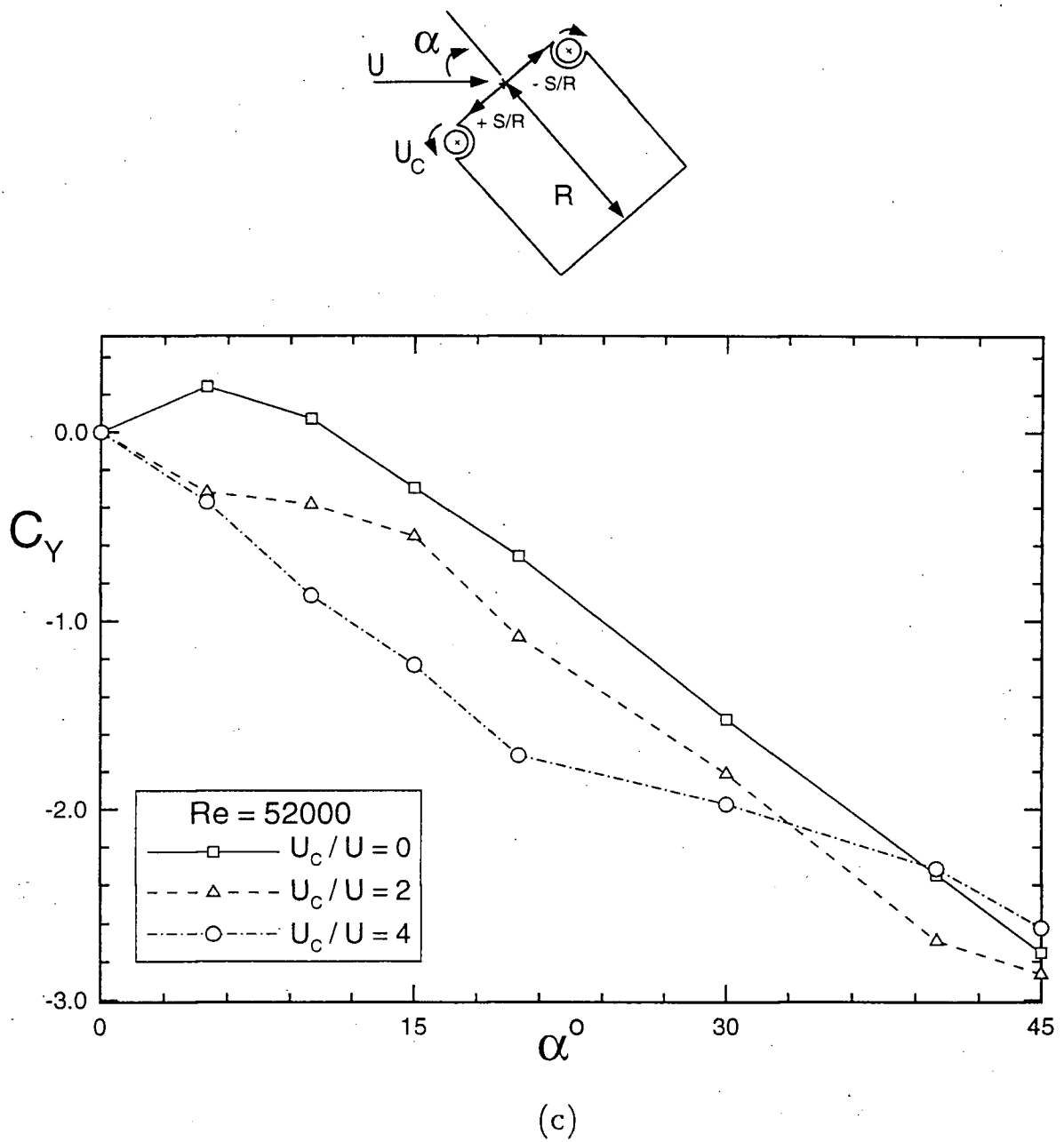
Figure 6-4(c) The square prism is unstable $(dC_y/d\alpha > 0)$ for $\alpha \leq 5^o$ in absence of momentum injection $(U_C/U = 0)$. With the cylinder rotation $(U_C/U = 2, 4)$ the stability is restored completely $(dC_y/d\alpha < 0)$.

The results for the square prism are shown in Figure 6-4(c). For $0 < \alpha < 5^{o}$, the system shows strong instability ($dC_y/d\alpha \approx +2.6$) in absence of the momentum injection. For $5^{o} \leq \alpha \leq 45^{o}$, $dC_y/d\alpha < 0$, and the square prism is stable. In presence of the momentum injection ($U_C/U = 4$), $dC_y/d\alpha$ becomes -4.6 ($\alpha \leq 5^{o}$) and the stability is restored. It may be pointed out that C_y vs. α curve for the square prism with rounded corners is somewhat different from that obtained by Parkinson and Brooks [180], though the general trend is similar. In the present case, the region of instability extends from 0 to 5° for the prism with round corners, whereas it is 0 to 15° for the prism with sharp corners. Thus, interestingly, mere presence of cylinders at the corners of the upstream face ($U_C/U = 0$) significantly reduces the range of galloping instability of a square prism.

6.4 Confirmation Through Dynamic Experiments

Though the wind tunnel data provide sufficient information to predict possible susceptibility of a structure to galloping instability, it was considered appropriate to conform the predictions through experiments. There are several reasons for this. In actual practice, a structure (e.g. a tall building with complicated geometry) is exposed to a a fluid stream that is normally turbulent. The structure generally has nonlinear elastic and damping characteristics. It is also known that vortex resonance could set in for any structure if the vortex shedding and structural frequencies are close enough. Thus it is necessary to confirm the effect of momentum injection in controlling both the vortex resonance and the galloping type of instabilities through actual dynamic experiments. Such experiments were performed on elastically mounted bluff body models (D-section, rectangular and square prisms) free to oscillate transverse to the flow in the wind tunnel. The description of the experimental set-up was explained in Section 2.2.4. The determination of the system parameters (total damping, natural frequency, mass, stiffness etc.) and the calibration of the displacement transducer

are given in Appendix D. The damped natural frequency of the system was found to be very close to the undamped frequency. The experiments were carried out at zero angle of attack.

6.4.1 Dynamical response of the square prism

Figures 6-5 to 6-7 show the amplitude response of the square prism at $\alpha = 0$ as affected by the momentum injection and damping. In absence of the momentum injection, as the wind speed (V) is increased form zero, the square prism experiences vortex- resonance (Figure 6-5) in the range of $0.9 \leq V \leq 1.25$. This finite band of velocities indicate the entrainment of the vortex shedding frequency by the system natural frequency. For $V > 1.25$, the square prism becomes stable as the vortex shedding frequency is now higher than the system natural frequency. With a further increase in the wind velocity, there is an onset of galloping instability at $V_C \approx 2.0$. Beyond this the amplitude of vibration grows quickly to its limiting value $(Y = 0.26)$. Any further increase in the wind velocity does not change the overall dynamical response. In contrast to this, with the momentum injection corresponding to U_C/U $=1$, the square prism does not exhibit either vortex resonance or galloping. The stability of the prism is restored completely. This is in accord with the prediction based on the simple stability criterion mentioned earlier. It is remarkable that despite completely different mechanisms responsible for vortex resonance and galloping type of instabilities, the momentum injection is effective in suppressing both of them.

With an increase in the damping coefficient (β) from 0.2693% to 0.9311% (Figure 6-6), the maximum amplitude of the vibrations is considerably reduced, both for the vortex resonance and galloping. As before, a small amount of momentum injection again restores the stability.

In the previous two cases, both the cylinders were made to rotate so as to inject momentum downstream. One can disrupt formation of the vortex street by rendering the flow asymmetric. This can be achieved by rotating only one of the

189
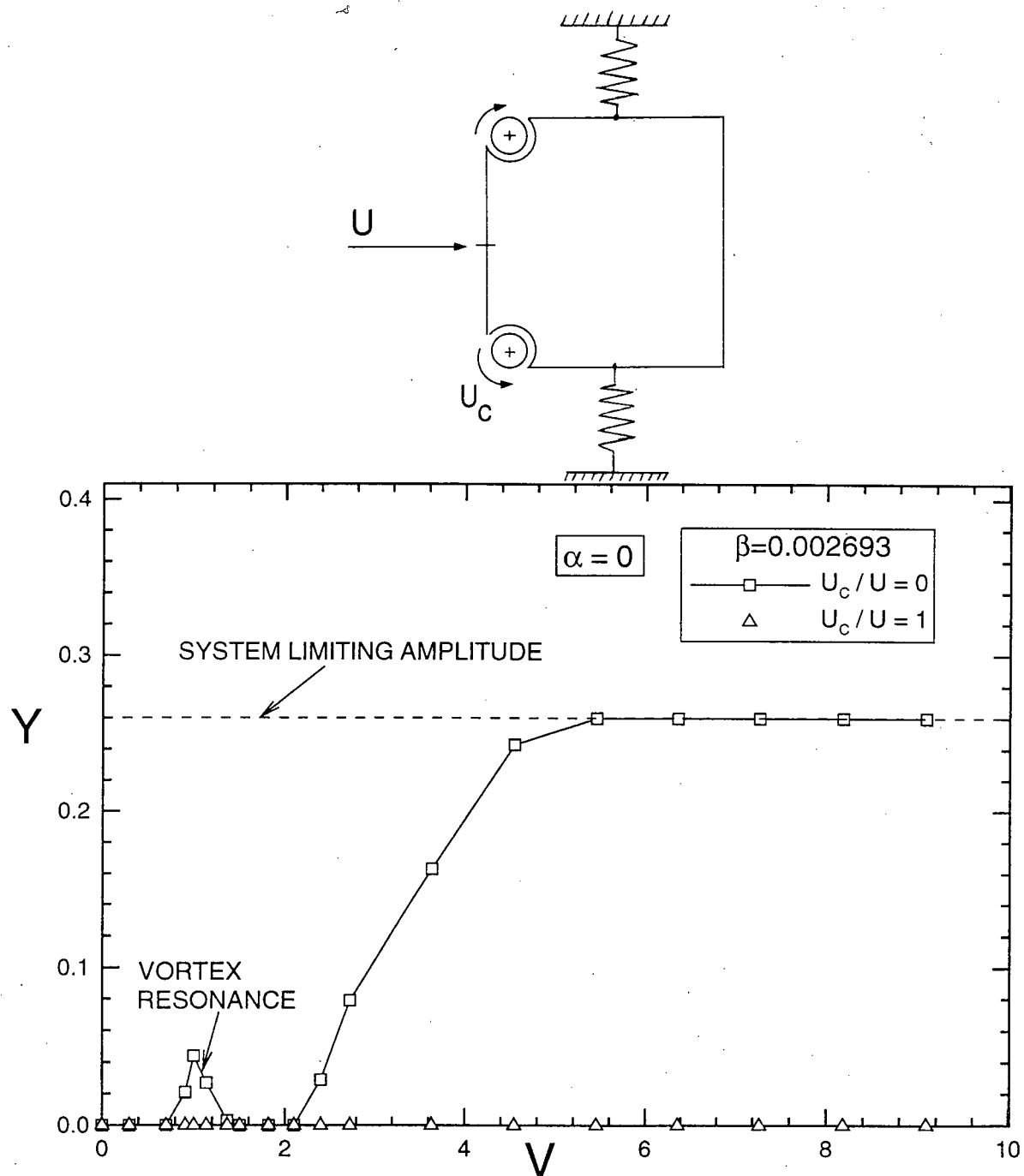
Figure 6-5   Dynamic response of the square prism without and with symmetric momentum injection. Note the presence of both vortex-resonance and galloping in absence of the momentum injection ($U_C/U = 0$). The square prism becomes completely stable in presence of the momentum injection as small as $U_C/U = 1$.

cylinders. Results for this case are presented in Figure 6-7. Note, the vortex excited vibrations disappear completely for $U_C/U = 1$ and the galloping is delayed to $V = 6.4$. With a small further increase in the injected momentum ($U_C/U = 1.5$), the galloping oscillation are suppressed for V as large as 10.

Recently, Kubo et al. [185] have also carried out similar experiments on a two- dimensional square prism. Their results also demonstrate that symmetric momentum injection is effective in suppressing galloping response of the square prism. But the vortex-resonance could not be eliminated completely in presence of symmetric momentum injection, though the peak amplitude showed significant reduction. To eliminate vortex-resonance completely, it was necessary to introduce asymmetric momentum injection (i.e. only one cylinder rotating). This difference in response may be attributed to the difference in the relative size of the rotating element with respect to the prism. In the present case, ratio of the rotating cylinder diameter to the side of the square prism is about 0.3, whereas for Kubo's model this ratio is 0.1 (i.e. the momentum injection elements are much smaller). This would mean that at a given rate of rotation, the cylinders in the present model can deliver larger amount of energy to the boundary-layer, and hence are more effective.

The oscillatory behaviour of the square prism without and with momentum injection is represented schematically in the phase space in Figure 6-8. With momentum injection, there are two control parameters, V and U_C/U. The oscillations are represented by trajectories in the phase space ($Y, \dot{Y}, V$ for a given U_C/U). With $U_C/U = 0$, the dynamic behaviour of the square prism can be observed qualitatively as the wind speed is increased from zero (Figure 6-8a). The system demonstrates bifurcation twice, once during the vortex-resonance and later during galloping. The bifurcation represents transformation of a stable focus (attractor) into an unstable focus (repeller) with the change in the wind velocity. A stable limit cycle (attractor) encompasses an unstable focus (repeller). For $V > V_C$ (i.e. in the region of galloping),
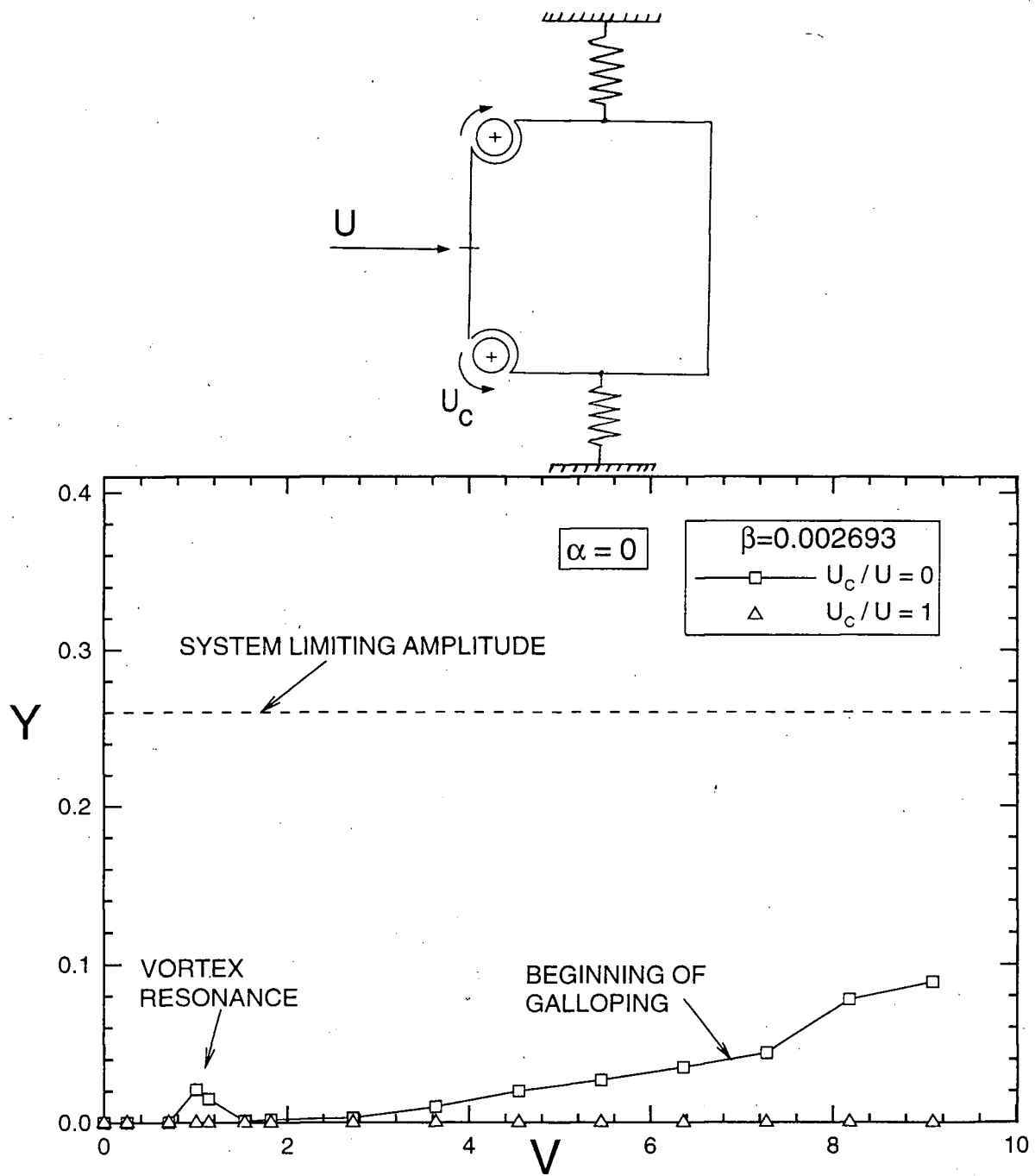
Figure 6-6   Effect of an increase in damping on the dynamic response of the square prism without and with symmetric momentum injection. Note, a significant reduction in the amplitude, particularly in galloping, in presence of the momentum injection. As before, the stability is restored for $U_C/U = 1$.
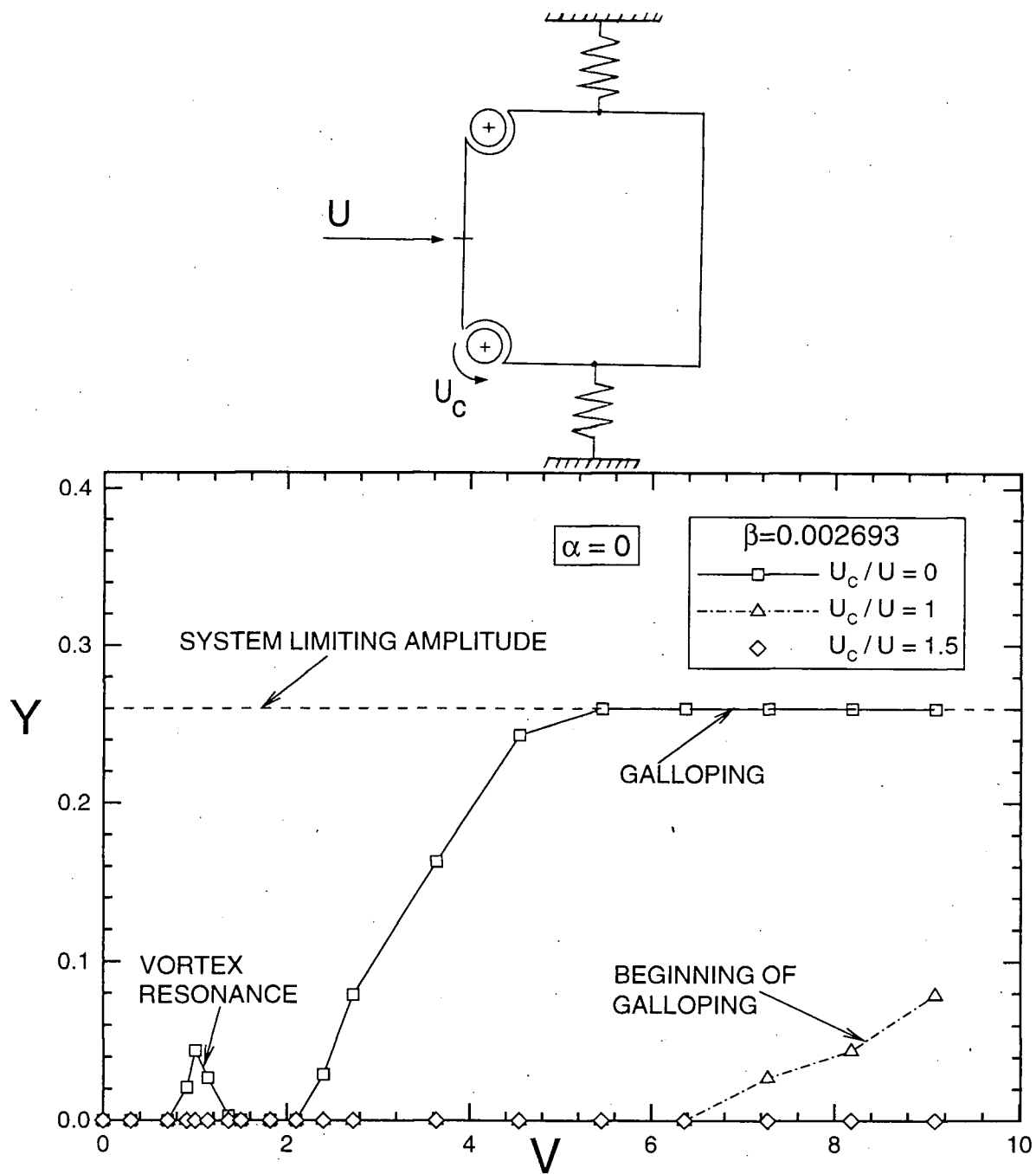
Figure 6-7   Effect of asymmetric momentum injection on the dynamic response of the square prism at various wind speeds. Note, it becomes necessary to increase the asymmetric momentum injection to at least $U_C/U = 1.5$ to restore complete stability.

(a)

$U_C/U = 1$

$U_C/U = 0$

ATTRACTOR

COMPLETE
STABILITY

ATTRACTING
LIMIT CYCLE

ATTRACTOR ATTRACTOR

REPELLER

VORTEX
RESONANCE

GALLOPING

(b)

$U_C/U = 1$

$U_C/U = 0$

COMPLETE
STABILITY

VORTEX
RESONANCE
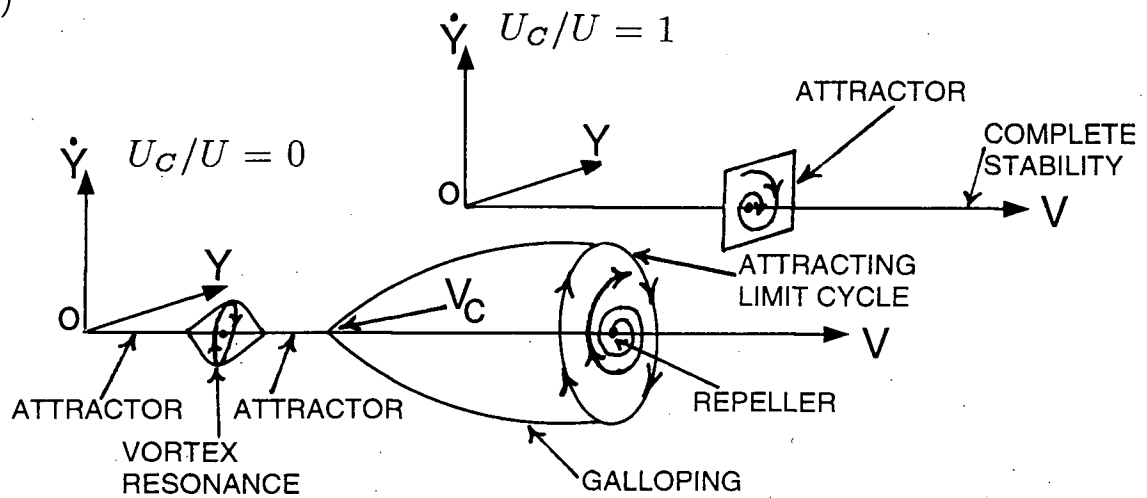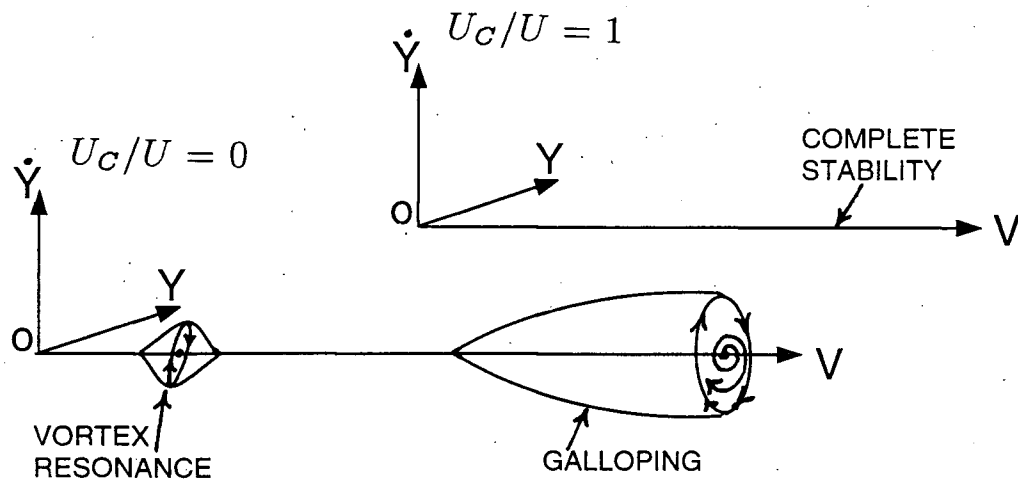
GALLOPING

Figure 6-8   Schematic diagrams showing dynamics of bluff bodies in the extended parameter space $(Y, \dot{Y}, V, U_C/U)$: (a) an unstable bluff structure displays both the vortex-resonance and galloping in absence of the momentum injection $(U_C/U = 0)$. Stability is completely restored with small amount of momentum injection $(U_C/U = 1)$; (b) increase in the system damping affects the critical wind speed and system amplitude.

194

with the momentum injection at $U_C/U = 1$, the galloping is completely eliminated. This is shown by an inwardly spiralling (stable) trajectory. With an increase in damping (Figure 6-8b), limit cycles representing vortex-resonance and galloping are separated further, and galloping occurs at a higher critical wind velocity. Also, the peak response is reduced.

Figure 6-9 is based on experimental observations and clearly emphasizes importance of maintaining the correct direction of rotation of the momentum injecting cylinders. For $V > V_C$, the square prism would gallop in absence of the momentum injection ($U_C/U = 0$). However, at $U_C/U \geq 0$, the vibrations become progressively smaller and vanish eventually when $U_C/U \geq 1.5$ (Figure 6-9a). Reversing the direction of momentum injection of both the cylinders, galloping can be induced even if $V < V_C$! Such behaviour was indeed confirmed during the dynamic experiments when the direction of cylinder rotation was reversed.

6.4.2   Dynamic response of the D-section and the rectangular prism

Dynamical responses for the D-section and the rectangular prism are shown in the Figures 6-10 and 6-11, respectively. Both the bluff bodies display vortex-resonance in absence of the momentum injection. For the D-section it is necessary to increase the momentum injection to $U_C/U = 1.5$ to completely suppress the motion. On the other hand, the rectangular prism becomes stable at $U_C/U = 1$ as the top and bottom faces promote reattachment. Increasing the wind speed to a value as high as 10, does not make either the D-section or the rectangular prism susceptible to galloping. This is in agreement with the theoretical predictions based on the static wind tunnel test data. Both the D-section and the rectangular prism are neutrally stable to galloping ($dC_y/d\alpha = 0$) for $\alpha = 20^o$, in absence of the momentum injection. With an appropriate level of momentum injection the stability is maintained as suggested by the results in Figures 6-10 and 6-11.

$V > V_C$

COMPLETE STABILITY $U_C/U \geq 1$

REPELLER

U_C/U

ATTRACTOR

ATTRACTING LIMIT CYCLE

(a)

$V < V_C$

U_C/U

(b)
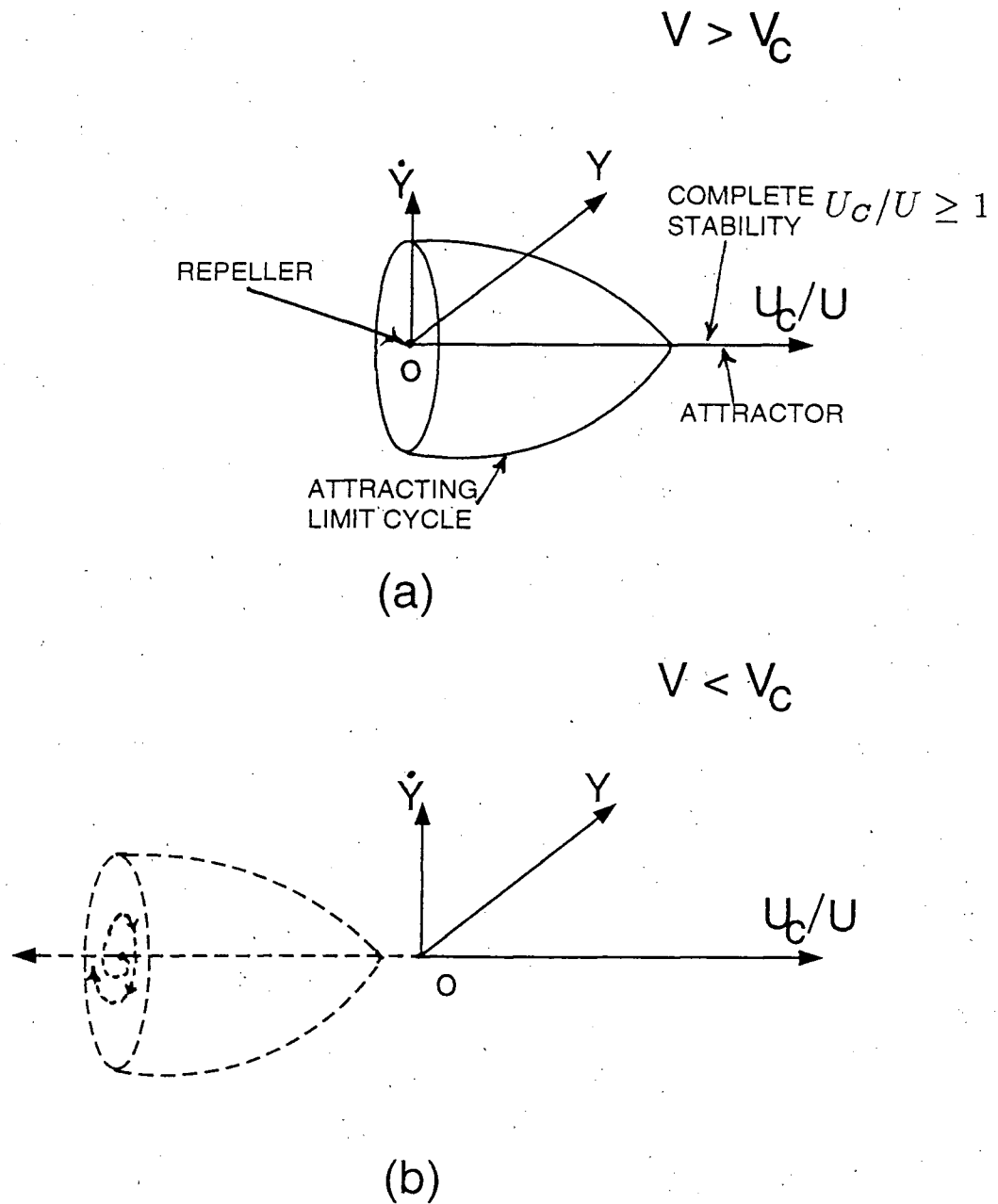
Figure 6-9   Effect of direction of the momentum injection on the galloping in-
stability: (a) for $V > V_C$, an inherently unstable system can be
stabilized by momentum injection in the right direction;(b) gallop-
ing instability at subcritical wind velocity ($V < V_C$) under adverse
direction of the momentum injection ($U_C/U < 0$).

196
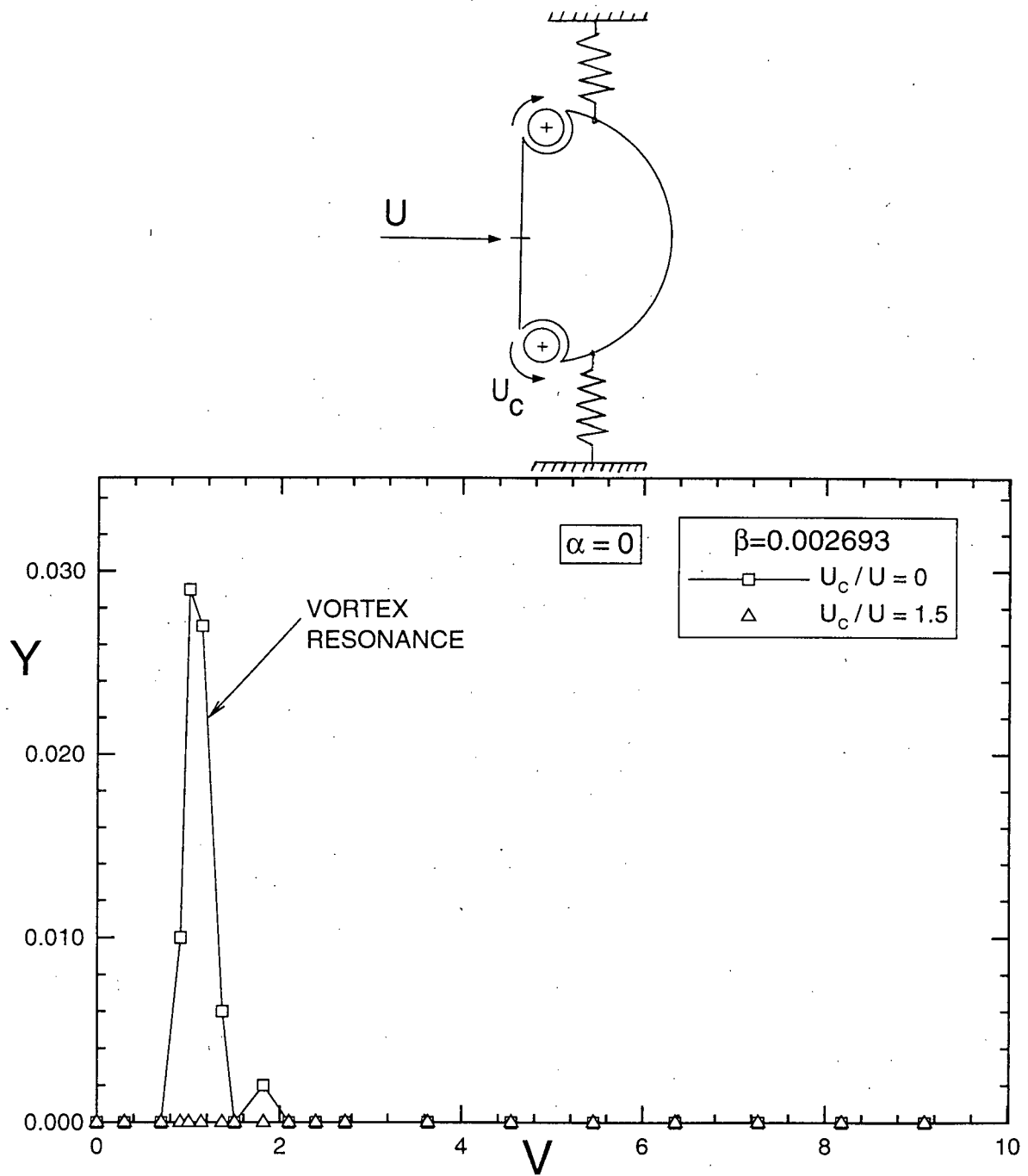
Figure 6-10 Dynamic response of the D-section as affected by the momentum injection. The D-section experiences vortex-resonance, but is stable in galloping.
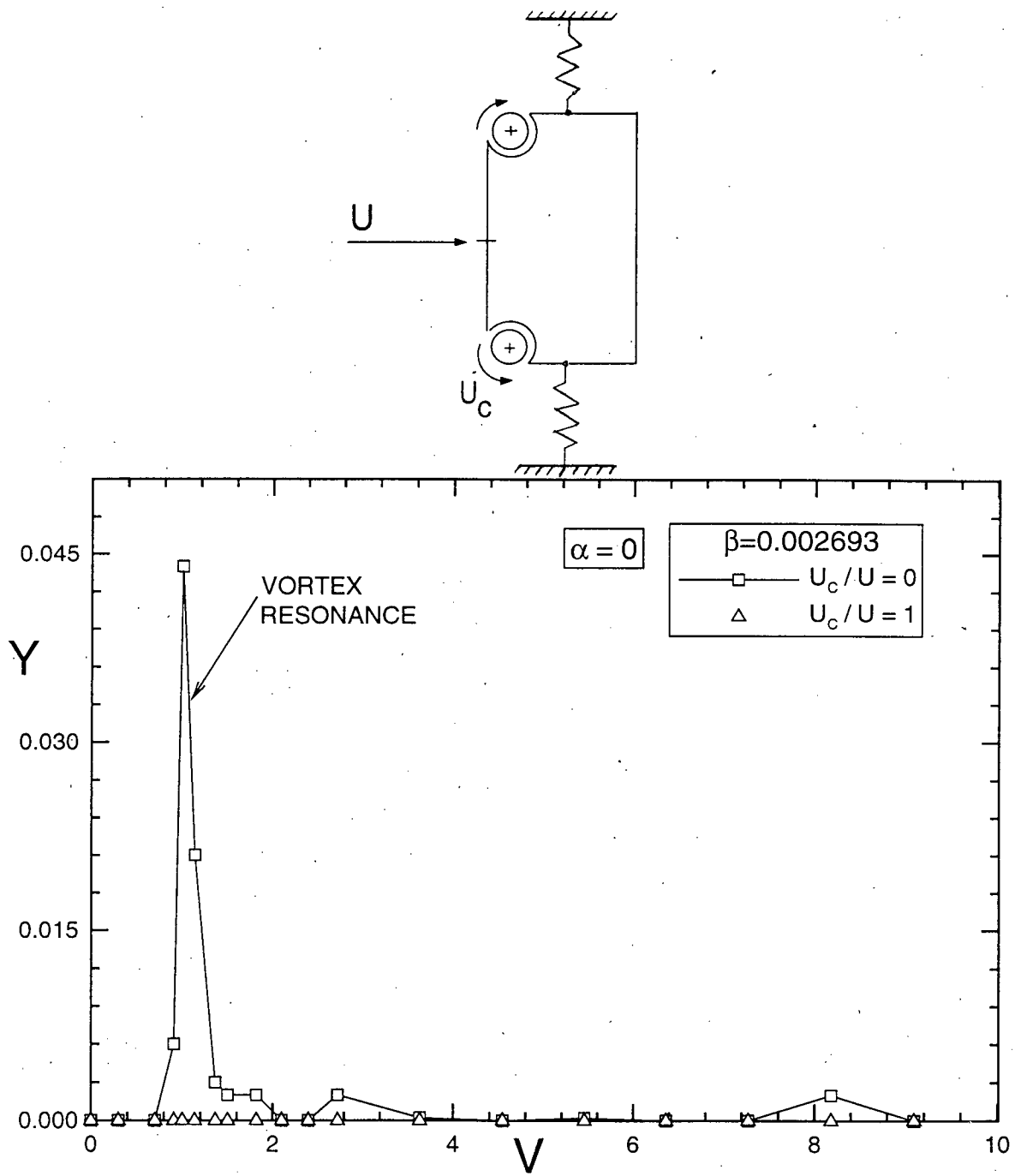
Figure 6-11   Effect of momentum injection on the galloping instability of a rectan-
gular prism (AR=0.5) at $\alpha = 0$. Note, the prism experiences vortex
resonance, but is stable in galloping.

6.5 Summary

The results pertaining to the dynamic response of three bluff bodies under consideration confirm effectiveness of the momentum injection in suppressing both the vortex-resonance and galloping type of instabilities. Even a small amount of the momentum injection $(U_C/U \approx 1\text{--}1.5)$ is sufficient to restore stability. The qualitative phase space representation provide insight into the complex character of the flow-induced vibrations and their dependence on various system parameters.

7. CLOSING COMMENTS

7.1 Summary of Conclusions

The thesis presents results of a rather fundamental study aimed at the Moving Surface Boundary-layer Control (MSBC) as applied to a family of two-dimensional bluff bodies represented by a symmetrical airfoil at high angles of attack, a D-section, and a set of rectangular prisms. The comprehensive character of the investigation is revealed by the four distinct approaches involved: static model wind tunnel tests, numerical simulations, flow visualization, and dynamical response of the system in vortex resonance and galloping, without as well as with the MSBC. The study shows original contributions in every phase. It reveals rather remarkable effectiveness of the MSBC in increasing lift, reducing drag, and suppression of both vortex resonance and galloping. Successful elimination of wind-induced instabilities establishes the MSBC as a vibration suppression method based on the control of excitation, and hence energy input to the system, rather than dissipation. More important conclusions based on the study may be summarized as follows:

(a)   One of the major parameters affecting the MSBC is the ratio U_C/U. In most applications the maximum value of U_C/U required to obtain desirable effect of the MSBC is limited to 4. In fact, the wind induced instabilities can be completely suppressed for U_C/U as small as 1.5, which agrees with the predictions based on the quasi-steady analysis.

(b)   The direction of the momentum injection depends on the location of the upstream stagnation point and requires reversal at critical orientations to promote reattachment of the separated boundary-layer.

(c)   Surface roughness of the rotating elements has significant effect on the efficiency of the momentum injection. In the present study, splined cylinders performed the best.

(d)   Effectiveness of the MSBC suffers when the rotating element is located in the separated shear layer.

(e)   Measurement of the vortex shedding frequency and signal amplitude shows that the shed vortices become weaker and eventually disappear as the momentum injection is increased from $U_C/U = 0$ to 2. This is accompanied by reduction in the size of the wake, rise in wake pressure (average 23% over $0 \leq \alpha \leq 90^o$ at $U_C/U = 4$), delay of flow separation, and reattachment of the separated shear layer.

(f)   In presence of the MSBC (splined cylinder), the peak lift coefficient for a symmetric Joukowsky airfoil increased by 210% with the stall delayed from 10° to 50°! Furthermore, the stall sets in rather gradually, i.e. $dC_L/d\alpha$ is relatively small, which is a desirable feature.

(g)   The presence of suction peaks at the rotating elements contribute significantly to the drag reduction of bluff bodies. The peak drag reduction was found to be as high as 75% with the average over $0 \leq \alpha \leq 90^o$ of around 36%.

(h)   Results of dynamic studies also reveal effectiveness of asymmetric momentum injection in eliminating wind-induced instabilities, which is based on the disruption of organized vortex shedding.

(i)   Previous as well as present estimates suggest that the power consumption in implementing the MSBC is quite small. This makes the MSBC essentially a semi-passive flow control procedure.

(j)   The analysis based on the universal Strouhal number (Su) confirms the observation that the wakes of different bluff bodies are similar except the changes in the geometric and velocity scales.

(k)   The simple modified panel method successfully predicts correct trends even for such complex flow field associated with multielement geometries in presence

201

of the momentum injection. This suggests that judiciously applied numerical approach, capturing physics of the system under consideration, can provide results of sufficient accuracy saving considerable computational time and effort.

(l)   The flow visualization study substantiates, rather spectacularly, effectiveness of the MSBC.

(m)   Such a comprehensive investigation of the bluff body aerodynamics and dynamics in presence of the momentum injection, based on extensive wind tunnel, numerical and flow visualization experiments, has never been reported before. It presents an exciting possibility of application to a wide variety of problems of contemporary interest.

7.2   Suggestions for Future Research

There are several avenues for further exploration of the fluid dynamics and dynamics of bluff bodies in presence of the MSBC. Some of the more important aspects, which are likely to advance the field further, are briefly touched upon below.

(i)   The present study focussed on the MSBC as applied to two-dimensional flows. The next logical step would be to consider its application to three-dimensional objects which would be closer to the real life situation. This suggests performance evaluation of the MSBC in presence of end effects.

(ii)   Application of the MSBC to supertall buildings of the future ($\geq$ 1,000 m), which are in the planning stage, should prove to be challenging both aerodynamically as well as structurally. Immersed in the atmospheric boundary-layer, they will be exposed to random gust-type loading as observed in the case of the Empire State Building. The reduced stiffness of such gigantic structures ($\leq$ 1 Hz.) will only accentuate the problem. This may require hybrid strategy involving the MSBC for reducing force excitation as well as passive nutation dampers for dissipation of energy. It is also imperative to obtain quantitative

202

estimate of the optimum size of a rotating cylinder as compared to the overall dimensions of a tall building.

(iii)   The next generation of bridge-towers for long suspension bridges have shown them to be prone to wind induced instabilities during wind tunnel tests. Application of the MSBC (without and with nutation dampers) may prove to be one of the viable solutions.

(iv)   The present study focussed on application of the MSBC to straight, rectangular wings. There is an exciting possibility of its implementation on a delta wing and its control surfaces. Injection of momentum may stabilize the twin helical vortices, delay or even suppress the vortex burst phenomenon and improve the overall aerodynamic performance. When applied to control surfaces (aileron, elevator, rudder), it can lead to highly maneuverable airplanes. A real wing is a complex system. Incorporation of a rotating cylinder on such a wing would require a careful analysis of its effect on the aerodynamics and dynamic stability of the aircraft.

(v)   A numerical study of a rotating cylinder having time-dependent rate of rotation has been reported by Ou [186]. For an aircraft undergoing unsteady manoeuvres, such a time-dependent momentum injection $(U_C(t)/U)$ may become necessary. Further information regarding this concept as applied to an actual aircraft is necessary.

(vi)   Application of the concept to control wing tip vortices and promote their dissipation may prove to be interesting. This may ease the problem faced by airtraffic controllers, particularly at large busy airports, who are forced to increase the time interval between successive landings to minimize the effect of wing tip vortices.

(vii)   Some wind tunnel model test results aimed at reduction of the aerodynamic drag experienced by highway trucks, with the MSBC applied at the top lead-

ing edge of the trailers, have been reported in the literature [59]. However, systematic road tests are necessary to confirm the results. Even 1% reduction in the drag can literally translate into millions of dollars of saving in the fuel cost.

(viii)   One aspect that is relevant in all the above mentioned studies concerns the effect of surface roughness of the rotating cylinder on the efficiency of the momentum injection process. In the present study, the cylinder with splined surface performed the best. There is a scope to arrive at an optimum config-uration of the splined surface geometry.

(ix)   Recent advances in digital image processing could be useful in analyzing the flow visualization data to obtain quantitative estimates of the vortex shedding process. This would provide further information as to the effect of the MSBC on the structure of the wake.

(x)   There is a scope for numerical simulation of such multielement systems using the complete Navier-Stokes equations in conjunction with appropriate turbu-lence model. It can provide a rather powerful and versatile tool, applicable to a large class of systems, when combined with the dynamics of the system.

REFERENCES

[1]   Rosenhead, L., "Vortex Systems in Wakes," *Advances in Applied Mechanics*, Vol. 3, 1966, Academic Press, New York, p. 189-198.

[2]   Prandtl, L., and Tietjens, O. G., *Applied Hydro and Aeromechanics*, Dover Publications, New York, 1934, p. 58.

[3]   Thwaites, B., *Incompressible Aerodynamics*, Dover Publications, New York, 1960, p. 587.

[4]   Kubo, Y., Yasuda, H., and Kotsubo, C., Hirata, K., "Active Control of Super-tall Structure Vibrations under Wind Action by a Boundary-layer Control Method," *Journal of Wind Engineering and Industrial Aerodynamics*, Vol. 50, 1995, pp. 361-372.

[5]   Kubo, Y., Hayashida, K., Kotsubo, C., and Kato, K., "On the Suppression of Aerodynamic Vibrations of a Square Prism in High Angles of Attack by boundary-Layer Control Method," *First World Conference on Structural Control*, Los Angeles, U.S.A., August 1994.

[6]   Wille, R., "Karman Vortex Streets," *Advances in Applied Mechanics, Academic Press*, New York, 1960, Vol. 6, pp. 273-287.

[7]   Marris, A. W., "A Review on Vortex Streets, Periodic Wakes, and Induced Vibration Phenomena," *Transactions of the ASME, Journal of Basic Engineering*, Series D., Vol. 86, 1964, pp. 185-196.

[8]   Morkovin, M. V., "Flow Around a Circular Cylinder - A Kaleidoscope of Challenging Fluid Phenomena," *ASME Symposium on Fully Separated Flows*, Philadelphia, 1964, pp. 102-118.

[9] Parkinson, G. V., "Wind Induced Instability of Structures," *Philosophical Transactions of the Royal Society of London, Series A*, Vol. 129, 1971, pp. 115-135.

[10] Cermak, J. E., "Application of Fluid Mechanics to Wind Engineering," Freeman Scholar Lecture, *Transactions of the ASME, Journal of Fluids Engineering,*, Vol. 97, No.1, 1975, pp. 9-38.

[11] Welt, F., "A Parametric Study of Nutation Dampers," *M.A.Sc. Thesis*, University of British Columbia, Vancouver, Canada, 1983.

[12] Welt, F., "A Study of Nutation Dampers with Application to Wind Induced Oscillations," *Ph.D. Thesis*, University of British Columbia, Vancouver, Canada, 1988.

[13] Modi, V. J., Welt, F., and Seto, M. L., "Control of Wind Induced Instabilities through Application of Nutation Dampers: A Brief Review," *Engineering Structures: Auxiliary Damping Systems for Vibration Mitigation*, Special Issue Guest Editor: J. D. Holms, in press.

[14] Tritton, D. J., *Physical Fluid Dynamics*, Clarendon Press, New York, 1988, 2nd Edition, pp. 18-29.

[15] *Fluid Vortices*, Editor: Green, S. I., Kluwer Academic Publishers, Boston, 1995, p. 537.

[16] Bearman, P. W., "Vortex Shedding from Oscillating Bluff Bodies," *Annual Review of Fluid Mechanics*, Vol. 16, 1984, pp. 195-222.

[17] Bearman, P. W., Gartshore, I. G., Maull, D. J., and Parkinson, G. V., "Experiments on Flow-Induced Vibrations of a Square-Section Cylinder," *Journal of Fluids and Structures*, Vol. 1, 1987, pp. 19-34.

[18] Parkinson, G. V., and Smith, J. D., "The Square Prism as an Aeroelastic Non-Linear

Oscillator," *Quarterly Journal of Mechanics and Applied Mathematics*, Vol. 17, Part 2, May 1964, pp. 225-239.

[19]   Parkinson, G.V., "Phenomenon and Modelling of Flow-Induced Vibrations of Bluff Bodies,"*Progress in Aerospace Sciences*, Vol. 26, 1989, pp. 169-224.

[20]   Bokaian, A. R., and Geoola, F., "Hydroelastic Instabilities of Square Cylinders," *Journal of Sound and Vibrations*, Vol. 92, No. 1, 1984, pp. 117-141.

[21]   Laneville, A., and Parkinson, G. V., "Effects of Turbulence on Galloping of Bluff Cylinders," *Proceedings of the 3rd International Conference on Wind Effects on Build-. ings and Structures*, Editors: Japan Organizing Comittee, Tokyo, 1971, pp. 787-797.

[22]   Gartshore, I. S., Khanna, J., and Laccinole, S., "The Effectiveness of Vortex Spoilers on Circular Cylinders in Smooth and Turbulent Flow," *Proceedings of the 5th International Conference on Wind Engineering*, Fort Collins, Colorado, USA, 1978.

[23]   Engineering News - Record, McGraw-Hill's Construction Weekly, October 30, 1975, pp. 11.

[24]   Welt, F., and Modi, V. J., "Vibration Damping Through Liquid Sloshing: Part 1 - A Nonlinear Analysis," *Transactions of ASME, Journal of Vibration and Acoustics*, Vol. 114, No.1, 1992, pp. 10-16.

[25]   Welt, F., and Modi, V. J., "Vibration Damping Through Liquid Sloshing: Part 2 - Experimental Results," *Transactions of ASME, Journal of Vibration and Acoustics*, Vol. 114, No.1, 1992, pp. 17-23.

[26]   Tamura, Y., Kousaka, R., and Modi, V. J., "Practical Application of Nutation Damper for Suppressing Wind-Induced Vibrations of Airport Towers," *Journal of Wind Engineering and Industrial Aerodynamics*, Vol. 41-44, 1992, pp. 1919-1930.

[27]   Goldstein, S., *Modern Developments in Fluid Mechanics*, Vol. I and II , Oxford University Press, Oxford, 1938.

[28]   Lachmann, G. V., *Boundary-Layer and Flow Control, Its Principles and Application*, Vol. I, Pergamon Press, New York, 1961, pp. 1-2.

[29]   Rosenhead, L. *Laminar Boundary Layers*, Clarendon Press, Oxford, 1966, pp. 111, 332-335, 547.

[30]   Schlichting, H., *Boundary Layer Theory*, McGraw-Hill Book Company, New York, 1968, pp. 362-390.

[31]   Chang, P.K., *Control of Flow Separation*, Hemisphere Publishing Corporation, McGraw-Hill Book Company, Washington, 1970, pp. 154-177.

[32]   Report of the Research Co-ordination Group on Boundary Layer Control to Suppress Separation, Associate Committee on Aerodynamics, *National Research Council*, September 1966.

[33]   Thwaites, B., *Incompressible Aerodynamics*, Dover Publications, New York, 1960, pp 105-106, 215.

[34]   Massey, B. S., *Mechanics of Fluids*, Van Nostrand Reinhold, Berkshire, U.K., 5th Edition, 1983, p. 346.

[35]   Swanson, W. M., "The Magnus Effect: A summary of Investigation to Date," *Transactions of the ASME, Journal of Basic Engineering*, Vol. 83, September 1961, pp. 461-470.

[36]   Iverson, J. D., "Correlation of Magnus Force Data for Slender Spinning Cylinders," *AIAA 2nd Atmospheric Flight Mechanics Conference*, Palo Alto, California, September 1972, Paper No. 72-966.

[37]   Betz, A., "History of Boundary Layer Control in Germany," *Boundary Layer and Flow Control*, Editor: G. V. Lachmann, Pergamon Press, New York, Vol. I, pp. 1-20.

[38]   Flettner, A., "The Flettner Rotor Ship," *Engineering*, Vol. 19, January 1925, pp. 117-120.

[39]   Favre, A., "Contribution a l'Etude Experimentale des Mouvements Hydrodynamiques a Deux Dimensions," *Thesis presented to the University of Paris*, 1938.

[40]   Alvarez-Calderon, A., and Arnold, F. R., "A study of the Aerodynamic Characteristics of a High Lift Device Based on Rotating Cylinder Flap," *Stanford University Technical Report RCF-1*, 1961.

[41]   Alvarez-Calderon, A., "Rotating Cylinder Flaps for V/STOL Aircraft," *Aircraft Engineering*, October 1964, pp. 304-309.

[42]   Brooks, D. A., "Effect of a Rotating Cylinder at the Leading and Trailing Edges of a Hydrofoil," *U.S. Naval Ordanance Test Station, Department of the Navy*, NAVWEPS Report 8042, April 1963.

[43]   Steele, B. N., and Harding, M. H., "The Application of Rotating Cylinder to Ship Maneuvering," National Physical Laboratory, Ship Division, U.K., Report No. 148, December 1970.

[44]   Aviation Week and Space Technology, Vol. 95, No. 16, October 18, 1971, p. 19.

[45]   Aviation Week and Space Technology, Vol. 95, No. 24, December 13, 1971, front cover and p. 7.

[46]   Tennant, J. S., "The Theory of Moving Wall Boundary Layer Control and its Experimental Applications to Subsonic Diffusers," *Ph.D. Dissertation*, Clemson University, May 1971.

[47]   Tennant, J. S., "A Subsonic Diffuser with Moving Walls for Boundary-Layer Control," *AIAA Journal*, Vol. 11, No. 2, February 1973, pp. 240-242.

[48]   Johnson, W. S., Tennant, J. S., and Stamps, R. E., "Leading- Edge Rotating Cylinder for Boundary-Layer Control on Lifting Surfaces," *Journal of Hydronautics*, Vol. 9, No. 2, April 1975, pp. 76-78.

[49]   Tennant, J. S., Johnson, W. S., and Krothapalli, A., "Rotating Cylinder for Circulation Control on an Airfoil," *Journal of Hydronautics*, Vol. 10, No. 3, July 1976, pp. 102-105.

[50]   Tennant, J. S., Johnson, W. S., and Keaton, D. D., "On the Calculation of Boundary Layers Along Rotating Cylinders," *Journal of Hydronautics*, Vol. 11, No. 2, April 1977, pp. 61-63.

[51]   Tennant, J. S., Johnson, W. S., and Keaton, D. D., "Boundary Layer Flows from Fixed to Moving Surfaces including Gap Effects", *Journal of Hydronautics*, Vol. 12, No. 2, April 1978, pp. 81-84.

[52]   Ericsson, L. E., "Moving Wall Effects in Unsteady Flow," *Journal of Aircraft*, Vol. 25, No. 11, November 1988, pp. 977-990.

[53]   Modi, V. J., Sun, J. L. C., Akutsu, T., Lake, P., McMillan, K., Swinton, P. G. and Mullins, D., "Moving Surface Boundary Layer Control for Aircraft Operation at High Incidence," *Journal of Aircraft, AIAA*, Vol. 18, November 1981, pp. 963-968.

[54]   Modi, V. J., Mokhtarian, F., Yokomizo, T., Ohta, G., and Oinuma, T., "Bound Vortex Boundary-Layer Control with Application to V/STOL Airplanes," *Proceedings of the IUTAM Symposium on Fundamental Aspects of Vortex Motion*, Tokyo, Japan, 1987, pp. 196-199; also Vortex Motion, Editors: H. Hashimoto and T. Kambe, North-Holland Publishing Company, Amsterdam, 1987, pp. 225-230.

[55] Mokhtarian, F., and Modi, V. J., "Fluid Dynamics of Airfoils with Moving Surface Boundary-Layer Control," *Journal of Aircraft*, Vol. 25, No. 2, February 1988, pp. 163-169.

[56] Modi, V. J., Ying, B., and Yokomizo, T., "Boundary-Layer Control of Bluff Bodies Through Momentum Injection," *SAE Transactions, Journal of Commercial Vehicles*, Section 2, Vol. 99, 1990, pp. 778-794.

[57] Modi, V. J., Mokhtarian, F., and Fernando, M.S.U.K., "Moving Surface Boundary Layer Control as applied to Two-dimensional Airfoils," *Journal of Aircraft*, Vol. 28, No. 2, 1991, pp. 104-112.

[58] Modi, V. J., Fernando, M.S.U.K., and Yokomizo, T., "Moving Surface Boundary-Layer Control : Studies with Bluff Bodies and Application," *AIAA Journal*, Vol. 29, No. 9, 1991, pp. 1400-1406.

[59] Modi, V. J., Shih, E., Ying, B. and Yokomizo, T., "Drag Reduction of Bluff Bodies Through Momentum Injection," *Journal of Aircraft*, Vol. 29, No. 3, May-June 1992, pp. 429-436.

[60] Modi, V. J., Ying, B., and Yokomizo, T., "Effect of Momentum Injection and Fences on the Drag of a Tractor-Trailer Truck Configurations," *AIAA 10th Applied Aerodynamics Conference*, Palo Alto, CA, USA, June 1992, Paper No. AIAA-92-2640.

[61] Brown, D. A., "Peruvians Study Rotating-Cylinder Flap," *Aviation Week and Space Technology*, Vol. 88, No. 23, December 1964, pp. 70-76.

[62] Lighthill, M. J., *An Informal Introduction to Theoretical Fluid Dynamics*, Clarendon Press, Oxford, 1986, pp. 174-182.

[63] Rauscher, M., *Introduction to Aeronautical Dynamics*, John Wiley & Sons, New York,

1953, Chapter VI, pp. 244-252.

[64]   Goldstein, S., *Modern Developments in Fluid Mechanics*, Vol. II, Oxford University Press, Oxford, 1938, pp. 545-549.

[65]   Chang, P. K., *Control of Flow Separation*, Hemisphere Publishing Corporation, McGraw-Hill Book Company, Washington, 1976, Chapter 5, pp. 286-298.

[66]   Modi, V. J., and Wiland, E., "Unsteady Aerodynamics of Stationary Elliptic Cylinders in Subcritical Flow," *AIAA Journal*, Vol. 8, October 1970, pp. 1814-1821.

[67]   Wiland, E., "Unsteady Aerodynamics of Stationary Elliptic Cylinders in Subcritical Flow," *M.A.Sc. Thesis*, Department of Mechanical Engineering, University of British Columbia, April 1968.

[68]   Lamb, H., *Hydrodynamics*, Cambridge University Press, Cambridge, 6th Edition, 1932, pp. 99-102.

[69]   Roshko, A., "A New Hodograph for Free-Streamline theory," *NACA TN 3168*, July 1954.

[70]   Parkinson, G. V., and Jandali, T., "A Wake Source Model for Bluff Body Potential Flow," *Journal of Fluid Mechanics*, Vol. 40, Part 3, pp. 577-594.

[71]   Blevins, R. D., *Flow-Induced Vibration*, McGraw-Hill Book Company, New York, 1990.

[72]   Simiu, E., and Scanlan, R. H., *Wind Effects on Structures: An Introduction to Wind Engineering*, John Wiley & Sons., New York, 1978.

[73]   Houghton, E. L., and Carruthers, N. B., *Wind Forces on Buildings and Structures - An Introduction*, Edward Arnolds, London, U.K., 1976.

[74]   Sachs, P., *Wind Forces in Engineering*, Pergamon Press, New York, 1972.

[75]   Walshe, D. E. J., *Wind-Excited Oscillations of Structures*, National Physical Laboratory, Department of Trade and Industry, Her Majesty's Stationary Office, London, U.K., 1972.

[76]   Bearman, P. W., and Davies, M. E., "The Flow about Oscillating Bluff Structures," *Proceedings of the 4th International Conference on Wind Effects on Buildings Structures, London, U.K.*, Editor: K. J. Eaton, Cambridge University Press, pp. 195-222.

[77]   Brooks, N. P. H., "Experimental Investigation of the Aeroelastic Instability of Bluff Cylinders," *M.A.Sc. Thesis*, Department of Mechanical Engineering, University of British Columbia, 1960.

[78]   Smith, J. D., "An Experimental Study of the Aeroelastic Instability of Rectangular Cylinders," *M.A.Sc. Thesis*, Department of Mechanical Engineering, University of British Columbia, 1962.

[79]   Heine, W., "On the Experimental Investigation of Vortex Excited Pressure Fluctuation," *M.A.Sc. Thesis*, Department of Mechanical Engineering, University of British Columbia, August 1964.

[80]   Ferguson, N., "The Measurement of Vortex Induced Effects in Flow Past Stationary and Oscillating Circular and D-section Cylinders," *M. A. Sc. Thesis*, Department of Mechanical Engineering, University of British Columbia, 1965.

[81]   Santosham, T. V., "Force Measurements on Bluff Cylinders and Aeroelastic Galloping of Rectangular Cylinder," *M.A.Sc. Thesis*, Department of Mechanical Engineering, University of British Columbia, 1966.

[82]   Feng, C. C., "The Measurement of Vortex Induced Effects in Flow Past Stationary and Oscillating Circular and D-section Cylinders," *M.A.Sc. Thesis*, Department of

Mechanical Engineering, University of British Columbia, October 1968.

[83]   Slater, J. E., and Modi, V.J., "On the Wind Induced Vibrations of Structural Angle Sections," *Proceedings of the 3rd International Conference on Wind Effects on Buildings and Structures*, Tokyo, Japan, 1971, Editors: Japan Organizing Comittee, pp. 1195-1205.

[84]   Novak, M., "Aeroelastic Galloping of Prismatic Bodies," *Proceedings of the ASCE*, EM1, 1969, pp. 115-142.

[85]   Zdravkovich, M. M., "Review and Classification of various Aerodynamic and Hydrodynamic Means for Suppressing Vortex Shedding," *Journal of Wind Engineering and Industrial Aerodynamics*, Vol. 7, No. 2, March 1981, pp. 145-189.

[86]   Zdravkovich, M. M., "Reduction of Effectiveness of Means For Suppressing Wind-Induced Oscillation," *Journal of Engineering Structures*, Vol. 6, October 1984, pp. 344-349.

[87]   Leschziner, M. A., "Computational Modelling of Complex Turbulent Flow - Reality and Prospects", *Proceedings of the First International Symposium on Computational Wind Engineering (CWE 92)*, Institute of Industrial Science, University of Tokyo, Tokyo, 1992, Editors: Japan Association for Wind Engineering, pp. 180-194.

[88]   Roache, P. J., *Computational Fluid Dynamics*, Hermosa Publishers, Albuquerque, USA, 1972.

[89]   Patankar, S. V., *Numerical Heat Transfer and Fluid Flow*, Hemisphere Publishing Corporation, McGraw-Hill, New York, 1980.

[90]   Anderson, D. A., Tannehill, J. C., and Pletcher, R. H., *Computational Fluid Mechanics and Heat Transfer*, Hemisphere Publishing Corporation, McGraw-Hill, Washington, 1984.

[91]   Zienkiewicz, O. C., and Taylor, R. L., *The Finite Element Method*, Vol. I & II, McGraw-Hill, New York, 1989.

[92]   Chung, T. J., *Finite Element Computational Fluid Dynamics*, McGraw-Hill, New York, 1978, pp. 170-265.

[93]   Baker, A. J., *Finite Element Computational Fluid Mechanics*, McGraw-Hill, New York, 1983, pp. 21-83.

[94]   Reddy, J. N., *An Introduction to Finite Element Method*, McGraw-Hill, New York, 1993.

[95]   Abernathy, F. H., and Kronauer, R. E., "The Formation of Vortex Streets," *Journal of Fluid Mechanics*, Vol. 13, Part 1, 1962, pp. 1-20.

[96]   Gerrard, J. H., "The Mechanics of the Formation Region of Vortices Behind Bluff Bodies," *Journal of Fluid Mechanics*, Vol. 25, Part 2, 1966, pp. 401-413.

[97]   Sarpakaya, T., "An Analytical Study of Separated Flow about Circular Cylinders," *Transactions of the ASME, Journal of Basic Engineering*, Vol. 90, No. 4, 1968, pp. 511-520.

[98]   Laird, A. D. K., "Eddy Formation Behind Circular Cylinders," *Journal of the Hydraulics Division, ASCE*, Vol. 97, No. HY6, Proceedings Paper 8170, June 1971, pp. 763-775.

[99]   Chaplin, J. R., "Computer Model of Vortex Shedding From a Cylinder," *Journal of the Hydraulics Division, Proceedings of the American Society of Civil Engineers*, January 1973, HY1, pp. 155-165.

[100] Sarpakaya, T., "An Inviscid Model of Two-Dimensional Vortex Shedding for Transient and Asymptotically Steady Separated Flow Over an Inclined Plate," *Journal of Fluid*

Mechanics, Vol. 68, 1975, pp. 109-128.

[101] Fage, A., and Johansen, F. C., "On the Flow of Air Behind an Inclined Flat Plate of Infinite Span," *Proceedings of the Royal Society*, A116, 1927, pp. 170-197.

[102] Kiya, M., and Arie, M., "Discrete-Vortex Simulation of Unsteady Separated Flow Behind a Nearlly Normal Plate," *Bulletin of the JSME*, Vol. 23, No. 183, 1980, pp. 1451-1458.

[103] Kiya, M., Sasaki, K., and Arie, M., "Discrete-Vortex Simulation of a Turbulent Separation Bubble," *Journal of Fluid Mechanics*, Vol. 120, 1982, pp. 219-244.

[104] Clements, R. R., "An Inviscid Model of Two-Dimensional Vortex Shedding," *Journal of Fluid Mechanics*, Vol. 57, 1973, pp. 321-336.

[105] Nagano, S., Naito, M., and Takata, H., "A Numerical Analysis of Two-Dimensional Flow Past a Rectangular Prism by a Discrete Vortex Model," *Computers and Fluids*, Vol. 10, 1983, No. 4, pp. 243-259.

[106] Richards, W. B., "Discrete-Vortex Calculation of Flow Past a Plate," *Report, NASA Lewis Research Center*, 1984.

[107] Kamemoto, K., Naohiro, O., and Aizawa, M., "Numerical Experiments on the Unsteady Separated Flow Behind Two Flat Plates in a Side by Side Arrangement Using the Discrete Vortex Method," *Bulletin of JSME*, Vol. 27, 1984, pp. 2118.

[108] Stanby, P. K., "A Numerical Study of Vortex Shedding Form One and Two Circular Cylinders," *Aeronautical Quarterly*, Vol. 32, Part 1, 1981, pp. 48-68.

[109] Chein, R., and Chung, J. N., "Discreet-Vortex Simulation of Flow Over Inclined and Normal Plates," *Computers and Fluids*, Vol. 16, No. 4, 1988, pp. 405-427.

[110] Leonard, A., "Vortex Methods for Flow Simulation," *Journal of Computational Physics*,

Vol. 37, 1980, pp. 289-335.

[111] Maull, D. J., *An Introduction to the Discrete Vortex Method*, Cambridge University, Cambridge, 1981.

[112] Leonard, A., and Koumoutsakos, P., "High Resolution Vortex Simulation of Bluff Body Flows," *First International Symposium on Computational Wind Engineering*, Tokyo, 1992, *Journal of Wind Engineering and Industrial Aerodynamics*, No. 52, August 1992, pp. 345-355.

[113] Pan, L. S., Chew, Y. T., and Lee, T. S., "A Proposed New Vortex Calculation Method Using Generalized Conservation of Circulation Method," *Proceedings of the Sixth Asian Congress of Fluid Mechanics*, Singapore, May 1995, Editors: Y. T. Chew and C. P. Tso, Vol. 1, pp. 445-448.

[114] Bienkiewicz, B., and Kutz, R. F., "Applying the Discrete Vortex Method to Flow about Bluff Bodies," *Journal of Wind Engineering and Industrial Aerodynamics*, Vol. 36, 1990, pp. 1011-1020.

[115] Fernando, M. S. U. K., and Modi, V. J., "A Numerical Analysis of the Unsteady Flow Past a Savonius Wind Turbine," *Journal of Wind Engineering and Industrial Aerodynamics*, Vol. 32, 1989, pp. 303-327.

[116] Ferziger, J., "Simulating of Complex Turbulent Flows: Recent Advances and Prospects in Wind Engineering," *Journal of Wind Engineering and Industrial Aerodynamics*, Vol. 46 – 47, 1993, pp. 195-212.

[117] Rodi, W., "On the Simulation of Turbulent Flow Past Bluff Bodies," *Journal of Wind Engineering and Industrial Aerodynamics*, Vol. 46 – 47, 1993, pp. 3-19.

[118] Franke, R., Rodi, W., and Schonung, B., "Analysis of experimental Vortex-Shedding Data with Respect to Turbulence Modelling," *Proceedings of the 7th Symposium on*

217

Turbulent Shear Flows, Stanford University, 1989, pp. 24.4.1 - 24.4.5.

[119] Deng, D. W., Picquet, J., Queutey, P., and Visonneau, M., "Vortex-Shedding Flow Predictions with Eddy-Viscosity Models," *Engineering Turbulence Modelling and Measurements 2*, Elsevier, New York, 1993.

[120] Nagano, Y., and Tagawa, M., "An Improved k-ϵ model for Boundary-Layer Flows," *Journal of Fluids Engineering*, Vol. 100, 1990, pp. 33-39.

[121] Jansson, S., "Numerical Investigation of Steady and Unsteady Flows Comparing Turbulence Models and Different Near-Wall Models," *Report ISRN CTH-TFD-PB-92/1/SE*, Chalmers University of Technology, Göteberg, Sweden, 1992.

[122] Norris, H. L., and Reynolds, W. C., "Turbulent Channel Flow with a Moving Wavy Boundary," Department of Mechanical Engineering Report, FM-10, Stanford University, 1975.

[123] Ferziger, J. H., "Higher Level Simulations of Turbulent Flow," *Computational Methods for Turbulent, Transonic, and Viscous Flows*, Editors: J.-A. Essers, Hemisphere, New York, 1983.

[124] Canuto, C., Hussaini, A., Quarteroni, A., and Zang, T. A., "*Spectral Methods in Fluid Mechanics*," Springer Verlag, New York, 1987.

[125] Kato, S., Murakami, S., Utsumi, Y., and Mizutani, K., "Application of Massive Parallel Computer to Computational Wind Engineering," *Journal of Wind Engineering and Industrial Aerodynamics*, Vol. 46 – 47, 1993, pp. 393-400.

[126] Murakami, S., "The Future of CFD in Civil Engineering: Large-Scale Computation with Vector and Massive Parallel Computers," *U.S.-Korea-Japan Trilateral Seminar on Frontier R & D for Constructed Facilities*, Honolulu, Hawai, 1991.

[127] Simon, H. D., van Dalsem, W. R., and Dagum, L., "Parallel CFD: Current Status and Future Requirements," *Parallel Computational Fluid Dynamics*, Editor: H. D. Simon, MIT Press, Massachusetts, 1992, pp.1-29.

[128] Hess, J. L., and Smith, A. M. O., "Calculation of Potential Flow About Arbitrary Bodies," *Progress in Aeronautical Sciences*, Vol. 8, Pergamon Press, New York, 1966, pp. 1-138.

[129] Farassat, F., and Brown, T. J., "A New Capability for Predicting Helicopter Rotor and Propeller Noise Including the Effect of Forward Motion," NASA TM-74037, June 1977.

[130] Lee, Y. J., and Yang, J. Y., "A Panel Method for Arbitrary Moving Boundaries Problems," *AIAA Journal*, Vol. 28, No. 3, March 1970, pp. 432-438.

[131] Yon, S., Katz, J., and Plotkin, A., "Effect of Airfoil (Trailing-Edge) Thickness on the Numerical Solution of Panel Methods Based on the Dirichlet Boundary Condition," *AIAA Journal*, Vol. 30, No. 3, March 1992, pp. 697-702.

[132] Kida, T., Nagata, T., and Nakajima, T., "Accuracy of the Panel Method with Distributed Sources Applied to Two-Dimensional Bluff Bodies," *Computational Fluid Dynamics Journal*, Vol. 2, No. 1, April 1993, pp. 73-90.

[133] Katz, J., and Plotkin, A., *Low-Speed Aerodynamics - From Wing Theory to Panel Methods*, McGraw-Hill Book Company, New York, 1991, 237-264.

[134] Mokhtarian, F., "Fluid Dynamics of Airfoils with Moving Surface Boundary-Layer Control," *Ph.D. Thesis*, Department of Mechanical Engineering, University of British Columbia, February 1988.

[135] Keller, H. B., and Cebeci, T., "Accurate Numerical Methods for Boundary-Layer Flows, Part 1, Two-dimensional Laminar Flows," *Lecture Notes in Physics, 8, Pro-*

ceedings of the Second International Conference on Numerical Methods in Fluid Dynamics, Springer-Verlag, New York, 1971, p. 92.

[136] Keller, H. B., and Cebeci, T., "Accurate Numerical Methods for Boundary- layer Flows, Part 2, Two-Dimensional Turbulent Flows," *AIAA Journal*, Vol. 10, 1972, p. 1193.

[137] Cebeci, T., and Smith, A. M. O., *Analysis of Turbulent Boundary Layers*, Academic Press, New York, 1974, p. 170.

[138] Cebeci, T., and Bradshaw, P., *Momentum Transfer in Boundary Layers*, Hemisphere-McGraw Hill, Washington, 1977, pp. 213-234.

[139] Celik, I., Patel, V. C., and Landweber, L., "Calculation of the Mean Flow Past Circular Cylinders by Viscous-Inviscid Interaction," *Transactions of the ASME, Journal of Fluids Engineering*, Vol. 107, June 1985, pp. 218-223.

[140] Maskew, B., and Dvorak, F. A., "The Prediction of $C_{L_{max}}$ Using a Separated Flow Model," *Journal of American Helicopter Society*, Vol. 23, , April 1978, pp. 2-8.

[141] Pearcy, M. M., Singh, S., Cash, R. F., and Matten, R.B., "Fluid Loading on Roughened Cylindrical Members of Circular Cross Section," *NMI Report 191*, January, 1985.

[142] Ribaut, M., "A Vortex Sheet Method for Calculating Separated Two-dimensional Flows," *AIAA Journal*, Vol. 21, August 1983, pp. 1079-1084.

[143] Mukherjea, S., and Bandyopadhyay, G., "Separated Flow about a Wedge," *The Aeronautical Journal of the Royal Aeronautical Society*, June-July 1990, pp. 196-202.

[144] Mukherjea, S., "Study of Incompressible Separated Flow Problems in Fluid Mechanics," *Ph.D. Thesis*, Department of Aerospace Engineering, I.I.T. Kharagpur, India, 1990.

[145] Lugt, H. J., "Autorotation", *Annual Review of Fluid Mechanics*, Vol. 15, 1983, pp. 123-147.

[146] Currie, I. G., *Fundamental Mechanics of Fluids*, McGraw-Hill Book Company, New York, pp. 220-221.

[147] Kellog, O. D., *Foundations of Potential Theory*, Frederick Ungar Publishing Company, New York, 1929, pp. 277-338.

[148] Lanchester, F. W., *Aerodynamics*, Constable, London, 1907, pp. 44.

[149] Cheers, F. A., "A Note on Galloping Conductors," *National Research Council of Canada Report No. MT-14*, June 30, 1950.

[150] Edwards, A. T., and Madeyski, A., "A Progress Report on the Investigation of Galloping of Transmission Line Conductors," *A.I.E.E. Transactions*, Vol. 75, Part III, 1956, pp. 666-686.

[151] Roshko, A., "On the Drag and Shedding Frequency of Two-dimensional Bluff Bodies", *NACA TN 3169*, 1954.

[152] Mair, W. A., and Maull, D. J., "Bluff Bodies and Vortex Shedding - A Report on Euromech 17", *Journal of Fluid Mechanics*, Vol. 45, Part 2, 1971, pp. 209-224.

[153] Berger, E., and Wille, R., "Periodic Flow Phenomena", *Annual Review of Fluid Mechanics*, Vol. 4, 1972, pp. 313-340.

[154] Den Hartog, J. P., *Mechanical Vibrations*, McGraw-Hill, New York, Fourth Edition, 1956, p. 299.

[155] Bearman, P. W., "On Vortex Street Wakes", *Journal of Fluid Mechanics*, Vol. 28, Part 4, 1967, pp. 625-641.

[156] Sirovich, L., and Lim, C., "Comparison of Experiment with the Dynamics of the Von Karman Vortex Trail", *Studies of Vortex Dominated Flows*, Editors: M. Y. Hussaini and M. D. Salas, Springer-Verlag, New York, 1987, pp. 44-60.

[157] Every, M. J., King, R. and Weaver, D. S., "Vortex Excited Vibrations of Cylinders and Cables and Their Suppression," *Ocean Engineering*, Vol. 9, 1982, pp. 135-157.

[158] Roshko, A., "On the Development of Turbulent Wakes from Vortex Streets", *NACA Report No. 1191*, 1954.

[159] Roshko, A., "On the Wake and Drag of Bluff Bodies", *Journal of Aeronautical Sciences*, February, 1955, pp. 124-132.

[160] Mclachlan, N. W., "Ordinary Nonlinear Differential Equations in Engineering and Physical Sciences," *Clarendon Press*, Oxford, 2nd Edition, 1955, pp. 140-141.

[161] "The Failure of Tacoma Narrows Bridge,"' *Federal Works Agency*, Washington, D.C., U.S.A., March 1941.

[162] Farquharson, F. B., "Aerodynamic Stability of Suspension Bridges with Special Reference to the Tacoma Narrows Bridge," *The University of Washington Press*, Seattle, 1949.

[163] Steinman, D. B., *Famous Bridges of the World*, Random House, New York, 1953, pp. 69, 90-91.

[164] Parkinson, G. V., "Wind-Induced Instability of Structures," *Philosophical Transactions of the Royal Society of London*, A269, pp. 395-409.

[165] Synge, J. L., and Griffith, B. A., *Principles of Mechanics*, McGraw-Hill Book Company, New York, 3rd edition, 1959, p. 435.

[166] Hartlen, R. T., and Currie, I. G., "Lift-Oscillator Model of Vortex-Induced Vibra-

tion," *Journal of the Engineering Mechanics, Proceedings of the ASCE*, October 1970, EM5, pp. 577-591.

[167] Iwan, W. D., and Blevins, R. D., "A Model for Vortex Induced Oscillation of Structures," *Transactions of the ASME, Journal of Applied Mechanics*, September 1974, pp. 581-586.

[168] Blevins, R. D., *Flow-Induced Vibrations*, McGraw-Hill Book Company, New York, 2nd edition, 1990, pp. 67-74.

[169] Verhulst, F., *Nonlinear Differential Equations and Dynamical Systems*, Springer-Verlag, Berlin, 1990, pp. 15-16.

[170] Minorsky, N., *Nonlinear Oscillations*, D. Van Nostrand Company, New York, 1962, p. 219.

[171] Nayfeh, A. H., and Mook, D. T., *Nonlinear Oscillations*, John Wiley & Sons, New York, 1979, pp. 3-6.

[172] Thompson, J. M. T., *Bifurcational Aspects of Catastrophe Theory*, Annals New York Academy of Sciences, Vol. 316, 1979, pp. 553-571.

[173] Thompson, J. M. T., *Instabilities and Catastrophes in Science and Engineering*, John Wiley & Sons, New York, 1982, pp. 1-34, 155-182.

[174] Stewart, I., "Applications of Catastrophe Theory to the Physical Sciences," *Physica 2D*, 1981, pp. 245-305.

[175] Poore, A. B., and Al-Rawi, A., "Some Applicable Hopf Bifurcation Formulas and an Application in Wind Engineering," *Annals New York Academy of Sciences*, Vol. 316, 1979, pp. 590-604.

[176] Holmes, P., and Marsden, J. E., "Qualitative Techniques for Bifurcation Analysis

of Complex Systems," *Annals New York Academy of Sciences*, Vol. 316, 1979, pp. 608-622.

[177] Poore, A. B., Doedl, E. J., and Cermak, J. E., "Dynamics of the Iwan- Blevins Wake Oscillator Model," *International Journal of Nonlinear Mechanics*, Vol. 21, No. 4, 1986, pp. 291-302.

[178] Hall, S. A., and Iwan, W. D., "Oscillations of a Self-excited, Nonlinear System," *Transactions of the ASME, Journal of Applied Mechanics*, Vol. 51, December 1984, pp. 892-898.

[179] Thompson, J. M. T., and Stewart, H. B., *Nonlinear Dynamics and Chaos - Geometrical Methods for Engineers and Scientists*, John Wiley & Sons, New York, 1986, pp. 59-62.

[180] Parkinson, G. V., and Brooks, N. P. H., "On the Aeroelastic Instability of Bluff Cylinders," *Transactions of the ASME, Journal of Applied Mechanics*, June 1961, pp. 252-258.

[181] Novak, M., "Galloping and Vortex Induced Oscillations of Structures," *Proceedings of the 3rd International Conference on Wind Effects on Buildings and Structures*, Tokyo, 1971, Editors: Japan Organizing Comittee, pp. 799-809.

[182] Richardson, A. S., "Predicting Galloping Amplitudes," ASCE Journal of Engineering Mechanics, Vol. 14, 1988, pp. 716-723.

[183] Lawson. T. V., *Wind Effects on Buildings - Volume 1, Design Applications*, Applied Science Publishers, London, 1980, Chapter 6, pp. 97-167.

[184] Novak, M., and Tanaka, H., "Effect of Turbulence on Galloping Instability," *ASCE Journal of the Engineering Mechanics Division*, Vol. 100, pp. 27-47.

[185] Kubo, Y., Modi, V. J., Yasuda, H., and Kato, K., "On the Suppression of Aerody-namic Instabilities Through the Moving Surface Boundary-layer Control," *Journal of Wind Engineering and Industrial Aerodynamics*, Vol. 41-44, 1992, pp. 205-216.

[186] Ou, Y. R., "Control of Oscillatory forces on a Circular Cylinder by Rotation," *Proceedings of the Fourth International Symposium on Computational Fluid Dynamics*, Davis, California, U.S.A., September 1991, Vol. 2, pp. 897-902.

APPENDIX A : INSTRUMENTATION USED IN THE STUDY

(1) Pressure Measurement System (SCANIVALVE CORPORATION, USA)

    - Model J (500 psi), scanivalve transducer

    - CTLR2/S2-S6, solenoid controller

    - SCSG2, signal conditioner

    - accuracy, 2.5381×10^{-3} mV/N/m^2

(2) Linear Variable Differential Transformer (CHAEVITZ ENGINEERING, USA)

    - model 3000 HR-1722

    - range = $\pm$ 3.0 inch (7.5cm), excitation = 3 volts @ 2500 Hz.

    - linearity = $\pm$ 0.14% of fullrange output

(3) Real Time Analyzer (SPECTRASCOPE, USA)

    - model SD335

    - range = 20 Hz. to 50 KHz.

    - bandwidth = 0.06 Hz.(@ 20 Hz.) to 150 Hz.(@ 50 KHz.)

(4) Variable Transformer (OHMITE MANUFACTURING COMPANY, USA)

    - catalogue no. VT8-F

    - input = 120 volts, 50-60 Hz.

    - output = 0-140 volts, 7.5A, D.C.

(5) D.C. Power Supply (EPSCO INC., USA)

    - input = 115 volts, 50-60 Hz.

    - output = 0-16 volts, 8A maximum or 0-32 volts, 4A @ 0.1% ripple

(6) High Speed A.C. Motors (DUMORE CORPORATION, USA)

    - catalogue no. 6-021, Model 8551, Superflex-623G

    - Specifications: 115 Volts, 3.8A, 0-60Hz., 1/4 h.p., noload 22000 rpm

(7) Digital Tachometer (SHIMPO, JAPAN)

- Model DT-205B

- range = 6-30,000 rpm

- accuracy = 2 rpm

(8) A/D Input-Output System (DATA TRANSLATION, INC., U.S.A.)

- DT 2801 Series

- Number of Channels = 8 or 16

- A/D Resolution = 12 bits

- Maximum Gain = 8

- A/D input = 13.7 KHz.

(9) IBM PC/486 Compatible Computer

(10) Barocel Pressure Sensor (DATAMETRICS, U.S.A.)

- Type 550-5

- Range 10 PSI ($690 \ N/m^2$)

- Resolution, 10^{-6} PSI ($6.9 \times 10^{-5} \ N/M^2$)

(11) Hotwire System (DANTEC; Denmark, DISA Elektronik; Denmark)

- DANTEC Probe Type 55 P11

- Sensor Resistance at 20°C, $R_{20} = 3.4\Omega$

- Leads Resistance, $R_L = 0.5\Omega$

- Sensor TCR, $a_{20} = 0.36\%$

- Total Resistance, $R = R_{TOT} a_{20} R_{20} (T_{sensor} - T_0)$

- measure R_{TOT} at ambient conditions

- DISA Type 55D 25 Auxilliary Unit

- DISA Type 55D 31 Digital Voltmeter

- DISA Type 55D 01 Constant Temperature Anemometer

- DISA Type 55D 35 RMS Unit

APPENDIX B : SINGULARITY ELEMENTS AND INFLUENCE COEFFICIENTS

B.1 Velocity Induced by a Two-dimensional Straight Vortex Filament

Figure B-1 shows a straight vortex filament with a constant vortex strength 'Γ'. According to the Biot-Savart Law, induced velocity due to an element dl is

$$\delta \vec{V}_\theta = \frac{\Gamma}{4\pi} \frac{\vec{dl} \times \vec{r}}{|r|^3}. \qquad (B.1)$$

For an infinitely long (two dimensional) vortex filament the Biot-Savart law gives

$$\delta \vec{V}_\theta = \int_{-\infty}^{+\infty} \frac{\Gamma}{4\pi} \frac{sin\,\beta}{r^2} dl. \qquad (B.2)$$

Substituting, $r_1 = r\,cos\,\theta$, $l = r_1\,tan\,\beta$, $dl = r_1 d\beta / cos^2\beta$; and for $-\infty \leq l \leq +\infty$ we get $0 \leq \beta \leq \pi$, reulting in

$$\delta \vec{V}_\theta = \frac{\Gamma}{4\pi r_1} \int_0^\pi sin\,\beta d\beta = \frac{\Gamma}{2\pi r_1}. \qquad (B.3)$$

B.2 Panel with Uniform Vortex Distribution

Figure B-2 shows a two-dimensional panel element composed of infinitely long vortex filaments distributed along the length of the panel. Each filament is perpendicular to the plane of the page. In this case one can apply equation (B.3). The strength of the vortex filament, γ_i per unit length, remains constant from one end of the panel to the other.

The velocity components du_e and dw_e at the point (x,z) due to the small element of vortex distribution on $d\xi$ are:

$$du_e(x,z) = \frac{\gamma_i}{2\pi} \left[\frac{z}{(x-\xi)^2 + z^2} \right] d\xi; \qquad (B.4)$$

$$dw_e(x,z) = -\frac{\gamma_i}{2\pi} \left[\frac{x-\xi}{(x-\xi)^2 + z^2} \right] d\xi. \qquad (B.5)$$

Therefore:

$$u_e(x,z) = \int_{-\delta_i/2}^{\delta_i/2} \frac{\gamma_i}{2\pi} \left[\frac{z}{(x-\xi)^2 + z^2} \right] d\xi, \qquad (B.6)$$

$$u_e(x,z) = \frac{\gamma_i}{2\pi} \left[tan^{-1} \frac{x + \frac{\delta_i}{2}}{z} - tan^{-1} \frac{x + \frac{\delta_i}{2}}{z} \right], \qquad (B.7)$$

$$u_e(x,z) = \gamma_i F(x,z,\delta_i); \qquad (B.8)$$

$$w_e(x,z) = \int_{-\delta_i/2}^{\delta_i/2} \frac{\gamma_i}{2\pi} \left[\frac{x-\xi}{(x-\xi)^2 + z^2} \right] d\xi, \qquad (B.9)$$

$$w_e(x,z) = -\frac{\gamma_i}{2\pi} ln \left[\frac{\left(x - \frac{\delta_i}{2}\right)^2 + z^2}{\left(x + \frac{\delta_i}{2}\right)^2 + z^2} \right], \qquad (B.10)$$

$$w_e(x,z) = \gamma_i F(x,z,\delta_i). \qquad (B.11)$$

Since the panels are at different orientations, the expressions of velocity components must be defined with respect to the coordinate system (X,Z) of the body (Figure B-3). For the vorticity distribution along a panel i, the velocity components u and w, taken relative to the reference coordinate system (X,Z), are:

$$u(X,Z) = \gamma_i \left\{ F(x,z,\delta_i) \cos \theta_i - G(x,z,\delta_i) \sin \theta_i \right\}; \qquad (B.12)$$

$$w(X,Z) = \gamma_i \left\{ F(x,z,\delta_i) \sin \theta_i - G(x,z,\delta_i) \cos \theta_i \right\}; \qquad (B.13)$$

where

$$x = (X - X_{mi}) \cos \theta_i + (Z - Z_{mi}) \sin \theta_i; \qquad (B.14)$$

$$z = -(X - X_{mi}) \sin \theta_i + (Z - Z_{mi}) \cos \theta_i. \qquad (B.15)$$

Here X_{mi} and Z_{mi} are the mid-points of panel i in the (X,Z) system. The velocity components on the jth panel (at the center of the panel, called the collocation point) due to the ith panel are:

$$u_{ji} = \gamma_i (F_{ji} \cos \theta_i - G_{ji} \sin \theta_i); \qquad (B.16)$$

$$w_{ji} = \gamma_i (F_{ji} \sin \theta_i + G_{ji} \cos \theta_i). \qquad (B.17)$$

For a collocation of N panels descretizing a body surface, this becomes:

$$u_j = \gamma_i \sum_{i=1}^{N} (F_{ji} \cos \theta_i - G_{ji} \sin \theta_i) = \sum_{i=1}^{N} A_{ji} \gamma_i; \qquad (B.18)$$

229

$$w_j = \gamma_i \sum_{i=1}^{N} (F_{ji} \sin\theta_i + G_{ji} \cos\theta_i) = \sum_{i=1}^{N} B_{ji}\gamma_i; \qquad (B.19)$$

where:

$$A_{ji} = A(x, z, \delta_i, \theta_i); \qquad (B.20)$$

$$B_{ji} = B(x, z, \delta_i, \theta_i); \qquad (B.21)$$

$$X_{ji} = (X_{mj} - X_{mi}) \cos\theta_i + (Z_{mj} - Z_{mi}) \sin\theta_i; \qquad (B.22)$$

$$X_{ji} = -(X_{mj} - X_{mi}) \sin\theta_i + (Z_{mj} - Z_{mi}) \cos\theta_i; \qquad (B.23)$$

$$\delta_i = [(X_{i+1} - X_i)^2 + (Z_{i+1} - Z_i)^2]; \qquad (B.24)$$

$$\cos\theta_i = (X_{i+1} - X_i)/\delta_i; \qquad (B.25)$$

$$\sin\theta_i = (Z_{i+1} - Z_i)/\delta_i. \qquad (B.26)$$

B.3   Panel with Linear Vortex Distribution

Consider a linearly varying vortex distribution across the panel i between $-\delta_i/2 < x < \delta_i/2$ with strengths γ_i and γ_{i+1} at x = $\pm\delta_i/2$, respectively, as shown in Figure B-4.

The variation of the vortex strength across the panel can be described as

$$\gamma_i = \frac{\gamma_{i+1} + \gamma_i}{2} - \frac{\gamma_{i+1} - \gamma_i}{\delta_i}\xi. \qquad (B.27)$$

Using equations (B.4) and (B.5), (B.14) and (B.15), and (B.27), the velocity components can be written as:

$$u(X, Z) = \frac{1}{2}\Big[\gamma_{i+1}\{(F(x, z, \delta_i) - zG(x, z, \delta_i)/(\frac{\delta_i}{2}) - xF(x, z, \delta_i)/(\frac{\delta_i}{2})) \cos\theta_i$$

$$-(G(x, z, \delta_i) - xG(x, z, \delta_i)/(\frac{\delta_i}{2}) + zF(x, z, \delta_i)/(\frac{\delta_i}{2}) - 1/\pi)\sin\theta_i\}$$

$$+\gamma_i\{(F(x, z, \delta_i) + zG(x, z, \delta_i)/(\frac{\delta_i}{2}) + xF(x, z, \delta_i)/(\frac{\delta_i}{2}))\cos\theta_i$$

$$-(G(x, z, \delta_i) + xG(x, z, \delta_i)/(\frac{\delta_i}{2}) - zF(x, z, \delta_i)/(\frac{\delta_i}{2}) + 1/\pi)\sin\theta_i\}\Big]; \qquad (B.28)$$

$$w(X, Z) = \frac{1}{2}\Big[\gamma_{i+1}\{(F(x, z, \delta_i) - zG(x, z, \delta_i)/(\frac{\delta_i}{2}) - xF(x, z, \delta_i)/(\frac{\delta_i}{2})) \, sin\,\theta_i$$

$$+(G(x, z, \delta_i) - xG(x, z, \delta_i)/(\frac{\delta_i}{2}) + zF(x, z, \delta_i)/(\frac{\delta_i}{2}) - 1/\pi)cos\theta_i\}$$

$$+\gamma_i\{(F(x, z, \delta_i) + zG(x, z, \delta_i)/(\frac{\delta_i}{2}) + xF(x, z, \delta_i)/(\frac{\delta_i}{2}))sin\theta_i$$

$$-(G(x, z, \delta_i) + xG(x, z, \delta_i)/(\frac{\delta_i}{2}) - zF(x, z, \delta_i)/(\frac{\delta_i}{2}) + 1/\pi)cos\theta_i\}\Big]. \qquad (B.29)$$

The velocity components at the j-th collocation point due to N panels on the body surface can be written in the form:

$$u_j = \sum_{i=1}^{N} a_{ji}\gamma_{i+1} + \sum_{i=1}^{N} b_{ji}\gamma_i = \sum_{i=1}^{N+1} A'_{ji}\gamma_i; \qquad (B.30)$$

$$w_j = \sum_{i=1}^{N} c_{ji}\gamma_{i+1} + \sum_{i=1}^{N} d_{ji}\gamma_i = \sum_{i=1}^{N+1} B'_{ji}\gamma_i; \qquad (B.31)$$

where:

$$a_{ji} = \frac{1}{2}\Big[(F(x, z, \delta_i) - zG(x, z, \delta_i)/(\frac{\delta_i}{2}) - xF(x, z, \delta_i)/(\frac{\delta_i}{2})) \, cos\,\theta_i$$

$$-(G(x, z, \delta_i) - xG(x, z, \delta_i)/(\frac{\delta_i}{2}) + zF(x, z, \delta_i)/(\frac{\delta_i}{2}) - 1/\pi)sin\theta_i\Big]; \qquad (B.32)$$

$$b_{ji} = \frac{1}{2}\Big[(F(x, z, \delta_i) + zG(x, z, \delta_i)/(\frac{\delta_i}{2}) + xF(x, z, \delta_i)/(\frac{\delta_i}{2}))cos\theta_i$$

$$-(G(x, z, \delta_i) + xG(x, z, \delta_i)/(\frac{\delta_i}{2}) - zF(x, z, \delta_i)/(\frac{\delta_i}{2}) + 1/\pi)sin\theta_i\}\Big]; \qquad (B.33)$$

$$c_{ji} = \frac{1}{2}\Big[(F(x, z, \delta_i) - zG(x, z, \delta_i)/(\frac{\delta_i}{2}) - xF(x, z, \delta_i)/(\frac{\delta_i}{2})) \, sin\,\theta_i$$

$$+(G(x, z, \delta_i) - xG(x, z, \delta_i)/(\frac{\delta_i}{2}) + zF(x, z, \delta_i)/(\frac{\delta_i}{2}) - 1/\pi)cos\theta_i\Big]; \qquad (B.34)$$

$$d_{ji} = \frac{1}{2}\Big[(F(x, z, \delta_i) + zG(x, z, \delta_i)/(\frac{\delta_i}{2}) + xF(x, z, \delta_i)/(\frac{\delta_i}{2}))sin\theta_i$$

$$-(G(x, z, \delta_i) + xG(x, z, \delta_i)/(\frac{\delta_i}{2}) - zF(x, z, \delta_i)/(\frac{\delta_i}{2}) + 1/\pi)cos\theta_i\}\Big]. \qquad (B.35)$$

Here:

$$A'_{ji} = a_{ji-1} + b_{ji};$$

$$B'_{ji} = c_{ji-1} + d_{ji};$$

$$A'_{j1} = b_{j1};$$

$$A'_{jN+1} = a_{jN};$$

$$B'_{j1} = d_{j1};$$

$$B'_{jN+1} = c_{jN}.$$

The quantities X_{ji}, Z_{ji}, δ_i, $\cos \theta_i$, and $\sin \theta_i$ are given by equations (B.20) to (B.26).
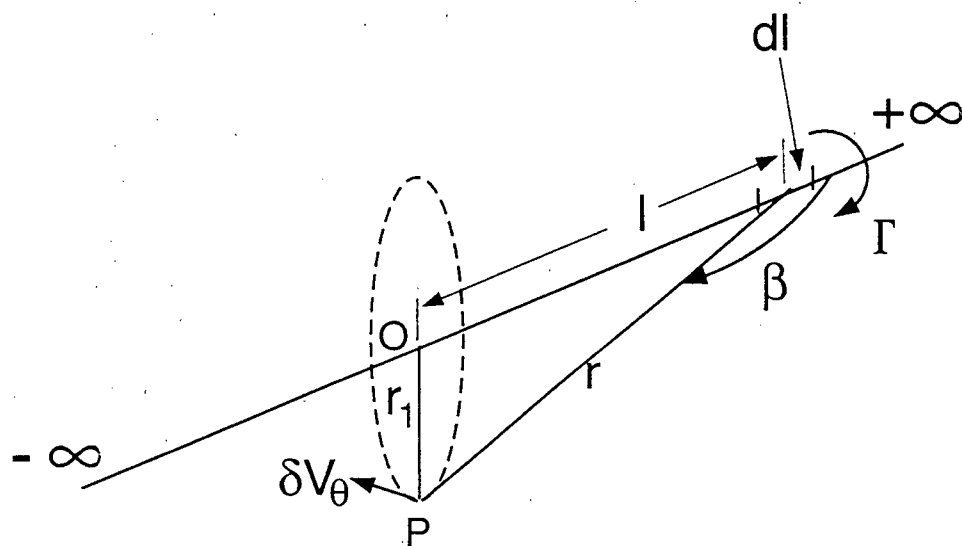
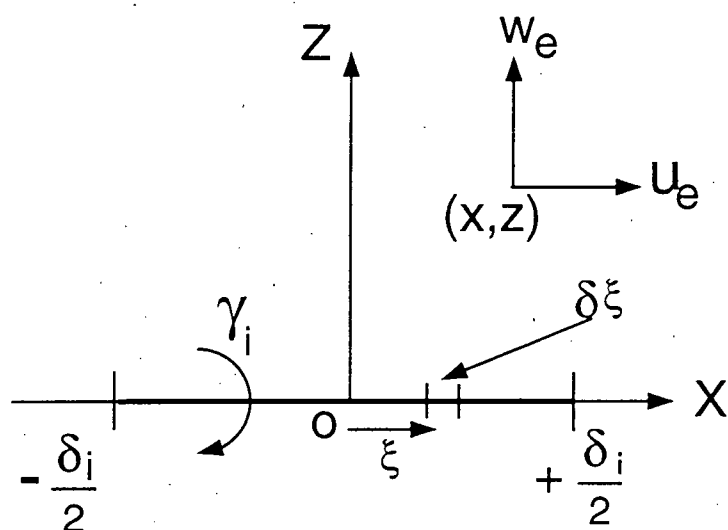**Figure B-1**   An infinitely long vortex filament.

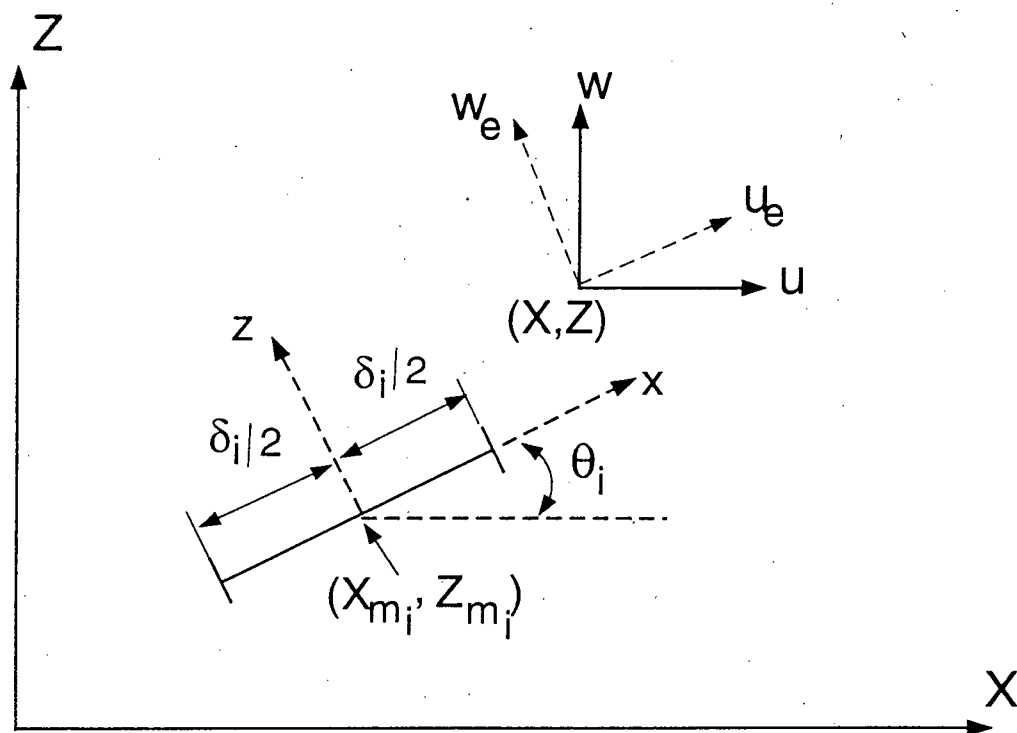**Figure B-2**   i-th panel with constant vortex distribution.

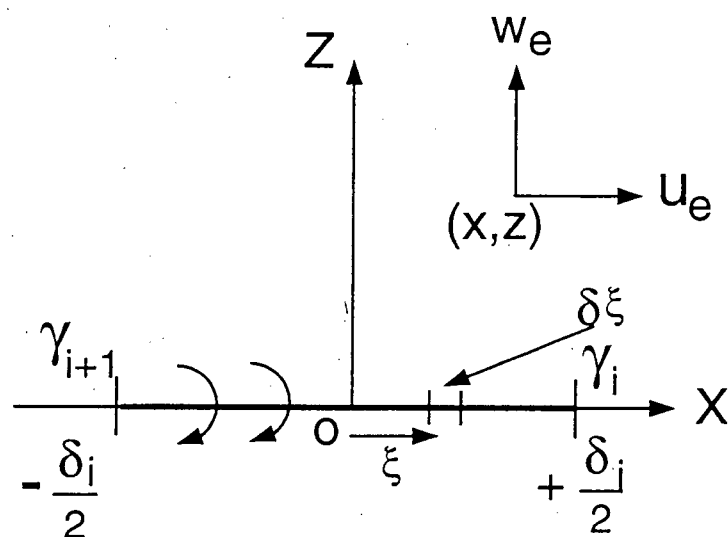**Figure B-3**   Reference coordinate system.

Figure B-4   i-th panel with linear vortex distribution.

APPENDIX C : POWER CONSUMPTION FOR THE MSBC

The MSBC being an active control method a remark concerning the amount of energy consumption would be appropriate. An aspect of importance is the relative gain in terms of power when the MSBC is used as a drag reduction device. Similarly it would be necessary to know the power required for lift augmentation on a wing. To answer such questions it was decided to obtain an estimate of the power requirements for real-life applications.

The rotating cylinder used for the bluff body model had a diameter of 38mm, a length of 733mm and weighed 2043 gm. It was fabricated from solid aluminium. The power consumption was calculated from the measured voltage and current required to rotate the cylinder. The cylinder rotation rate was fixed at various values to obtain appropriate rates of the momentum injection (U_C/U). The results of the experiment are shown in Figure C-1. At the maximum rate of the momentum injection $(U_C/U = 4)$, the power consumption is about 0.22 h.p. Most of the energy is expended in overcoming the bearing friction, the contribution due to aerodynamic resistance being marginal. For a full-scale truck, it is estimated that the rotating cylinder would be ten times as heavy (assuming a hollow cylinder made of thin sheet of aluminium). The power consumption also would be ten times as much, ≈ 2.5 h.p., The truck engine power is around 400 – 500 h.p. Similar estimates for a rotating cylinder applied to a 60 storey (240m) tall building for vibration control would require a cylinder about 80m long (1/3rd the height of the building). Such a cylinder would weigh 100 times (≈ 200 kg) and would need about 25 h.p.. For a building one requires cylinders at all the four corners, and thus the total power requirement would be about 100 h.p. Note, all the estimates are highly conservative.

A rotating cylinder applied to the leading-edge of the wing of a Cessna type aircraft has been flight-tested to evaluate its performance. The results suggest that the power consumption is about 2% of the engine power. NASA has flown the OV-10A aircraft built by the ROCKWELL international, which was fitted with rotating cylinders at the leading-edge of the flap. The OV-10A has two engines, each

about 730 h.p., so a 2% power requirement translates into about 15 h.p. per each rotating cylinder.
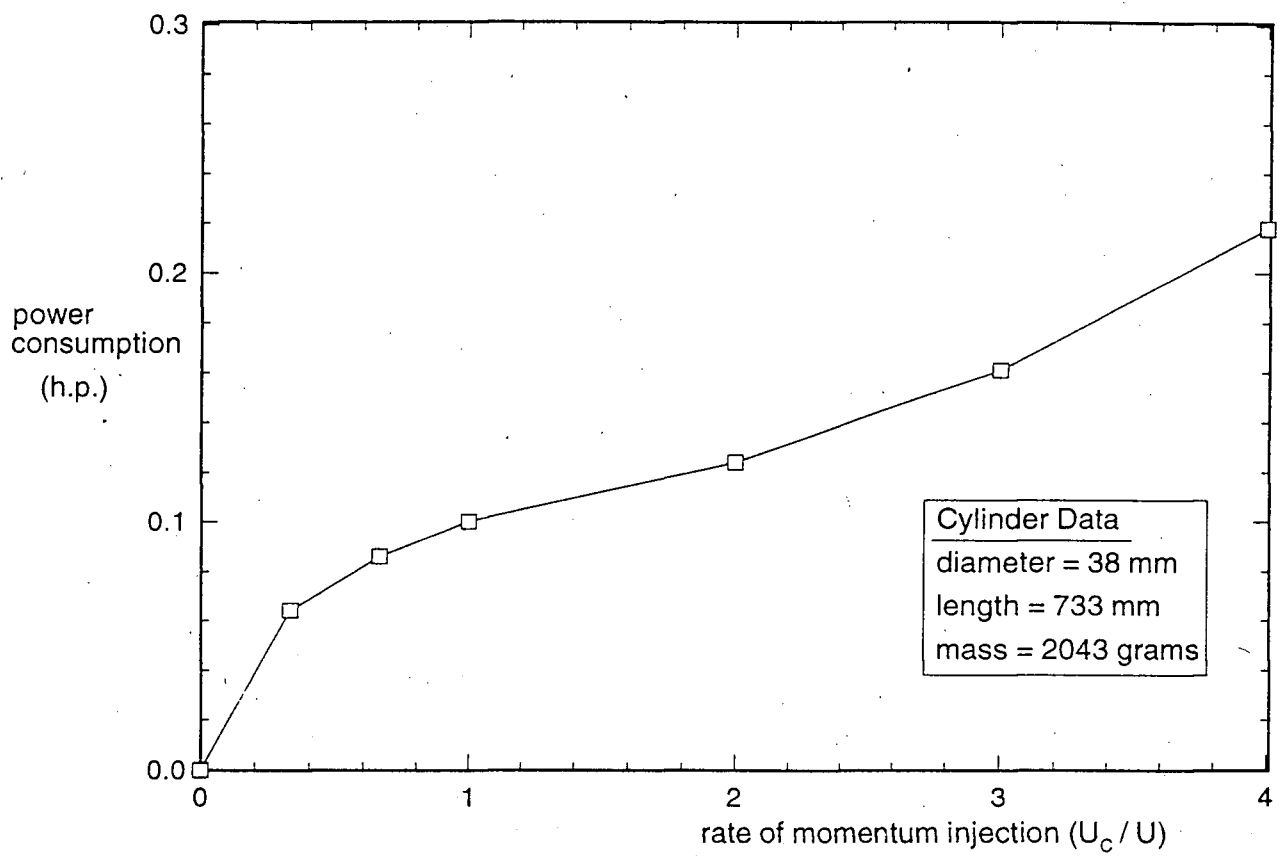
Figure C-1 Experimentally measured power consumption of a momentum injecting rotating cylinder.

APPENDIX D : DYNAMIC SYSTEM PARAMETERS

In the dynamic experiments to study the flow-induced vibrations it is necessary to determine the system natural frequency and damping factor. The set-up for the dynamic experiments is shown in Figure 2-9. The system natural frequency and damping factor were determined from a typical amplitude vs. time signal of the bluff body model undergoing free vibrations (Figure D-1). The signal sampling period (T) was 100 seconds and the sampling rate was 100 times per second. The FFT analysis showed that the natural frequency of the vibration (f_n) is 1.39 Hz (Figure D-2). The amplitude of vibrations in Figure D-1 is shown in terms of the computer output which can be calibrated in terms of the displacement. The calibration of the displacement transducer is shown in Figure D-3.

The logarithmic decrement for the decaying vibrations is defined as,

$$\delta = \frac{1}{\mu - 1} ln \frac{A_0}{A_{\mu-1}}, \qquad \mu = 0, 1, 2, ..., \qquad (D.1)$$

where: A_0 = initial amplitude of the vibration; A_μ = amplitude of vibration after μ cycles; and μ = number of cycles. From Figure D-1, the logarithmic decrement δ is determined to be 0.16923. The circular natural frequency $\omega_n = 2\pi f_n = 8.7336$ rad/s. The stiffness (k_1) of each spring (Figure 2-9) is 40,712 gm/s^2. There are four springs in parallel, giving a total stiffness (k) of 4×40712 gm/s^2. Figure D-4 shows the force vs. displacement characteristics of the spring, as well as the operating range. The circular natural frequency is given by

$$\omega_n = \sqrt{\frac{k}{m_e}}. \qquad (D.2)$$

The system effective mass (m_e) as determined from equation (D.2) is 2,135 gm.

The damping factor (β) is given by

$$\beta = \sqrt{\frac{1}{1 + (2\pi/\delta)^2}}. \qquad (D.3)$$

The value of β was found to be 0.002693.

The system parameters may be summarized as follows:

model length, $l_1 = 671$ mm;

model height, $h_1 = 127$ mm;

system mass, $m_e = 2135$ grams;

natural frequency, $f_n = 1.39$ Hz;

damping factor, $\beta = 0.002693$;

total stiffness, $k \doteq 4 \times 40712$ gm/s^2;

air density, $\rho = 1.2$ kg/m^3;

mass parameter, $m = \rho h_1{}^2 l_1 / 2m_e = 0.003042$;

Strouhal number of the square section model, $St = 0.161$;

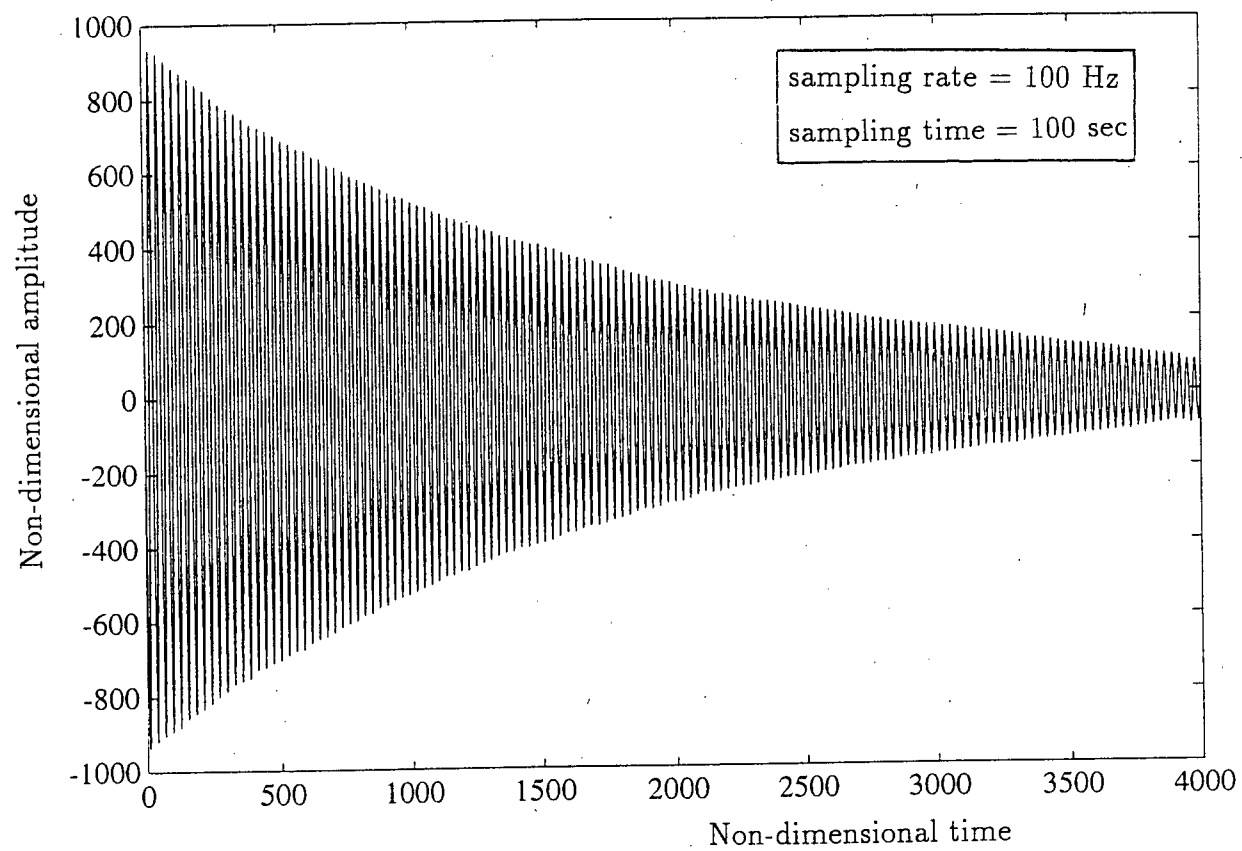critical wind velocity for resonance, $V_c = f_n h_1 / St = 1.1$ m/s.

Figure D-1 Amplitude vs. time history of the bluff body model (square-section) undergoing free vibrations.
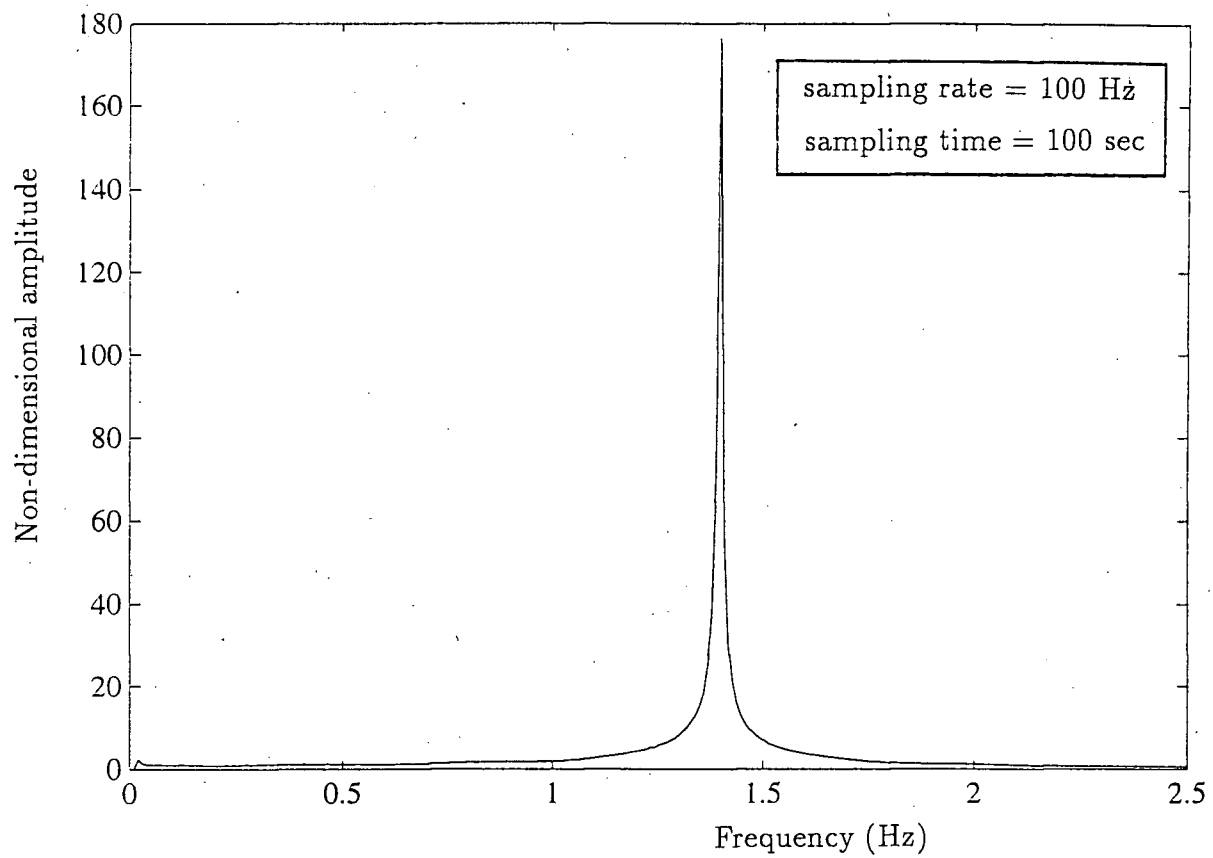
Figure D-2   Natural frequency of the vibrating bluff body (square-section) as obtained through the FFT analysis of the amplitude vs. time history.
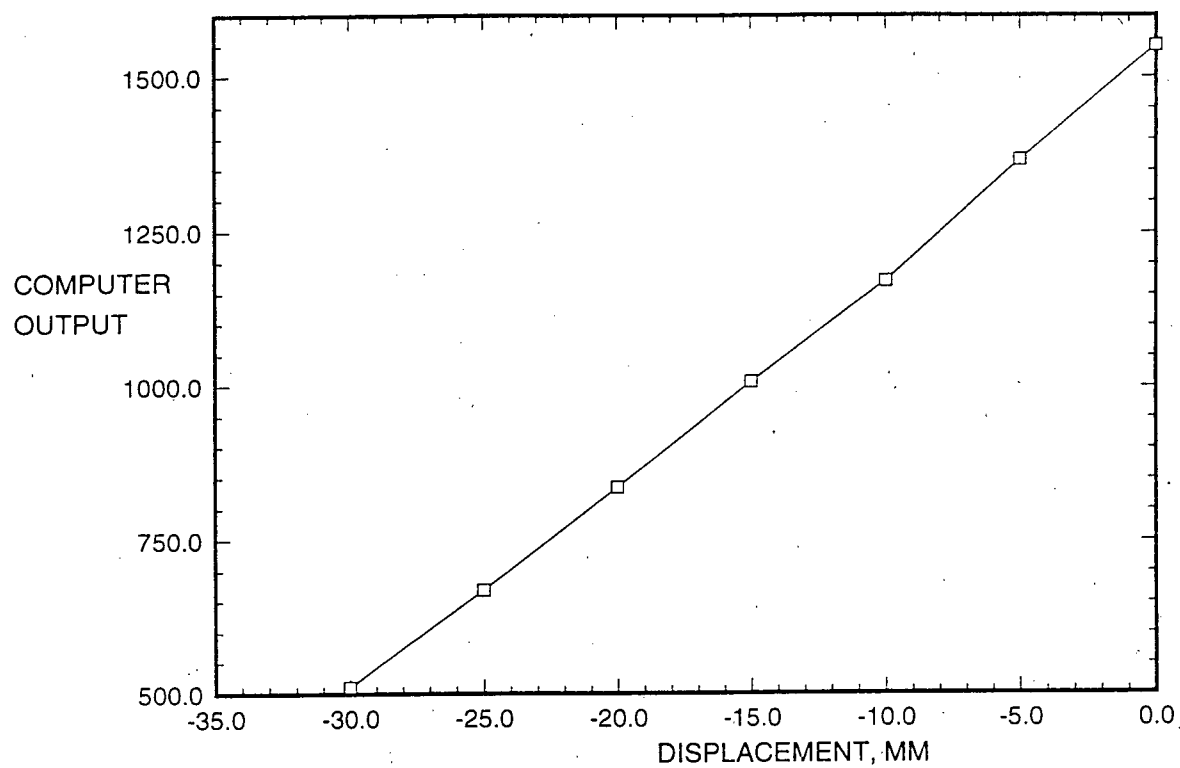
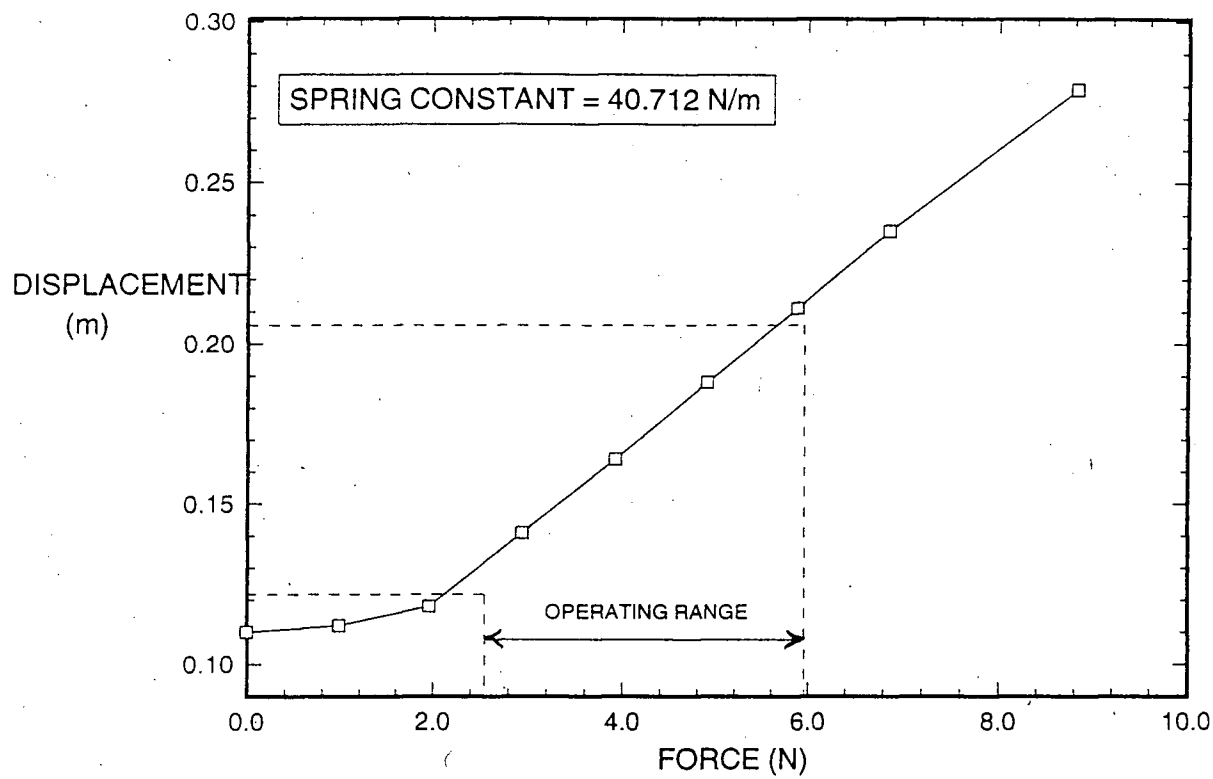**Figure D-3**   Calibration of the displacement transducer

Figure D-4   Calibration of the spring used for the dynamic test set-up.